

# Wind Threshold Review

## Wind Threshold Study Queensferry Crossing

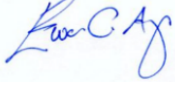
17 FB 1203 039 /R004 Revision 02

December 2021



**Document Control Sheet**

Project Name:	Wind Threshold Study Queensferry Crossing
Project Number:	17 FB 1203 039
Report Title:	Wind Threshold Review
Report Number:	R004

<b>Issue Status/Amendment</b>	<b>Prepared</b>	<b>Reviewed</b>	<b>Approved</b>
00 Draft Issue for comment	Name: Patrick Madden Signature: Date:	Name: Angus Bruce Signature: Date:	Name: Ewan Angus Signature: Date:
01 Issue following comments	Name: Patrick Madden Signature:  Date: 25/10/2021	Name: Ewan Angus Signature:  Date: 29/10/2021	Name: Ewan Angus Signature:  Date: 29/10/2021
02 Updated based on comments	Name: Patrick Madden Signature:  Date: 16/12/2021	Name: Ewan Angus Signature:  Date: 17/12/2021	Name: Ewan Angus Signature:  Date: 17/12/2021
	Name: Signature: Date:	Name: Signature: Date:	Name: Signature: Date:

## Executive Summary

The Queensferry Crossing has wind shielding across the entire length of the main crossing to reduce the impact of wind on the vehicles using the bridge. The current operational wind thresholds on the Queensferry Crossing are based on the wind shielding reducing the overturning potential of vehicles, induced by a wind speed, by half. This is based on the existing wind tunnel testing report which confirmed that this was achieved. This reduction in overturning potential is then applied to the original Forth Road Bridge thresholds, the unshielded condition, to determine the equivalent Queensferry Crossing, shielded condition, thresholds.

Amey reviewed the existing studies and information available and concluded that the current thresholds could not be changed based on the information available, as handed over by the Designer (Ramboll) and Transport Scotland's Engineers (Jacobs/Arup).

The threshold for closure of the bridge to double decker buses, which is currently set to 60mph winds, is of particular interest to the study. The key objectives of the review are to ensure safety of, and to minimise disruption to bridge users. The project is part funded by the Scottish Road Research Board (SRRB).

To provide greater insight into how effective the as-built barriers are at reducing potential overturning moment Amey conducted a study that included:

- 2D CFD Modelling of the As Built wind barrier condition. Funded by the SRRB.
- Wind Tunnel Testing of the As Build wind barrier condition. Funded by the SRRB
- Lidar survey of the wind field around the bridge. Funded by Transport Scotland.

Following this study Amey have concluded that:

- Interim recommendations made following the CFD modelling to restrict double deck buses from using the hard shoulder as a bus lane are no longer required based on the more representative wind tunnel results.
- Wind direction should not be incorporated into the wind threshold protocol due to the variable and transient flow field across the bridge that makes the accurate monitoring of wind direction for the bridge operationally challenging.

- Based on this work the existing 60mph threshold for double decker buses is reasonable while maintaining the ability to use the hard shoulder as a bus lane.
- A recommendation of additional work which has the potential to allow the threshold to be increased by restricting the use of the hard shoulder as a bus lane has also been made. This will require additional wind tunnel tests to be carried out by the current bridge operator in partnership with the University of Nottingham. Some modifications to the existing wind tunnel model will be required, but the base model should be suitable to be reused.

## Contents

<b>Executive Summary</b> .....	<b>i</b>
<b>Introduction</b> .....	<b>1</b>
1.1 Queensferry Crossing.....	1
1.2 QC Wind Shielding .....	1
1.3 Designer’s testing and analysis .....	3
1.4 Current Wind Thresholds.....	4
1.5 Limitations of available data .....	6
1.6 Project Summary.....	7
<b>CFD Modelling</b> .....	<b>9</b>
2.1 Methodology .....	9
2.2 Results .....	12
<b>Wind Tunnel Study</b> .....	<b>26</b>
3.1 Methodology .....	26
3.2 Results .....	29
<b>Lidar Survey</b> .....	<b>34</b>
4.1 Methodology .....	34
4.2 Results .....	41
<b>Comparative analysis</b> .....	<b>44</b>
5.1 Comparing normalised wind speed data across studies .....	44
<b>Conclusion and recommendation</b> .....	<b>47</b>
6.1 Recommendation for additional work .....	48
<b>References</b> .....	<b>49</b>
<b>Appendix A</b> <b>Extract from Employer’s Requirements</b>	<b>A</b>
<b>Appendix B</b> <b>CFD modelling report</b>	<b>B</b>
<b>Appendix C</b> <b>Wind Tunnel Testing</b>	<b>C</b>
<b>Appendix D</b> <b>Lidar Survey</b>	<b>D</b>

## Figures

Figure 1: Section and Elevation of wind shielding used across the main sections of the bridge. ....	2
Figure 2 Section of QC at towers showing wind shielding configuration at edge of deck and around towers .....	2
Figure 3 QC Tower wind shield, flanking tower on either side.....	3
Figure 4 Forth Road Bridge wind speed procedures, The Forth Bridges (2018).....	4
Figure 5 Queensferry Crossing Wind Speed Procedures, The Forth Bridges (2018).....	5
Figure 6: a) Tested wind barrier Hansen, et al. (2012), b) image of constructed wind barrier on site, c) constructed barrier on main crossing showing VRS. ....	7
Figure 7: An overview of the CFD model boundary conditions with vehicle located in the Hard shoulder (University of Nottingham (UoN)) .....	11
Figure 8: Instantaneous velocity field showing unsteady flow and vortex generation in wake of wind barrier (6m/s, 0° AoA) (UoN).....	13
Figure 9: Time averaged velocity field showing high speed jets through gaps and shear layer above wind barrier (6m/s, 0° AoA) (UoN) .....	13
Figure 10: Time averaged velocity field with carriageway section and vehicles overlain for clarity (Note: vehicles not included in this simulation) (6m/s, 0° AoA) (UoN).....	13
Figure 11: Variation of the normalised time-averaged wind speed magnitude profile at locations across the bridge deck, (6m/s, 0° AoA). X-axis normalised by upstream wind speed. Y-axis normalised by height of bus (4.2m). Horizontal dashed line indicates the normalised height of the wind barrier. (UoN) .....	15
Figure 12: <i>Profile of the time-averaged wind speed magnitude at different wind speeds, estimated at (a) centre of the hard shoulder, (b) centre of the left lane and (c) centre of the right lane.</i> ....	16
Figure 13: <i>Profiles of the time-averaged wind speed magnitude at the centre of (a) the hard shoulder, (b) left lane and (c) right lane, at the wind speed of 2 ms<sup>-1</sup> and at different angles of attack. The dashed line indicates the normalised height of the wind barrier.</i> .....	16
Figure 14: Contour plots of the time-averaged velocity field, comparing the flow field when the vehicle is (top) at the centre of the hard shoulder and (bottom) at the centre of the left lane, at the angle of attack of, left: -4°, middle: 0°, right: +4°. ....	18

Figure 15: Variation of the RMS pressure coefficient around the vehicle with respect to the angle of attack, when the vehicle is at the centre of the hard shoulder. .... 19

Figure 16: Variation of the RMS pressure coefficient around the vehicle with respect to the angle of attack, when the vehicle is at the centre of Lane 1. .... 19

Figure 17: Comparison of as built wind barrier (left) and FCBC wind tunnel model (right)..... 22

Figure 18: Time averaged velocity field of the as built wind barrier (2m/s, 0° AoA) (UoN)..... 23

Figure 19: Time averaged velocity field of the approximated FCBC wind tunnel wind barrier (2m/s, 0° AoA) (UoN) ..... 23

Figure 20: Wind tunnel model, with carriageway section, wind barrier, and model vehicle located in the hard shoulder (UoN) ..... 27

Figure 21: Wind tunnel reference vehicle with location of pressure tap rings indicated ..... 28

Figure 22: *Profile of the normalised time-averaged wind speed magnitude, at 0° AoA, for different wind speeds, estimated at (a) centre of the hard shoulder, (b) centre of the left lane and (c) centre of the right lane.*..... 30

Figure 23: *Profile of the normalised time-averaged wind speed magnitude, at different AoA, for 6m/s wind speed, estimated at (a) centre of the hard shoulder, (b) centre of the left lane and (c) centre of the right lane.*..... 30

Figure 24: No wind barrier - Distribution of the mean pressure coefficient around the five rings at the wind speed of 6 m/s and 0° angle of attack. Left (sub-figure) – outer (side) face; Right – inner (side) face; Top – top face; Bottom – bottom face..... 31

Figure 25: Gantry 08 – Lidar location relative to QC ..... 35

Figure 26: Mesoscale PPI Scan overlaid on map ..... 36

Figure 27: a) PPI Microscale 0.5° b) PPI Microscale 0.6° ..... 36

Figure 28: PPI scan intercepting wind barrier..... 38

Figure 29: Scan showing location of sections through the data, scan: 04/03/2020 00:07:09..... 39

Figure 30: Orientation of Queensferry Crossing and the 245° to 290° wind direction data range sampled ..... 40

Figure 31: Reconstructed wind speed (m/s) and direction on 18/03/2020 at 13:00:47 – area zoomed in for clarity..... 42

Figure 32: Heatmap visualisation of normalised radial wind speed - 0.6° PPI scan, 270° direction ..... 43

Figure 33: Heatmap visualisation of normalised radial wind speed - 0.5° PPI scan, 270° direction ..... 43

Figure 34: Hard shoulder normalised wind speed results compared across Lidar, CFD, and  
Wind Tunnel tests. .... 45

Tables

Table 1: CFD Simulation Summary of variables tested ..... 11  
Table 2: Velocity sampling references and corresponding locations..... 14  
Table 3: Vehicle in Hard Shoulder - Rolling coefficients, and associated reduction factors. .... 20  
Table 4: Vehicle in Lane 1 - Rolling coefficients, and associated reduction factors. .... 20  
Table 5 Rolling coefficients compared for both wind barrier configurations ..... 24  
Table 6: CFD Simulation Summary of variables tested ..... 28  
Table 7: Vehicle in Hard Shoulder - Rolling coefficients, and associated reduction factors. .... 32  
Table 8: Survey scan summary table by Leosphere ..... 37  
Table 9: Number and type of scans carried out within each scanning sequence ..... 38

---

## **Introduction**

On behalf of Transport Scotland, Amey are carrying out a review of the current wind thresholds on the Queensferry Crossing. The threshold for closure of the bridge to double decker buses, which is currently set to 60mph winds, is of particular interest to the study. The key objectives of the review are to ensure safety of, and to minimise disruption to bridge users. The project is part funded by the Scottish Road Research Board (SRRB).

### **1.1 Queensferry Crossing**

The Queensferry Crossing (QC) opened on the 30<sup>th</sup> August 2017 and replaces the Forth Road Bridge (FRB) as the primary carrier of road vehicles crossing the Firth of Forth between Fife to the North and Edinburgh, including links to the M8 and M9, to the south. The main structure is a 2.7km long, three tower, cable-stayed bridge. It carries the northbound and southbound carriageways of the M90, each with two running lanes and an additional hard shoulder which can be used as a bus lane if required.

The QC has wind shielding across the entire length of the main crossing, located on the east and west deck edge beams, to reduce the impact of wind on the vehicles using the bridge. There is also stepped height wind shielding located in the central reserve on both sides of the three main towers.

### **1.2 QC Wind Shielding**

The Queensferry Crossing wind shielding is designed to achieve a 50% reduction on the overturning moment on the critical adjacent road lane for wind speeds perpendicular to the bridge compared to the exposed condition, as per the Employers Requirements section 4.2.2, Transport Scotland (2011), see Appendix A.

The wind shielding across the main length of the bridge, as shown in Figure 1 and Figure 2, is a  $\approx$ 3.3m high barrier comprised of 6 horizontal louvres supported by an angled post and has a solidity ratio of 56%. Following the wind shielding's original installation two additional wires have been retrofitted on the shielding, within the 400mm gap just above the crank in its cross-section, to reduce the risk of self-harming.

Flanking the towers additional shielding is provided in the central reserve. These wind shields transition from 4m high at the face of the tower, down to 1m high at a distance away from the tower, as shown in Figure 2 and Figure 3, and are designed to ensure that the overturning forces, and the rate of change of loads on a defined typical vehicle do not exceed the limits outlined within section 4.2.4 of the Employers Requirements, Transport Scotland (2011), see Appendix A.

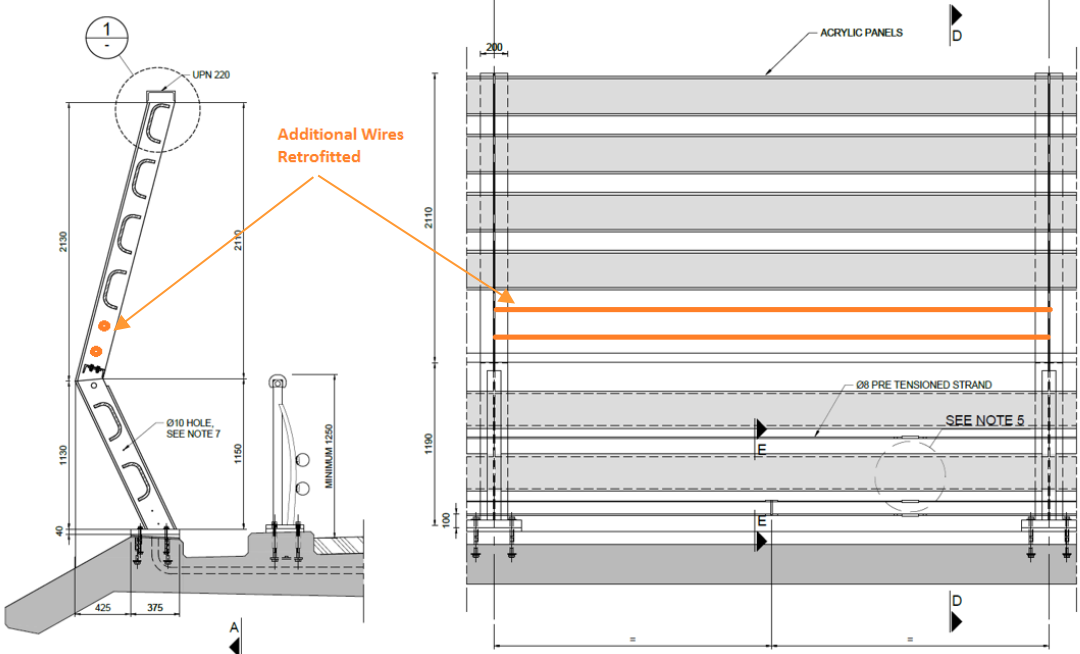


**Figure 1: Section and Elevation of wind shielding used across the main sections of the bridge.**

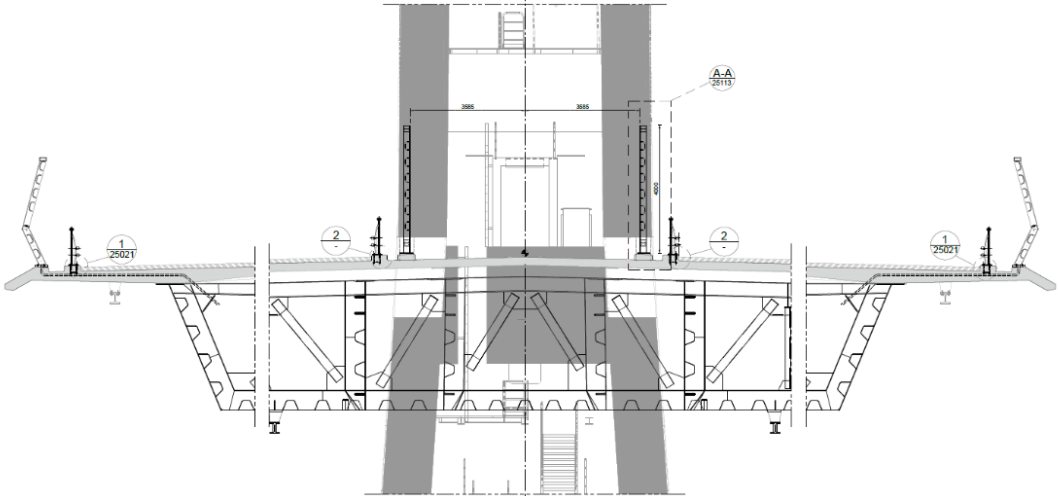


**Figure 2 Section of QC at towers showing wind shielding configuration at edge of deck and around towers**

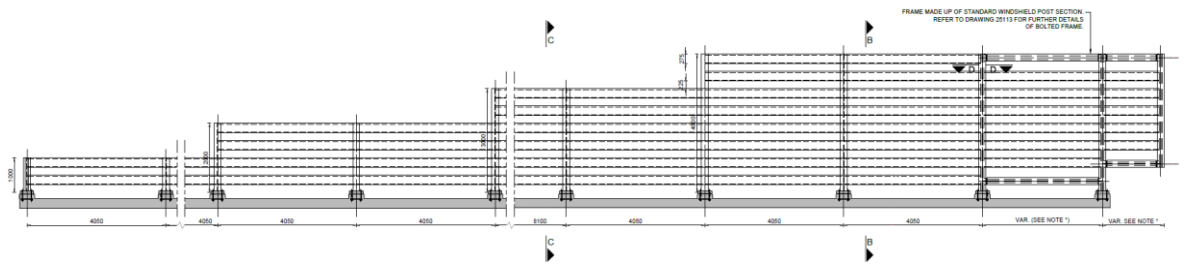


**Figure 3 QC Tower wind shield, flanking tower on either side**

### 1.3 Designer's testing and analysis

The designer's wind tunnel tests, the results of which are presented by Rocchi, et al. (2009) and Hansen, et al. (2012), indicated that the conditions outlined in the Employer's Requirements were achieved within the design for the wind shields. The requirements specified that a 50% reduction in overturning moments of a vehicle on the critical adjacent road lane for wind speeds normal to the bridge is achieved, and set limits for the overturning forces, and the rate of change of forces acting on a defined vehicle around the towers.

Access to the data from the designer's wind tunnel testing is not currently available, however Hansen, et al., (2012) reported that, for the lane adjacent to the wind shielding, a reduction in the overturning moment of 51.3% and 50.7% are achieved for 5m/s and 8m/s wind tunnel speeds respectively compared to the unshielded condition. The report also indicated that additional testing was carried out for various bus positions on the bridge, including in the two middle lanes on the bridge. The report states that *"far larger overturning moments occur when the bus is located on the upstream hard shoulder"* implying that the benefit of the wind shielding increases away from the barrier. This is echoed in the Jacobs Arup report where it is stated that *"the benefit of the shielding increases away from the barrier to about 35 – 40% of the original load in the middle of the bridge"*. However, neither report documents the exact data of these tests.

The 50% reduction in overturning moments, provided by the wind shielding, infers that a wind speed 1.4 times higher is required to produce the same overturning moment as that for an unshielded situation with winds normal to the bridge acting on a vehicle in the critical adjacent road lane, in this case the hard shoulder/bus lane.

The Jacobs Arup (2017) report outlining the effect high winds will have on traffic on the Queensferry Crossing, utilises Prof. Chris Baker’s method to calculate the wind velocity that could lead to vehicle overturning. The Baker method is considered an appropriate simplification of the variation in vehicle types, grouping vehicle types together in terms of mass, wheelbase, height etc., to determine their vulnerability to a single critical wind speed for overturning a stationary vehicle.

The assessment uses a characteristic vehicle wind speed for an unshielded condition that is then increased to account for the benefits of the wind shielding, based on the results of the wind tunnel tests carried out to design the wind shields for the bridge. The Jacobs Arup report also details the influence that wind direction can have on the overturning effect for the Queensferry Crossing, and how this could possibly be used to relax any wind restrictions on the bridge. This is based on assumptions *"believed to be conservative"* as no wind tunnel test data is available for skewed wind directions.

The results in the Jacobs Arup report, and work by the Operator to determine the current thresholds are based on the wind shielding achieving the 50% reduction in the overturning moments as stated in the wind tunnel tests report.

**1.4 Current Wind Thresholds**

The Forth Road Bridge was designed and built without wind shielding. Over the years of operation traffic speed and vehicle restrictions were developed and refined to ensure the safety of vehicles crossing the bridge during high wind speed conditions, ensuring the safety of bridge users and minimising disruption. These restrictions are outlined in Figure 4 and formed the basis for the restrictions applied to the QC, Figure 5.

**High wind procedures:  
Forth Road Bridge**

Wind Speed	Restrictions
Gusts > 35 mph	40mph speed limit on bridge
Gusts > 45 mph	Closed to double-deck buses
Gusts > 50 mph	Closed to: ~ Motorcycles ~ Bicycles ~ Pedestrians
Gusts > 65 mph	Closed to all traffic

**Figure 4 Forth Road Bridge wind speed procedures, The Forth Bridges (2018)**

## High wind procedures: Queensferry Crossing

Wind Speed	Restrictions
Gusts > 50 mph ●	40mph speed limit on bridge
Gusts > 60 mph ●	Closed to double-deck buses
Gusts > 70 mph ●	Closed to: ~ All high-sided vehicles ~ Transit van style with modification ~ Vehicles with trailers or caravans ~ Vehicles with roof boxes or wind-susceptible roof rack items ~ Motorcycles ~ Three-wheeled cars ~ Any other vehicle which appears, in the judgement of bridge staff or the police, to be clearly at risk
Gusts > 90 mph ●	Closed to all vehicles except cars 30mph speed limit on bridge
Gusts > 100 mph ●	Closed to all traffic

**Figure 5 Queensferry Crossing Wind Speed Procedures, The Forth Bridges (2018)**

The restrictions for the Queensferry Crossing are based on the results from the wind tunnel testing of the wind shielding, as described in Section 1.3, and the Forth Road Bridge speed procedure thresholds. The wind tunnel testing report stated that the wind shielding reduced the overturning potential of vehicles induced by a wind speed, by approximately half. Therefore, a wind speed 1.4 times higher is required to produce the same overturning moment as that for an unshielded situation, for winds normal to the bridge acting on a vehicle in the critical adjacent road lane, in this case the hard shoulder/bus lane. The reduction in overturning potential is then applied to the original Forth Road Bridge thresholds, the unshielded condition, to determine the equivalent Queensferry Crossing, shielded condition, thresholds.

The Jacobs Arup (2017) study used the results from the wind tunnel testing, i.e. the reduction in overturning potential, combined with the Baker method to confirm these thresholds as suitable, based on available information. However, it suggested that the double-deck bus limit could potentially be increased from 60mph to 65mph, and that considering wind direction in the thresholds could possibly be used to relax any wind restrictions on the bridge. This is not currently considered a viable solution from an operational point of view, as set out below.

---

## 1.5 Limitations of available data

The reports commenting on the wind tunnel tests provide limited insight into either the exact parameters of the tests carried out or the detailed results, other than to state that the Employers Requirements were achieved. Without access to the full set of wind tunnel test data it is difficult to make insightful decisions other than those based on what is reported.

The reports state that the 50% reduction in overturning moment is achieved in the wind tunnel model, and that additional reduction is achieved further away from the wind shield, believed to be up to an additional 10 to 15% reduction of the original load.

The changing influence of the wind shielding across the carriageway is of interest as it may help refine the wind procedures for the QC. The Jacobs Arup report states the “middle of the bridge”, suggesting that it occurs in the central reserve area between the two carriageways. However, this is not reflective of the wind tunnel testing report by Hansen, et al. (2012) which stated that the overturning moments were far less in the “middle lanes” of the bridge than in the upstream hard shoulder, although it is not clear if this means the middle lane of each carriageway, or the offside lane of each carriageway, i.e. the lane closest to the middle of the bridge.

There are also some inconsistencies between the wind tunnel model wind shielding and the as-built wind shielding, see Figure 6. The differences are subtle, mainly relating to the shape and position of the louvres, which influences the position of the larger gap in the barrier relative to the ground. It is noted that the porosity ratio of the two wind shields remain the same, and the designer had informed the EDT that the changes in the design do not interfere with the performance of the barrier. It is also noted that in the designer’s wind tunnel model a VRS with closely spaced horizontal elements is included. This is different to the design of the VRS installed on site. The model VRS is located at the same level as the largest gap in the model wind barrier louvres, raising questions as to its influence on the test results, whereas the VRS installed on site has larger gaps between its horizontal elements, and is situated behind the wind shielding louvres, below the gap in the wind shield.

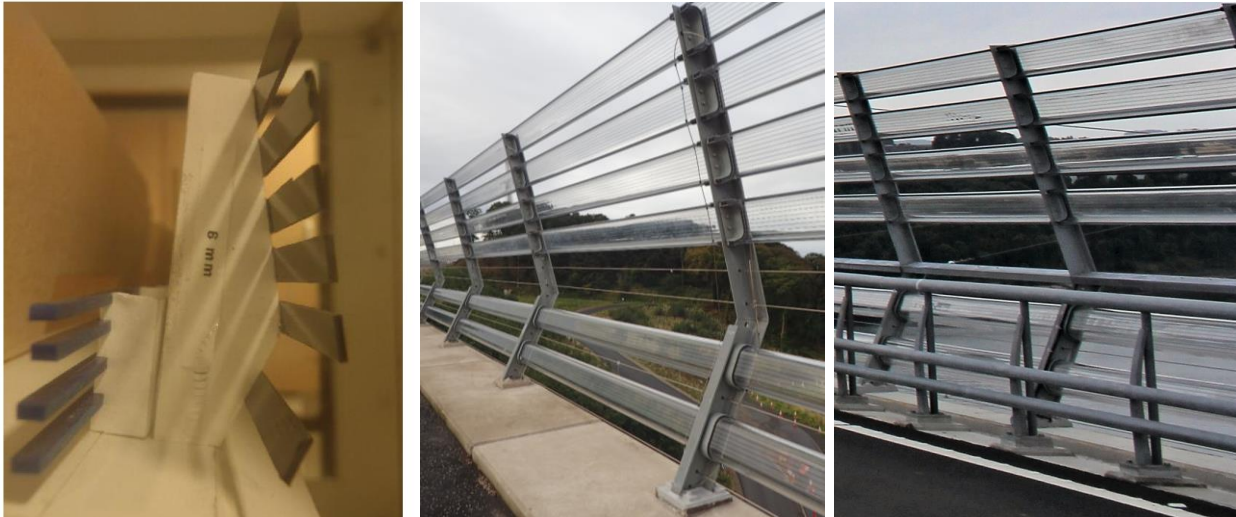


**Figure 6: a) Tested wind barrier Hansen, et al. (2012), b) image of constructed wind barrier on site, c) constructed barrier on main crossing showing VRS.**

While the current thresholds do not consider wind direction, primarily due to operational challenges in implementing such a system, as it is mentioned in the Jacobs Arup (2017) report it may be revisited/implemented in the future. The operational challenges for implementing a system based on wind direction is discussed in 4.2.1.

## **1.6 Project Summary**

The current thresholds on the Queensferry Crossing are based on the wind shielding reducing the overturning potential of vehicles, induced by a wind speed, by approximately half. This is based on the existing wind tunnel testing report which confirmed that this had been achieved. This reduction in overturning potential is then applied to the original Forth Road Bridge thresholds, the unshielded condition, to determine the equivalent Queensferry Crossing, shielded condition, thresholds.

Amey have reviewed the existing studies and information available and have concluded that the current thresholds cannot be changed based on the current information available, as handed over by the Designer (Ramboll) and Transport Scotland's Engineers (Jacobs/Arup).

The existing wind tunnel report, while it confirms that the overturning effect has been reduced, provides limited information on the output from these tests. There are also different physical and dimensional characteristics between the model tested in the wind tunnel and the barrier built on site.

---

Amey proposed that a more detailed understanding of the performance of the as-built wind shielding was required to confirm if any changes could be made to the current thresholds. This required further research and on-site measurements.

Under instruction from Transport Scotland Amey progressed with a study of the effectiveness of the as-built wind barriers. This included:

- 2D CFD Modelling of the As Built wind barrier condition – to provide an initial insight into the effect of the barrier and deliver early indicative results while the more accurate wind tunnel modelling was being developed. This stage is funded by the SRRB.
- Wind Tunnel Testing of the As Build wind barrier condition – to provide a more accurate representation of the wind field around the as-built wind barrier than the CFD modelling would allow. This enables a comparison between the results from the designer tested barrier and the as built condition results and will help confirm or otherwise the effect on vehicles sheltered by the wind barrier. This stage is funded by the SRRB
- Lidar survey of the bridge to provide insight into the wind field around the bridge, and to validate the response observed in modelling with respect to wind speed interaction around with the barriers. This stage is funded by Transport Scotland.

The three elements of the study output individual reports detailing their specific finding. This report summarises each study and combines the results to provide a holistic overview of the findings.

---

## CFD Modelling

The Computational Fluid Dynamics (CFD) study of the as-built wind barrier was carried out in partnership with the University of Nottingham (UoN), taking advantage of the University's experience in CFD modelling and their High-Performance Computing System for running the simulations. This part of the project was funded by the SRRB.

The aim of the CFD modelling was to provide an initial insight into the effect the barrier has on the wind flow, and to deliver early indicative results of the impact the wind barrier has on the overturning moment of vehicles, while the more accurate wind tunnel modelling was being developed.

This section summarises the methodology for the study and presents the key findings of the study. A more detailed description of the CFD modelling and simulation results is available in the study report produced by UoN, see Appendix B.

### 2.1 Methodology

#### 2.1.1 Overview

A 1:10 scale, 2D, CFD model was generated based on the as-built records for the wind barrier. The barrier dimensions were confirmed during a dimensional survey conducted on 26/09/2019, undertaken at a section of barrier at the northern end of the Queensferry Crossing.

An additional model based on the original Forth Crossing Bridge Constructor's (FCBC) wind tunnel model was also generated. This model was approximated from information available, as detailed drawings were not available, and was developed to better understand observed differences between the CFD as-built model results and the FCBC wind tunnel results.

The simulations looked at the differences between the shielded and unshielded condition, considering different wind speeds, vertical angles of attack, and position of vehicles to improve the understanding of the effect the wind barrier has on the flow field and vehicle overturning moment.

---

### **2.1.2 Simulations**

Simulation model wind speeds of 2, 4 and 6m/s, equivalent to 14, 28 and 42mph at full scale, were tested, with a vertical angle of attack of  $0^\circ$ ,  $\pm 2^\circ$ ,  $\pm 4^\circ$ . Positive angles referring to wind approaching the bridge from below, and negative angles refer to wind approaching the bridge from above. The simulations were URANS (Unsteady Reynolds Averaged Navier Stokes) SST (Shear Stress Transport) k- $\omega$  turbulence models.

As early review of the different wind speeds tested showed consistency in the recorded response across all speeds considered. A similar time-averaged wind speed magnitude profile, which indicates the % reduction of wind speed behind the barrier, was recorded for each speed considered. However, it was noted that the faster wind speeds had a destabilising effect on the simulation model as it ran, requiring smaller steps to complete the simulations and greatly slowing progress. This destabilising effect is fundamentally a computational issue. While we were utilising a High-Performance Computing (HPC) System with 31TB of RAM to run the models the system still has limits. The faster a wind speed moves through the model the more difficult it is for the processing to keep up and the easier it is for the model to become unstable. Adding the vehicle into the model exacerbated the stabilisation issue, therefore subsequent models focused on the 2m/s wind speed.

A full summary of the base models, and simulation variables tested are presented in Table 1. This resulted in a total of 35 individual simulations.

The vehicle modelled in the simulations was based on a simplified standard double deck bus, of height 4.2m and width 2.52m. The 2D nature of the model negated the need for the length of the vehicle to be modelled. Figure 7 provides a schematic of the 2D simulation arrangement including boundary conditions and mesh zones.

**Table 1: CFD Simulation Summary of variables tested**

Mesh ref.	Base Model components						Simulation variables								Number of simulations
	Wind Barrier			Vehicle			Wind Speed			Angle of attack (°)					
	As Built	No barrier	FCBC model	No vehicle	Vehicle in H/S	Vehicle in Lane 1	2 m/s	4 m/s	6 m/s	- 4	- 2	0	+ 2	+ 4	
C1	x			x			x	x	x	x	x	x	x	x	15
C2	x				x		x			x	x	x	x	x	5
C3	x					x	x			x		x		x	3
C10		x		x			x			x		x		x	3
C20		x			x		x			x		x		x	3
C30		x				x	x			x		x		x	3
F1			x	x			x					x			1
F2			x		x		x					x			1
F3			x			x	x					x			1
<b>Total number of simulations:</b>														<b>35</b>	

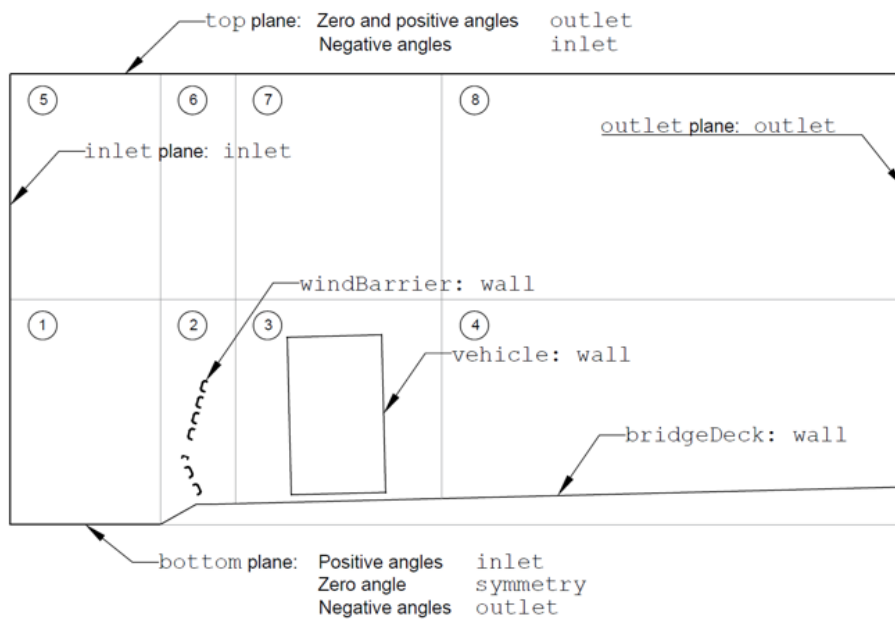


**Figure 7: An overview of the CFD model boundary conditions with vehicle located in the Hard shoulder (University of Nottingham (UoN))**

---

## **2.2 Results**

The results from the CFD simulations can be reviewed in a number of ways. The instantaneous and time averaged velocity field contour and vector plots provide a clear visual display of the flow field as it interacts with the barrier and vehicles. Velocity samples can also be extracted by probes at pre-defined mid-air locations within the simulation, allowing comparative analysis of mean wind speed, mean wind angle, turbulence, and 1s gust factors at different locations within the simulation. Probes can also be used to extract surface pressure information from solid objects, in our case the vehicle, allowing force and moment components to be considered.

In each simulation there is an initial transient stage where the flow field is developing across the model. The data generated in this period is not considered in the results as it does not represent an accurate account of the flow field. To accommodate this the initial 10s of each simulation is removed from the data set prior to any results being processed. The majority of simulations run for 40s model time.

### ***2.2.1 Flow field***

Contour and vector plots provide a clear visual of how the wind barriers interact with the flow field.

Figure 8, Figure 9, and Figure 10 provide a clear indication that the wind barrier reduces the wind speed in its wake across the carriageway, as expected, with blue indicating a decrease in wind speeds and yellow and reds indicating an increase. They also provide insight into the un-uniform and unsteady nature of the flow. Figure 8 is an instantaneous snapshot from one simulation and highlights the volatility of the velocity field close to the barrier as jets pass through the gaps in the barrier, this in turn generates small vortices that move across the carriageway as the jets interact with the slow flow behind the louvres. Figure 9 shows the time averaged velocity field which gives a clearer understanding of the jets that pass through the gaps in the wind barrier and extend into the hard shoulder. It also clearly highlights the shear layer which develops directly above the barrier.

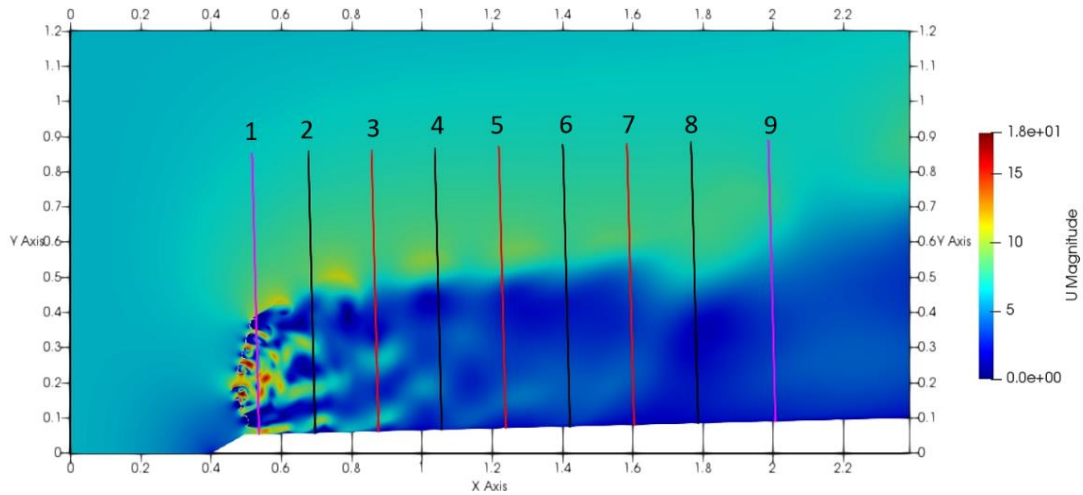


**Figure 8: Instantaneous velocity field showing unsteady flow and vortex generation in wake of wind barrier (6m/s, 0° AoA) (UoN)**

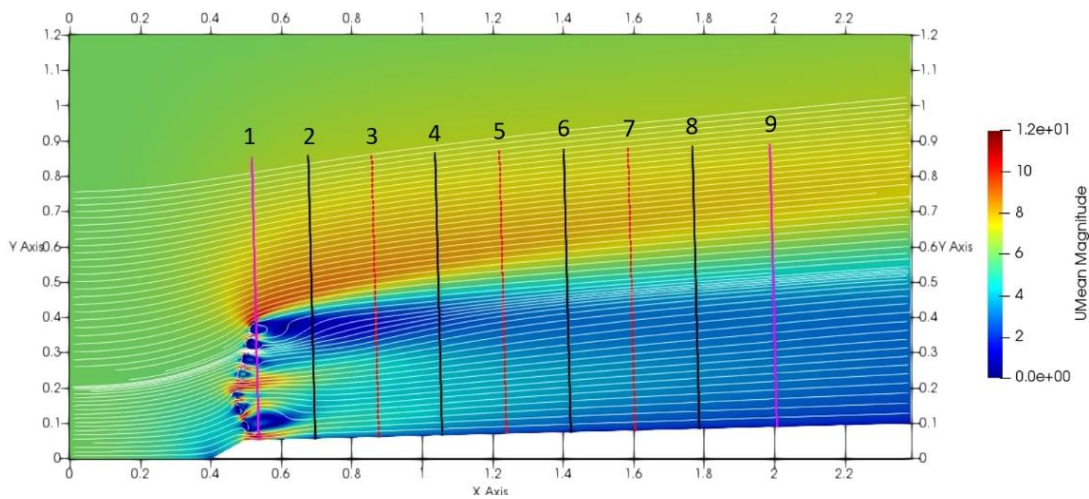


**Figure 9: Time averaged velocity field showing high speed jets through gaps and shear layer above wind barrier (6m/s, 0° AoA) (UoN)**

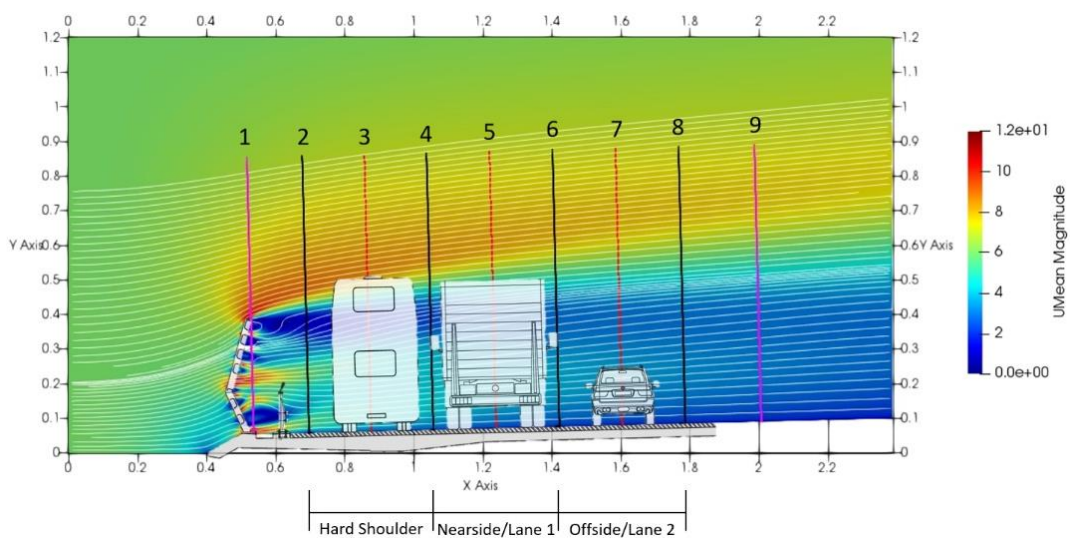


**Figure 10: Time averaged velocity field with carriageway section and vehicles overlain for clarity (Note: vehicles not included in this simulation) (6m/s, 0° AoA) (UoN)**

The numbered vertical lines overlain in these Figures represent the location of the sample probes within the simulation. Confirmation of the probe reference number and the descriptive location on the bridge is provided in Table 2. Figure 10 overlays a cross section of the bridge carriageway showing the wind barrier and the position of the different lanes, including the potential to use the hard shoulder as a bus lane, onto Figure 9 to provide context to the location of the sample probes and the observed velocity field. This is provided for reference only and the vehicles shown are not included in this simulation.

**Table 2: Velocity sampling references and corresponding locations**

Sampling line No.	Position on the bride deck
1	Directly behind the wind barrier (WB)
2	Edge of the hard shoulder (HS)
3	Centre of the hard shoulder
4	Line between the hard shoulder and left lane (LL)
5	Centre of the left lane
6	Line between the left lane and right lane (RL)
7	Centre of the right lane
8	Edge of the right lane
9	End of the carriageway

The normalised mean wind speed data, recorded at sampling lines 2 to 9, during a 6m/s, 0° AoA simulation are presented in Figure 11. Sample line 1 is omitted as it is located directly behind the wind barrier in an area behind the VRS, and the data is dominated by the high-speed jets through the barrier. The mean wind speed, x-axis, is normalised by the upstream wind speed, therefore any value above 1 shows an increase, and a value below 1 is a decrease in the wind speed.

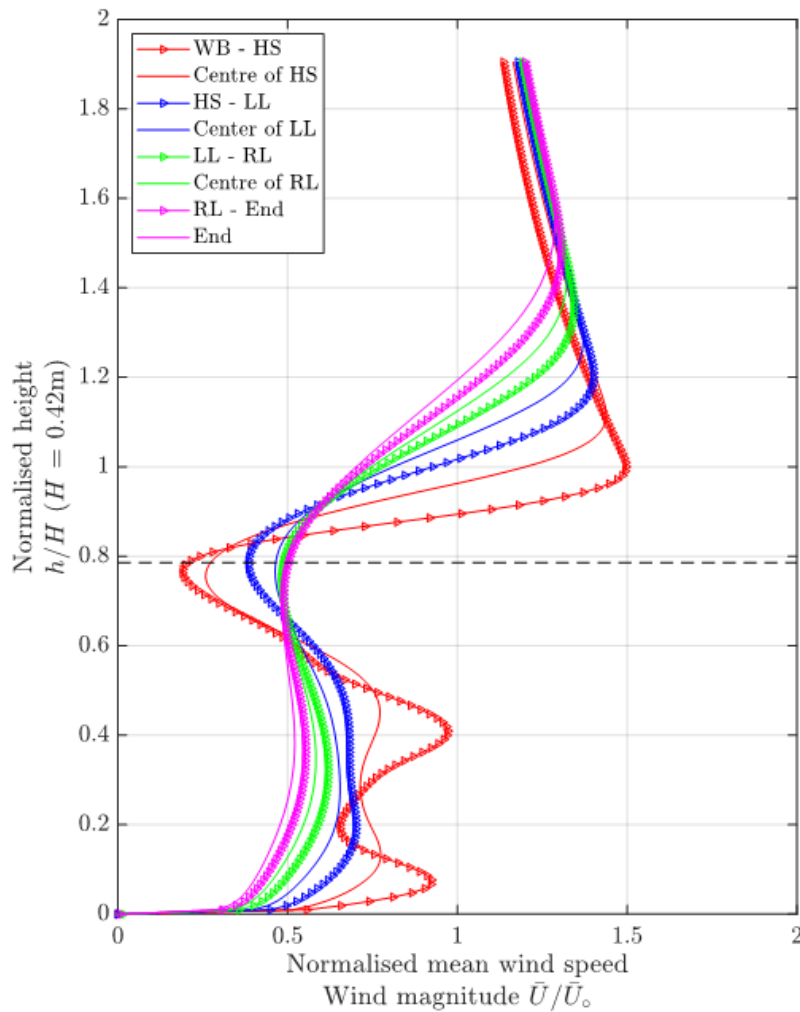


**Figure 11: Variation of the normalised time-averaged wind speed magnitude profile at locations across the bridge deck, (6m/s, 0° AoA). X-axis normalised by upstream wind speed. Y-axis normalised by height of bus (4.2m). Horizontal dashed line indicates the normalised height of the wind barrier. (UoN)**

As the high-speed jets pass through the gaps in the wind barrier they interact and mix with the shielded areas behind the louvres and slowly dissipate to a more uniform wind speed profile. This can be observed in the transition from the red line, closest to the wind barrier and therefore most influenced by the jets, to the blue, green and finally pink lines as we cross Lane 1 and Lane 2 to the end of the carriageway. The “WB – HS” line refers to sample line 2, which is located at the edge of the hard shoulder next to the hard strip, i.e. the side of the hard shoulder closest to the wind barrier. Two peaks in normalised mean wind speed, located at approximately 0.1 and 0.4 normalised height, coincide with the jets through the gaps in the wind barrier. This dissipates by the time we reach Lane 1, “HS – LL” line. The high-speed shear layer directly above the wind barrier, that rises up as it crosses the carriageway is also evident.

Three wind speeds were originally considered, 2, 4, and 6m/s. Figure 12 overlays the time averaged mean wind speed profile from each wind speed simulation, at the hard shoulder, lane 1, and lane 2. There is very good agreement between each data set, indicating that the performance of the barrier isn't influenced by wind speed. This provided confidence that the more stable 2 m/s simulations would provide accurate performance data in subsequent model configurations.

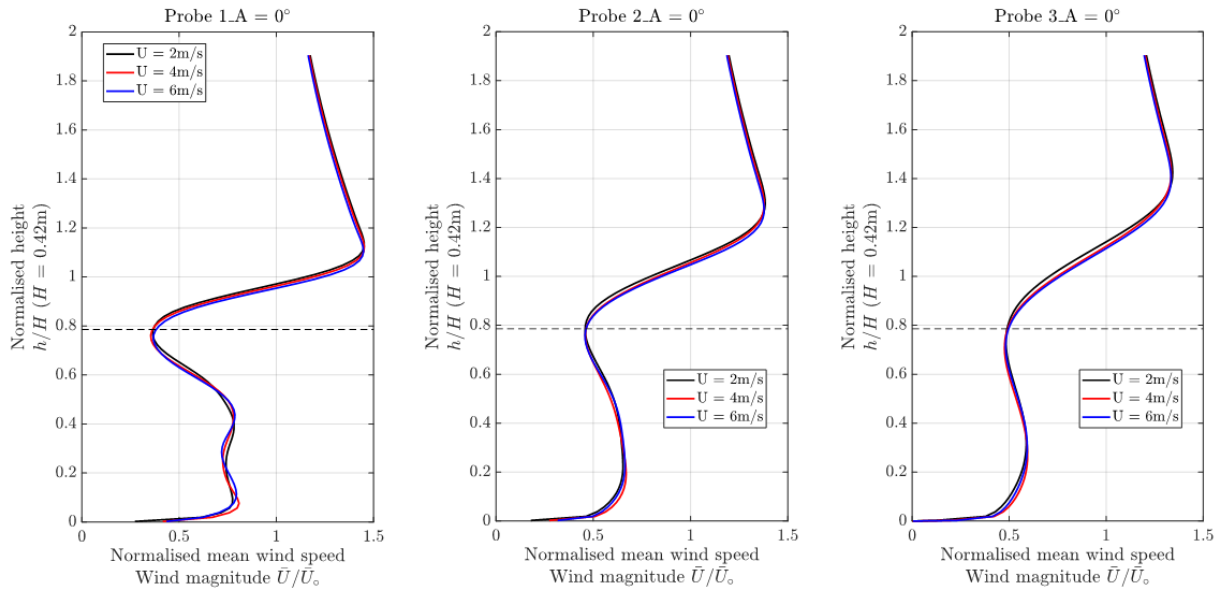


**Figure 12: Profile of the time-averaged wind speed magnitude at different wind speeds, estimated at (a) centre of the hard shoulder, (b) centre of the left lane and (c) centre of the right lane.**

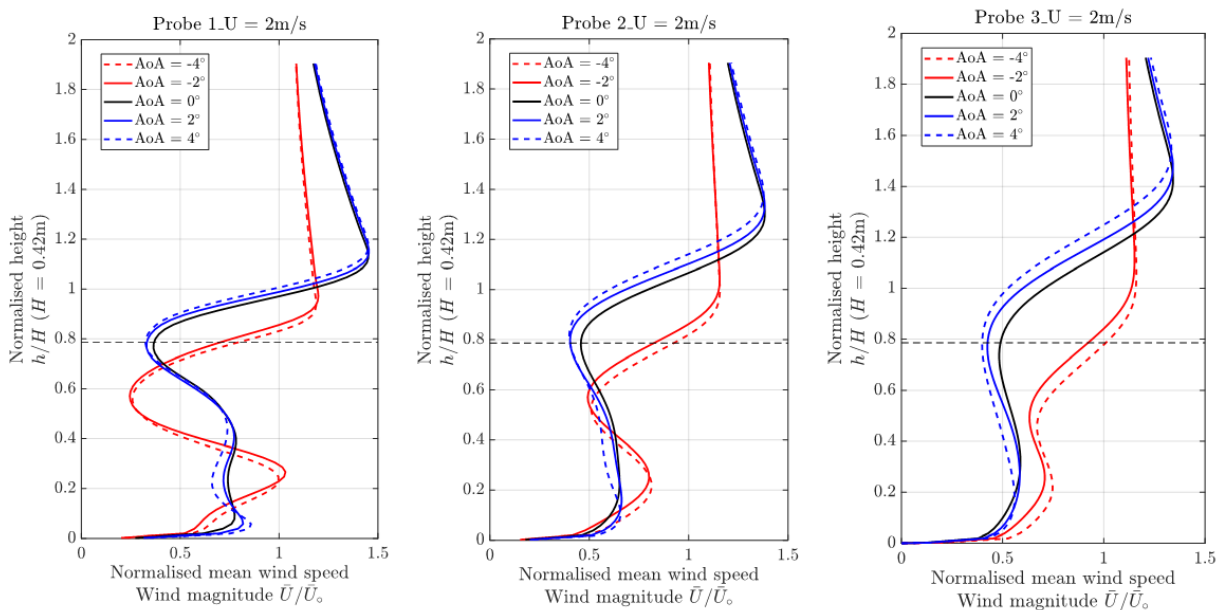


**Figure 13: Profiles of the time-averaged wind speed magnitude at the centre of (a) the hard shoulder, (b) left lane and (c) right lane, at the wind speed of 2 ms<sup>-1</sup> and at different angles of attack. The dashed line indicates the normalised height of the wind barrier.**

---

Figure 13 looks closer at the influence the vertical angle of attack, (AoA), has on the performance.

During instances of positive AoA, i.e. wind from below, the wind barrier has a similar performance to the neutral angle condition. However, for the negative AoA the influence of the wind barrier on the wind flow changes. The profile shape changes, as the shear layer above the barrier is suppressed, and the jets coming through the gaps in the barrier extend further across the carriageway. Therefore, vertical angles of attack should be considered when reviewing the performance.

### **2.2.2 Flow field with vehicle**

Adding a vehicle to the model changes the flow field across the carriageway, compared to that observed for the empty carriageway in Figure 9. Figure 14 allows a comparison of the differences in the flow field due to the positioning of the vehicle at different points on the carriageway, i.e. the hard shoulder or lane 1, considered across three vertical angles of attack.

Changing the position of the vehicle on the carriageway influences how quickly the wind has to move around the vehicle. Therefore, the wind has less time to dissipate before it interacts with a vehicle in the hard shoulder compared to a vehicle in Lane 1.

Changing the AoA displays similar behaviour as that previously observed in Figure 13, with the positive angles, i.e. wind from below, displaying a response similar to that of the neutral AoA, and the negative angles, i.e. wind from above, exhibiting a different response. The profile of the bridge deck edge beam may be influencing the neutral AoA, directing it slightly upwards, making it more consistent with the intentionally positive AoA.

The pressure coefficient on each side of the vehicle when located in the hard shoulder and Lane 1, Figure 15 and Figure 16, confirms the effect this has on how the wind interacts with the vehicle, with both position and angle of attack influencing the root mean squared (RMS) pressure coefficient around the vehicle.

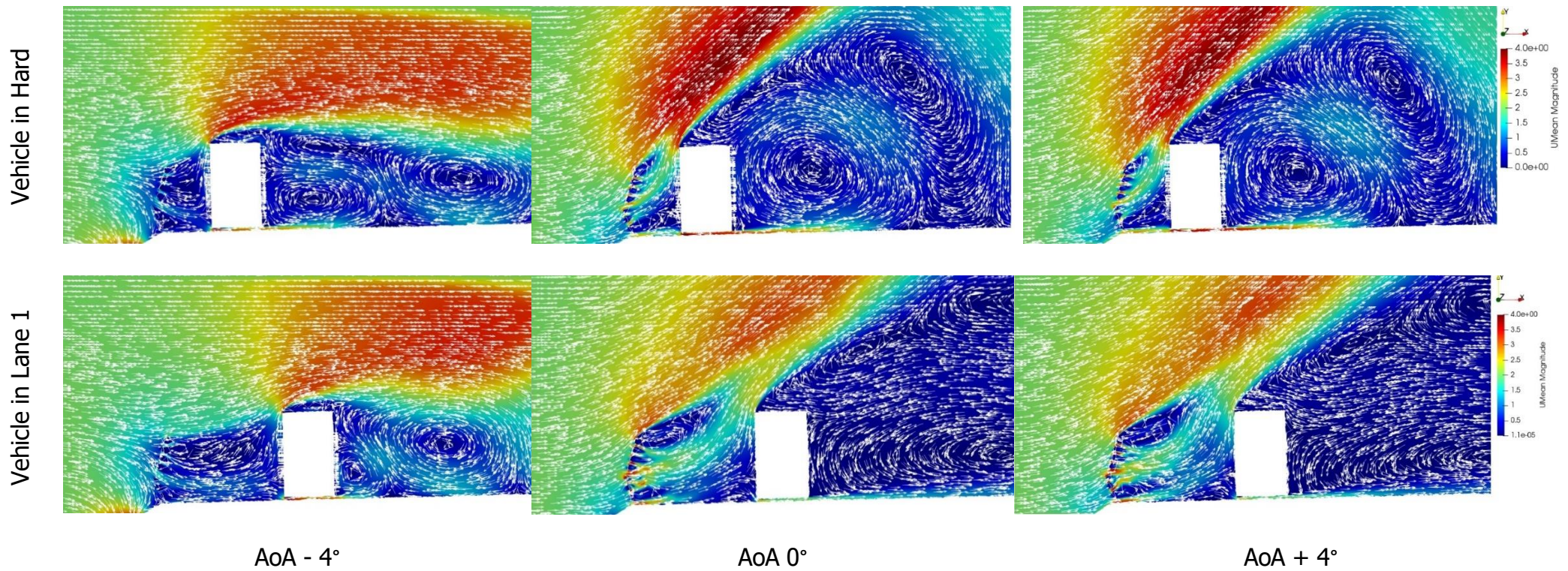


**Figure 14: Contour plots of the time-averaged velocity field, comparing the flow field when the vehicle is (top) at the centre of the hard shoulder and (bottom) at the centre of the left lane, at the angle of attack of, left: -4°, middle: 0°, right: +4°.**

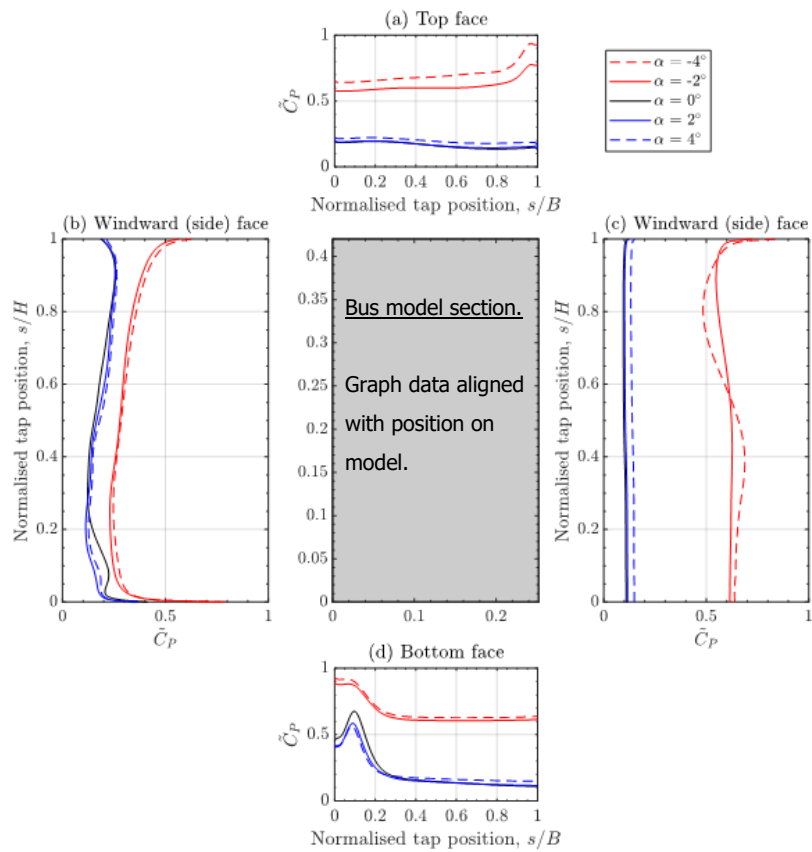


**Figure 15: Variation of the RMS pressure coefficient around the vehicle with respect to the angle of attack when the vehicle is at the centre of the hard shoulder.**

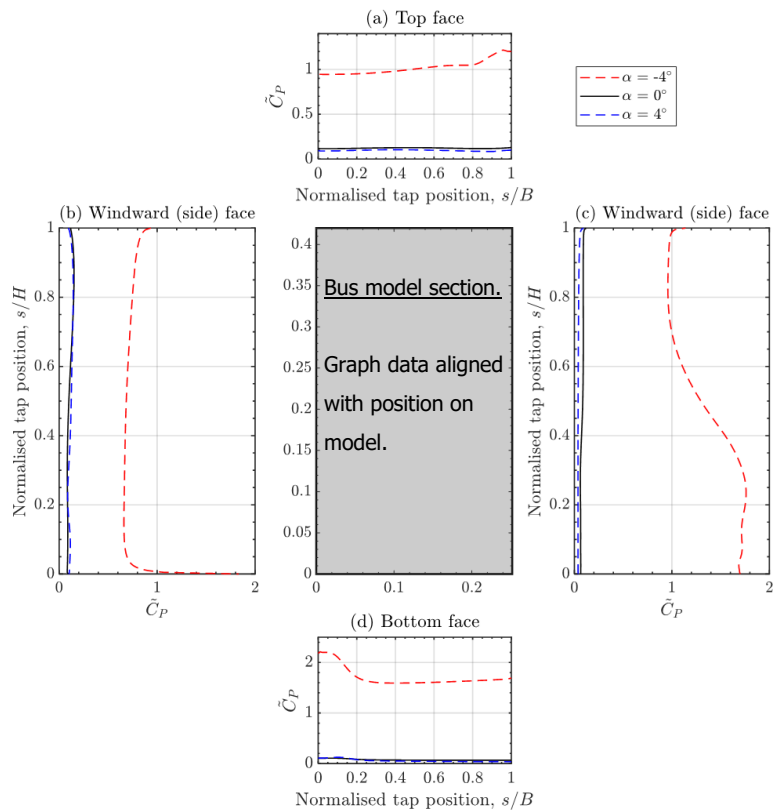


**Figure 16: Variation of the RMS pressure coefficient around the vehicle with respect to the angle of attack when the vehicle is at the centre of Lane 1.**

### 2.2.3 Vehicle overturning moment

The overturning moment, or rolling coefficient, of the vehicles was calculated for both the shielded and unshielded conditions. This provided us with a corresponding reduction factor. Table 3 and Table 4 summaries the reduction in the rolling coefficient for a vehicle located in the hard shoulder and lane 1. The different angles of attack are also considered as they were found to have an influence on the response.

**Table 3: Vehicle in Hard Shoulder - Rolling coefficients, and associated reduction factors.**

Wind speed	Angle of attack	Rolling coefficient		Reduction factor
$U$ (ms <sup>-1</sup> )	AoA (°)	Shield, $C_{M,S}$	Unshielded, $C_{M,U}$	$R = C_{M,S}/C_{M,U}$
2	-4	-1.36	-1.46	0.93
2	0	-1.38	-1.85	0.74
2	+4	-1.33	-1.76	0.76

**Table 4: Vehicle in Lane 1 - Rolling coefficients, and associated reduction factors.**

Wind speed	Angle of attack	Rolling coefficient		Reduction factor
$U$ (ms <sup>-1</sup> )	AoA (°)	Shield, $C_{M,S}$	Unshielded, $C_{M,U}$	$R = C_{M,S}/C_{M,U}$
2	-4	-1.30	-1.55	0.84
2	0	-0.67	-1.00	0.67
2	4	-0.61	-0.94	0.65

The CFD model calculated reduction factors are significantly higher than the values recorded in the FCBC wind tunnel tests. The FCBC wind tunnel test results were reported by Hansen, et al., (2012), as a reduction in the overturning moment of 51.3% and 50.7% achieved for 5m/s and 8m/s wind tunnel speeds respectively, for the lane adjacent to the wind shielding, compared to the unshielded condition.

---

The higher values imply that the wind barrier modelled in the CFD model is potentially less effective than the one in the FCBC wind tunnel tests. It is understood that the barrier designer confirmed that the as-built barrier would be as effective as the wind tunnel model barrier, therefore it is believed that the difference in the output from the CFD modelling and the reported values from the wind tunnel model may be a result of the 2D nature of the CFD modelling. Without comparable data from the original wind tunnel tests, it is difficult to compare them directly. To try to understand this difference another CFD model was produced, this time based on the FCBC wind tunnel model. The following section outlines this part of the study.

#### ***2.2.4 As-Built barrier and FCBC wind tunnel model barrier comparative review.***

The as built wind barrier and the barrier modelled as part of the designer's wind tunnel modelling are compared in Figure 17.

The two barriers differ in their arrangement and shape of the louvres. The height, and overall porosity remain the same for both barriers. The FCBC wind tunnel model was modelled with a VRS included in the simulation, see Figure 17. The VRS in the wind tunnel model is positioned behind the main gap in the model barrier, which may have had an influence on the jets of fast-moving wind passing through the gaps in the barrier.

To allow direct comparison between the as built barrier and the wind tunnel model barrier a CFD model of the designer's wind tunnel model barrier was built and tested under the 2m/s wind speed, 0° angle of attack, condition. Without access to detailed drawings of the FCBC wind tunnel model certain details had to be assumed for the CFD model. This was considered sufficient to provide insight.

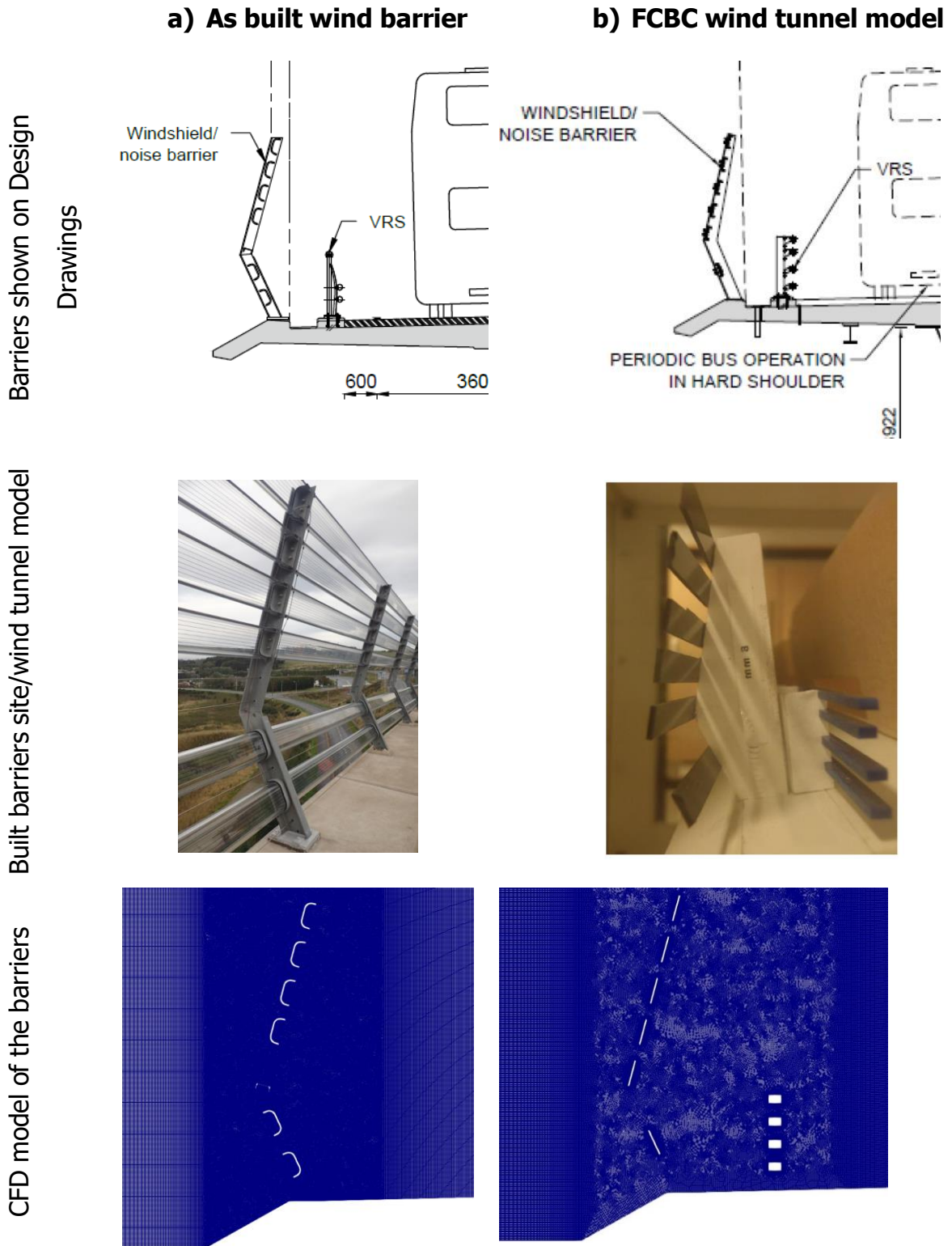
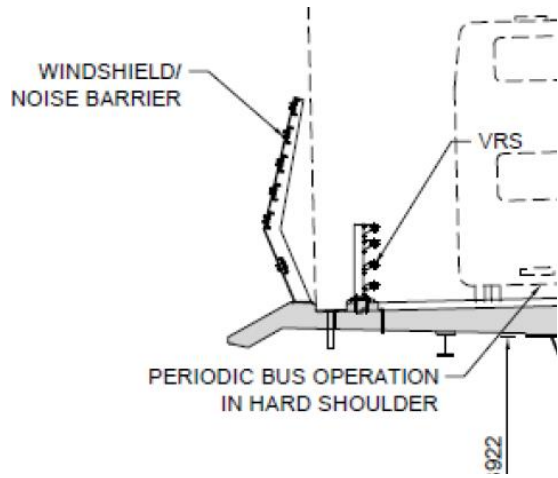
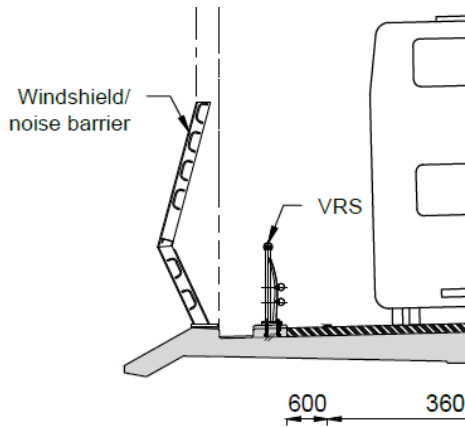
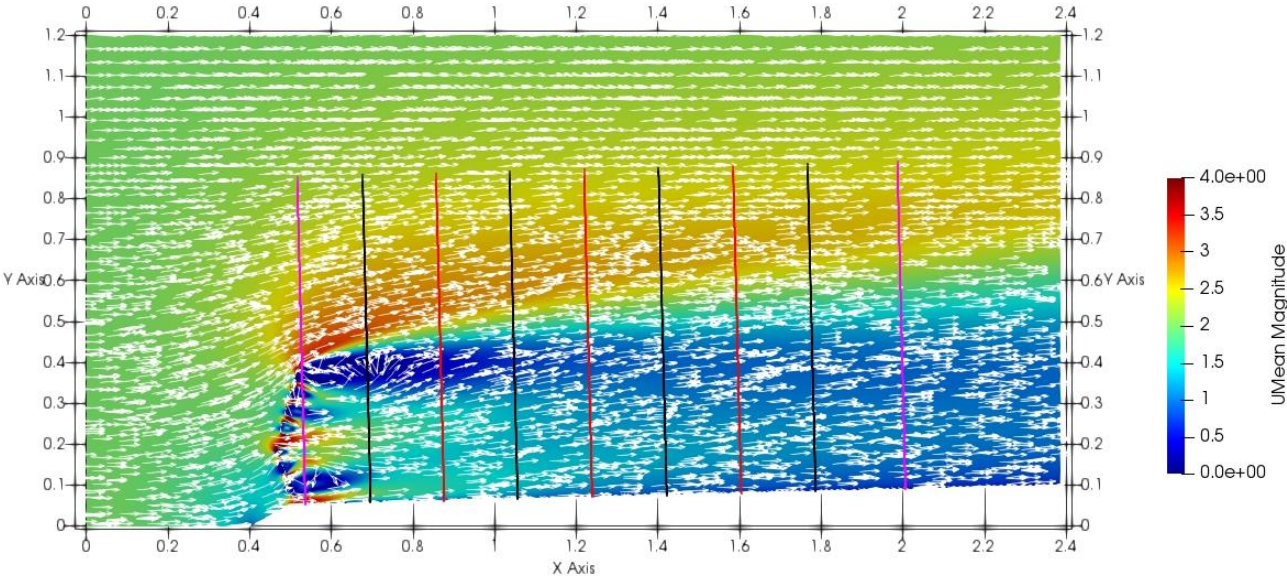


Figure 17: Comparison of as built wind barrier (left) and FCBC wind tunnel model (right)



Reviewing the velocity field generated in the CFD model for both the simulated as built barrier and simulated FCBC wind tunnel model barrier, Figure 18 and Figure 19, shows a clear difference in how the two barriers influence the flow field. The VRS included in the FCBC model appears to deflect the jet that is passing through the gap upwards, providing additional shelter to the area directly behind it.



**Figure 18: Time averaged velocity field of the as built wind barrier (2m/s, 0° AoA) (UoN)**

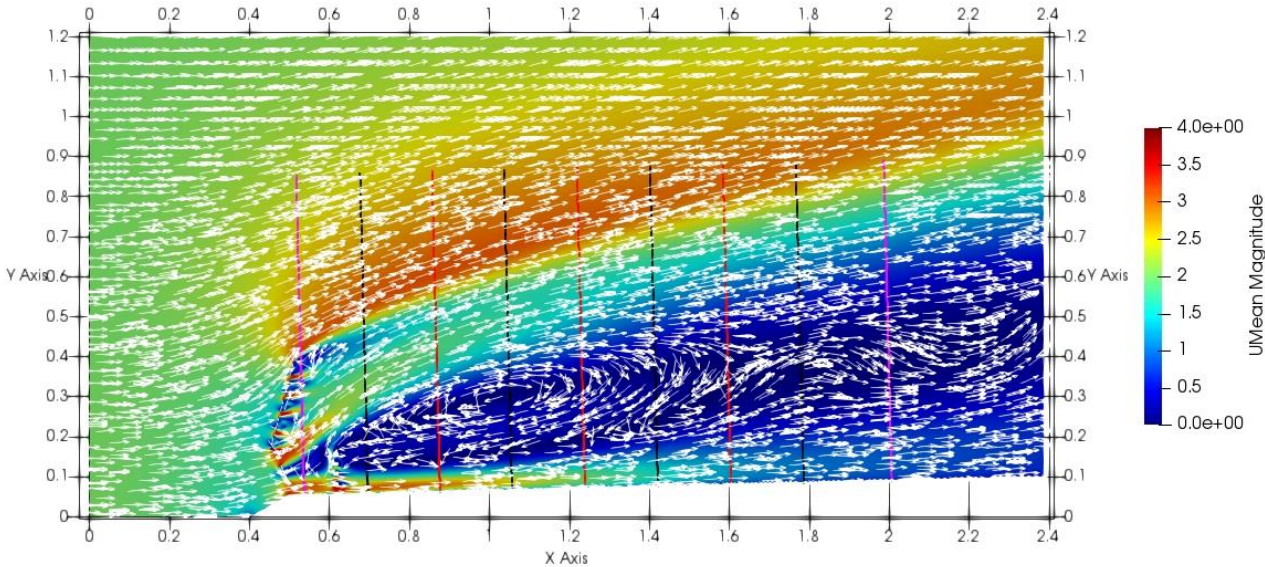


**Figure 19: Time averaged velocity field of the approximated FCBC wind tunnel wind barrier (2m/s, 0° AoA) (UoN)**

Calculating the rolling coefficient for a vehicle behind the FCBC wind tunnel barrier, as simulated in the CFD model, and comparing it to the result from the as built barrier, as simulated in the CFD model, gives a better understanding of how the difference in the two barriers impacts the vehicles, see Table 5. The FCBC model barrier did show an improved reduction factor for both the hard shoulder and Lane 1 locations. However, the hard shoulder improvement was minimal, and still significantly above the designer’s wind tunnel model results. The designer’s wind tunnel model results were reported by Hansen, et al., (2012), as a reduction in the overturning moment of 51.3% and 50.7% for 5m/s and 8m/s wind tunnel speeds respectively, for the lane adjacent to the wind shielding, compared to the unshielded condition. This suggests that the main difference in the results is from the 2D nature of the CFD modelling and the 3D nature of the wind tunnel model.

**Table 5 Rolling coefficients compared for both wind barrier configurations**

Wind barrier	Location of the vehicle	Rolling coefficient		Reduction factor
		Shield, $C_{M,S}$	Unshielded, $C_{M,U}$	$R = C_{M,S}/C_{M,U}$
As built	Hard shoulder	-1.38	-1.85	0.74
	Left lane	-0.67	-1.00	0.67
Approximated FCBC wind tunnel model	Hard shoulder	-1.30	-1.85	0.70
	Left lane	-0.38	-1.00	0.38

**2.2.5 CFD modelling conclusion**

The CFD modelling provided us with a clearer indication of how the wind barriers affect the velocity field as it crosses the carriageway. High speed jets extend through the barrier, quickly dissipating by the time they reach the hard shoulder, but their effect can be observed far into the carriageway.

Other carriageway structures, such as VRS, can also influence the velocity field, as observed in the CFD simulation of the FCBC wind tunnel model.

---

The reduction in overturning coefficient calculated from the CFD modelling was not as significant as the FCBC wind tunnel report. This is believed to be significantly impacted by the 2D nature of the CFD modelling, where wind cannot travel around the front and rear of the vehicle, as would be the case in a 3D model. The wind tunnel model of the as built condition will confirm the reduction factor.

While waiting on the data from the wind tunnel model to confirm, or otherwise, the results from the CFD model, the recommendation was made to restrict Double Deck buses from using the hard shoulder of the QC during higher winds close to the threshold. The hard shoulder is rarely used as a bus lane therefore this decision will have negligible impact on disruption, and it ensures that the buses remain on a section of the carriageway where they are further protected by the influence of the barrier.

---

## **Wind Tunnel Study**

The wind tunnel study, of the as-built wind barrier, was carried out using the atmospheric boundary layer wind tunnel facility at the University of Nottingham (UoN). The facility has a maximum working area cross section of 2.4m by 1.8m and allows the controlled input and recording of a wind field around a model. This part of the project was funded by the SRRB.

The aim of the wind tunnel modelling was to provide a detailed insight into the effect the barrier has on the wind flow, and on the overturning moment of vehicles, to improve on the insight gained from the 2D CFD model.

This section summarises the methodology for the wind tunnel study and presents the key findings of the simulations. A more detailed description of the wind tunnel modelling and simulation results is available in Appendix C.

### **3.1 Methodology**

#### ***3.1.1 Overview***

A 1.6m long, 1:50 scale, sectional model of the Queensferry Crossing deck and wind barrier was built at UoN. The dimensions and details of the carriageway and wind barrier are based on the as-built records for the Queensferry Crossing. Only the deck and edge wind barrier are modelled, other components such as VRS, stay cables, street furniture, are not included in the model to ensure only the effect of the wind barrier is recorded.



**Figure 20: Wind tunnel model, with carriageway section, wind barrier, and model vehicle located in the hard shoulder (UoN)**

The simulations considered the differences between the shielded and unshielded condition, reviewing different wind speeds and vertical angles of attack, with a vehicle positioned in the hard shoulder, to improve the understanding of the effect the wind barrier has on the flow field and vehicle overturning moment.

### ***3.1.2 Simulations***

Simulation model wind speeds of 4, 6 and 8m/s have been tested, with an angle of attack of  $0^\circ$ ,  $\pm 2^\circ$ ,  $\pm 4^\circ$ . A full summary of the base models, and simulation variables tested are presented in Table 6. This resulted in a total of 64 individual simulations.

The wind velocity component was recorded using a Dantec 55P11 single-wire probe, seen in Figure 20, during the simulation. The probe's position was adjustable and enabled detailed profiles of velocity to be recorded at three positions across the carriageway, the centre of hard shoulder, Lane 1, and Lane 2. The sampling frequency for velocity was set at 2000Hz.

A Scannivalve MPS4264 pressure scanner was used to measure the surface pressure recorded around the reference vehicle at 80 No. pressure taps, distributed in 5 evenly spaced rings around the vehicle, see Figure 21: Wind tunnel reference vehicle with location of pressure tap rings indicated. The sampling frequency for pressure measurement was set at 500Hz.

**Table 6: CFD Simulation Summary of variables tested**

Test ref.	Base Model components				Simulation variables								Number of simulations
	Wind Barrier		Vehicle		Wind Speed (m/s)			Angle of attack (°)					
	As Built	No barrier	No vehicle	Vehicle in H/S	4 m/s	6 m/s	8 m/s	- 4	- 2	0	+ 2	+ 4	
1	x		x		x	x	x	x		x		x	9
2	x		x			x		x	x	x	x	x	5
3	x			x	x	x	x	x	x	x	x	x	25
4		x		x	x	x	x	x	x	x	x	x	25
<b>Total number of simulations</b>												<b>64</b>	

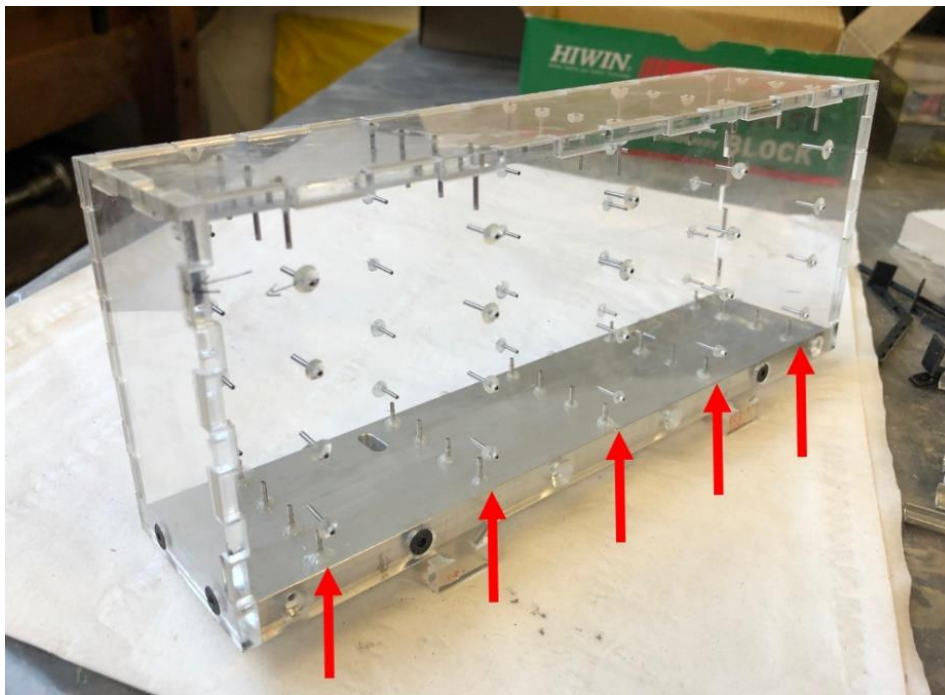


**Figure 21: Wind tunnel reference vehicle with location of pressure tap rings indicated**

---

## 3.2 Results

Unlike the CFD modelling the wind tunnel model does not provide us with a contour or vector visualisation of the wind field around the model. Instead, the flow field is recorded by the velocity probe at multiple locations in the model, positioned to correspond with the sampling probe locations in the CFD model. This allows a calculation of the mean wind speed, turbulence, and turbulence length to be estimated.

### 3.2.1 Flow Field

The normalised time averaged wind speed profile is recorded at the hard shoulder, lane 1, and lane 2. The wind speeds profiles are normalised by the input windspeed upstream, values above 1 indicate an increase in wind speed, values below 1 indicate a decrease. The record showed good agreement across all wind speeds simulated, see Figure 22. This observation is in line with that observed in the CFD modelling, however the shape and data range of the profile, particularly in the hard shoulder, does differ slightly from the CFD model profiles presented in Figure 12. This is due to the more accurate 3D nature of the wind tunnel model compared to the 2D CFD model. In the wind tunnel model, the wind is free to dissipate in all 3 dimensions, and elements not modelled in the CFD modelling, such as the vertical posts, may also be having an influence on the response. In both wind tunnel model and CFD model the shear layer directly above the wind barrier is evident. It is also noted that the vertical angle of attack plays a more significant role than changes in wind speed, see Figure 23. While this was also noted in the CFD model, the variation is slightly different.

All scenarios considered in both Figure 22 and Figure 23 identify the fast jet of wind through the gap in the wind barrier, between normalised height range of 0.2 to 0.4, extending into the hard shoulder. The jet of wind is below normalised wind speed 1 by the time it reaches the middle of the hard shoulder, indicating a reduction compared to the upstream wind speed. As it reaches the middle of lane 1 it has partially dissipated, and the normalised wind speed has reduced to approximately 0.65 or below. By lane 2 the jet has fully dissipated, and the entire shielded area has a normalised mean wind speed of approximately 0.5 or below.

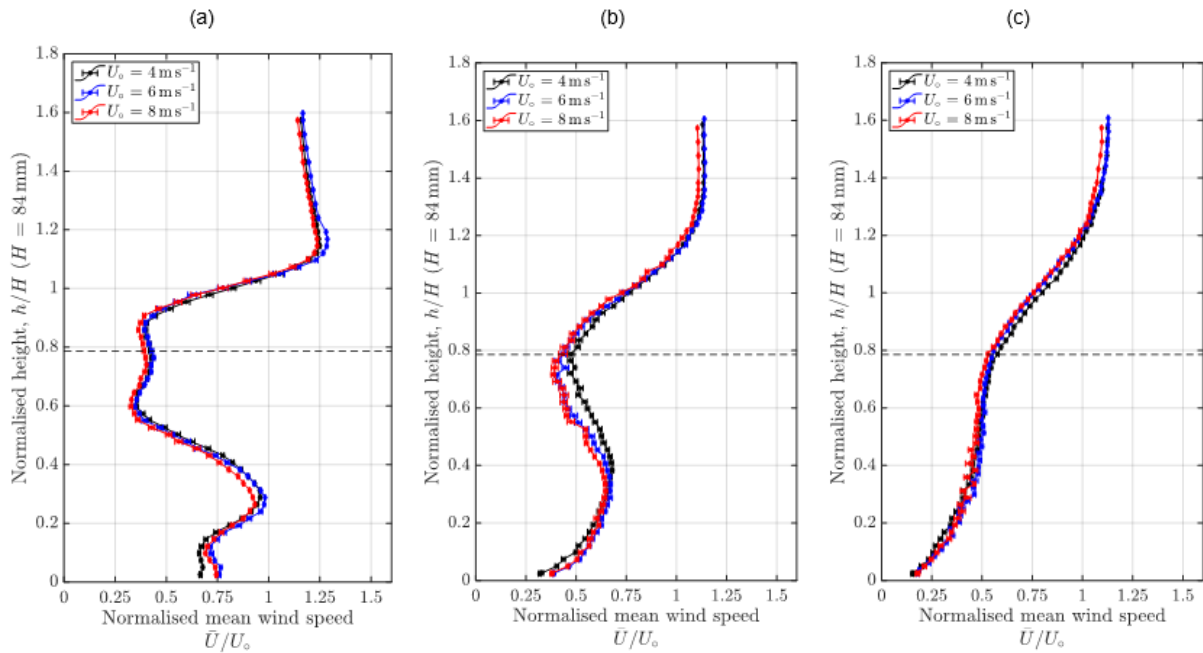


**Figure 22: Profile of the normalised time-averaged wind speed magnitude, at  $0^\circ$  AoA, for different wind speeds, estimated at (a) centre of the hard shoulder, (b) centre of the left lane and (c) centre of the right lane.**

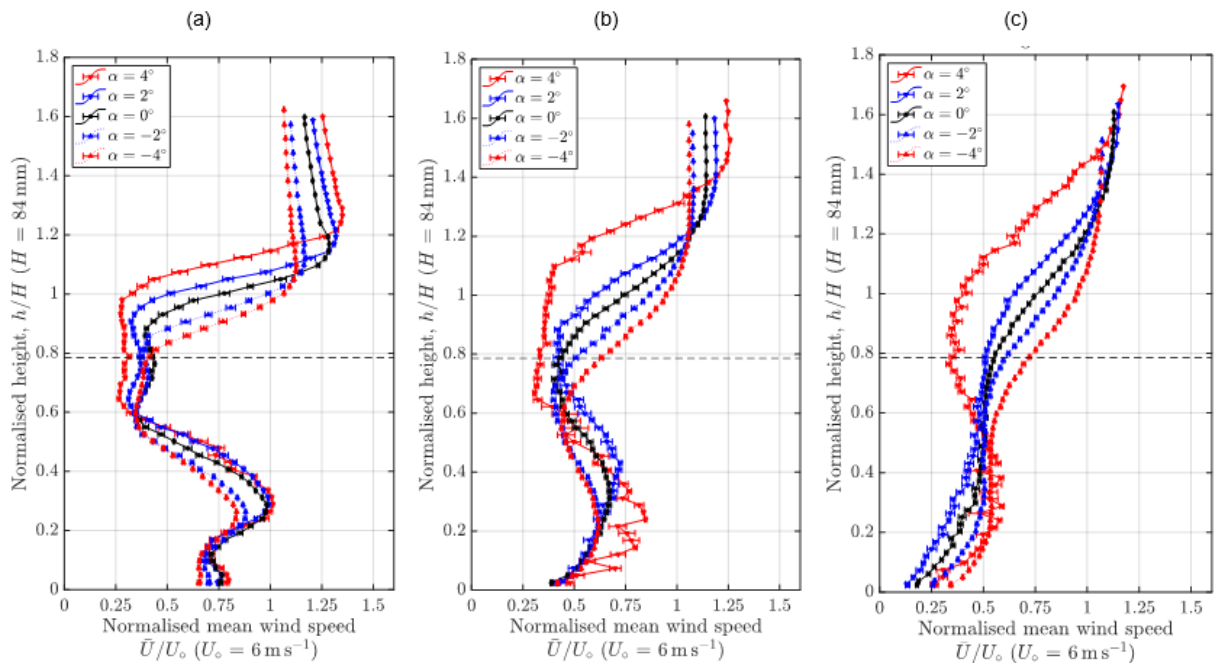


**Figure 23: Profile of the normalised time-averaged wind speed magnitude, at different AoA, for 6m/s wind speed, estimated at (a) centre of the hard shoulder, (b) centre of the left lane and (c) centre of the right lane.**

The report by UoN, Appendix C, goes into further detail regarding the estimated turbulence intensity and turbulence length scale recorded during these tests, which provide additional information on the flow field composition and help inform the comparative review of the wind speed and angle of attack.

### 3.2.2 Pressure distribution across the vehicle

Reviewing the pressure distribution on the vehicle during the simulations provides a better indication of the 3D effect of the wind across the surface of the vehicle that was not modelled in the CFD simulations. The results in Figure 24 are recorded at the pressure tap ring locations highlighted in Figure 21. Ring 3 is in the centre of the vehicle, Ring 1 is near the front of the vehicle, and Ring 5 is near the rear. The results from the three centre rings, 2, 3, and 4, are all very similar. Focusing on the left sub-figure in Figure 24, we can see that the front and rear rings show significantly reduced mean pressure coefficient, a similar reduction is observed at the upper point on the other three rings. This is a result of the wind being able to move around the vehicle at these locations, reducing their impact on the vehicle.

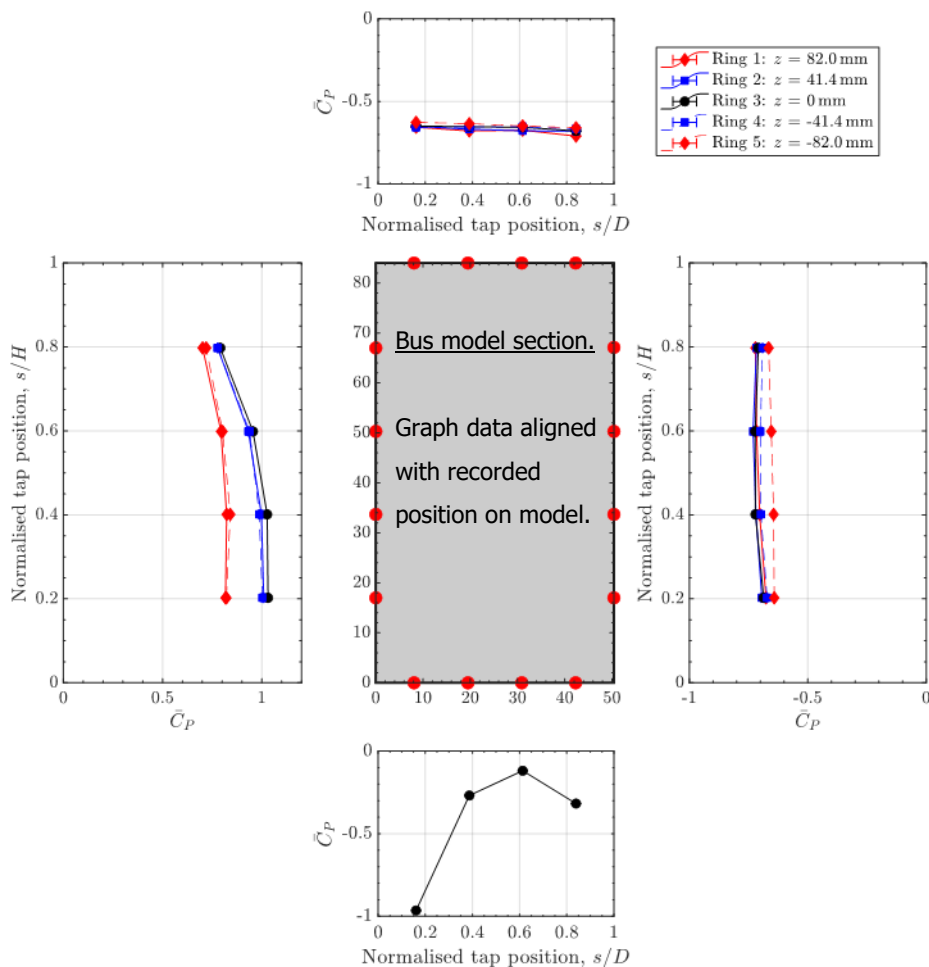


**Figure 24: No wind barrier - Distribution of the mean pressure coefficient around the five rings at the wind speed of 6 m/s and 0° angle of attack. Left (sub-figure) – outer (side) face; Right – inner (side) face; Top – top face; Bottom – bottom face.**

### 3.2.3 Vehicle overturning moment

Considering the overturning moment calculated from the wind tunnel simulations for both the shielded and unshielded conditions, at multiple angles of attack, for a vehicle in the hard shoulder, we can see that the reduction factor is more in line with the values reported by the designer's wind tunnel report. Even the more onerous angle of attack simulated,  $-4^\circ$ , shows a reduction factor of 51.6%, which is close to the 51.3% and 50.7% reduction of overturning moment values reported by the designer wind tunnel results.

**Table 7: Vehicle in Hard Shoulder - Rolling coefficients, and associated reduction factors.**

Wind speed	Angle of attack	Rolling coefficient		Reduction factor
$U$ (ms <sup>-1</sup> )	AoA (°)	Shield, $C_{M,S}$	Unshielded, $C_{M,U}$	$R = C_{M,S}/C_{M,U}$
6	- 4	-0.377	-0.731	0.516
6	- 2	-0.387	-0.760	0.509
6	0	-0.379	-0.791	0.479
6	+ 2	-0.368	-0.820	0.449
6	+ 4	-0.355	-0.842	0.422

### 3.2.4 Wind Tunnel Study conclusion

The wind tunnel study provided us with a clearer indication of how the wind barriers affect the velocity field as it crosses the carriageway in a more realistic 3D environment, compared to the 2D nature of the CFD modelling.

It confirmed the presence of high-speed jets extend through the barrier, quickly dissipating as they cross the carriageway. At the middle of the hard shoulder the normalised wind speed is recorded below 1 over the entire normalised height of the wind barrier. Reducing further as it crosses into Lane 1, normalised wind below approximately 0.65, and Lane 2, normalised wind below approximately 0.5.

---

The reduction in overturning coefficient calculated from the wind tunnel modelling for a vehicle located in the hard shoulder behind the wind barrier, i.e. the highest risk location, was in line with the result from the FCBC wind tunnel report. Indicating that the as built wind barrier is as effective as the one tested in the original designer wind tunnel model despite apparent differences in composition. A reduction factor between 0.422 and 0.516 was reported, with the difference influenced by the difference in vertical angle of attack of the initial wind condition. A negative angle of attack, wind from above the carriageway, exhibited a reduced effect on the overturning coefficient compared to neutral or positive angle initial conditions.

The overturning coefficient of a vehicle was only modelled in the hard shoulder under the scope of this study, however, the enhanced effect of the wind barrier on the normalised wind speed was recorded further into the carriageway in lane one and lane two.

Considering the above the original recommendation made following the CFD modelling stage, restricting double deck buses from using the hard shoulder as a bus lane, is no longer considered necessary under existing threshold levels. However, it is worth bearing in mind that vehicles in Lane 1 will be better protected than those in the hard shoulder.

The study was conducted with a smooth flow wind condition, as opposed to a turbulent initial condition, and with a stationary vehicle, similar to the designer's original wind tunnel tests. The smooth flow condition did not indicate there were any issues that would require further investigation under turbulent flow analysis. The stationary vehicle analysis allows direct comparison to be made to both the designer's original wind tunnel output, and the Jacobs Arup wind speed threshold report, which uses the stationary vehicle overturning variable to define the wind thresholds.

---

## **Lidar Survey**

The Lidar Survey, conducted between February and May 2020, was used to record the dynamics of the wind field around the bridge, providing valuable insight into the behaviour of wind around the Queensferry Crossing and measuring the effectiveness of the wind barrier in situ. This part of the project was funded by Transport Scotland.

The Windcube 100S scanning wind Doppler Lidar system was used for the survey. Its multi scanning mode, and controllable scanning profile, facilitated controlled directional scans around the bridge. It enabled the collection of almost instantaneous data from critical areas, helped build a clear picture of the wind field, and provided a comparable upstream and downstream record of the wind relative to the wind barrier. A more detailed description of the Lidar survey, and data processing is available in Appendix D. This section summarises the method and results of the survey.

### **4.1 Methodology**

#### **4.1.1 Overview**

The Lidar scanner uses Doppler pulsed Lidar to record the movement of aerosols in the wind and determine if they are moving towards or away from the sensor, and at what speed. This provides an accurate record of the radial component of wind speed.

To do this the Lidar emits pulses (100,000 pulses per second) which interact with the minute aerosols in the air (water vapour, dust, smoke etc.). The pulses generate secondary emissions when they reflect off aerosols, and a minute amount of these secondary emissions are reflected back to the Lidar. If the aerosol is moving towards the Lidar it will “squash” the frequency of the signal, if it is moving away it will elongate the frequency of the signal, this minute shift in frequency can be used to determine the radial speed component of the wind. This is carried out at multiple locations along each Lidar beam and gives a reading almost instantaneously. The minute difference in frequency can be used to determine the direction and speed of the radial component of the wind. If enough radial wind speed components are recorded, in a wide enough azimuth, then the software is able determine the actual direction and wind speed of each individual component.

The Lidar sensor was installed on Gantry 08, located at the southern end of the Queensferry Crossing, see Figure 25. The sensor had a clear line of sight of the prevailing wind upstream of the bridge and across the carriageway helping us understand the base condition prior to interference from the bridge and wind barriers.



**Figure 25: Gantry 08 – Lidar location relative to QC**

**4.1.2 Scanning scenario**

Two main types of scan were programmed:

- PPI mode (Plan Position Indicator): constant elevation angle scenario
- RHI mode (Range Height Indicator): constant azimuthal angle scenario

Three PPI scans were carried out. A wide view PPI scan gave an understanding of the characteristics of the wind surrounding the bridges, see Figure 26. This gives an understanding of the large-scale behaviour of the wind field around the bridge. Larger wind structures, gusts, and turbulence around the southern end of the bridge can be observed within the data.

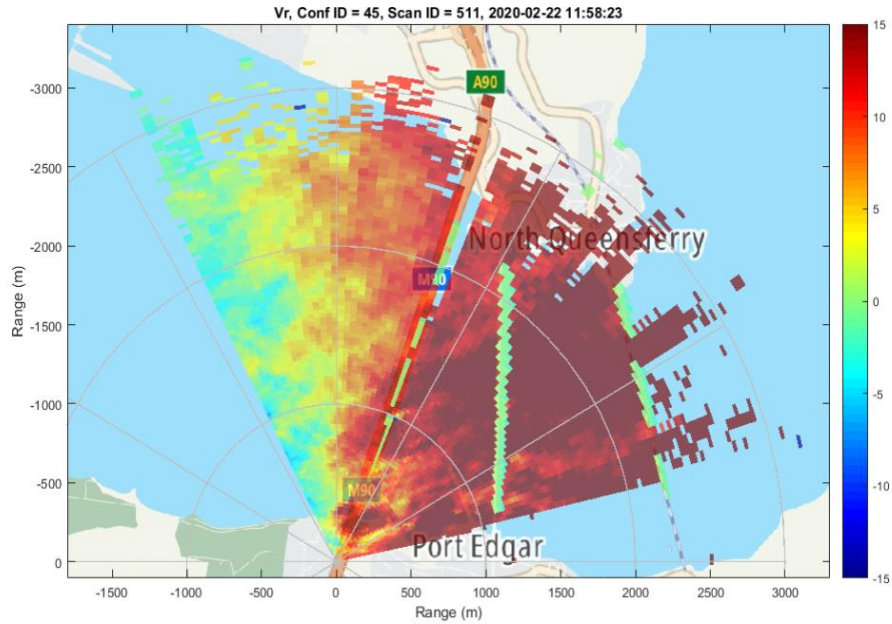


**Figure 26: Mesoscale PPI Scan overlaid on map**

The other two PPI scans were more localised, refined microscale scans. These scans targeted the area closer to the bridge and the refined area allowed a more detailed resolution to be achieved. The higher resolution allowed the smaller wind structures near the windshield to be identified, see Figure 27. These scans had a resolution of 5m along the line of sight and approximately every 1m transverse. The different angles of the two PPI Microscale scans allowed them to intersect the bridge at different locations.

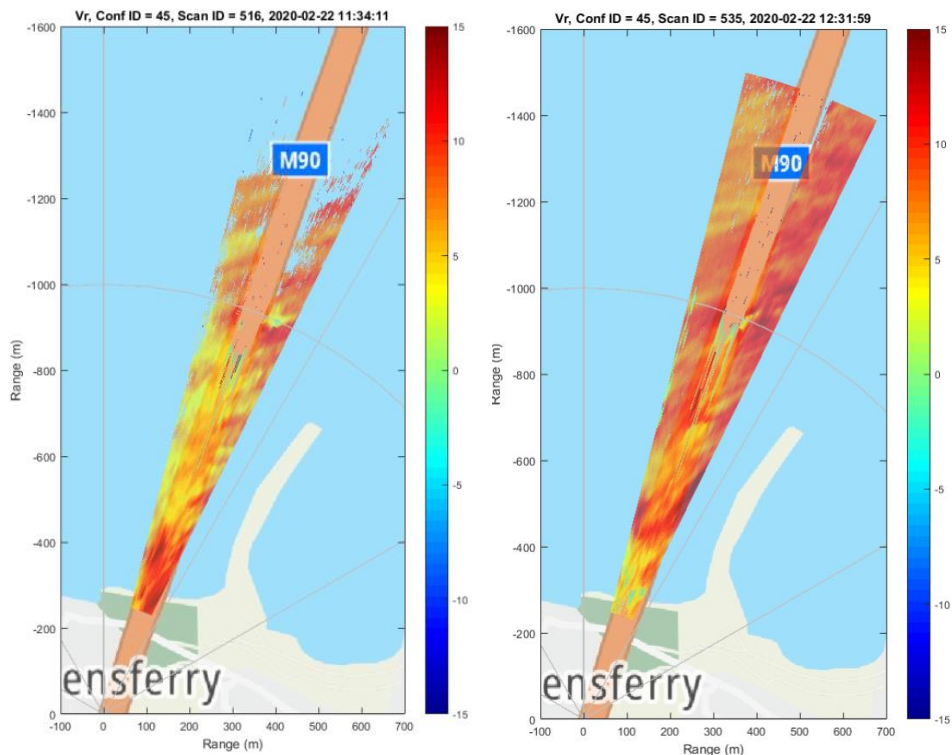


**Figure 27: a) PPI Microscale 0.5° b) PPI Microscale 0.6°**

Two RHI scans were also carried out, at an azimuth of 19.8° and 19.9°, in an attempt to provide a better understanding of the 3D effect of the wind. While these scans provided information on the 3D wind field, the volatile nature of the wind field meant these scans were not suitable for assessing the impact of the wind barrier. The PPI scans proved more beneficial. Each scanning sequence lasted approximately one hour. Table 8 and Table 9 summarise the scans that were undertaken during each sequence.

**Table 8: Survey scan summary table by Leosphere**

Scan parameter	PPI Mesoscale	PPI Microscale	RHI
Azimuth angle (°)	120	6	19.8 – 19.9
Elevation angle (°)	0.55	0.5 – 0.6	3
Accumulation time per line of sight (ms)	500	100	100
Angular resolution (°)	1.5	0.06	0.02
Rotation speed (°/s)	3	0.6	0.2
Range gate length (m)	25	25	25
Number of gates	129	259	250
Minimum range (m)	100	255	250
Display resolution (m)	25	5	5
Max range (m)	3300	1545	1495

**Table 9: Number and type of scans carried out within each scanning sequence**

Number of scans	Type of scan	Angle of scan
120	PPI Microscale	0.5°
120	PPI Microscale	0.6°
15	PPI Mesoscale	0.55°
18	RHI	19.8°
18	RHI	19.9°

#### 4.1.3 Data Processing

As the PPI scans cross the bridge, they intercept the wind barrier and carriageway. The position where the scan dips below the barrier can be identified within the data, which in turn allows a comparison of upstream and downstream wind speeds to be carried out. Figure 28 illustrates the identification of the wind barrier, and other bridge elements such as the cables and bridge deck, within the scan. The data points close to these bridge elements will suffer significant interference and therefore the elements and the area of interference is filtered out of the data, see right hand side image in Figure 28 showing the data post filter.

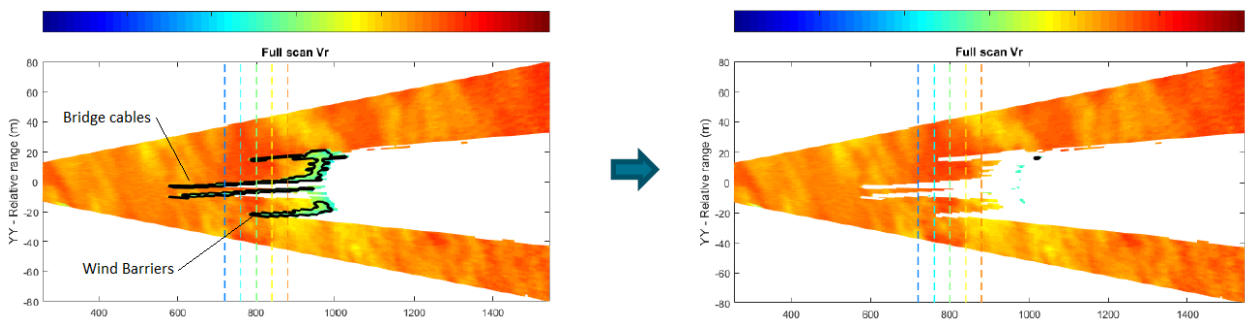


**Figure 28: PPI scan intercepting wind barrier**

Within the data set it was also noted that traffic, both physical vehicles, and the wake generated by the vehicles, can have a significant influence on the data. This cannot easily be filtered out, and therefore must be considered in any interpretation of the data.

To compare data upstream and downstream of the wind barriers sections are taken through the scan data. The positions of these sections, as shown in Figure 29, were defined to provide information above and below the wind barrier height.

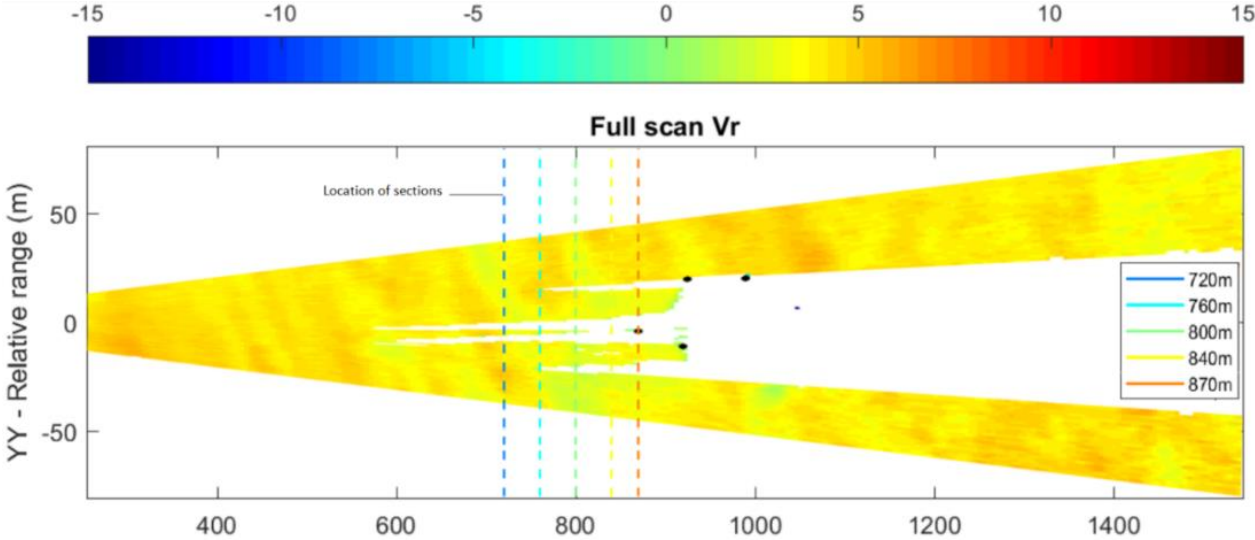


**Figure 29: Scan showing location of sections through the data, scan: 04/03/2020 00:07:09**

Normalising the section data by a value upstream of the wind barrier gives a clearer indication of the influence of the wind barrier. However, the dynamic nature of the wind around the Queensferry Crossing meant that considering individual scans in isolation was not sufficient to gain a clear insight into the effect of the wind barrier.

Differences in wind speeds across the scan, observed as diagonal stripes in the colour gradient of Figure 29, coupled with wind directions not aligned perpendicular with the bridge, resulted in the upstream and downstream values of a section not always aligning with the same wind gust which can distort the wind barrier influence review. Wind direction and flow dynamics continually change during a scan, and between subsequent scans, making extracting definitive conclusions from individual scan sections very difficult. Additional batching and processing of the full data set can help assist in obtaining a more representative data set.

Easterly and westerly winds interact with different wind barriers on the bridge therefore need to be considered separately in any analysis. The position of the Lidar provided a better line of sight for the west side barrier providing a cleaner and more complete set of scan data. Therefore, comparative results will focus on westerly winds only.

A full 180° range was considered too broad a range to average the data across to obtain representative comparisons. Therefore, the data set was divided into smaller 45° range sets, to provide more representative behaviour while still retaining a significant number of samples.

Ideally only winds at exactly 90° to the barrier would be considered, as this is most comparable with the CFD and wind tunnel modelling. Perpendicular westerly wind to the QC is from a 290° direction. Throughout the campaign only 5% of the data recorded was within 5° of this direction (within a range of 285° and 295°). As noted in Leosphere’s report, see Appendix D, wind close to perpendicular to the wind barriers were recorded primarily during periods of low wind speed, less than 10mph, making the radial component significantly distorted by vehicle wake interference and therefore not suitable for direct analysis. Two of the 45° range sets straddle the 290° direction, 245° to 290°, and 290° to 335°. A review of the data from this quadrant revealed that a significant proportion of the recorded data falls into the 245° to 290° range direction, with a reasonable number of samples, equivalent to 37% of the total data sampled during the campaign. Data from 290° to 335° is infrequent, accounting for only 6% of the full campaign data set, and a significant proportion of this small data set was incomplete in the area of interest. Considering the above, the data from the 245° to 290° direction only, see Figure 30, is used for further analysis. In the following sections any data referred to as the “270° direction” represents data averaged across the 245° to 290° direction.

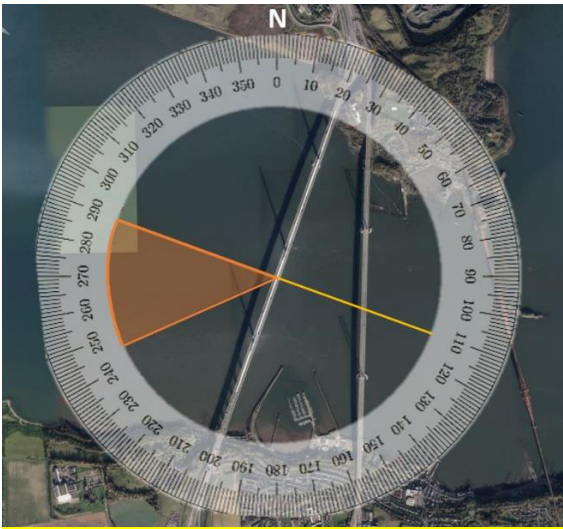


**Figure 30: Orientation of Queensferry Crossing and the 245° to 290° wind direction data range sampled**

---

## **4.2 Results**

### ***4.2.1 Wind field around the Queensferry Crossing***

As the PPI scans cross the bridge the Mesoscale scans give a good overview of the complexity of the wind around the QC and FRB. In a previous review of the wind speed thresholds for QC, undertaken by Jacobs and Arup, they reviewed the possibility of considering directionality as part of the QC wind thresholds. This is not currently implemented in the operational thresholds for the QC as the wind direction is known to change quite quickly in the Forth and therefore difficult to manage from an operational point of view. However, it remains an approach that may be considered again in the future.

The Lidar study observed that not only does wind direction change quickly with time, the flow is unsteady and non-uniform across the bridge at any one time, making it even more difficult to manage a system that considers directionality. The direction recorded at a stationary point, i.e. a weather station, may not be the same as the wind direction across the length of the bridge. Figure 31 gives an example of the fluctuating behaviour. Therefore, any system that relies on directionality is not considered suitable for the Queensferry Crossing.

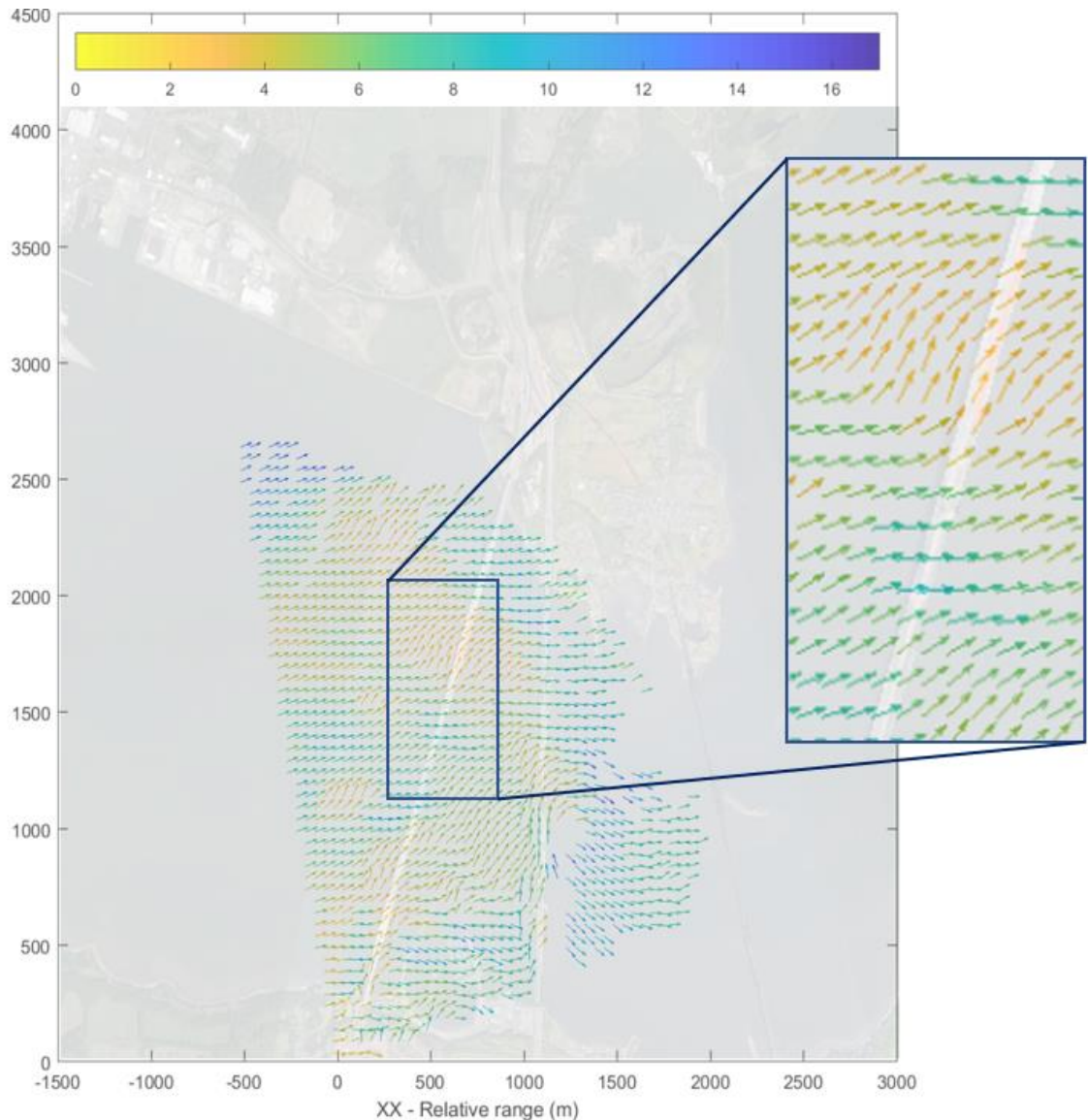


**Figure 31: Reconstructed wind speed (m/s) and direction on 18/03/2020 at 13:00:47 – area zoomed in for clarity.**

#### **4.2.2 Heat Maps**

Following the processing outlined in Section 4.1.3, the cross sections taken through the scans were assembled to generate heatmaps of the data. This assisted with visualising the impact of the wind barrier and identifying other obstacles within the scan. The heatmaps for the normalised radial wind speed, averaged across the 45° direction range, are presented in Figure 32 and Figure 33, overlain on a section of the bridge. The 0.6° scan, and the corresponding sections through the data, sit higher relative to the bridge barrier and carriageway than the 0.5° scan.

Both scans identify the wind barriers on both sides of the bridge, and the cables in the central reserve. The area very close to these points is slightly distorted by the filtering process. In both scans the presence of vehicles in Lane 1 and their subsequent wake, extending above the vehicle, is observed. This indicates that wind recorded in this area is heavily influenced by these vehicles. Vehicles in Lane 2 are not as obvious, as fewer vehicles use this lane and the averaging may be slightly masking the influence. As expected, the area around the hard shoulder does not appear to show any influence from vehicles. This provides a relatively clean data set in this area which can be further analysed. The Lidar Survey data from the hard shoulder area of the carriageway will be further reviewed as part of Section 0 Comparative analysis.

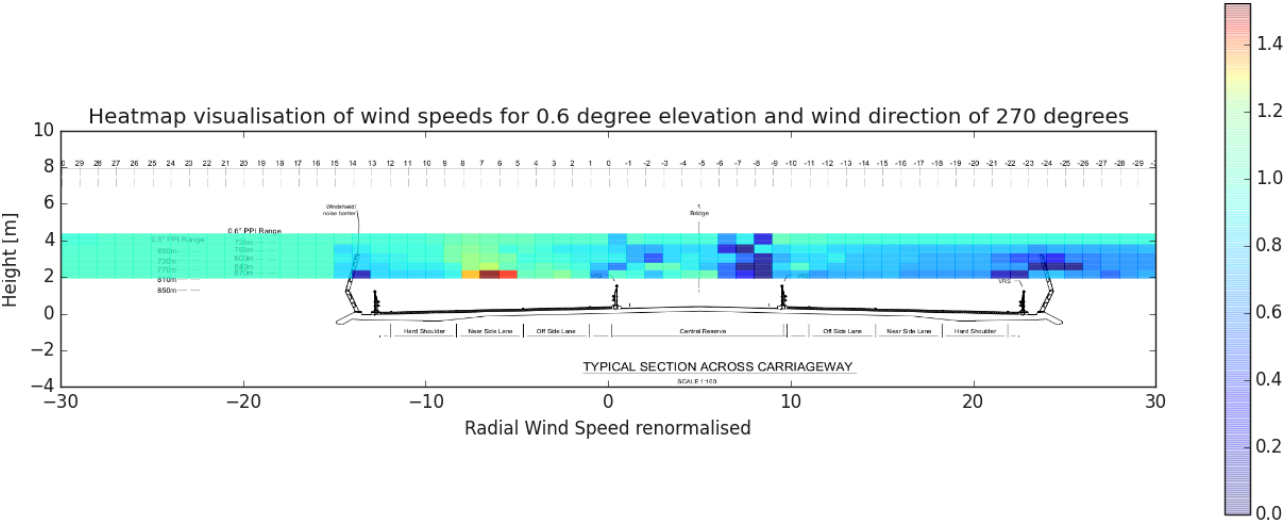


**Figure 32: Heatmap visualisation of normalised radial wind speed - 0.6° PPI scan, 270° direction**

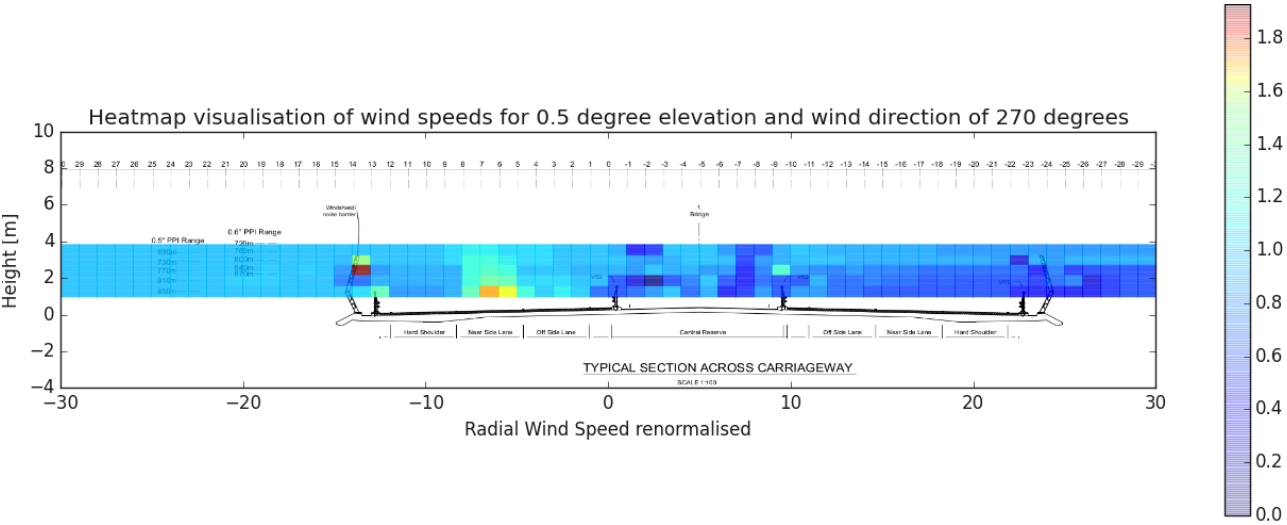


**Figure 33: Heatmap visualisation of normalised radial wind speed - 0.5° PPI scan, 270° direction**

---

## Comparative analysis

### 5.1 Comparing normalised wind speed data across studies

The CFD and Wind Tunnel results, for wind speed reduction behind the wind barrier, recorded in the hard shoulder, are in broad agreement with each another, as shown in Figure 34. In all cases in Figure 34 the wind speed is normalised by a wind speed upstream of the wind barriers, and the height is normalised by the height of a double deck bus, approximated to be 4.2m. The differences in the model results can be accounted for by the 2D nature of the CFD modelling compared to the 3D wind tunnel, and the variance between a computer simulation and physical model. Both model simulations identify a change in the profile of the normalised wind speed behind the barrier when different angles of attack are considered. However, while multiple wind speeds were tested only the maximum wind speed of 6m/s for each of these models are presented as wind speed did not have a significant effect on the profile shape. Therefore, the results for the CFD and Wind Tunnel modelling include the extreme vertical angles of attack that were considered, +/- 4°, alongside the neutral 0° angle of attack results, to show the variance in the response when vertical angle of attack is modified. Figure 34 also includes the normalised site data recorded by the Lidar survey, green data points, for comparison.

The CFD and Wind Tunnel models both use a uniform upstream wind profile from a direction exactly perpendicular to the wind barrier. These controlled simulations allow detailed results to be extracted and display more refined profile shapes for the downstream normalised wind. The Lidar results are coarser sampled data, compared to the controlled model data, and are displayed as individual points on the graph, rather than a line. Lidar results for chainage 9, 10, and 11 are presented as they are within the hard shoulder area of the carriageway. Chainages in the lidar data are approximated from the offside edge VRS of the northbound carriageway, as indicated in Figure 32 and Figure 33.

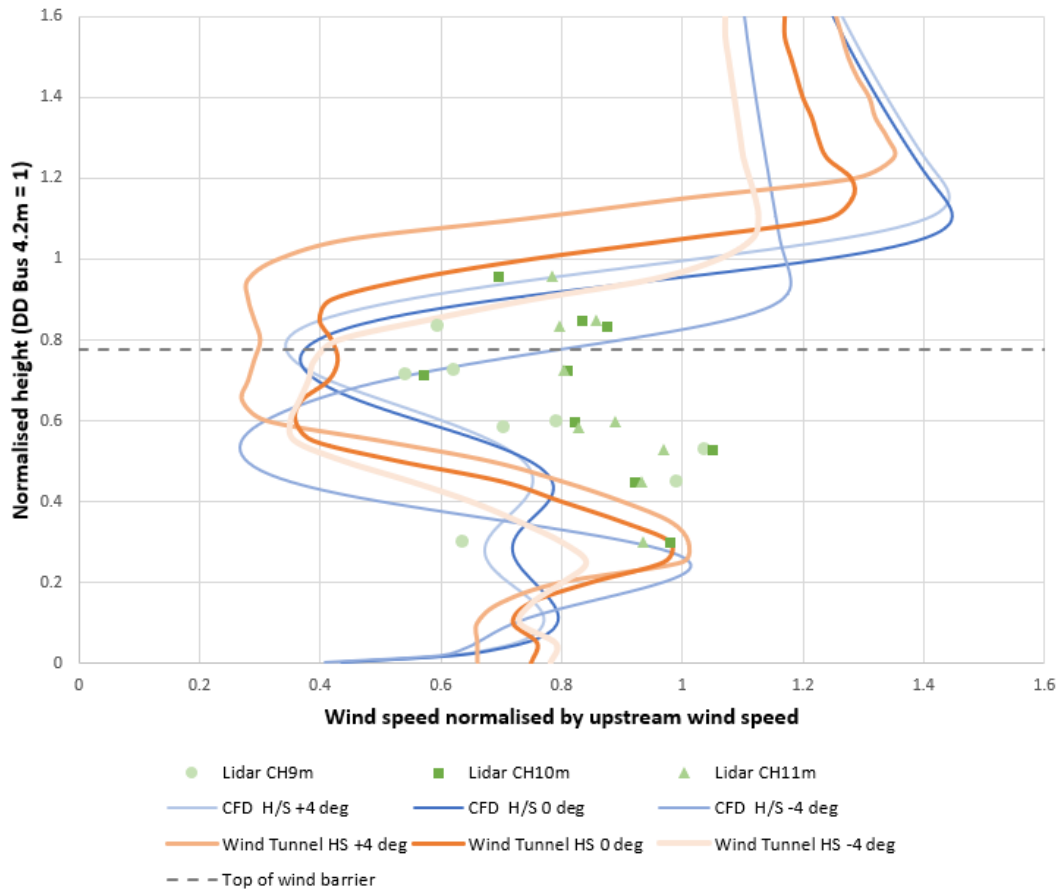


**Figure 34: Hard shoulder normalised wind speed results compared across Lidar, CFD, and Wind Tunnel tests.**

There is broad general agreement in the simulations and site data, but there are some notable differences. In all three cases, CFD, wind tunnel test, and Lidar data, a distinctive “S” shape is noted. In general, the wind speed behind the barrier for the models averages around 0.6 of the upstream wind, whereas for the Lidar data it averages around 0.8 of the upstream wind. The lower “nose” of the “S” shape for the model data aligns well with the gap in the wind barrier, which equates to approximately 1.3m above the carriageway, whereas for the Lidar data the “nose” sits higher up, at around 2.1m above the carriageway.

There are a number of factors that could explain the discrepancy between the models and the site data:

- The models allow a greater number of positions to be recorded, in a more controlled setting, with greater precision, providing a clearer, more accurate profile of wind barrier performance than can be achieved on site.

- 
- Vertical angle component of the wind on site is not known. The models show that this can have a significant effect, however this parameter is not recorded on site.
  - The VRS is not modelled in CFD or Wind Tunnel models, as it is not part of the wind barrier. However, the VRS may be acting to deflect wind gusts coming through the gap in the barrier upwards. A similar effect was noted in the CFD modelling when the FCBC wind tunnel model barrier was modelled for general comparison. This single simulation included the VRS (as it was included in the FCBC wind tunnel model) and a hi-speed jet was observed deflecting the flow upwards, as shown in Figure 19. The as-built VRS is not as dense as the one modelled in that CFD simulation, so it is not expected to produce the exact same result, but it may still have an effect.
  - The exact position of the lidar data point relative to the wind barrier may not be accurate. A lot of care was taken to align the Lidar data results with the bridge and wind barrier. However, pinpointing a single 3D point in a large (1km) scan relative to a comparatively small stationary object (wind barrier is approx. 3.26m high) is challenging. Small discrepancies in this alignment could move the position of this point and explain a 1m difference in position.
  - Lane 1 traffic can affect the results. Both the turbulence caused by vehicles in Lane 1, and the traffic flow influencing the direction of the wind as opposed to the speed, change the radial component of the wind, which the Lidar measures.
  - Averaging of data is not sufficiently able to account for the alignment of the gusts affecting the data.

---

## Conclusion and recommendation

As part of the review of the current wind thresholds on the Queensferry Crossing Amey have undertaken additional research to provide greater insight into how effective the as-built barriers are at reducing potential overturning moment and to better understand the influence of the as built wind barriers on the flow field across the carriageway.

Building on existing information made available by the bridge designer and Transport Scotland, Amey have carried out:

- 2D CFD Modelling of the As Built wind barrier condition. Funded by the SRRB.
- Wind Tunnel Testing of the As Build wind barrier condition. Funded by the SRRB
- Lidar survey of the wind field around the bridge. Funded by Transport Scotland.

Following the 2D CFD modelling Amey made a recommendation to Transport Scotland to restrict double deck buses from using the hard shoulder as a bus lane during high wind events. This was based on the apparent effectiveness of the barrier based on the CFD modelling alone. It was noted that the 2D nature of this modelling may be underestimating the effectiveness of the wind barrier, but the impact of such a restriction was considered minimal compared to the risk and therefore a reasonable interim recommendation. Following the completion of the wind tunnel testing this is no longer considered necessary under existing threshold levels. However, it is worth bearing in mind that vehicles in Lane 1 will be better protected by the wind barrier than those in the hard shoulder.

Previous work by Jacobs Arup (2017) suggested that wind direction could be incorporated into the wind thresholds on the Queensferry Crossing. This has not been implemented as it was considered impractical from an operational point of view. The Lidar survey has highlighted the transient and variable nature of the wind direction across the bridge. Wind gust direction varying +/- 90 degrees across the length of the bridge. Wind threshold protocols are based on stationary weather stations that record wind direction at a single point. Therefore, including wind direction within existing thresholds is not considered practical.

The wind tunnel tests carried out as part of this study reported a worst-case reduction factor of 0.516. This was recorded for a negative angle of attack of 4°.

---

Based on this reduction factor the maximum wind speed threshold for double decker buses, which will maintain an equivalent wind speed pressure behind the barrier below 45mph, in line with the FRB unshielded condition wind speed threshold, is 62mph. Therefore, the existing 60mph Queensferry Crossing wind speed threshold for double decker buses is considered appropriate, where double decker buses retain the ability to use the hard shoulder if required.

### **6.1 Recommendation for additional work**

This study has identified additional work that may facilitate the potential to increase the wind threshold for double decker buses by restricting double decker buses to Lane 1 and Lane 2, removing the ability to use the hard shoulder as a bus lane, but taking advantage of the increased protection provided by the wind shielding to those lanes. This will require an additional wind tunnel test that fell out with the scope of this study to date but could be undertaken by the current bridge operator in partnership with the University of Nottingham. Modifications to the existing wind tunnel model would be required to position the vehicle in lane 1 and lane 2 and measure the rolling effect in these lanes, allowing the calculation of the reduction factor for those lanes to be obtained. The reduction factor should be calculated for the different angles of attack and the worst case considered. As a guide, a reduction factor of 0.45 or below would need to be measured in the worst-case condition for Lane 1 to increase the threshold to 65mph, with restrictions on hard shoulder use as a bus lane. To increase the threshold to 70mph, with restrictions on hard shoulder use as a bus lane, a reduction factor below 0.40 would need to be measured in the worst-case condition for Lane 1.

---

## References

- Hansen, S., Svendsen, M., Brøndum, S., , , & . (2012). *Forth Replacement - Wind tunnel test report*.
- Jacobs Arup, . (2017). *Queensferry Crossing - Effect of High Winds on Traffic*.
- Rocchi, D., Argentini, T., Sbroisi, M., & Rosa, L. (2009). *Wind tunnel tests - Wind shield modelling for the Forth Replacement Crossing*.
- The Forth Bridges. (2018). *Wind and Weather*. Retrieved from The forth bridges:  
<https://www.theforthbridges.org/plan-your-journey/wind-and-weather/>
- Transport Scotland. (2011). *Forth Replacement Crossing - Principal contract for the Design, Construction and Completion of the Forth Replacement Crossing - Employer's Requirements*.

---

## **Appendix A   Extract from Employer's Requirements**

**4 Ancillary Items****4.1 Deck Furnishing: Road Restraint Systems**

- 4.1.1 The Contractor shall ensure that the VRS is made of painted galvanised steel elements.
- 4.1.2 The VRS shall be in accordance with TD19 of the DMRB.
- 4.1.3 The Contractor shall ensure that the VRS is compatible with the road restraint systems to which they are, or shall be, connected.
- 4.1.4 VRS of concrete construction or combined metal and concrete construction shall not be permitted on the Main Crossing except at movement joints.

**4.2 Deck Furnishing: Wind Shields**

- 4.2.1 The Contractor shall provide wind shields along the full extent of the outer edges of the deck to permit the Main Crossing to remain open to traffic including wind susceptible vehicles in high wind conditions.
- 4.2.2 The Contractor shall design these wind shields to reduce the overturning moment on a high-sided vehicle which shall be assumed to be a double-deck bus, as shown in Figure 2 and Figure 3 below. The overturning moment on the vehicle when located in the hard shoulder shall be 50 per cent or less than the overturning moment on the same vehicle in the same location with no wind shields present. Fulfilment of this criterion shall be verified by the Contractor through wind tunnel tests with winds perpendicular to the centreline of the bridge as shown in Figure 4.



Figure 2 Definition of a double-deck bus (1)

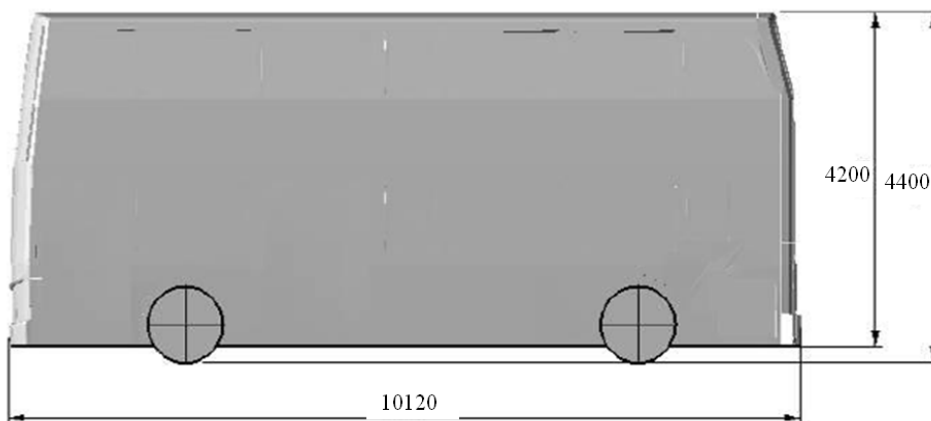


Figure 3 Definition of a double-deck bus (2)

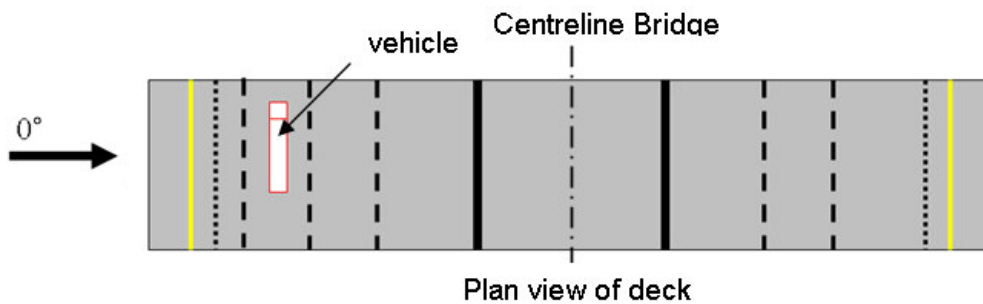


Figure 4 Definition of wind angle

4.2.3 The Contractor shall also provide wind shield barriers at the inner edges of each carriageway in the central reserve at each tower location. These wind shields shall gradually reduce in height in accordance with the Definition Drawings.

4.2.4 The wind shields in Section 4.2.3 above, shall be designed to ensure that the overturning forces and rate of change of load coefficient at the cab-end of a high-sided lorry shall not exceed the maximum values stated in Table 4 below:

**Table 4 Wind forces on static vehicles with tower wind shield barriers.**

Description	Criterion	Maximum Value
Transverse Mean Force Coefficient	$\max  C_{Fy} $	0.35
Rate of Change of Overturning Coefficient on Cab End of Lorry	$\max \left  (0.5) \frac{\Delta C_{Fy}}{\Delta x} - (1.6) \frac{\Delta C_{Mz}}{\Delta x} \right $	0.02 m <sup>-1</sup> (per $\Delta x \leq 10\text{m}$ longitudinal distance)

where:

(a) The transverse force coefficient is defined as;

$$C_{Fy} = \frac{\overline{F}_y}{qLH}$$

where  $\overline{F}_y$  is the mean transverse force measured on a static model of a high-sided lorry shown in Figure 5 and Figure 6,  $\overline{q} = 0.5\rho V^2$  is the mean oncoming wind pressure in which  $\rho$  is the air density and V is the mean oncoming wind speed, and L and H are the characteristic length and height of the vehicle (L=16.56 metres, H=3.84 metres for the high-sided lorry selected and shown in Figure 5 and Figure 6);

(b) The mean torque coefficient is defined as;

$$C_{Fy} = \frac{\overline{M}_z}{qL^2H}$$

where  $\overline{M}_z$  is the mean torque around a vertical axis measured on the high-sided lorry model. Note that the torque is normalized using L<sup>2</sup>; and

(c) in calculation of the rate of change of overturning coefficient on a cab end of the lorry  $\Delta C_{Fy}$  and  $\Delta C_{Mz}$  represent the change in mean side force and torque within a distance of  $\Delta x = x_2 - x_1 \leq 10\text{m}$  which represents two positions of the lorry on the carriageway in the wake of the tower.

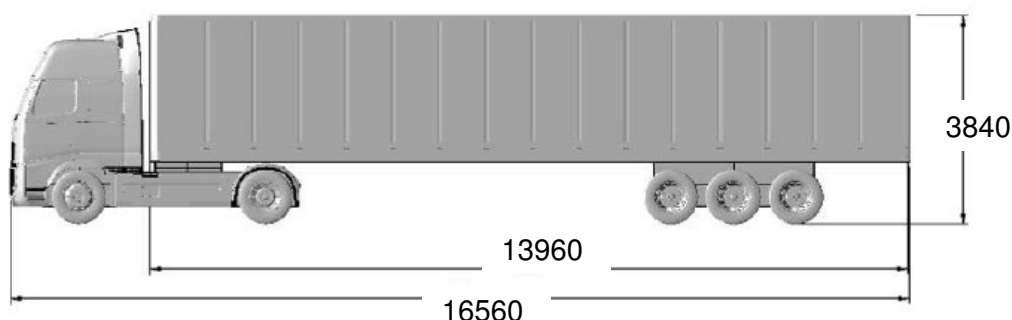


**Figure 5 Definition of a high-sided lorry (1), dimensions in millimetres**

---

## **Appendix B CFD modelling report**



University of  
**Nottingham**  
UK | CHINA | MALAYSIA

# Report

# Investigation of Wind barriers on the Queensferry Crossing

Computational Fluid Dynamics Study

18 September 2020

# Change Record

---

Revision Number:

Reason for change	Date	Pages	Paragraph(s)
-------------------	------	-------	--------------

---

## Table of Contents

1	Introduction.....	4
2	Method.....	4
2.1	Computational domain.....	4
2.2	Numerical application.....	7
2.3	Sampling and processing data.....	8
3	Flow field across an empty carriageway.....	11
3.1	Angle of attack $0^\circ$ .....	11
3.2	Other angles of attack.....	20
4	Aerodynamics of the vehicle.....	26
4.1	Vehicle on the centre of the hard shoulder.....	26
4.2	Vehicle on the centre of the left lane.....	34
4.3	Comparison of flow field.....	42
4.4	Reduction factor of overturning moment.....	46
5	FCBC Wind Barrier.....	50
5.1	Empty carriageway.....	50
5.2	Vehicle on the carriageway.....	55
6	Summary.....	59

# 1 Introduction

The Computational Fluid Dynamics (CFD) study of the as-built wind barrier on the Queensferry Crossing (QFC) was carried out to numerically investigate the effect the barriers have on the flow field and aerodynamics of vehicles using the bridge. This information will assist the review of the existing wind thresholds for the bridge.

## 2 Method

### 2.1 Computational domain

Using the dimensions from the provided technical drawings and the dimensional survey (conducted on 26/09/2019), 1:10 scale CAD (computer-aided design) models were created of a half of the upper surface of the bridge-deck cross section, louvres and a reference vehicle. Three examples of these CAD models are shown in Figure 2.1. Certain details on the surface of the bridge deck (such as Details 2, 3 and 6 in the drawing AB-FRC-P-CSB-026-D-MC-DEC-17502) were ignored. Effects of these features on the flow field is expected to be significantly less compared to the wind barriers. Also, modelling these details at the scale of 1:10 results in a very fine mesh, which will increase both computational time and resource to complete each simulation. The slope and height of the road surface as well as the wind fairing and louvres were modelled based on the provided dimensions, since these features are essential for modelling the flow across the bridge deck. The reference vehicle is a 1:10 scale double-decker bus and was modelled as a rectangular box with the dimension of 0.252 m by 0.420 m. The vehicle was placed at two locations across the deck: at the centre of the hard shoulder and at the centre of the near side lane (which is hereafter called the left lane), as shown in Figure 2.1b and Figure 2.1c.

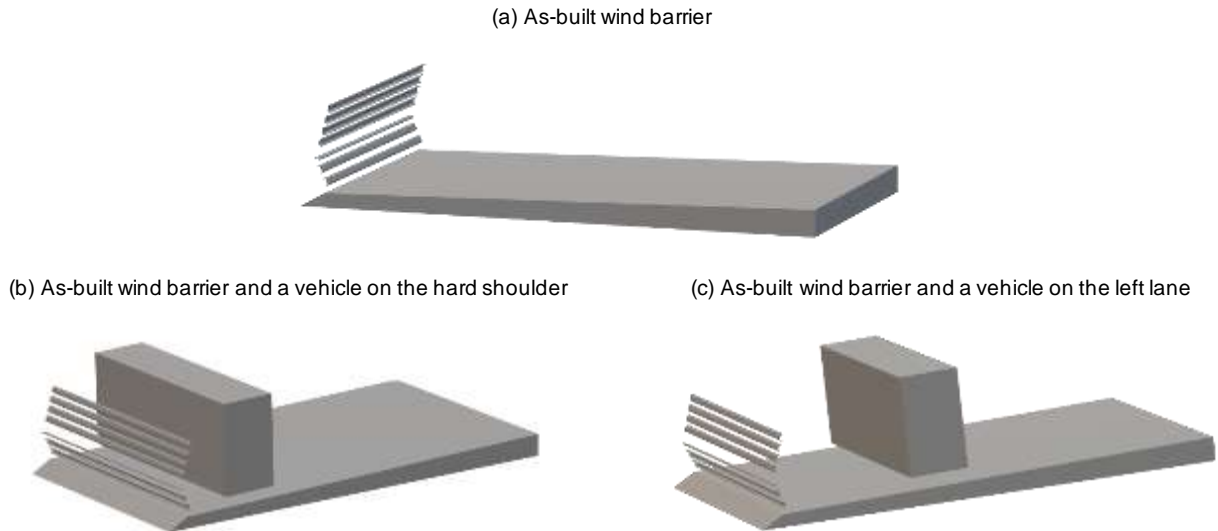


**Figure 2.1.** CAD models used when generating the CFD mesh

A 2D (two dimensional) computational domain was constructed from each CAD model using ANSYS-Geometry within Workbench. As an example, Figure 2.2a shows the computational domain of Mesh C2 having the as-built wind barrier and the reference vehicle at the centre of the hard shoulder. The domain is divided into 8 blocks. Dimensions of the blocks are varied to accommodate different geometries of the wind barriers and location of the vehicle. The boundary conditions are also summarised in Figure 2.3a. It is noted that the boundary conditions of the `top` and `bottom` planes vary based on the angle of attack, while the others remain unchanged.

The meshing operation to the computational domain was done using ANSYS-Meshing within Workbench and OpenFOAM utility `fluentMeshToFoam`. The domain was discretised using a 2D hybrid-hexahedral grid, where the cell size was controlled by a combination of the face sizing and edge sizing. An example is shown in Figure 2.2b, which details meshing parameters for Mesh C2. Facing sizing (written in red) is used to control the cell size of Blocks 2 and 3 containing the wind barrier and the vehicle, respectively, whereas edge sizing (written in black along the edges) is used for the remaining blocks. The arrows indicate the direction of growing in cell size; the numbers in the bracket are the size of the first cell and the growth rate, respectively. Also, an inflation layer which is a six-cell-thick structured grid is imposed around each louvres and the vehicle where the thickness and length of the cells next to the wall is  $2.5 \times 10^{-4}$  m and grows by a ratio of 1.3. The thickness of the cells next to the bridge deck is  $1.0 \times 10^{-3}$  m. An overview of Mesh C2 as well as a close-up view around the wind barrier is shown in Figure 2.3.

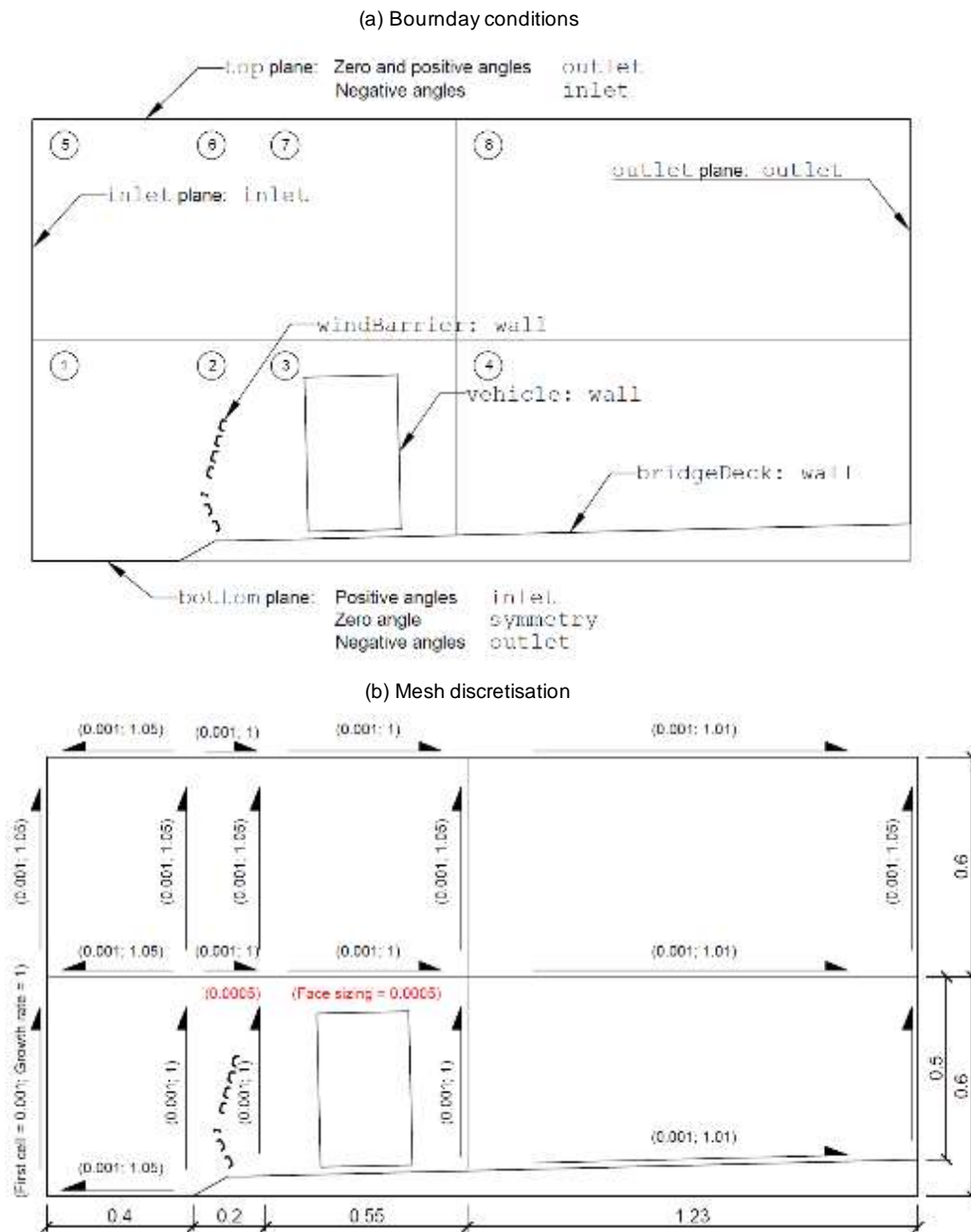


**Figure 2.2.** (a) Boundary conditions and (b) detailed discretisation of Mesh C2. All dimensions in sub-figure b are in metres. Growth rate is the ratio of two adjacent cells' size.

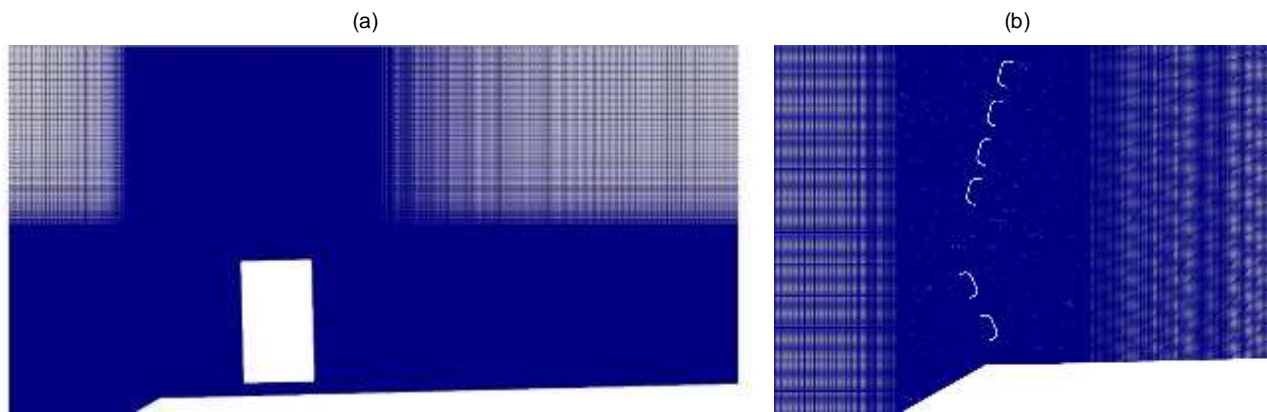


**Figure 2.3.** (a) An overview of Mesh C2 and (b) a close-up view around the wind barrier.

CFD simulations were also conducted for the wind barrier found in the FCBC (Forth Crossing Bridge Constructors) wind tunnel model (hereafter referred as the FCBC wind barrier) in order to compare the performance of the as built and FCBC wind barriers. Since the FCBC wind tunnel model was not available, dimensions of the wind barriers were estimated. The key properties including the height and the porosity are similar to the as-built wind barrier. The louvres on the FCBC wind barrier were modelled as sharp-edge flat plates that have the same height as the C-shaped louvres on the as-built wind barrier. Their positions were based on the FCBC wind tunnel model. It is noted that the gaps in the lower part of the FCBC wind barrier is larger than those in the as-built wind barrier. The vehicle restraint system (VRS) was also modelled as it was included in the FCBC wind tunnel model, whereas the VRS was not included in the model of the as-built wind barrier. Figure 2.4 is a close-up view around the FCBC wind barrier in Mesh F1.

In total, nine different meshes were used in the CFD study and the details of the wind barrier geometry, the position of the vehicle and the total number of cells are summarised for each mesh in Table 2.1.

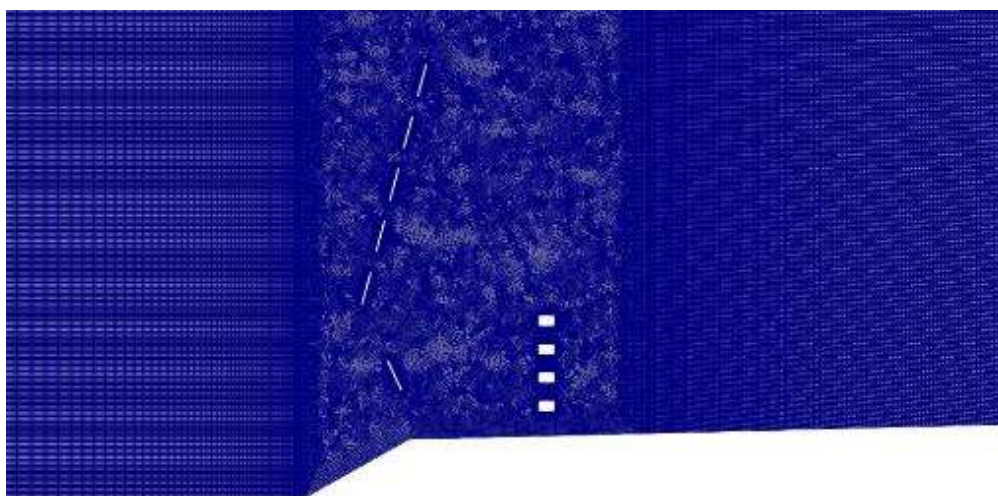


**Figure 2.4.** A close-up view around the FCBC wind barrier in Mesh F1.

**Table 2.1:** Summary of nine meshes used in the CFD study.

Mesh ID	Descriptions				Number of cells
	Wind barriers		Vehicle		
	As-built	FCBC	Hard shoulder	Left lane	
Mesh C1	x				696,000
Mesh C10					311,000
Mesh C2	x		x		552,000
Mesh C20			x		532,000
Mesh C3	x			x	706,000
Mesh C30				x	675,000
Mesh F1		x			342,000
Mesh F2		x	x		501,000
Mesh F3		x		x	706,000

## 2.2 Numerical application

The computation was conducted using the open-source CFD software OpenFOAM v6 on the High Performance Computing system at the University of Nottingham.

The unsteady flow across the wind barrier and the bridge deck and around the vehicle was modelled using URANS (Unsteady Averaged Navier Stokes) SST (Shear Stress Transport)  $k-\omega$  turbulence model. The pressure-velocity coupling was achieved by means of the PIMPLE algorithm, which is merged of PISO (Pressure Implicit with Splitting of Operator) and SIMPLE (Semi-Implicit Method for Pressure-Linked Equations) solvers. During one time-step, two PISO loops were performed, leading to better coupling between pressure and velocity and allowing bigger time-steps and, hence, Courant number. The governing equation was discretised using second-order numerical schemes. Non-orthogonal correction was enabled to take into account the skewness and non-orthogonality of unstructured grid. The temporal discretisation was achieved using the first-order differencing scheme. The time-step size was variable to keep the maximum Courant number below 4 across the mesh.

The OpenFOAM solver `pimpleFoam` was used to simulate the flow across the bridge deck at three different CFD-scaled wind speeds, 2, 4 and 6  $\text{ms}^{-1}$  and at the five angles of attack varying from  $-4^\circ$  to  $4^\circ$  in  $2^\circ$  increments. The inflow condition was very low turbulent having the turbulence intensity of 0.1% and the turbulence length scale of 0.010 m. Table 2.2 shows the values of the wind speed and the angle of attack for each mesh and the number of simulations in this study.

**Table 2.2:** Matrix of simulations.

Mesh ID	Wind speed ( $\text{ms}^{-1}$ )			Angle of attack ( $^\circ$ )					Number of simulations
	2	4	6	-4	-2	0	2	4	
Mesh C1	x	x	x	x	x	x	x	x	15
Mesh C10	x			x		x		x	3
Mesh C2	x			x	x	x	x	x	5
Mesh C20	x			x		x		x	3
Mesh C3	x			x		x		x	3
Mesh C30	x			x		x		x	3
Mesh F1	x					x			1
Mesh F2	x					x			1
Mesh F3	x					x			1
<b>Total number of simulations</b>									<b>35</b>

## 2.3 Sampling and processing data

### 2.3.1 Velocity field

During a simulation, OpenFOAM function `probe` was used to sample the velocity file at one position on the bridge deck. Velocity sampling points are arranged in a rake comprising 100 points equally distributed at 0.008 m intervals. The rake is oriented perpendicular to the bridge deck and is placed at three different positions across the bridge deck, which are the centre of the hard shoulder, left lane and right lane. These velocity sampling rakes are highlighted red in Figure 2.5. In some simulations, additional rakes are placed directly behind the wind barrier, in between lanes and at the end of the carriageway. These rakes, which are highlighted blue in Figure 2.5, enable more detailed investigation on how the normal velocity profile varies across the deck. The exact location of these velocity sampling rakes is summarised in Table 2.3. At each sampling point, the wind velocity components that are parallel and normal to the bridge deck are sampled at the rate of 500 Hz.

Having time-histories of the parallel and normal component,  $u(t)$  and  $w(t)$  respectively, the following temporal statistics can be evaluated:

- Mean wind speed
- Mean wind angle
- Turbulence intensity of the wind velocity component parallel to the bridge deck
- Turbulence intensity of the wind velocity component normal to the bridge deck
- 1-s gust factor

It is noted that an early part of the time histories shows significant variation because the flow is still developing across the bridge deck. This transient stage is therefore removed, prior to estimating the temporal statistics. This treatment is applied to other processes of sampling and analysing pressure and force coefficient data.

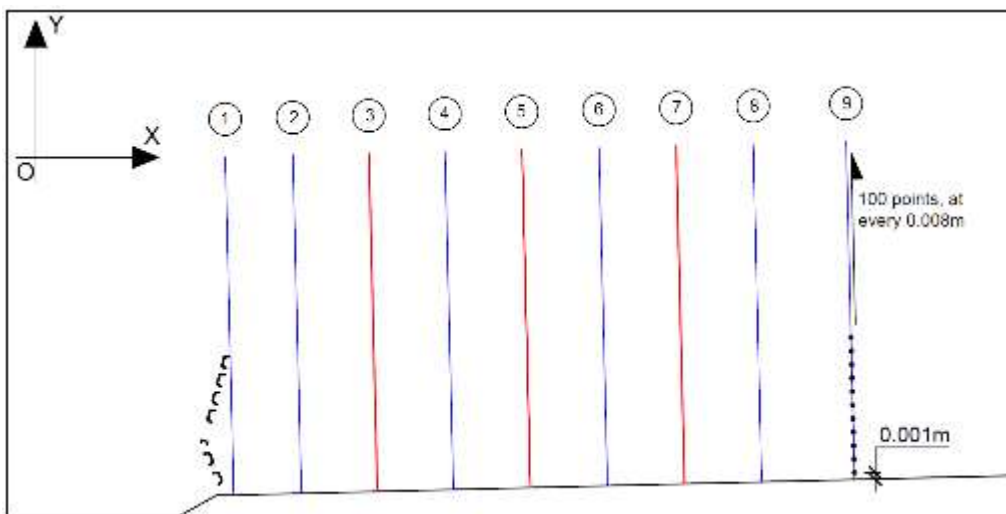


Figure 2.5. Velocity sampling rakes.

**Table 2.3:** Location of the velocity sampling rakes across the bridge deck.

Sampling line No.	Position on the bride deck
1	Right behind the wind barrier (WB)
2	Edge of the hard shoulder (HS)
3	Centre of the hard shoulder
4	Line between the hard shoulder and left lane (LL)
5	Centre of the left lane
6	Line between the left lane and right lane (RL)
7	Centre of the right lane
8	Edge of the right lane
9	End of the carriageway

### 2.3.2 Surface pressure around the vehicle

The OpenFOAM function `probe` was also used to sample surface pressure around the vehicle. 101 pressure sampling points are uniformly distributed along a shorter side at 0.0021 m while a longer side is covered by 201 points evenly distributed at 0.00252 m, as shown in Figure 2.6. At each point, surface pressure is sampled at the rate of 500 Hz.

Time-histories of the pressure coefficients are calculated by normalising the surface pressure by the upstream mean wind speed  $U_0$ , as follows:

$$c_p(t) = \frac{p(t)}{0.5 \rho U_0^2} \quad (1)$$

Temporal statistics such as the mean and RMS values of the pressure coefficients are then evaluated after transient data has been removed.

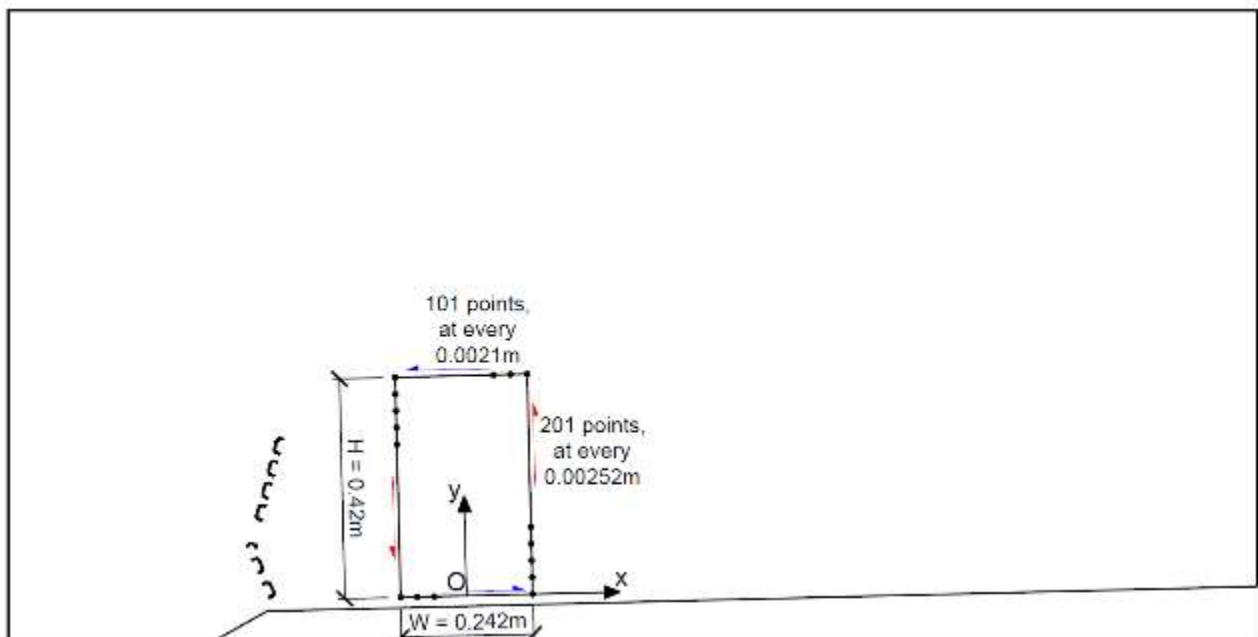


**Figure 2.6.** Pressure sampling points around the vehicle

### 2.3.3 Vehicle aerodynamic force and moment coefficients

The aerodynamic forces and moments acting on the vehicle are defined according to the coordinate system attached to the vehicle as shown in Figure 2.6. As 2D URANS simulations are performed, the following force and moment components are considered:

- Drag force  $F_D(t)$ , i.e. the side force acting along the x axis
- Lift force  $F_L(t)$ , i.e. the vertical force acting along the y axis
- Rolling moment  $M(t)$ , i.e. the moment around the z axis.

The aerodynamic forces and moment are normalised by the air density  $\rho = 1.225 \text{ kgm}^{-3}$ , the geometry of the vehicle (the side area  $A = 0.042 \text{ m}^2$  and the height  $H = 0.420 \text{ m}$ ), and the upstream mean wind speed  $U_0$ , yielding time-histories of force and moment coefficients, as follows:

- Drag coefficient 
$$c_D(t) = \frac{F_D(t)}{0.5 \rho A U_0^2} \quad (2)$$

- Lift coefficient 
$$c_L(t) = \frac{F_L(t)}{0.5 \rho A U_0^2} \quad (3)$$

- Rolling coefficient 
$$c_M(t) = \frac{M(t)}{0.5 \rho A H U_0^2} \quad (4)$$

Having time-histories of the force and moment coefficients, temporal statistics can be estimated, including mean, 1-second peak, and root-mean-squared (RMS) values after transient data has been removed.

### 3 Flow field across an empty carriageway

This section presents results of CFD simulations and discusses key features highlighting effects of the wind barriers on the flow field across an empty carriageway and how a variation in the angle of attack influences these features.

#### 3.1 Angle of attack $0^\circ$

Using the wind speed of  $6 \text{ ms}^{-1}$  as an example, Figure 3.1 shows a view of the instantaneous flow field across the bridge deck at  $0^\circ$  angle of attack. Superimposed on the contour plots are the nine straight lines representing the velocity sampling rakes as described in Table 2.3.

As shown in Figure 3.1a, overall, the presence of the wind barrier helps reduce the wind speed across the bridge deck. Noticeable reduction can be observed on the left lane and right lane. Closer to the wind barrier, even though the wind speed is slowed down, the hard shoulder sees an increase in the unsteadiness in the flow. This is caused by the high-speed jets as the flow accelerates passing through gaps between the louvres. For example, as shown in Figure 3.1**Error! Reference source not found.**b, a three-fold increase in the instantaneous wind speed magnitude can be observed in the gaps between the bridge deck and the bottom louvre and between the two top louvres. These high-speed jets are unstable and quickly interact downstream of the wind barriers, leading to the generation of small vortices and subsequently a high level of unsteadiness in the flow.

In addition, the bluff body of the C-shaped louvres encourages the vortex shedding phenomena. This effect is more noticeable on the top louvres where a vortex street is generated from the upper flange and propagates across the bridge deck while dissipating their energy (Figure 3.1b).

Averaging the flow field throughout the duration of the CFD simulation produces the time-averaged velocity field as shown by the contour and vector plots in Figure 3.2. The contour plot represents the magnitude of the wind speed; red indicates speeding up while blue indicates slowing down. The plot shows the acceleration of the wind passing through the gaps on the wind barrier as well as just above the shear layer, which is highlighted, by the red box in Figure 3.2. The streamline plot, which represents the mean wind direction, indicates the combined effect of the wind fairing and wind barrier on deflecting the wind away from the bridge deck surface.

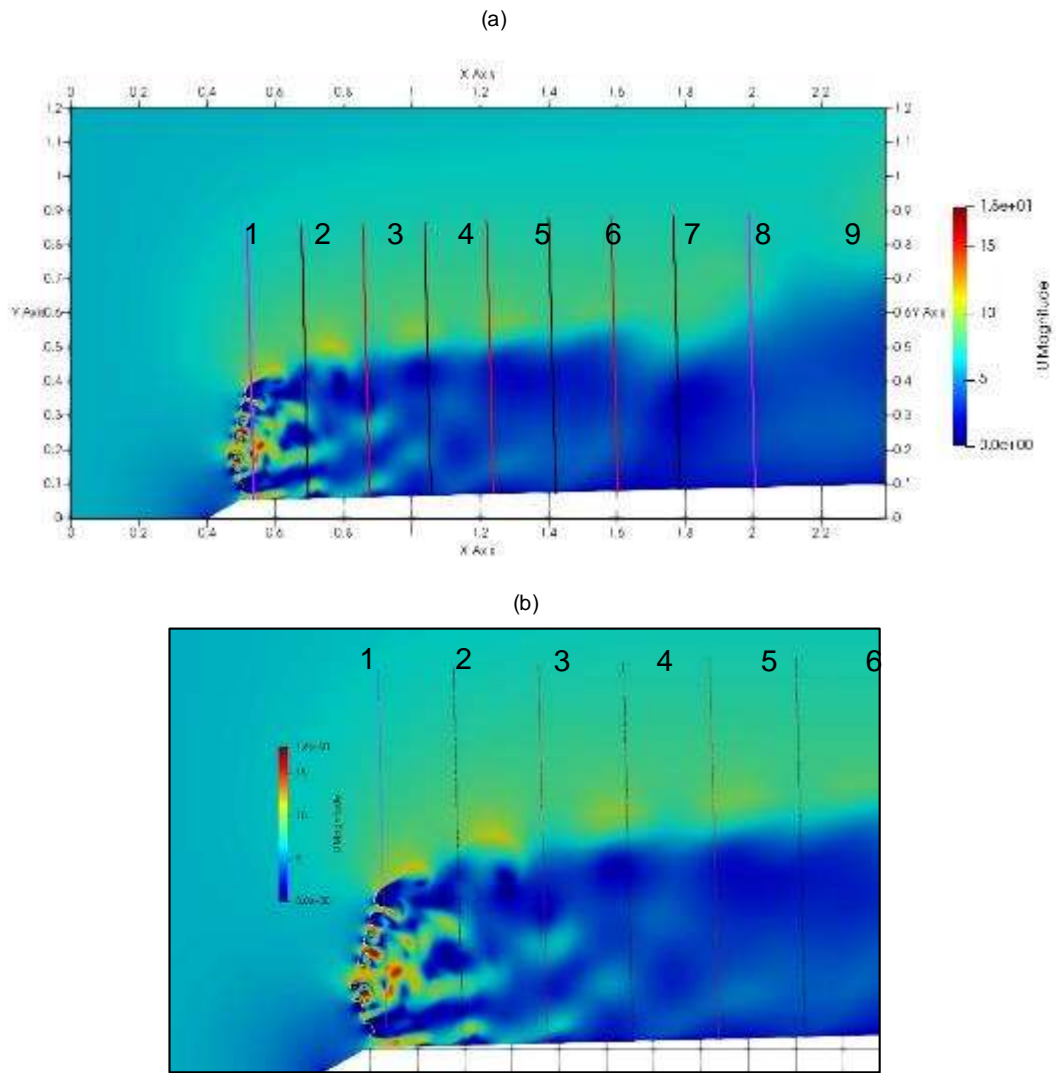


**Figure 3.1.** Contour plots of the instantaneous velocity field (a) across half the bridge deck and (b) around the wind barrier, at the wind speed of  $6 \text{ ms}^{-1}$ .

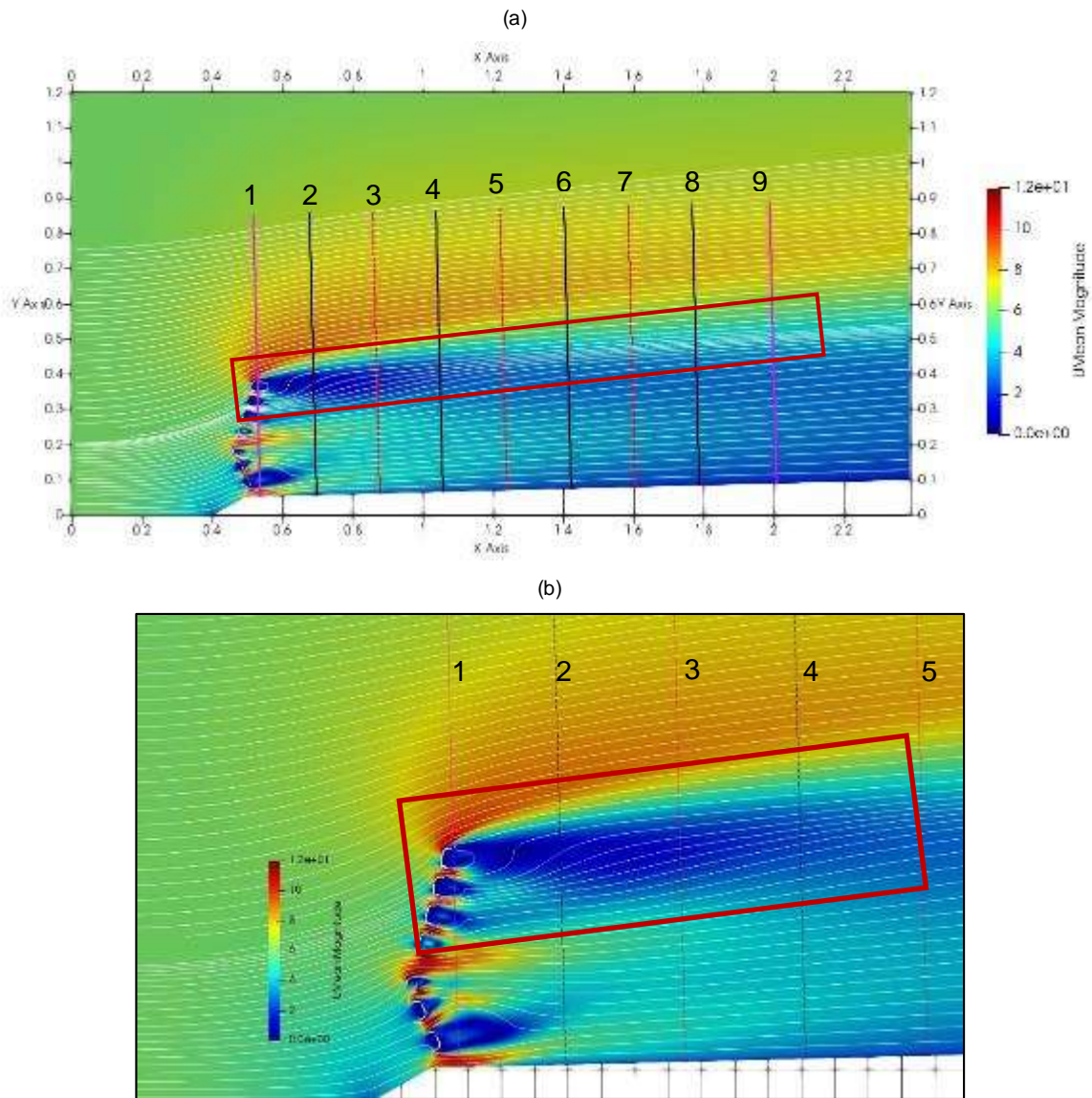


**Figure 3.2.** Contour and streamline plots of time-averaged velocity field (a) across half the bridge deck and (b) around the wind barrier, at the wind speed of  $6\text{ms}^{-1}$ . The shear layer is highlighted by the red box.

Figure 3.3 and Figure 3.4 compare the profiles of the normalised time-averaged wind speed magnitude and flow angle estimated at the nine velocity sampling rakes across the bridge deck (as described in Table 2.3). The height of the profiles is normalised by  $H = 0.420\text{ m}$ , which is the scaled height of a reference vehicle, i.e. a double-decker bus. The dashed lines indicate the normalised height of the wind barriers. The time-averaged wind speed magnitude is normalised by the up-stream wind speed, i.e.  $6\text{ ms}^{-1}$  in this case. Normalised wind speeds greater than 1 indicate wind speed acceleration and vice versa. The profiles close to the wind barriers are removed in Figure 3.3b and Figure 3.4b for better clarification.

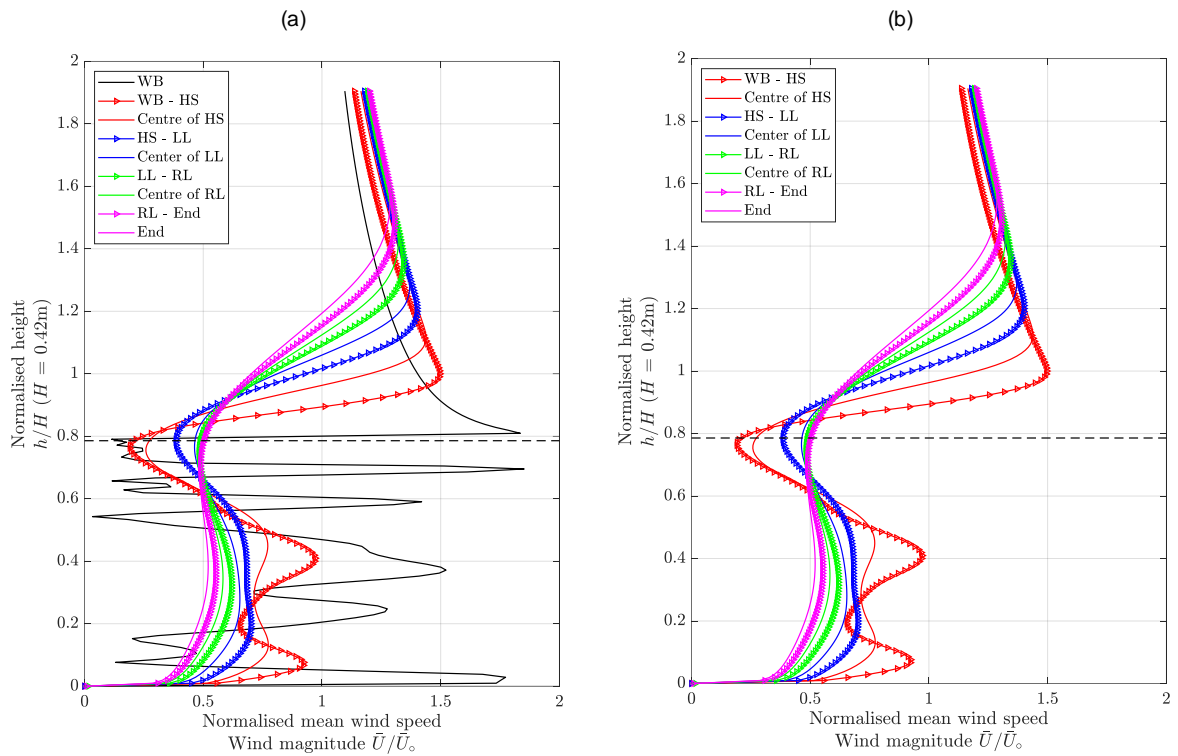


**Figure 3.3.** Variation of the profile of the normalised time-averaged wind speed magnitude across the bridge deck, at the wind speed of  $6\text{ms}^{-1}$ . All locations are included in (a) while the profile close to the wind barrier is removed in (b). The dashed line indicates the normalised height of the wind barrier.

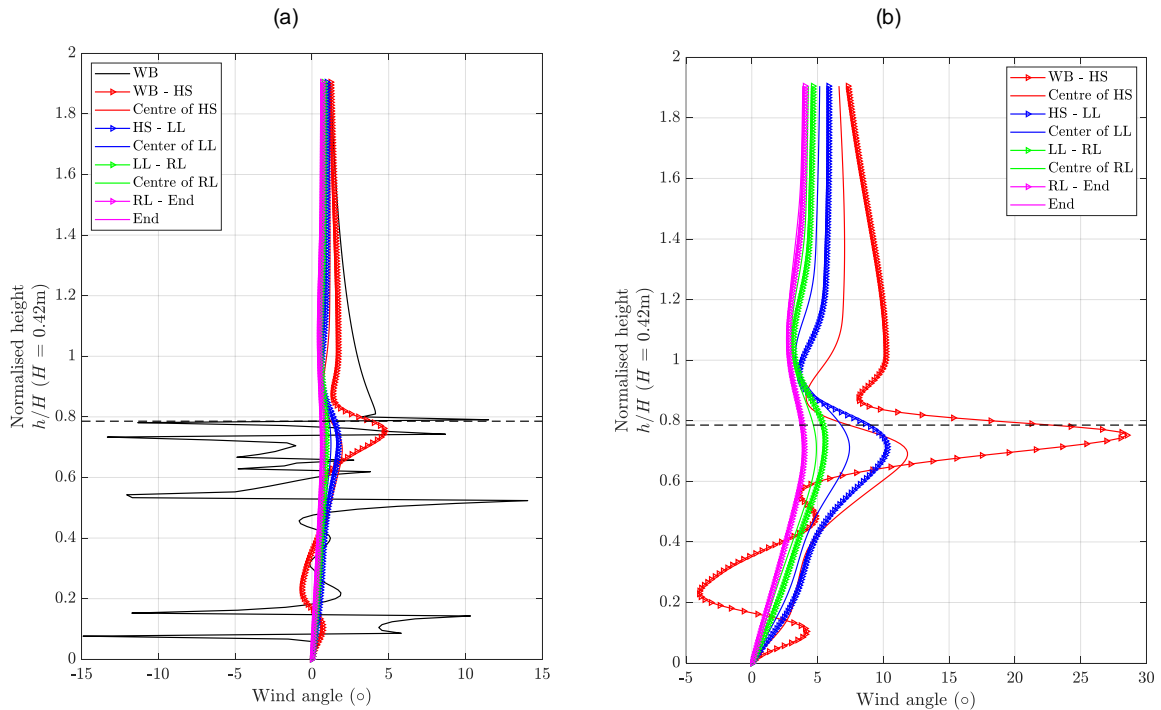


**Figure 3.4.** Variation of the profile of the time-averaged wind angle across the bridge deck, at the wind speed of  $6\text{ms}^{-1}$ . All locations are included in (a) while the profile close to the wind barrier is removed in (b). The dashed line indicates the normalised height of the wind barrier.

As shown in Figure 3.3a and Figure 3.4a, close to the wind barriers, high-speed jets are observed as the wind accelerates through the gaps. The location of these jets agrees with the position of the gaps on the wind barrier. The jets quickly interact and dissipate downstream of the wind barriers, resulting in a signature wind speed profile in the wake region of the wind barrier. The signature wind profile comprises the following features:

- From 0 to 0.6 normalised height, there are two jet-type flow features moving at higher wind speeds. These features are driven by the wind accelerating through the gap between the bridge deck and the bottom louvres and through the big gap between the second and third louvres where the UNP160 section is also located. These flow features gradually dissipate along the bridge deck.
- From 0.6 normalised height, the profile is dominated by the shear layer consisting of very fast- and slow-moving flows above and below the wind barrier height respectively. The shear layer broadens and lifts up across the bridge deck, leading to a reduction in the velocity gradient. Therefore, further away from the wind barrier, the fast-moving flow above the wind barrier height slows down. The broadening effect of the shear layer can also be inferred from the variation of the mean wind angle. Above the wind barrier height, the profiles of wind speed magnitude and angle converge onto the same profile.

The signature wind speed profile discussed in this section is also observed in other CFD simulations at  $0^\circ$  angle of attack and lower wind speeds,  $2 \text{ ms}^{-1}$  and  $4 \text{ ms}^{-1}$ , as shown in Figure 3.5 and Figure 3.6. It is noticed that there is a difference in the time-averaged wind angle just below the wind-barrier height, between the wind speed of  $2 \text{ ms}^{-1}$  and the higher wind speeds,  $4 \text{ ms}^{-1}$  and  $6 \text{ ms}^{-1}$ . This difference is due to a slightly longer extent of the circulation region behind the top louvre at the wind speed of  $2 \text{ ms}^{-1}$  compared to the higher wind speeds, as indicated by the red arrows in Figure 3.7.

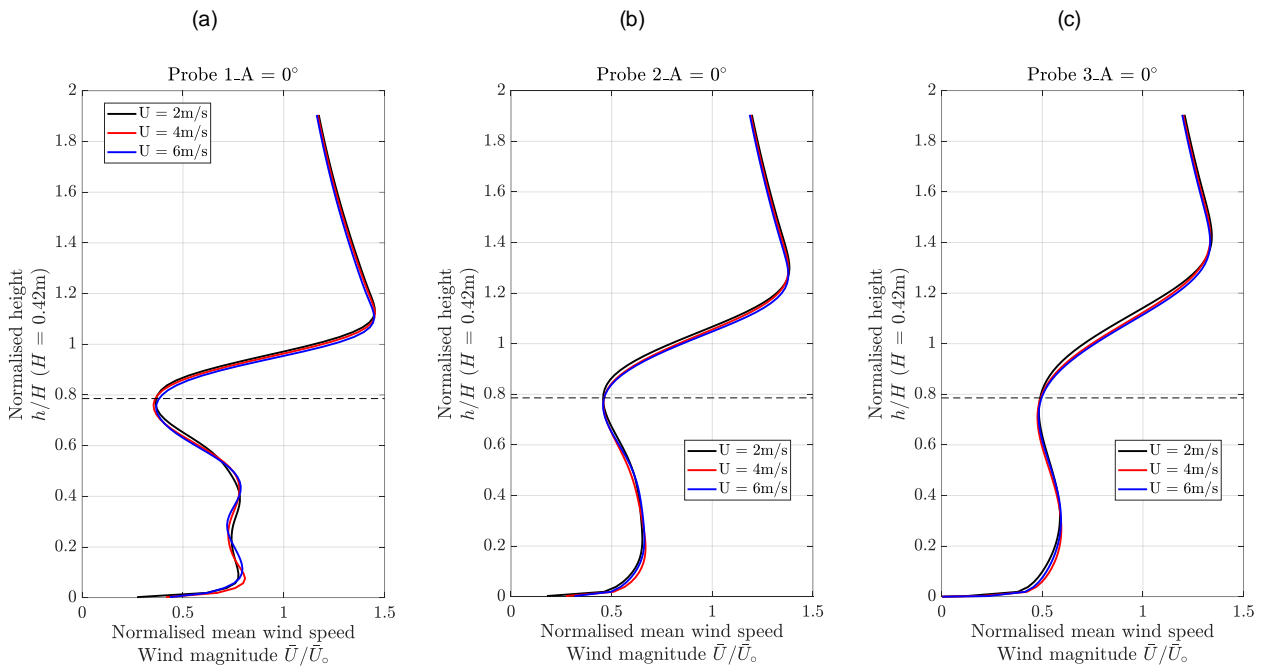


**Figure 3.5.** Profile of the time-averaged wind speed magnitude at different wind speeds, estimated at (a) centre of the hard shoulder, (b) centre of the left lane and (c) centre of the right lane.

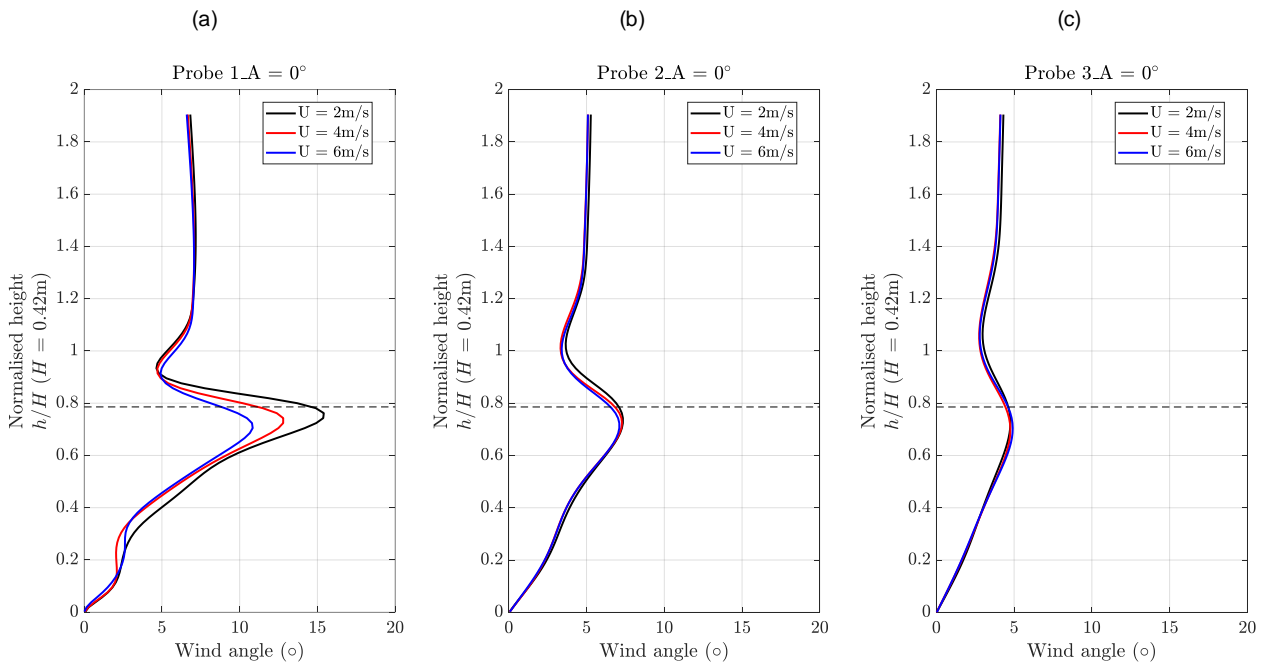


**Figure 3.6.** Profile of the time-averaged wind angle at different wind speeds, estimated at (a) centre of the hard shoulder, (b) centre of the left lane and (c) centre of the right lane.

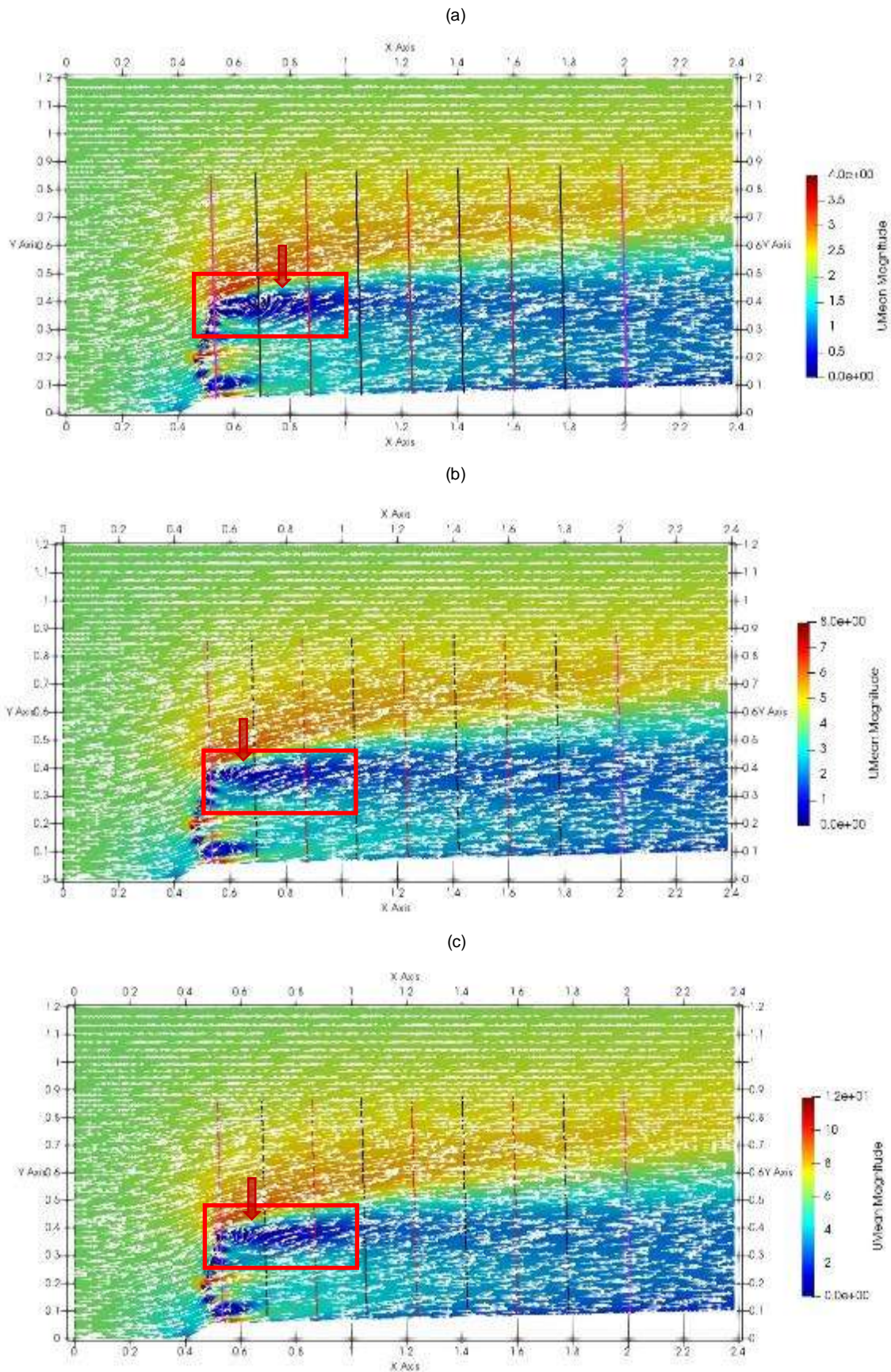


**Figure 3.7.** Contour and vector plots of the time-averaged wind speed magnitude at: (a)  $2 \text{ ms}^{-1}$ , (b)  $4 \text{ ms}^{-1}$  and (c)  $6 \text{ ms}^{-1}$ . The red boxes highlight the circulation region behind the top louvres and its extent is indicated by the red arrow.

In addition to the time-averaged component, the unsteady component of the flow field at different wind speeds also shows good agreement. This is represented by the turbulence intensity of the wind velocity component parallel and normal to the bridge deck and the 1-second gust factor, which are shown in Figure 3.8, Figure 3.9 and Figure 3.10, respectively. Regardless of upstream wind speeds, the results show that the presence of the wind barrier creates a highly unsteady flow field behind the wind barrier, which dissipates across the bridge deck. Also, the location of the maximum level of turbulence intensity shifts upwards away from the bridge deck, which represents the shear layer broadening and lifting up as discussed above.

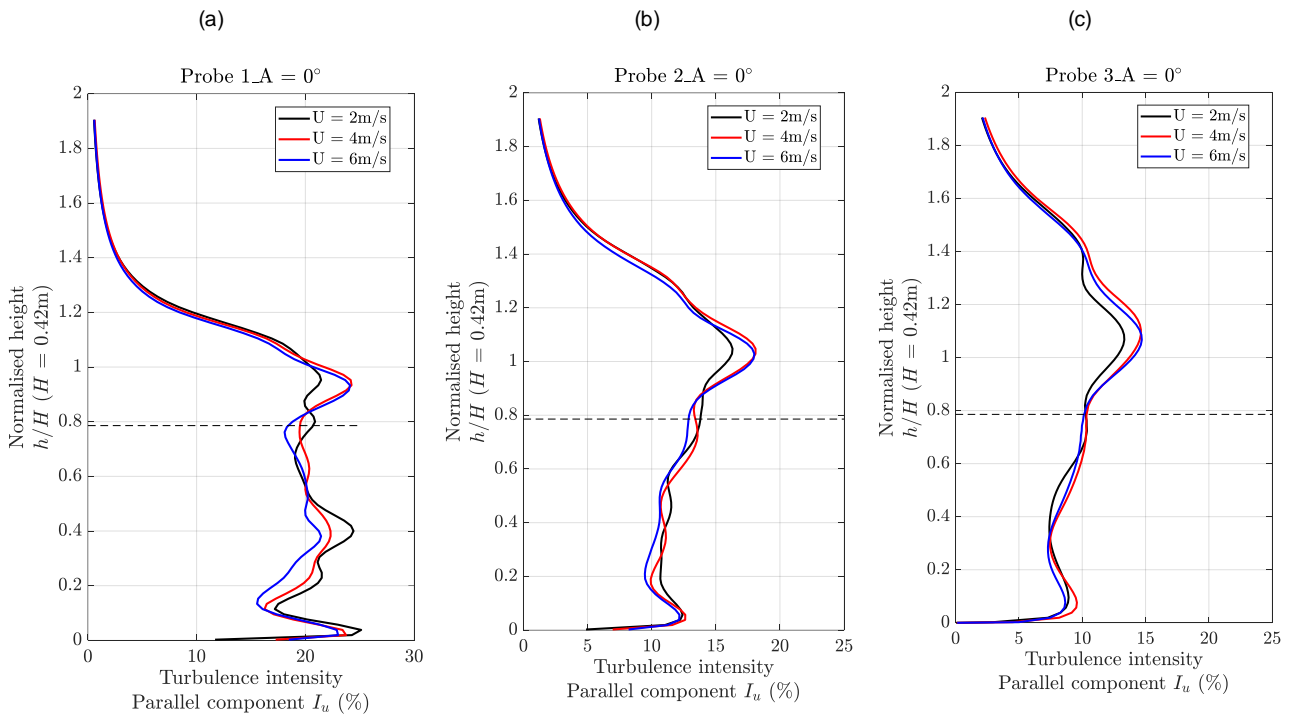


**Figure 3.8.** Profiles of the turbulence intensity of the wind velocity component parallel to the bridge deck at different wind speeds, estimated at: (a) centre of the hard shoulder, (b) centre of the left lane and (c) centre of the right lane.

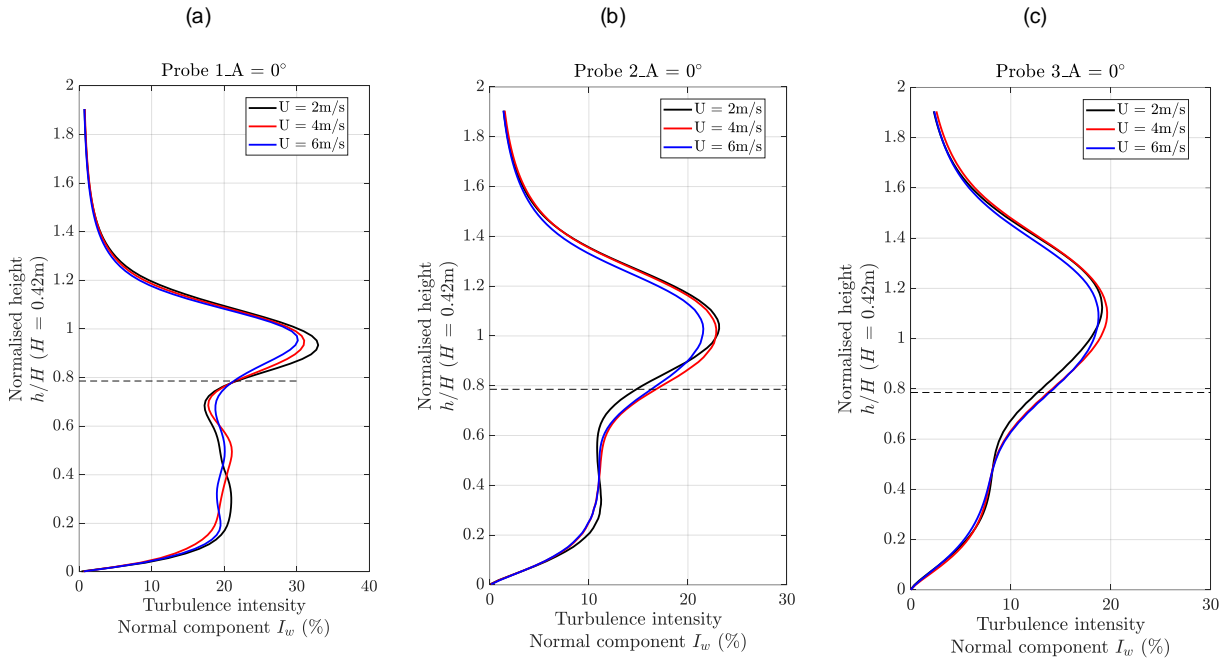


**Figure 3.9.** Profiles of the turbulence intensity of the wind velocity component normal to the bridge deck at different wind speeds, estimated at: (a) centre of the hard shoulder, (b) centre of the left lane and (c) centre of the right lane.

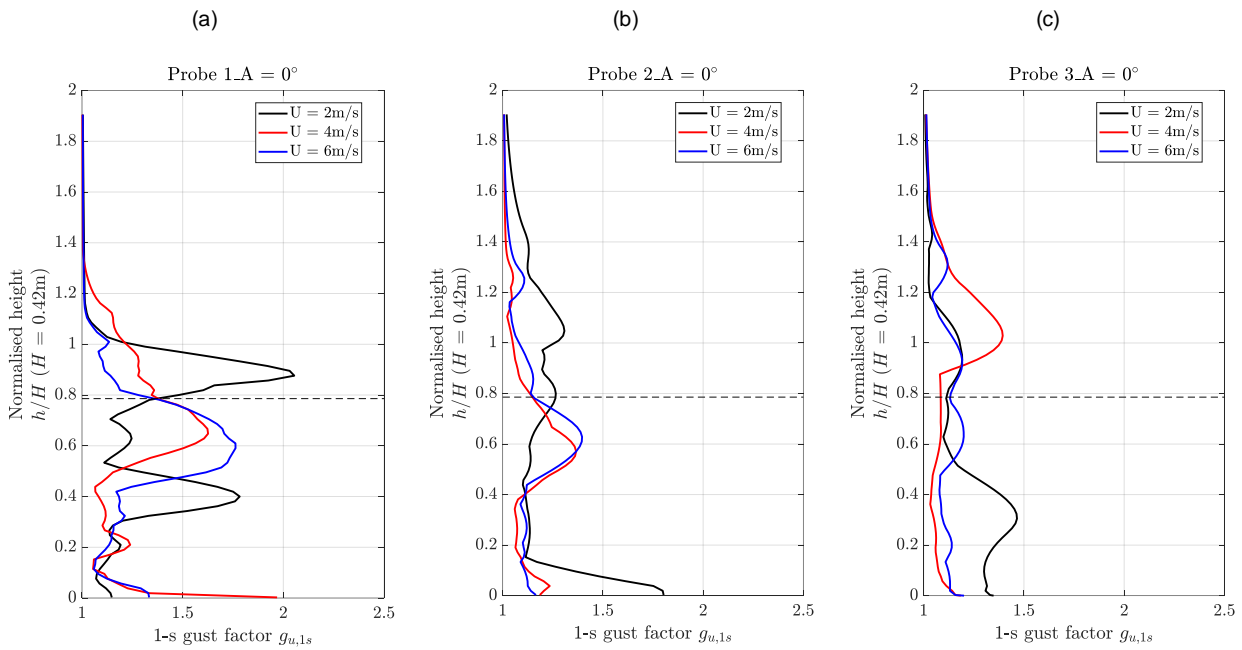


**Figure 3.10.** Profiles of the 1-second gust factor at different wind speeds, estimated at: (a) centre of the hard shoulder, (b) centre of the left lane and (c) centre of the right lane.

## 3.2 Other angles of attack

Figure 3.11 compares the contour and vectors plot of the time-averaged velocity field across the carriageway, estimated at the wind speed of  $2\text{ms}^{-1}$  and three angles of attack  $4^\circ$ ,  $0^\circ$  and  $-4^\circ$ . It is noted that positive angles of attack represent the wind coming from underneath the bridge deck while the negative angles of attack represent the wind coming from above. Superimposed on the plots are the nine straight lines representing velocity sampling rakes whose locations are described in Table 2.3.

Figure 3.11a and Figure 3.11b show very similar time-averaged flow fields between the angle of attack  $4^\circ$  and  $0^\circ$ . In both cases, there are high-speed jets as the flow accelerates across the gaps on the wind barriers. On average, a two-fold increase in the speed can be seen between the bottom louvre and the bridge deck and at the location of the UNP160 section. An elongated recirculation region is formed behind the top louvre. A shear layer is seen to extend from the top louvres to as far as the end of the carriageway. Across the deck, the shear layer broadens and lifts up, leading to a reduction in its velocity gradient.

Comparing these time-averaged flow fields against that in Figure 3.11c reveals significant differences in the flow field at  $-4^\circ$  angle of attack. There is now a larger circulation region formed behind the upper part of the wind barrier. This recirculation region helps funnel the flow through the gap where the UNP160 section is, which creates a jet passing across the surface of the bridge deck. A shear layer is created from the top louvre. However, in contrast to the other angles of attack, the shear layer does not broaden or lift up as it moves across the bridge deck. It remains fairly parallel to the bridge surface and its velocity gradient reduces.

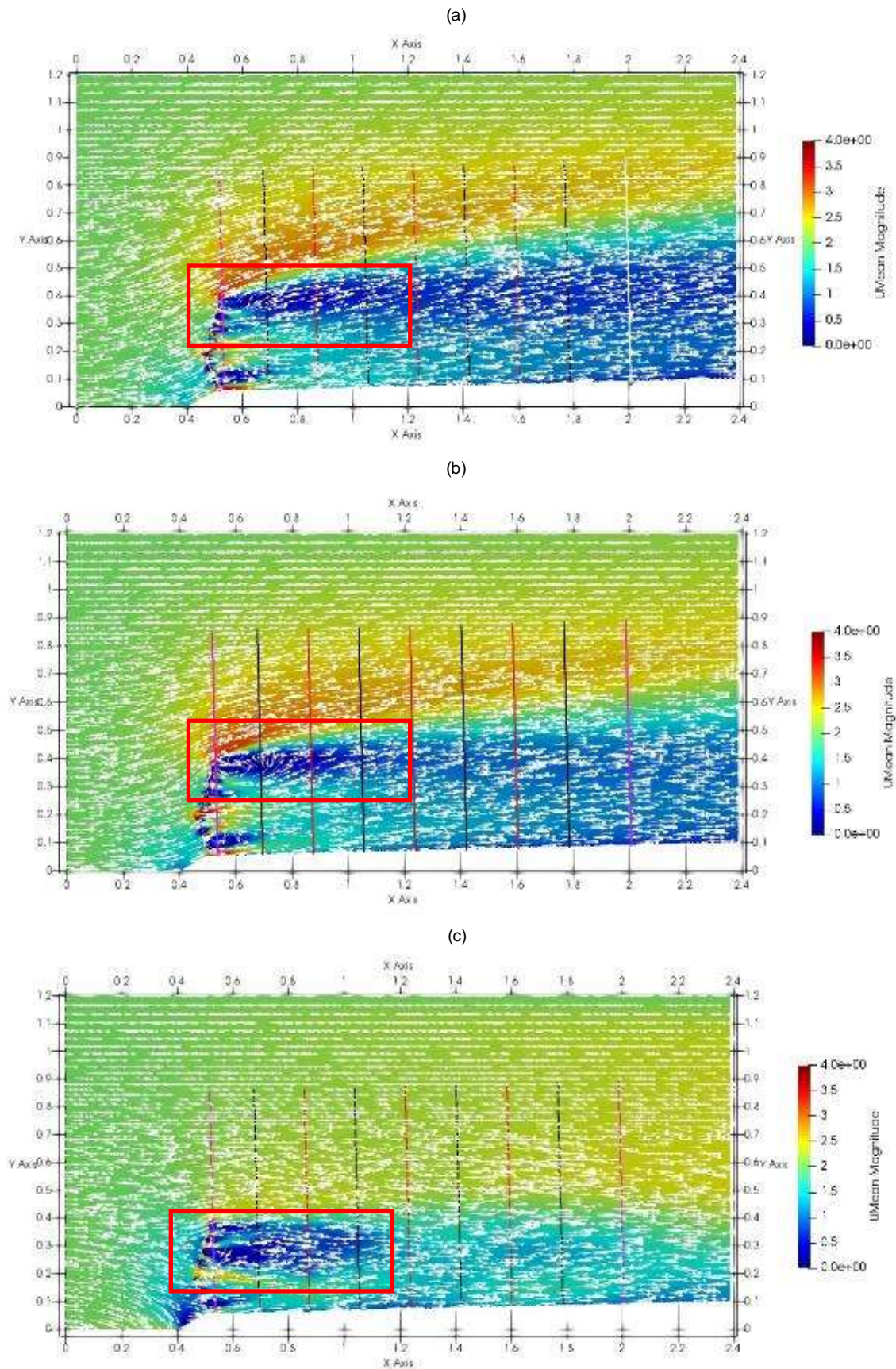


**Figure 3.11.** Contour and vector plots of the time-averaged wind speed magnitude at the wind speed of  $2 \text{ m s}^{-1}$  and at the angle of attack: (a)  $4^\circ$ , (b)  $0^\circ$  and (c)  $-4^\circ$ . The red boxes highlight the circulation region behind the top louvers.

Figure 3.12 and Figure 3.13 compare the profiles of the time-averaged wind speed and wind angle at the centre of the hard shoulder, left lane and right lane. Similar to the observations on the contour and vector plots, the profiles at the angles of attack  $0^\circ$  and  $4^\circ$  are similar to each other, but differ from those at the angle of attack  $-4^\circ$ .

A close examination reveals some small deviations between the wind profiles at the angles of attack  $0^\circ$  and  $4^\circ$ . Below the wind barrier height, the profile of the time-averaged wind speed at the centre of the hard shoulder contains two noses where the wind speed is higher than elsewhere. These noses are caused by high-speed jets as the wind accelerates through the gaps between louvres. The extent of these noses is clearer for the angle of attack  $4^\circ$ , particularly for the lower one closer to the bridge deck. Above the wind barrier height, the profile of the wind speed contains another nose, which is caused by the fast-moving flow within the shear layer. When the angle of attack is positive, the noses occur at slightly higher positions compared to when the angle of attack is zero. The profiles of the time-averaged wind angle at the angle of attack  $0^\circ$  and  $4^\circ$  share a similar shape, except that the values are higher for the positive angle.

For the angle of attack  $-4^\circ$ , below the wind barrier height, the three wind speed profiles contain a nose at the same normalised height of about 0.25. This nose represents a jet passing across the surface of the bridge deck, which is induced by the flow accelerating through the gap where the section UNP160 is. The strength of the jet dissipates as it projects across deck; however, it is still evident at the right lane. Above this jet is a region of low wind speed, which is part of the shear layer. Similar to the observation from the time-averaged flow field, the width and the position of the shear layer relative to the deck remain unchanged even though its strength (i.e. the velocity gradient) reduces as it propagates across the carriageway.

In Figure 3.14 and Figure 3.15, this comparison is extended to other angles of attack  $2^\circ$  and  $-2^\circ$ , which shows a clear separation between the negative angles of attack ( $-2^\circ$  and  $-4^\circ$ ) and higher angles ( $0^\circ$ ,  $2^\circ$  and  $4^\circ$ ). Investigating the unsteadiness in the flow field results in a similar observation. As shown Figure 3.16, Figure 3.17 and Figure 3.18, for the negative angles of attack, the unsteadiness of the flow field was confined beneath the height of the wind barrier and slowly decayed across the deck. At higher angles of attack, the unsteadiness was reduced beneath the height of the barrier and spread upwards away from the bridge deck.

The effects of the angle of attack are summarised as follows:

- For the angles of attack  $0^\circ$ ,  $2^\circ$  and  $4^\circ$ , the wind barrier is found to dictate both the time-averaged and unsteady components of the flow field and a variation in the angle of attack has little influence. At the positive angles of attack, the fact that the wind comes from under the bridge deck slightly lifts up the shear layer and creates a high-speed jet between the bottom louvre and the deck.
- For the negative angles of attack  $-2^\circ$  and  $-4^\circ$ , the fact that the wind comes from above the bridge deck influences the flow field by suppressing the shear layer, preventing it from broadening and lifting up. Also, the downwards wind creates a high-speed jet through the gap where the section UNP160 is. This jet passes across the surface of the deck and its effect is still evident at the right lane. Since the shear layer remains relatively flat, the unsteadiness is confined under the wind barrier height and only dissipates slowly. The shielding effects of the wind barrier also reduce. At the centre of the right lane, the wind speed at the vehicle height is found to be as large as the upstream wind speed. As a very rough estimation, an angle of attack  $-4^\circ$  can be thought equivalent to a turbulence intensity of about 7% for the vertical cross-wind component, for the case of the static bridge deck and vehicle. However, in general, the angle of attack can be attributed to other factors such as the twisting and vertical motion of the bridge deck and the interaction between the dynamic motion of the bridge deck and vehicle.

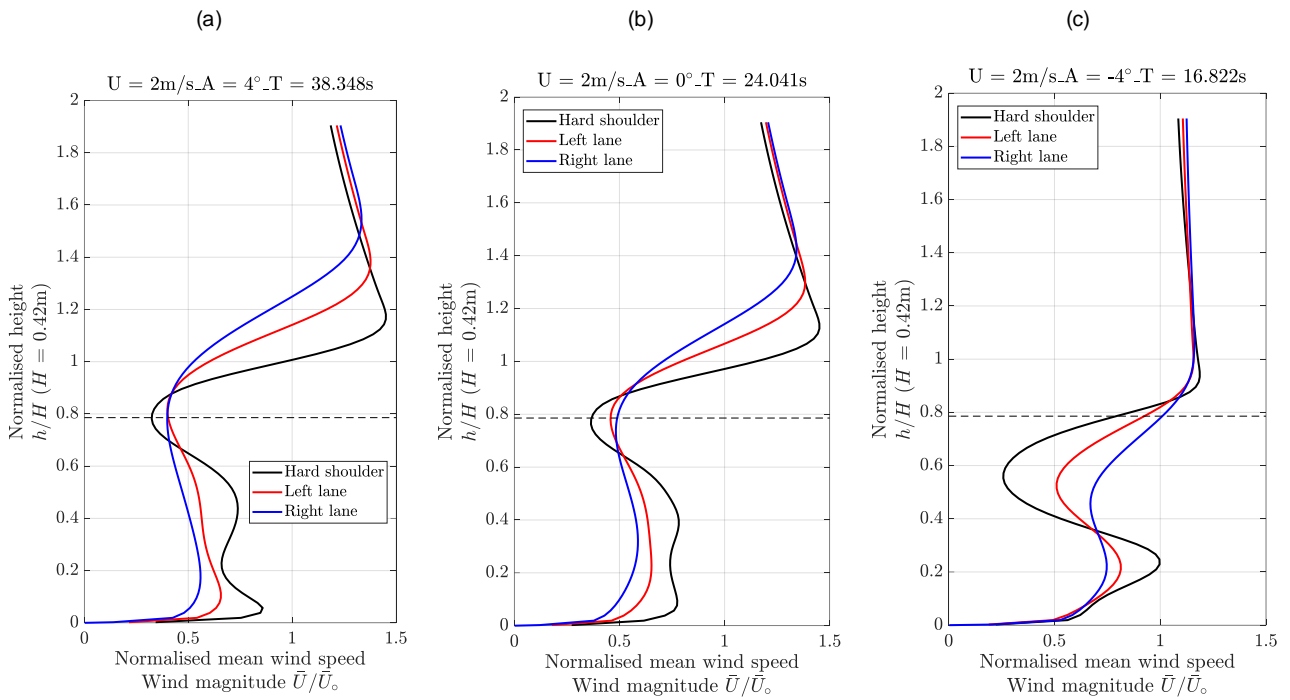


**Figure 3.12.** Variation of the profile of the normalised time-averaged wind speed magnitude across the bridge deck, at the wind speed of  $2\text{ms}^{-1}$  and at the angle of attack: (a)  $4^\circ$ , (b)  $0^\circ$  and (c)  $-4^\circ$ . The dashed line indicates the normalised height of the wind barrier.

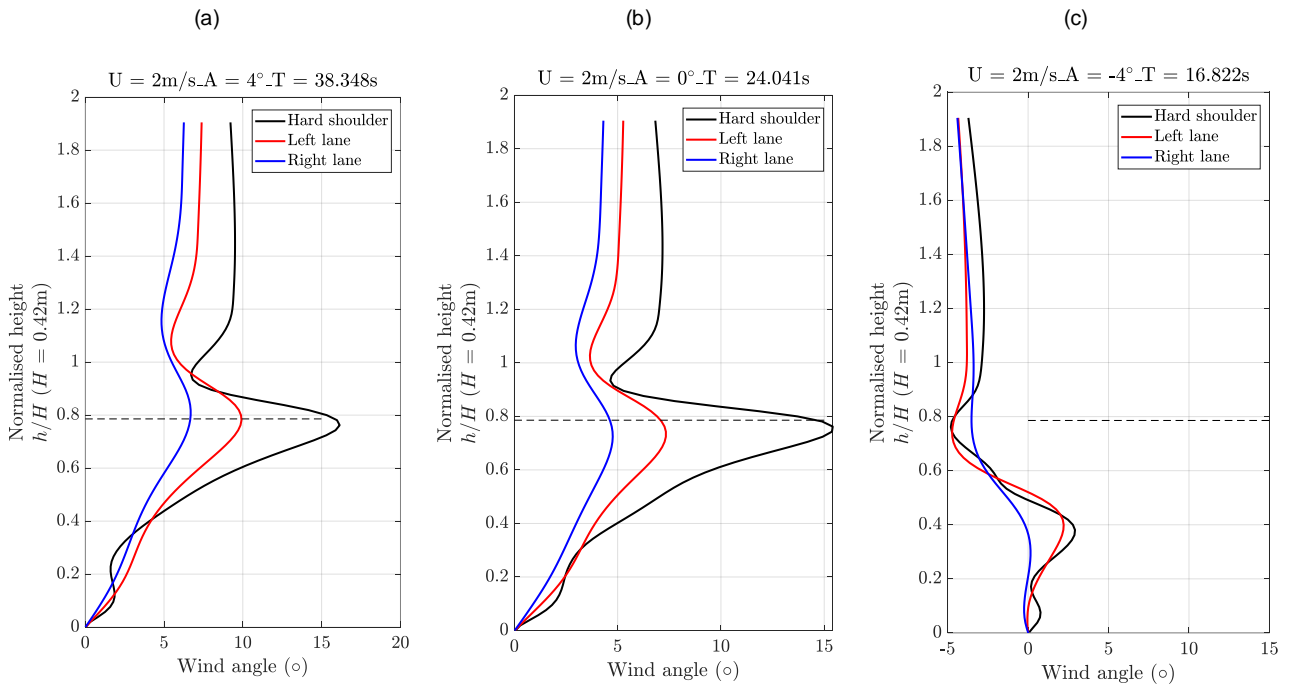


**Figure 3.13.** Variation of the profile of the time-averaged wind angle across the bridge deck, at the wind speed of  $2\text{ms}^{-1}$  and at the angle of attack: (a)  $4^\circ$ , (b)  $0^\circ$  and (c)  $-4^\circ$ . The dashed line indicates the normalised height of the wind barrier.

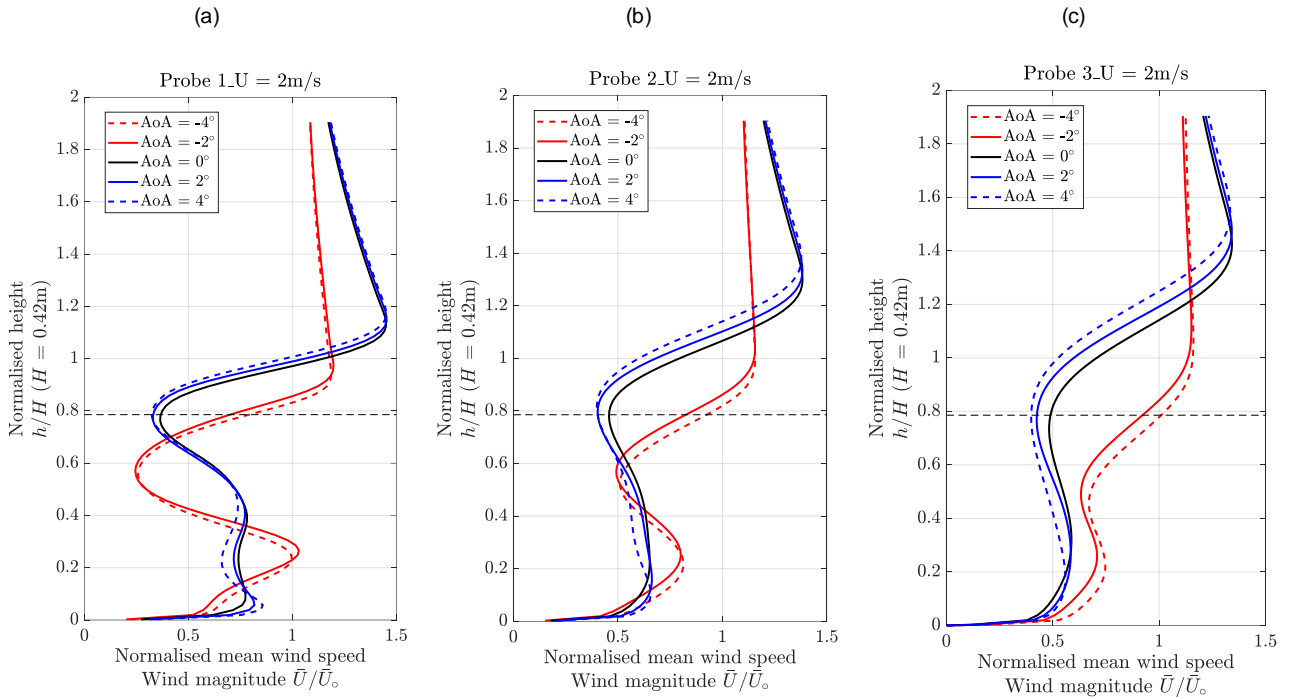


**Figure 3.14.** Profiles of the time-averaged wind speed magnitude at the centre of (a) the hard shoulder, (b) left lane and (c) right lane, at the wind speed of  $2 \text{ ms}^{-1}$  and at different angles of attack. The dashed line indicates the normalised height of the wind barrier.

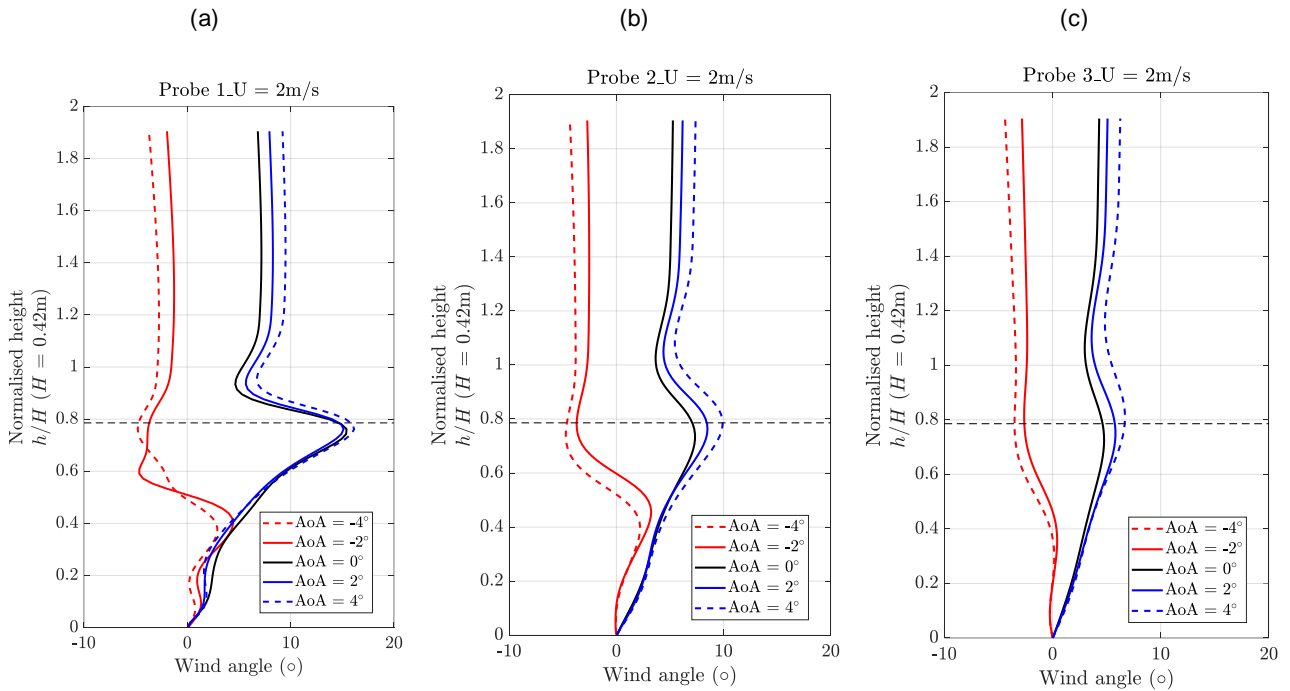


**Figure 3.15.** Profiles of the time-averaged wind angle at the centre of (a) the hard shoulder, (b) left lane and (c) right lane, at the wind speed of  $2 \text{ ms}^{-1}$  and at different angles of attack. The dashed line indicates the normalised height of the wind barrier.

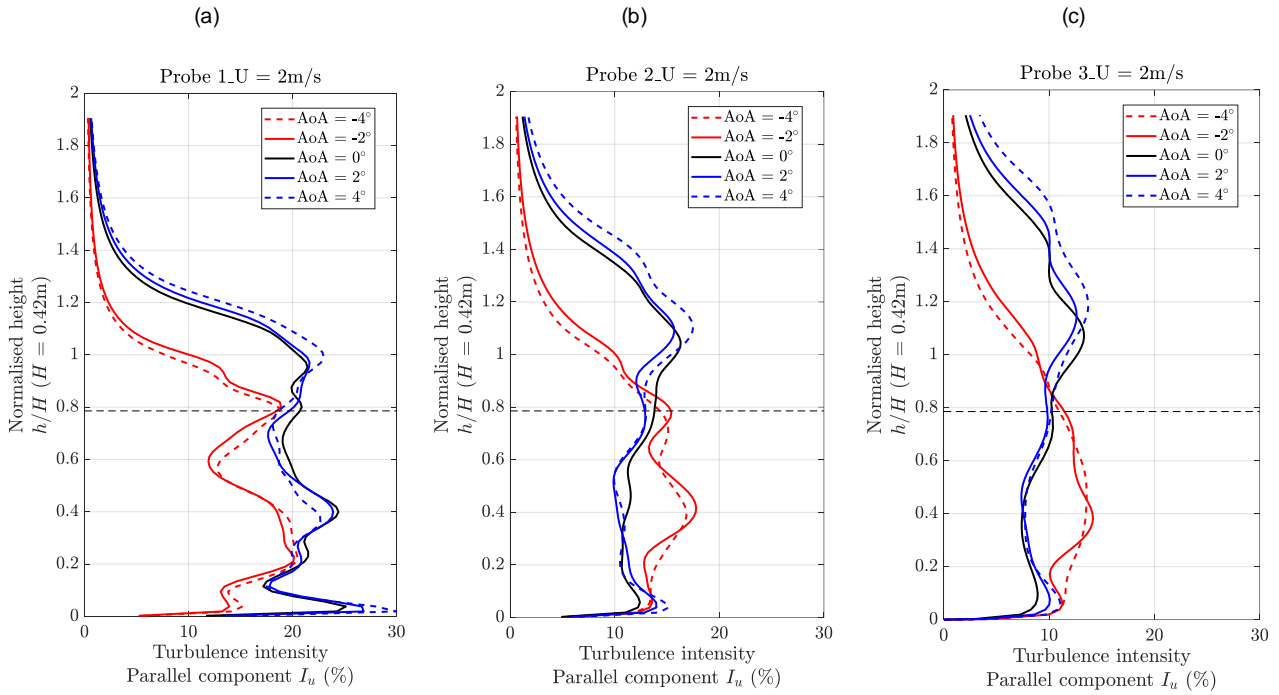


**Figure 3.16.** Profiles of the turbulence intensity of the wind velocity component parallel to the bridge deck at the centre of (a) the hard shoulder, (b) left lane and (c) right lane, at the wind speed of  $2\text{ m s}^{-1}$  and at different angles of attack. The dashed line indicates the normalised height of the wind barrier.

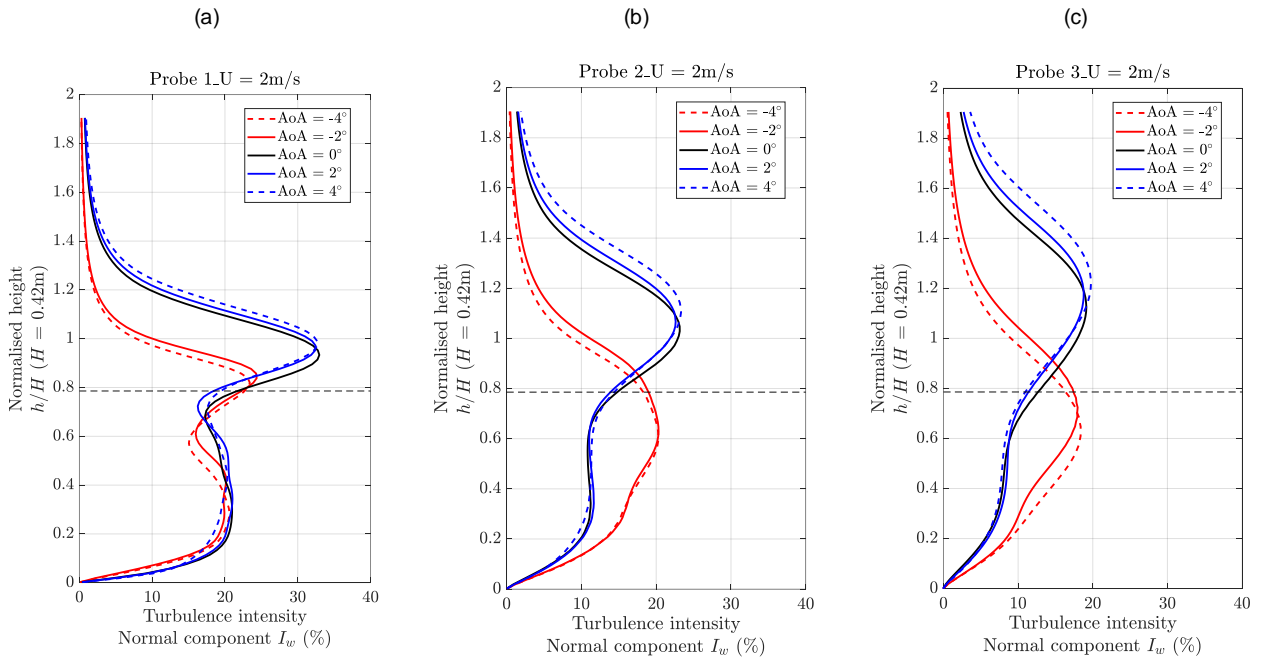


**Figure 3.17.** Profiles of the turbulence intensity of the wind velocity component normal to the bridge deck at the centre of (a) the hard shoulder, (b) left lane and (c) right lane, at the wind speed of  $2\text{ m s}^{-1}$  and at different angles of attack. The dashed line indicates the normalised height of the wind barrier.

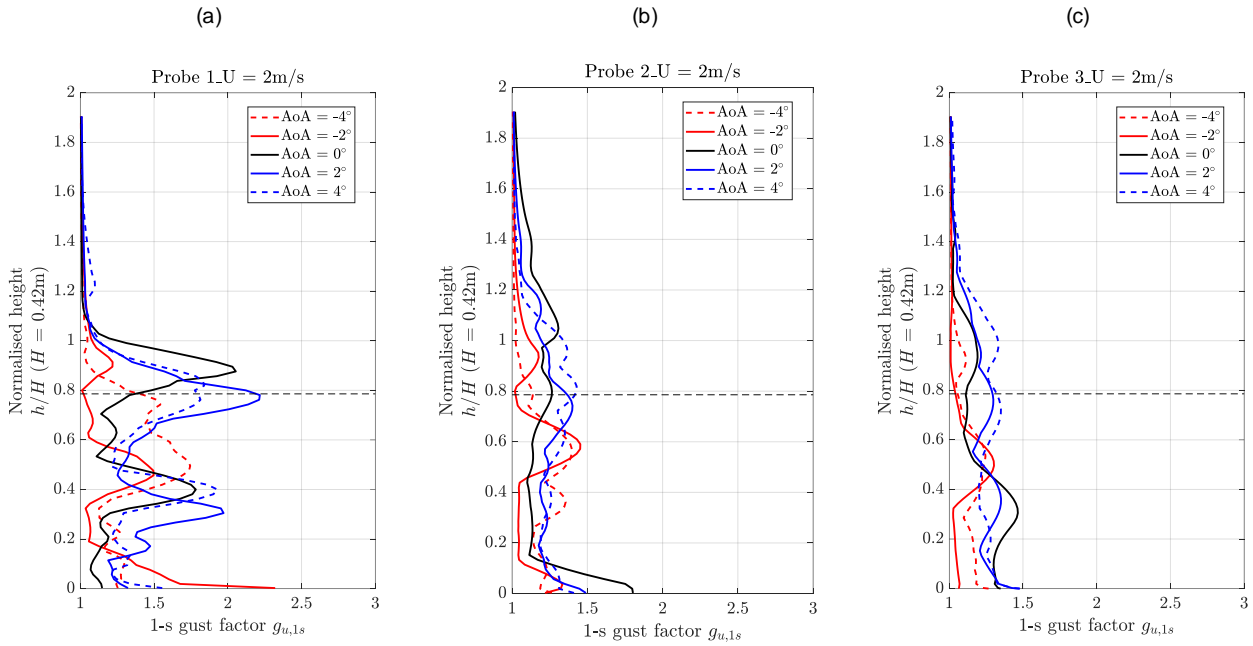


**Figure 3.18.** Profiles of 1-second gust factor at the centre of (a) the hard shoulder, (b) left lane and (c) right lane, at the wind speed of  $2\text{ms}^{-1}$  and at different angles of attack. The dashed line indicates the normalised height of the wind barrier.

## 4 Aerodynamics of the vehicle

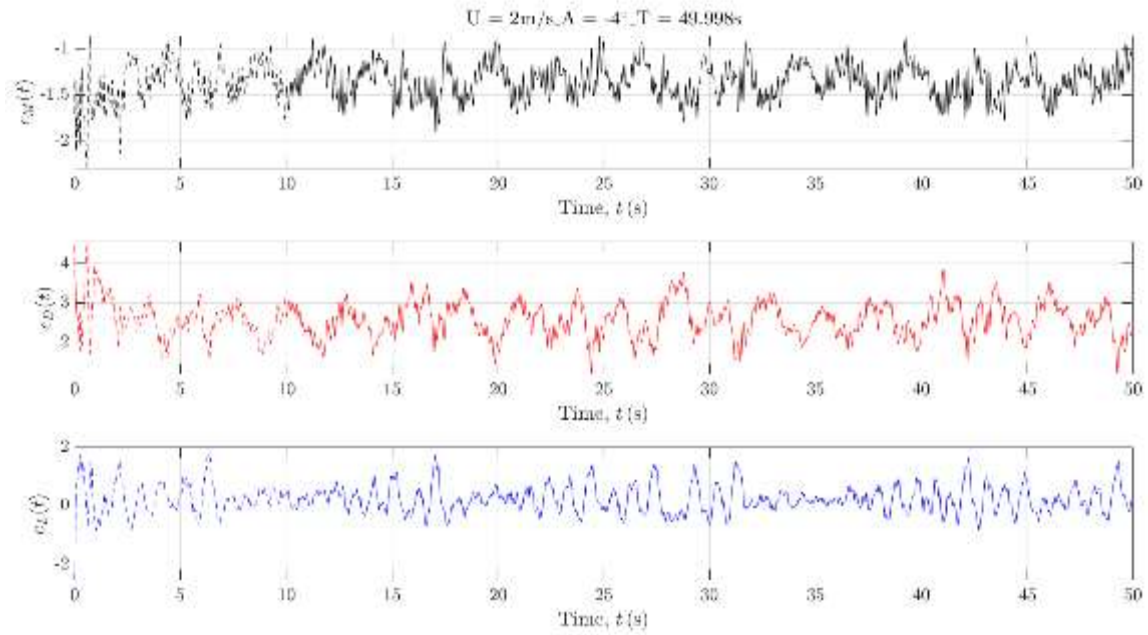
### 4.1 Vehicle on the centre of the hard shoulder

Figure 4.1 to Figure 4.5 show time histories of the aerodynamic coefficients at different angles of attack, when the vehicle is on the centre of hard shoulder. The 10-second transient stage is represented by the dashed line and is removed, prior to estimating the statistical parameters that are reported in Figure 4.6.

When comparing these time histories, it is noted:

- At negative angles of attack, the time-histories of aerodynamic coefficients contain periodic patterns. It is likely that these patterns are caused by vortex shedding either from the top louvre or from the top windward edge of the vehicle.
- At zero or positive angles of attack, no such periodic patterns are seen in any time-histories. Instead, very slow and small variations (at the time scale of about 5 seconds or more) occur randomly. This is more visible on the drag coefficients.

The statistical parameters reported in Figure 4.6 also reflect the observations mentioned above. The presence of noticeable periodic patterns leads to a significant increase in the 1-second peak and RMS value of the aerodynamic coefficients at negative angles of attack. It is noted that, the 1-second peak of the rolling coefficient is negative due to the sign convention. Together with these increases, the mean value of the aerodynamic coefficients shows an abrupt change, when the angle of attack becomes negative.



**Figure 4.1.** Time histories of rolling coefficient ( $c_M$ ), drag coefficient ( $c_D$ ) and lift coefficient ( $c_L$ ) at the angle of attack  $-4^\circ$ , when the vehicle is at the centre of hard shoulder.

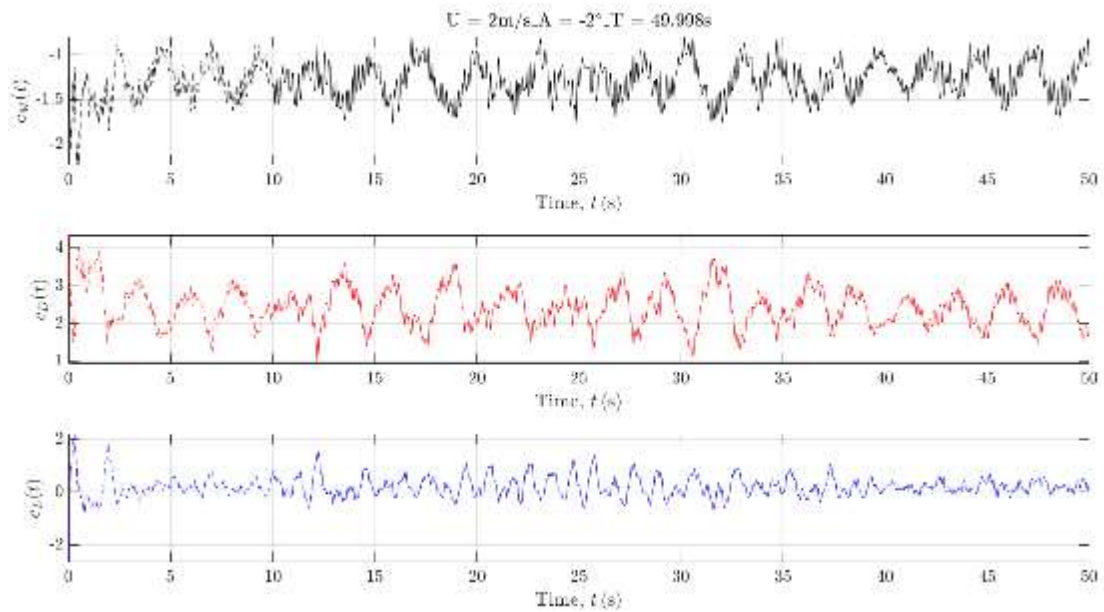


**Figure 4.2.** Time histories of rolling coefficient ( $c_M$ ), drag coefficient ( $c_D$ ) and lift coefficient ( $c_L$ ) at the angle of attack  $-2^\circ$ , when the vehicle is at the centre of hard shoulder.

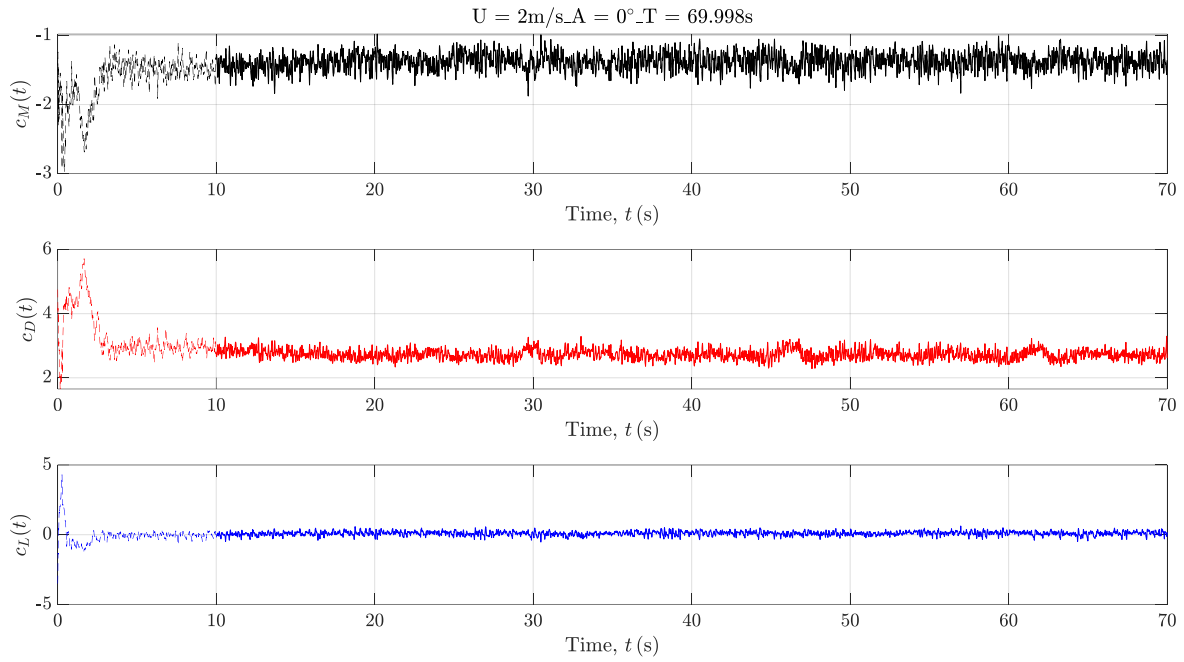


**Figure 4.3.** Time histories of rolling coefficient ( $c_M$ ), drag coefficient ( $c_D$ ) and lift coefficient ( $c_L$ ) at the angle of attack  $0^\circ$ , when the vehicle is at the centre of hard shoulder.

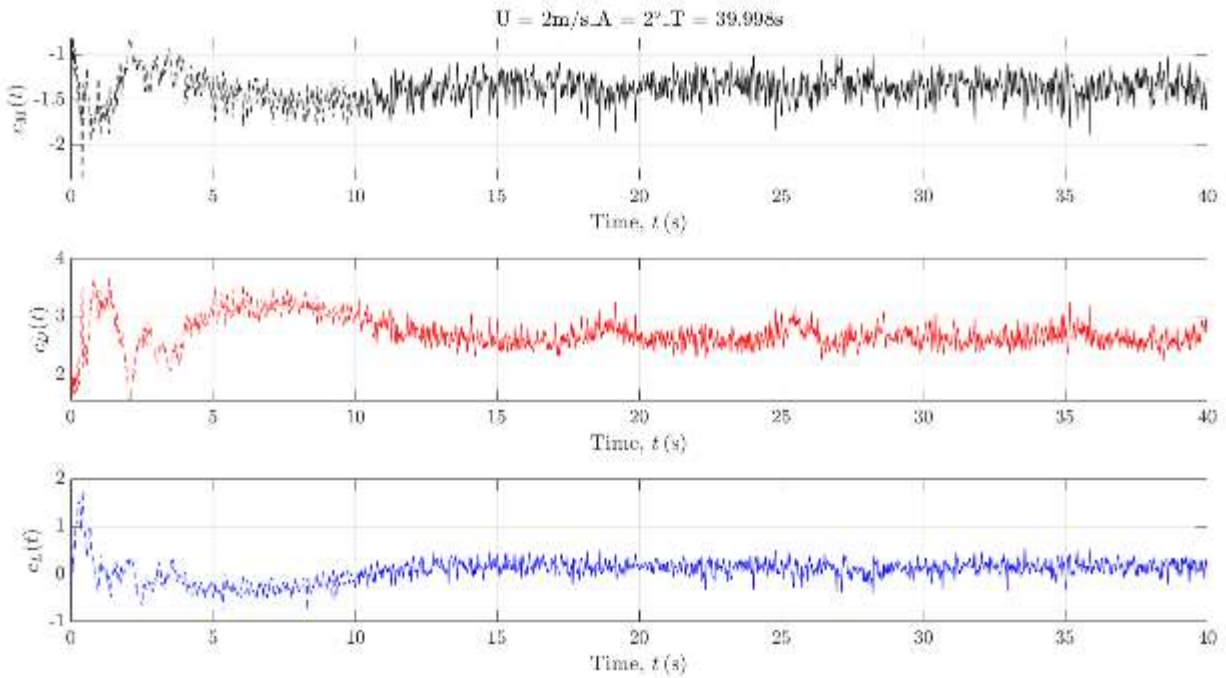


**Figure 4.4.** Time histories of rolling coefficient ( $c_M$ ), drag coefficient ( $c_D$ ) and lift coefficient ( $c_L$ ) at the angle of attack  $2^\circ$ , when the vehicle is at the centre of hard shoulder.

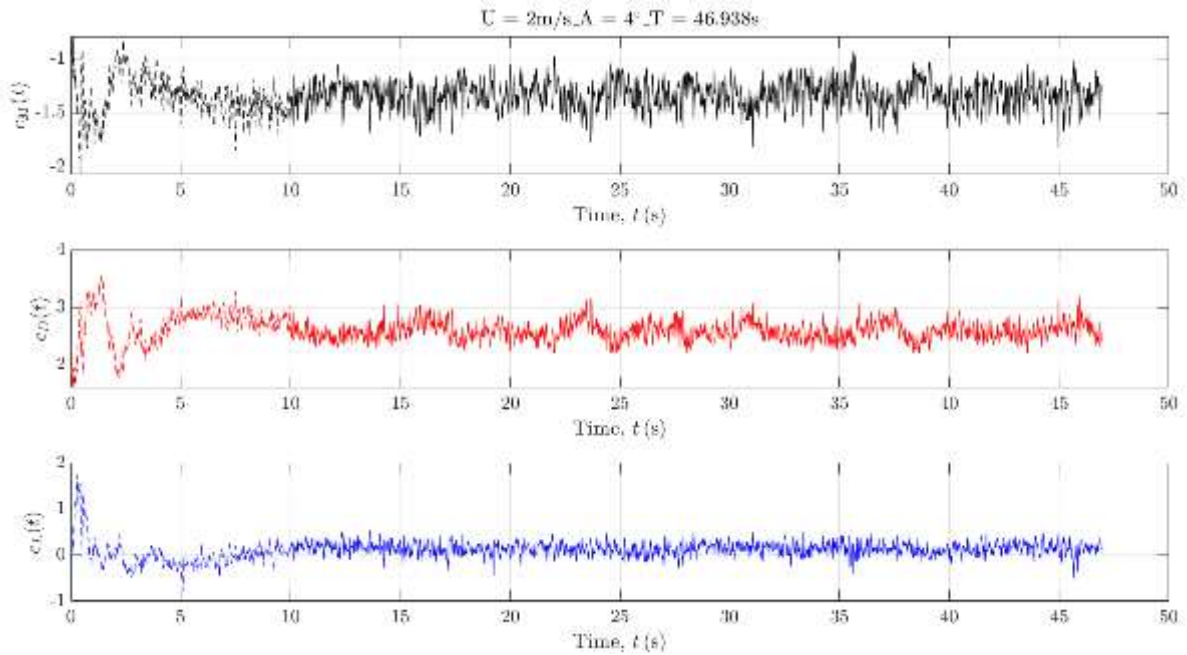


**Figure 4.5.** Time histories of rolling coefficient ( $c_M$ ), drag coefficient ( $c_D$ ) and lift coefficient ( $c_L$ ) at the angle of attack  $4^\circ$ , when the vehicle is at the centre of hard shoulder

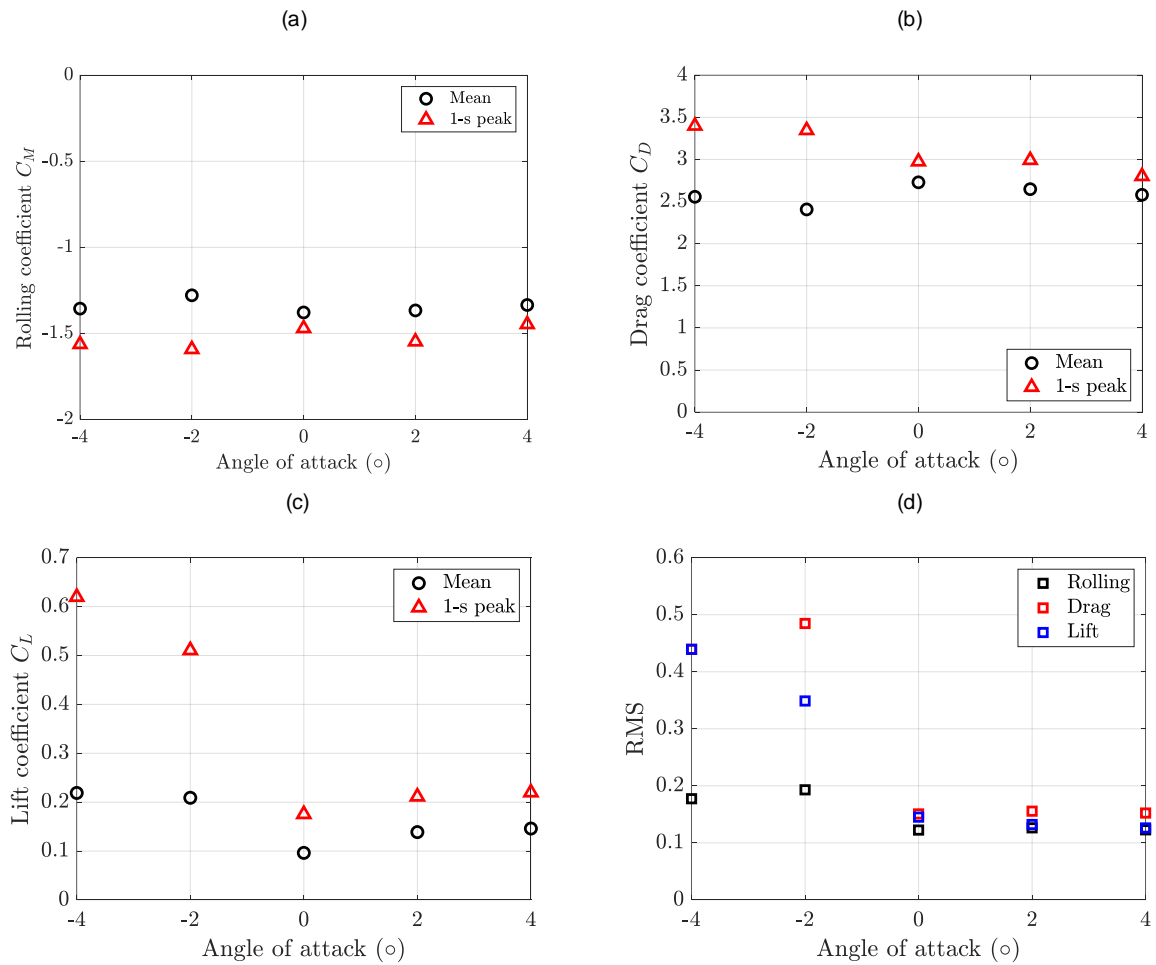


**Figure 4.6.** Variation of the mean and 1-s peak of (a) rolling coefficient, (b) drag coefficient and (c) lift coefficient as well as (d) the RMS value of force coefficient against the angle of attack, when the vehicle is at the centre of hard shoulder.

The variation of the distribution of the mean and RMS pressure coefficient around the vehicle are shown in

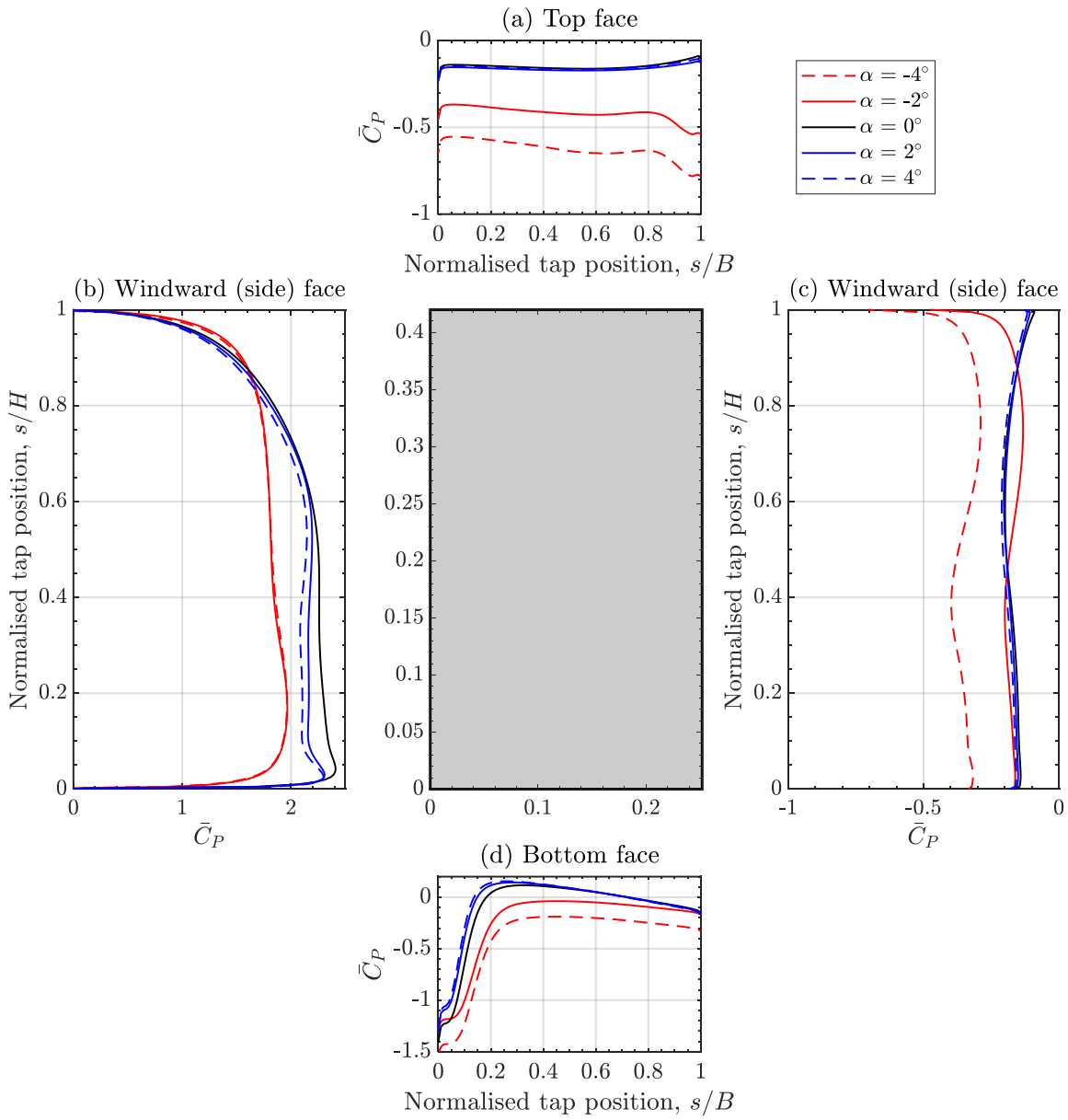
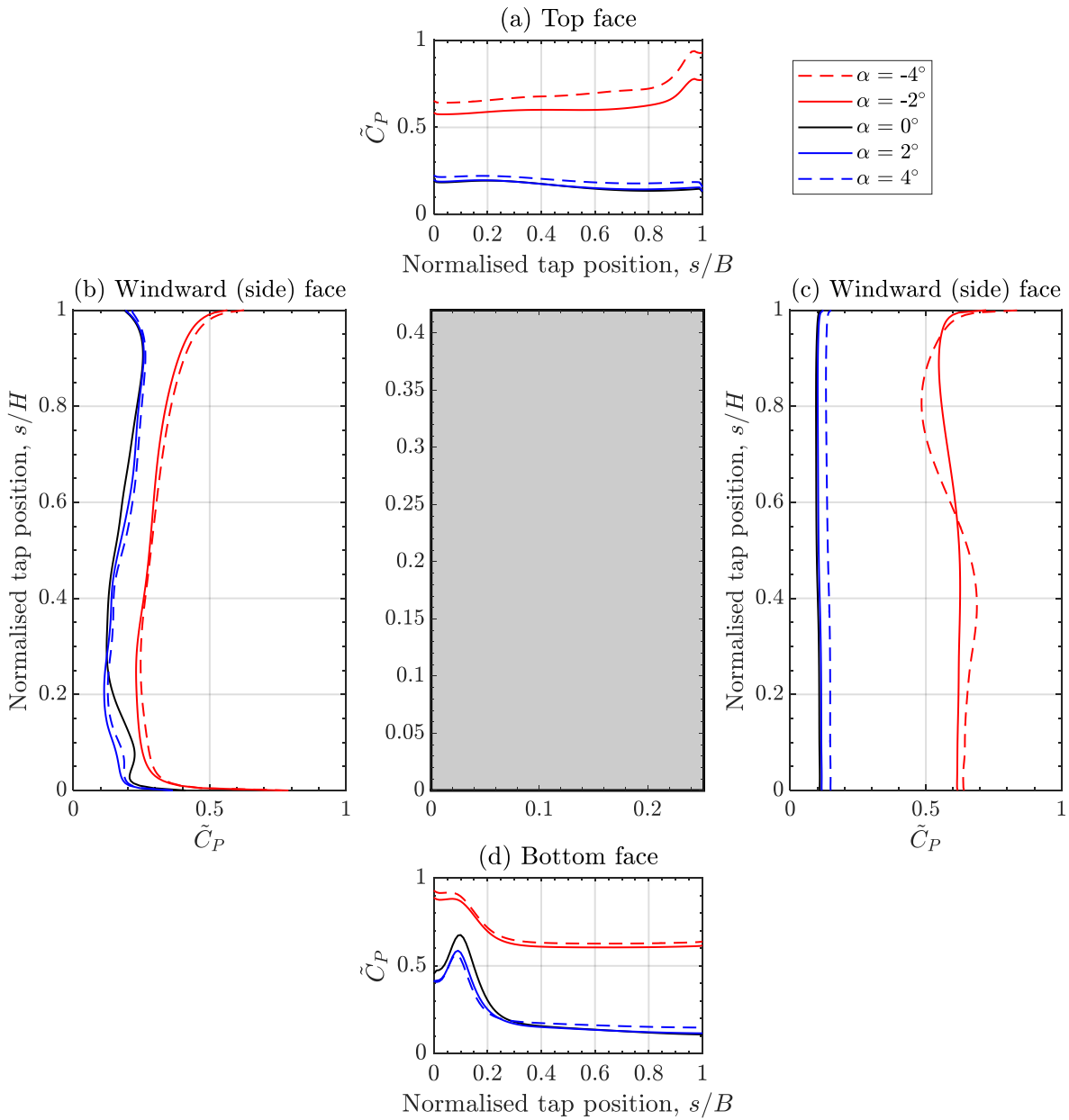


Figure 4.7 and



**Figure 4.8** respectively, which also show the influence of the angle of attack. The mean pressure coefficient represents time-averaged effects of wind-on the vehicle, i.e. related to the mean aerodynamic coefficients. On the other hand, the RMS pressure coefficient represents fluctuating wind effects on the vehicle, i.e. related to the 1-second peak and RMS value of the aerodynamic coefficient.

Changing the angle of attack from positive to negative induces significant changes to the distribution of both mean and RMS pressure coefficients. These changes are seen not only on the values of the pressure coefficient itself but also on the shape of the distribution. These changes are summarised as follows:

- On the top surface, there is a significant increase in suction and dynamic fluctuation, which are shown by a reduction in the mean value and an increase in RMS value respectively. Such variations are also seen on the leeward (side) face and bottom face, although the magnitude of the variations is slightly smaller, compared to that observed on the top face.
- The windward (side) face exhibits the smallest variations among the four faces.

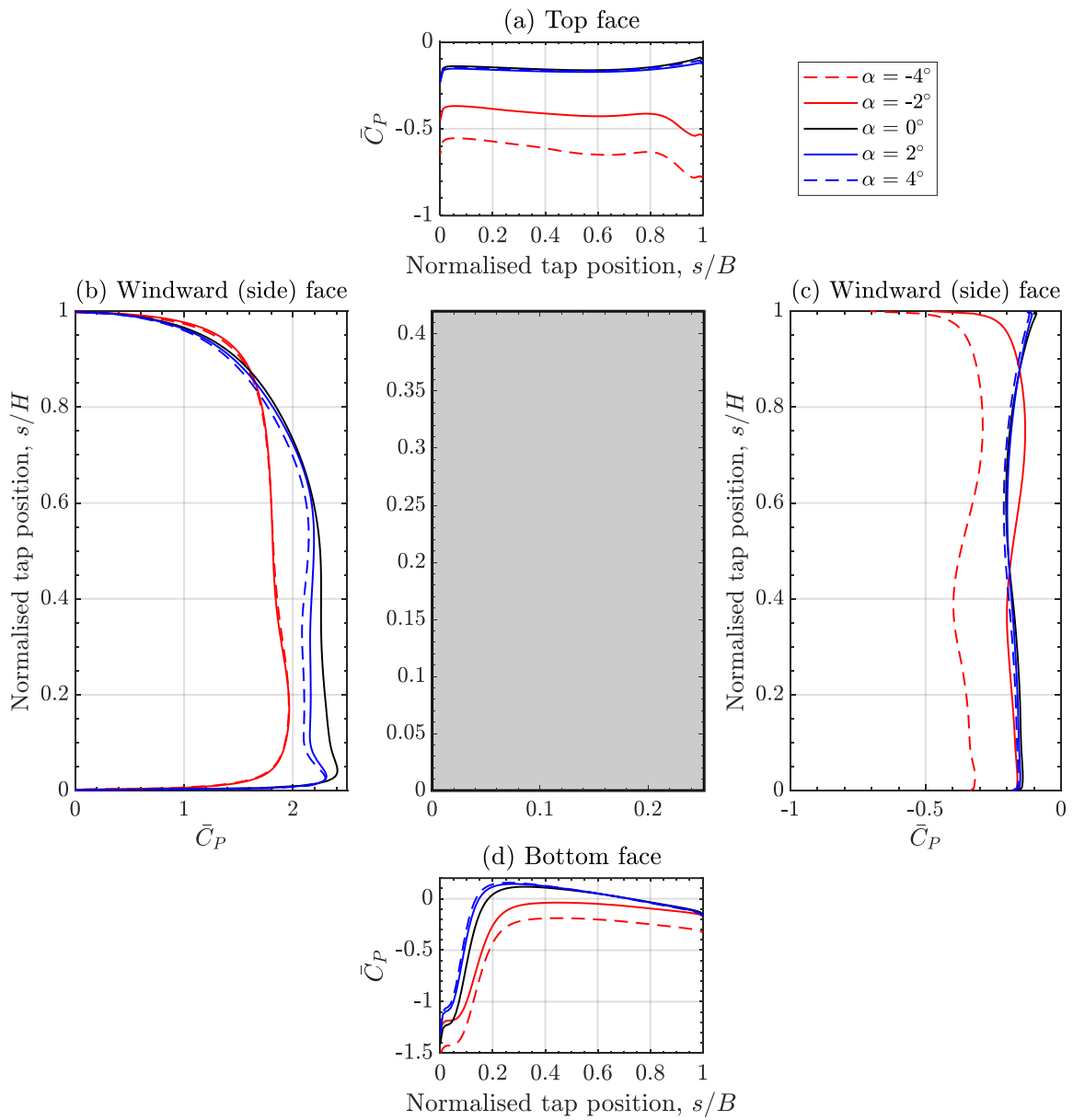


**Figure 4.7.** Variation of the mean pressure coefficient around the vehicle with respect to the angle of attack, when the vehicle is at the centre of hard shoulder.

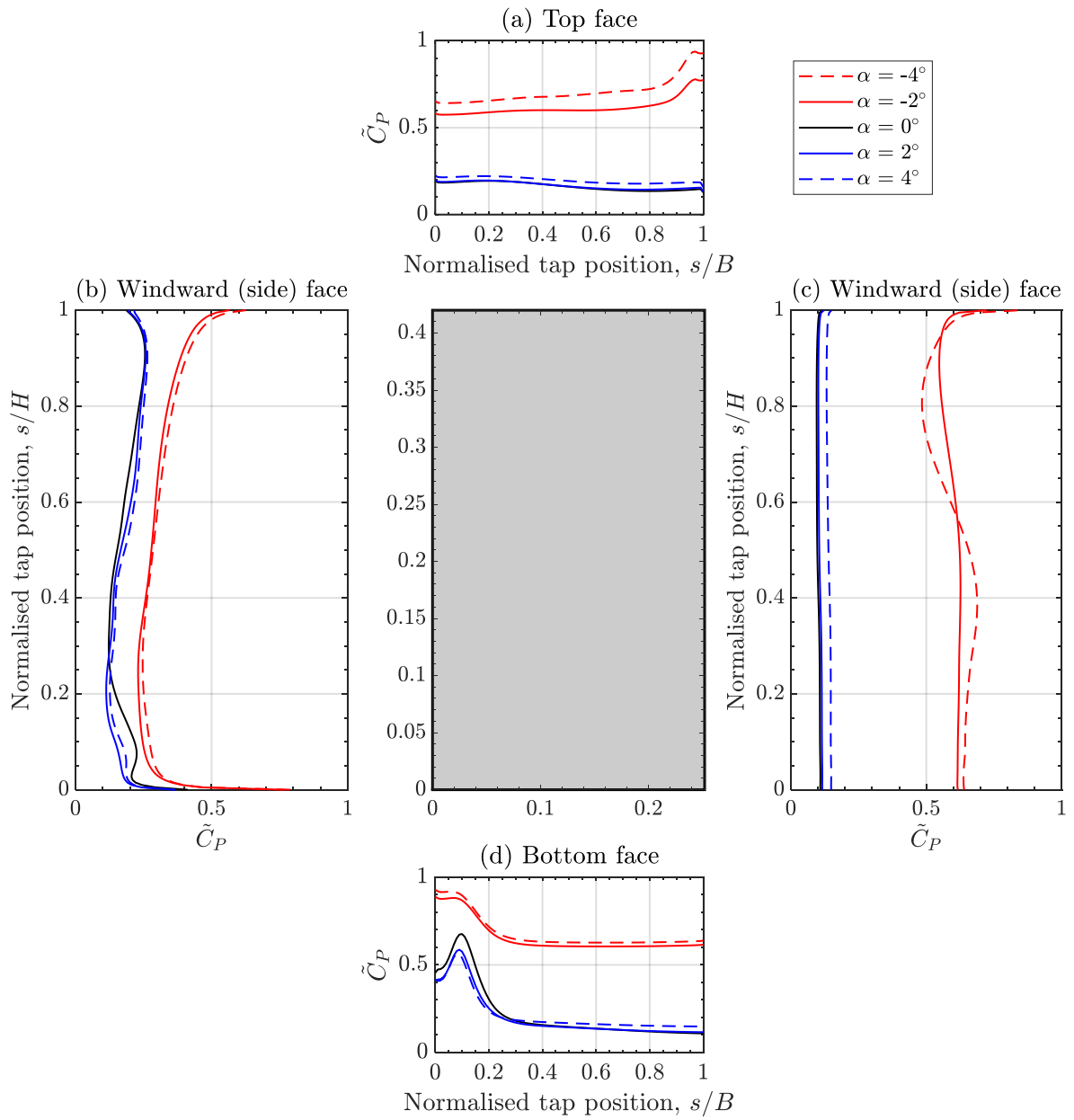


**Figure 4.8.** Variation of the RMS pressure coefficient around the vehicle with respect to the angle of attack, when the vehicle is at the centre of the left lane.

## 4.2 Vehicle on the centre of the left lane

Figure 4.9 to Figure 4.11 show the time histories of the aerodynamic coefficient at different angles of attack, when the vehicle is on the centre of lane 1. The 5-second transient stage is represented by the dashed line and are removed prior to estimating statistical parameters.

When the angle of attack is negative, the time -histories of aerodynamic coefficients show the presence of periodicity, which appears stronger than when the vehicle is on the hard shoulder. Also, the frequencies are different, particularly for the lift and moment coefficients. These periodic patterns are less clear when the angle of attack is zero or positive. Consequently, as can be seen in Figure 4.12, the 1-second peak and RMS value of aerodynamic coefficient at negative angles of attack show a notable deviation from those at zero or positive angles of attack. Together with the variation in the statistics describing the extreme and fluctuation in the aerodynamic coefficients, there is a large change in the mean value, particularly for the rolling and drag coefficients.

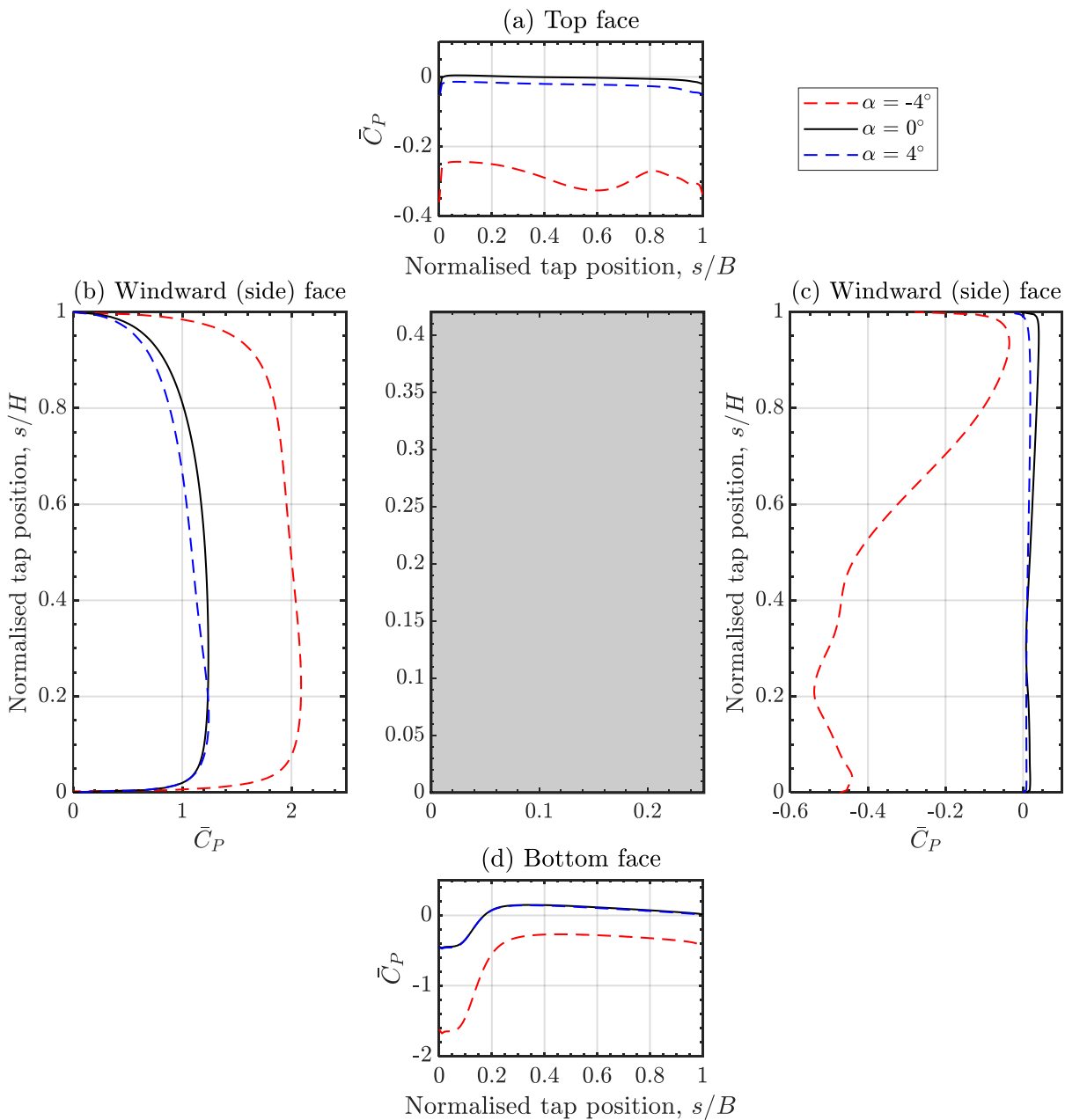


Figure 4.13 and

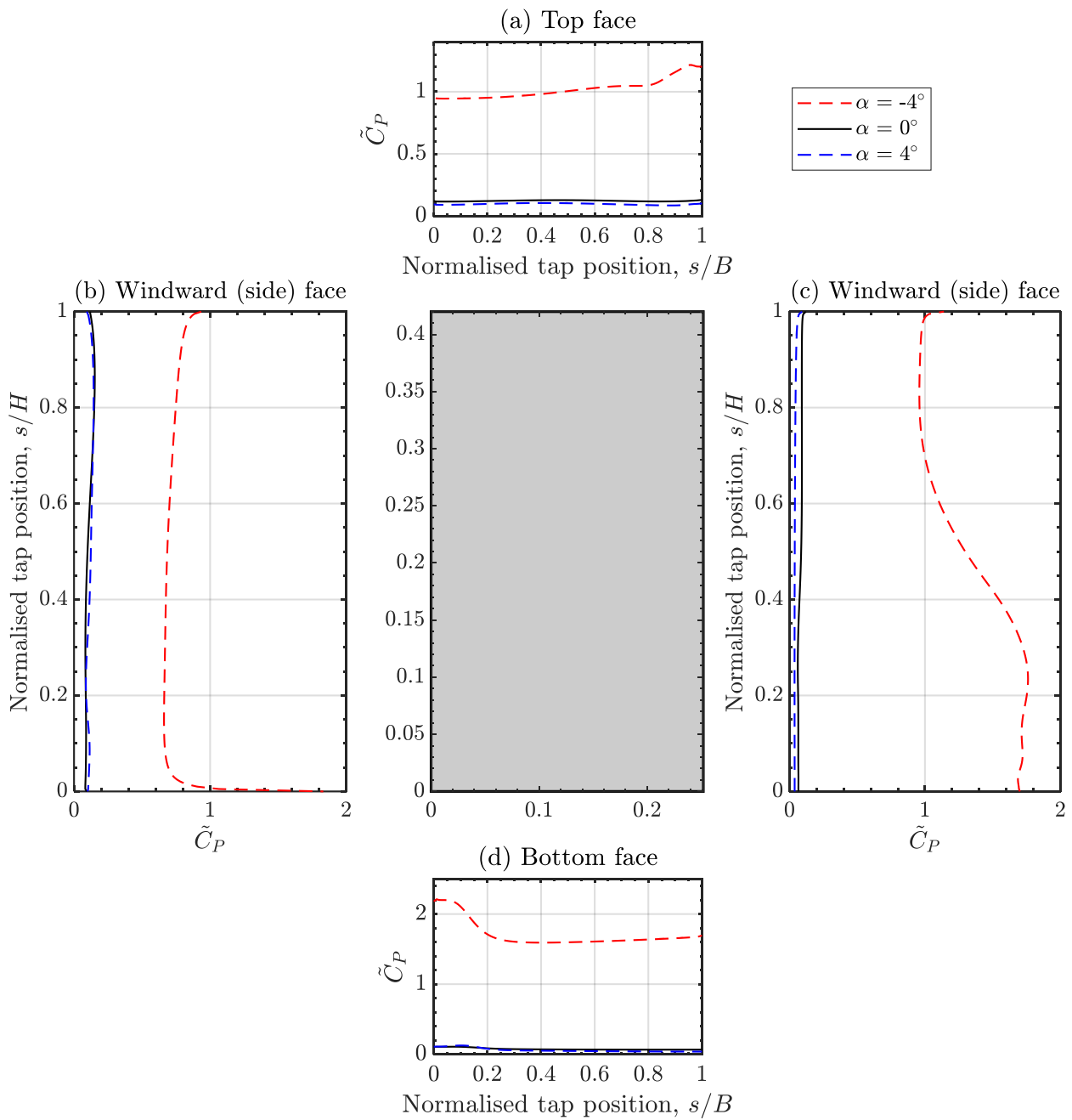
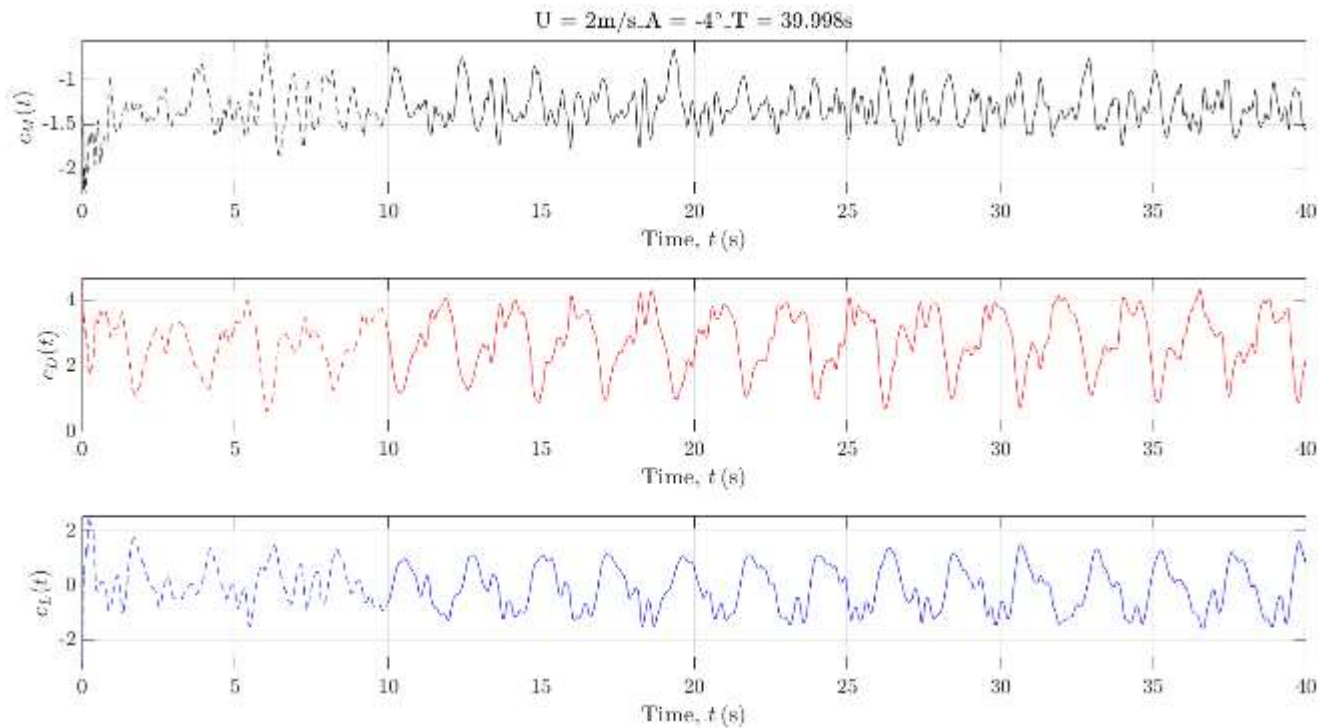
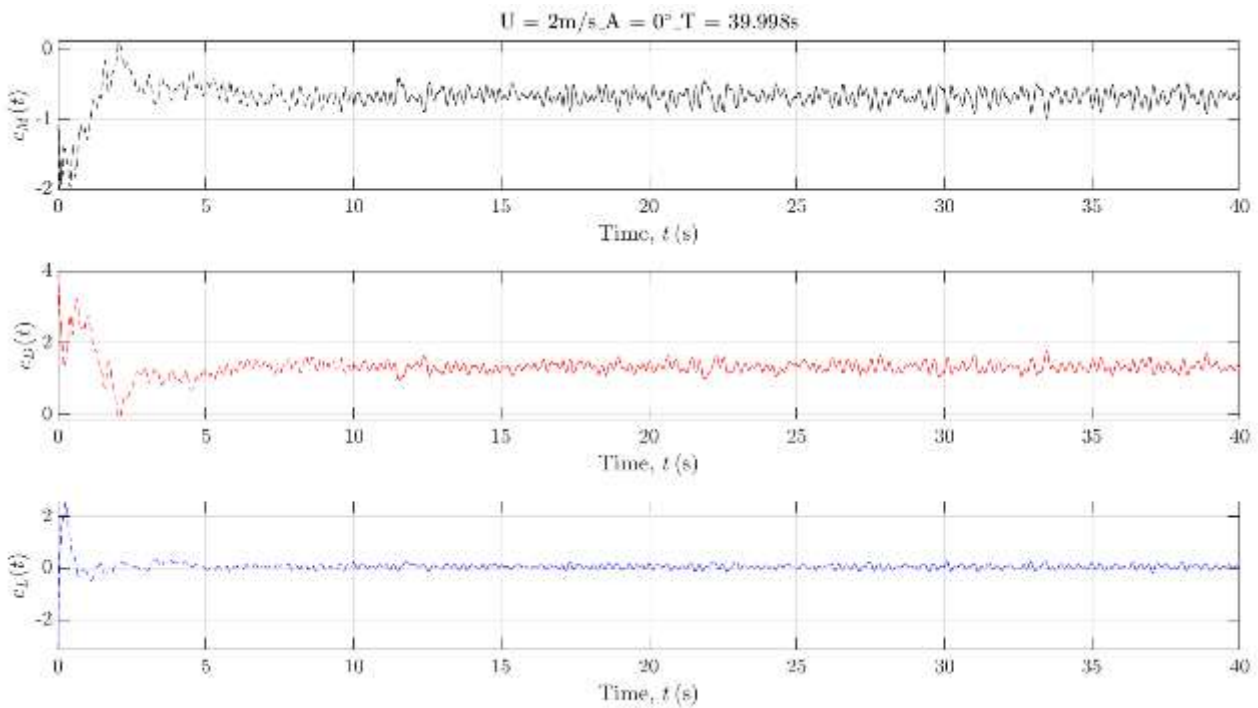


Figure 4.14 show the variation of the surface distribution of the mean and RMS pressure coefficient around the vehicle, respectively, with respect to the angle of attack. Similar to the case that the vehicle is on the centre of the hard shoulder, when the angle of attack decreases from positive to negative, there is a significant increase in suction and dynamic pressure fluctuation. Among the four surfaces, the top, leeward (side) and bottom faces show the largest variations.



**Figure 4.9.** Time histories of rolling coefficient ( $c_M$ ), drag coefficient ( $c_D$ ) and lift coefficient ( $c_L$ ) at the angle of attack  $-4^\circ$ , when the vehicle is at the centre of the left lane.



**Figure 4.10.** Time histories of rolling coefficient ( $c_M$ ), drag coefficient ( $c_D$ ) and lift coefficient ( $c_L$ ) at the angle of attack  $0^\circ$ , when the vehicle is at the centre of the left lane.

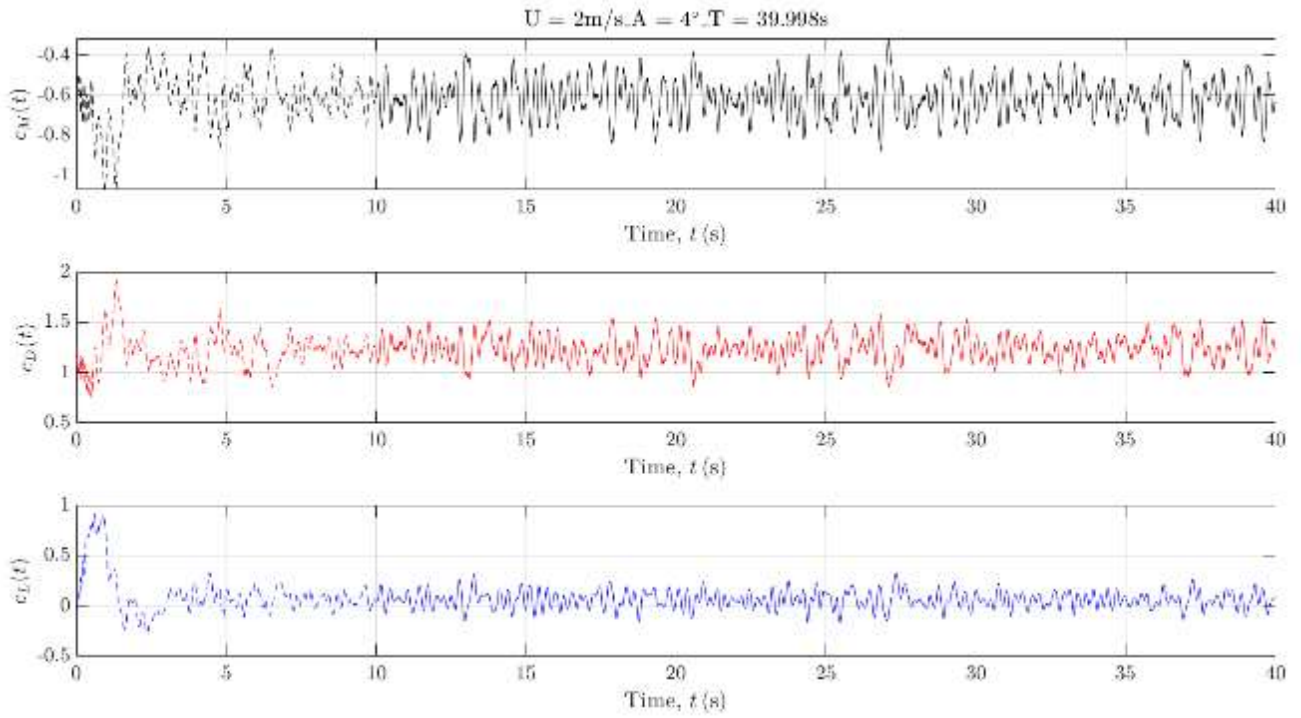


**Figure 4.11.** Time histories of rolling coefficient ( $c_M$ ), drag coefficient ( $c_D$ ) and lift coefficient ( $c_L$ ) at the angle of attack  $4^\circ$ , when the vehicle is at the centre of the left lane.

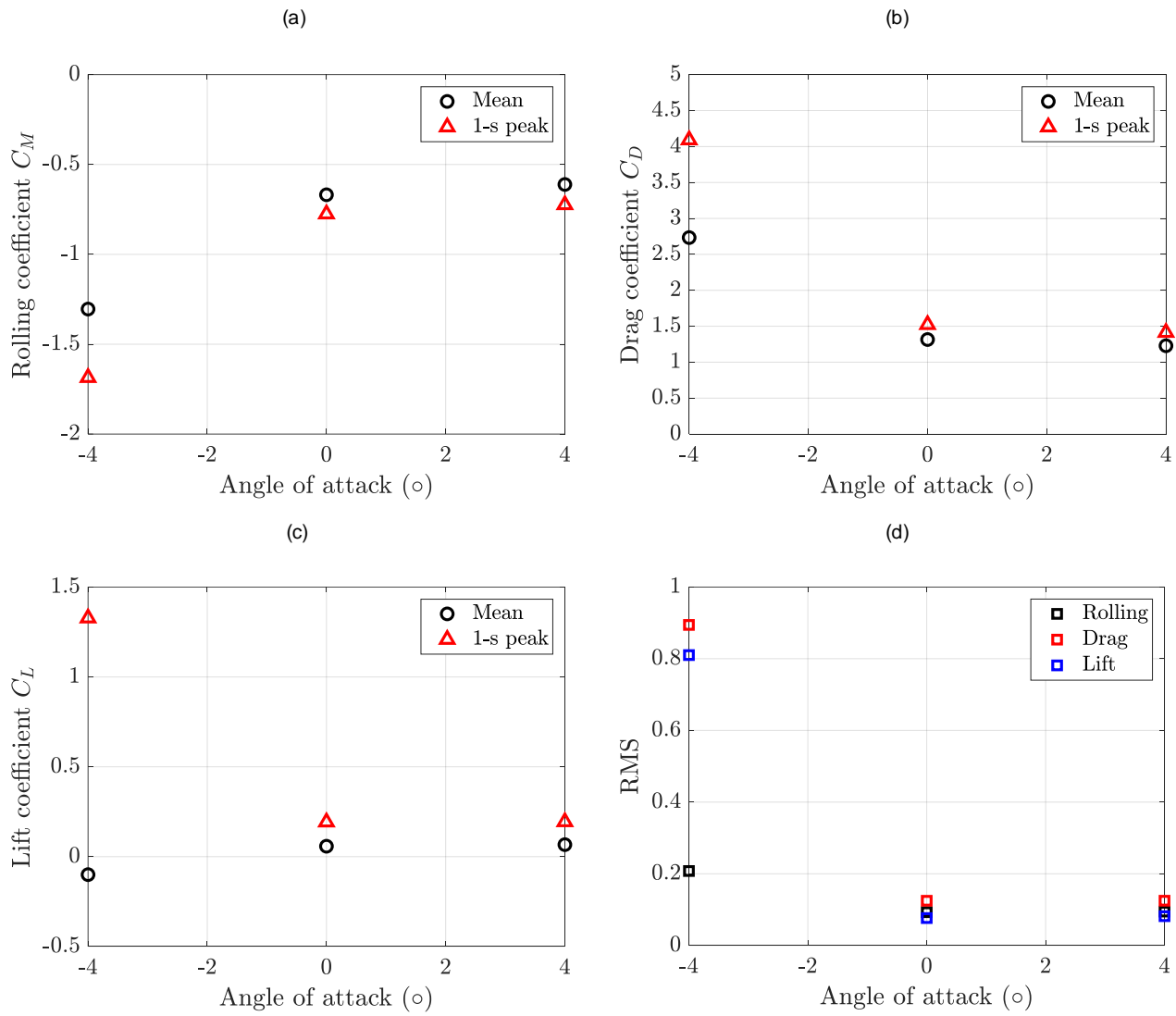


**Figure 4.12.** Variation of the mean and 1-s peak of (a) rolling coefficient, (b) drag coefficient and (c) lift coefficient as well as (d) the RMS value of force coefficient against the angle of attack, when the vehicle is at the centre of the left lane.

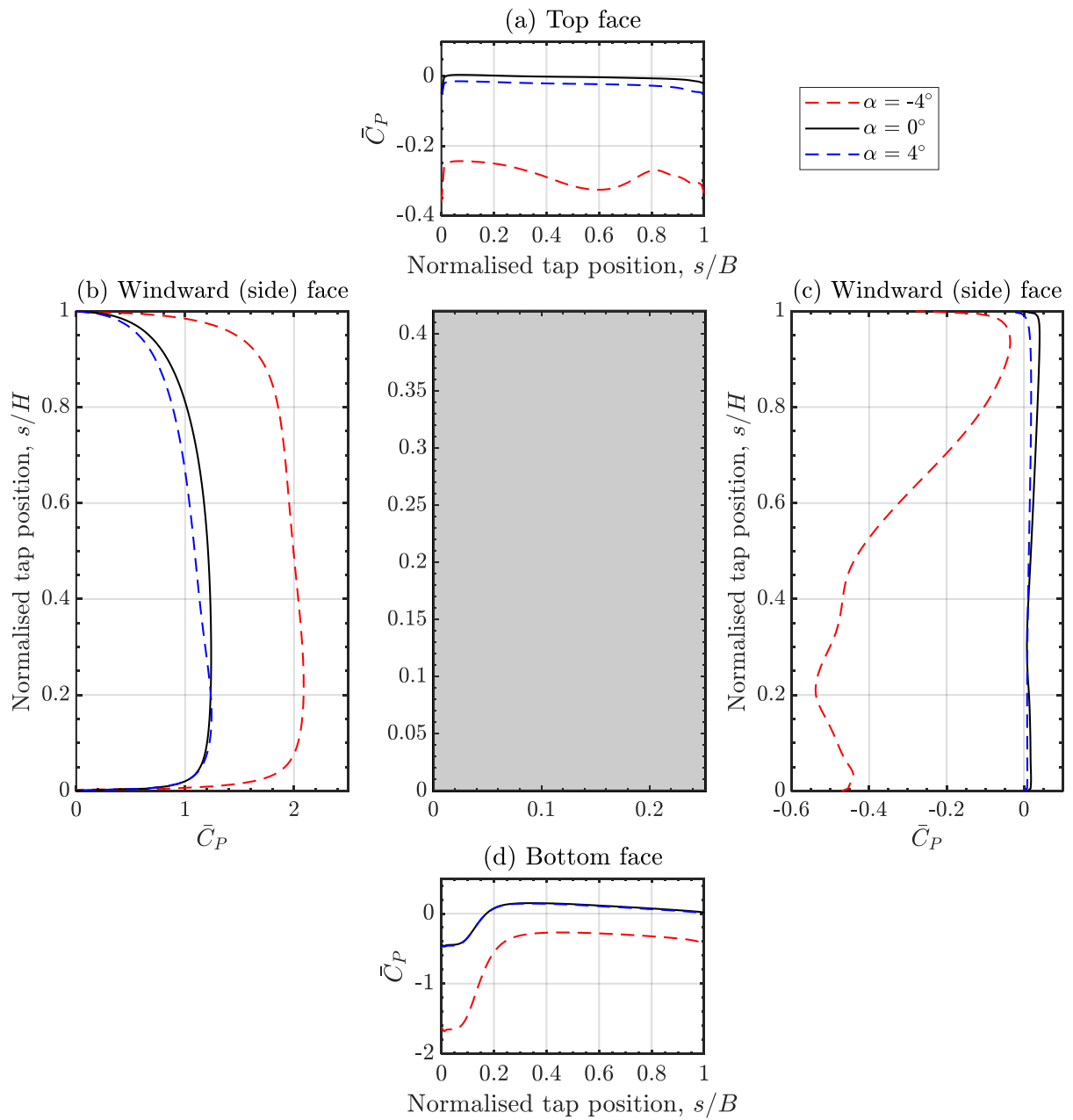


**Figure 4.13.** Variation of the mean pressure coefficient around the vehicle with respect to the angle of attack, when the vehicle is at the centre of the left lane.

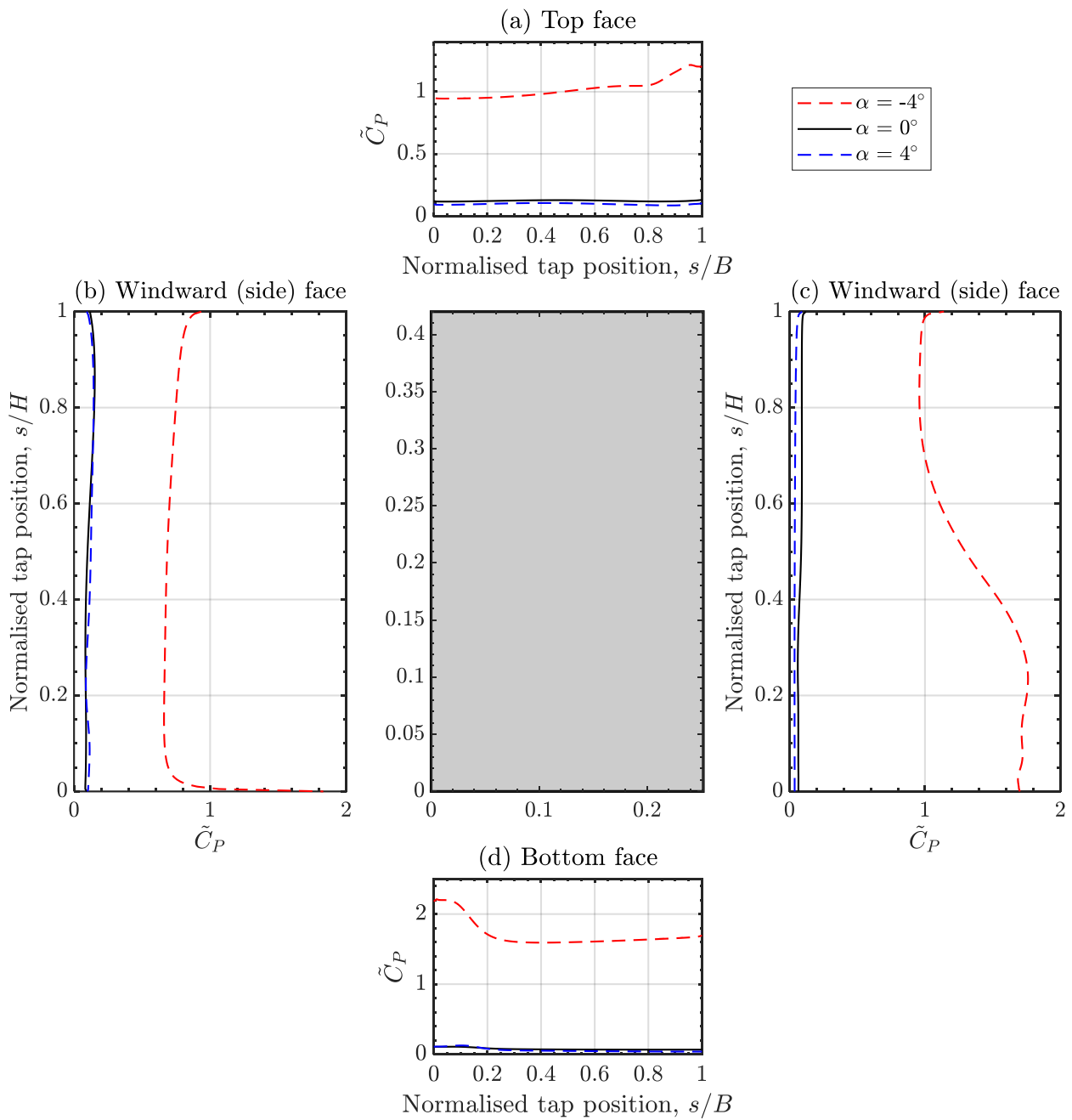


**Figure 4.14.** Variation of the RMS pressure coefficient around the vehicle with respect to the angle of attack, when the vehicle is at the centre of the left lane.

### 4.3 Comparison of flow field

In Sections 4.1 and 4.2, significant changes in aerodynamic coefficients and surface distribution of pressure coefficients on the bus were reported when the angle of attack becomes negative. By investigating the time-averaged flow field as reported in Figure 4.15 to Figure 4.17, these changes are found to be associated with an alteration in the flow field around the vehicle.

#### Hard shoulder

For the case when the angle of attack is zero or positive (Figure 4.15a and Figure 4.16a, respectively), the averaged flow field shows very similar features:

- There is a steep shear layer originated from the top windward leading edge of the vehicle. The shear layer is represented by the light blue band in the contour plots.
- Trapped under the shear layer is the wake region of the vehicle which is essentially a recirculation zone comprising three large-scale vortices.

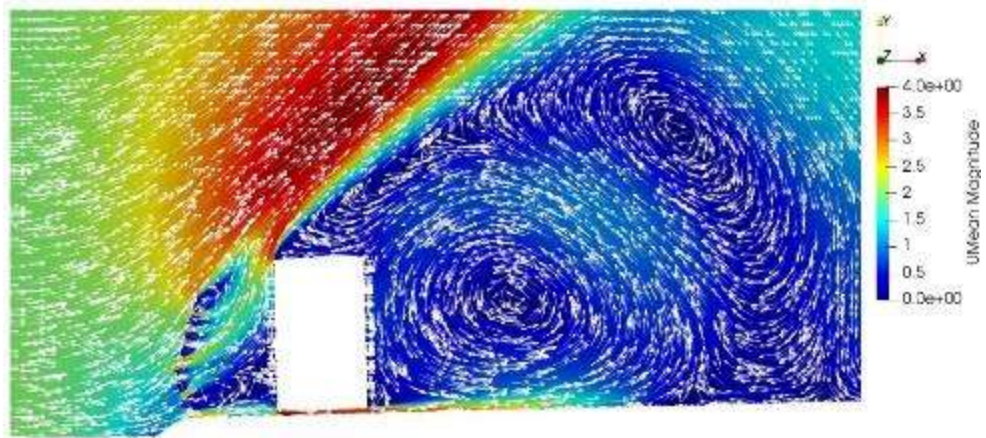
When the angle of attack becomes negative,

- The shear layer becomes nearly parallel to the horizontal.
- The depth of the wake region or the recirculation zone significantly reduces, which not only rearranges the vortices but also decreases their size. Also, another recirculation region develops on the top surface, which is potentially related to the vortex shedding phenomenon from the top leading edge of the vehicle and causes an increase in suction and dynamic pressure fluctuation.

#### Left lane

Although the arrangement of vortices in the wake region or circulation zone differs from that seen in Case 1, the variation of the flow field when the angle of attack becomes negative is very similar. The shear layer becomes more horizontal, the depth of the wake region significantly reduces, the size of vortices decreases, and another recirculation region appears on the top surface.

(a) Hard shoulder



(b) Left lane

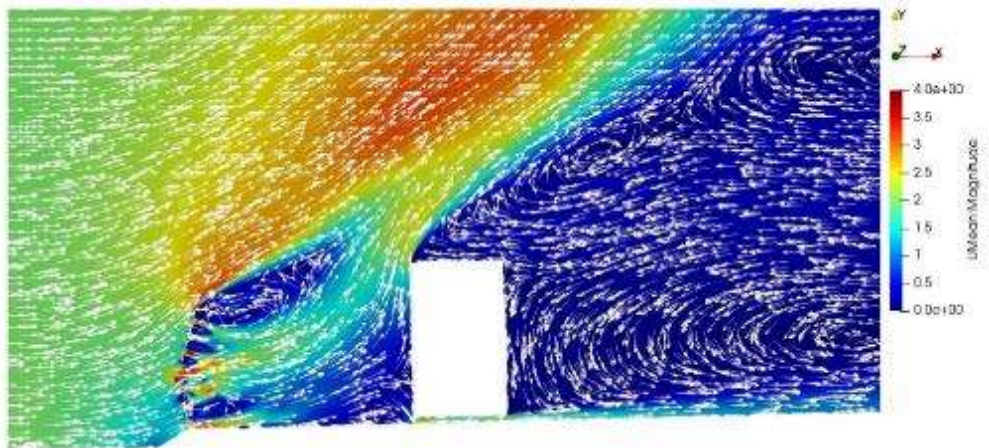
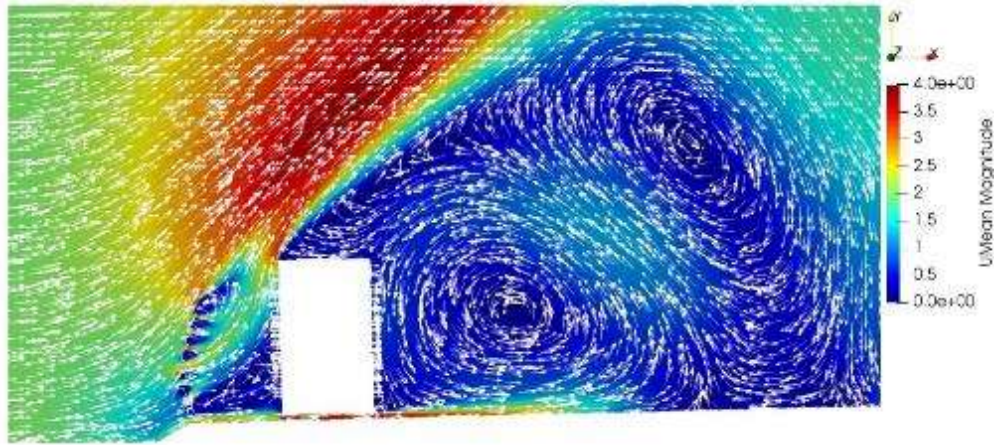


**Figure 4.15.** Contour plots of the time-averaged velocity field, comparing the flow field when the vehicle is (a) at the centre of the hard shoulder and (b) at the centre of the left lane, at the angle of attack  $0^\circ$ .

(a) Hard shoulder



(b) Left lane

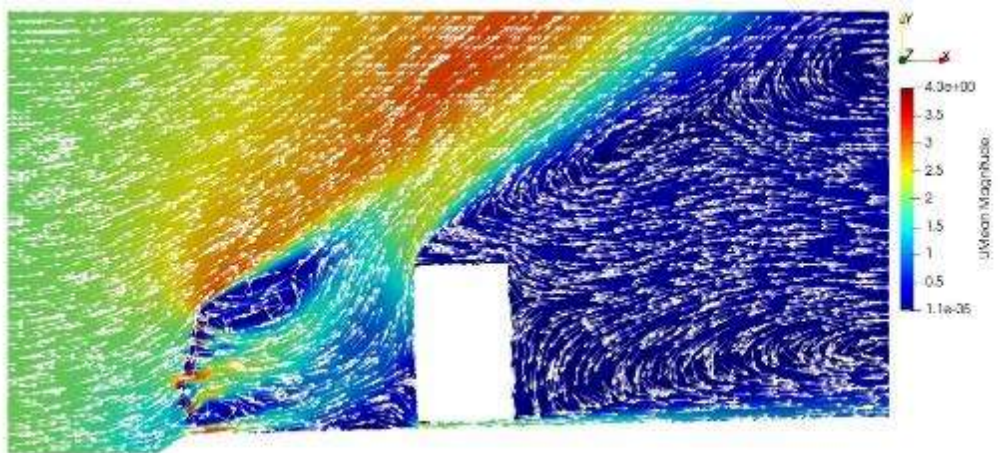
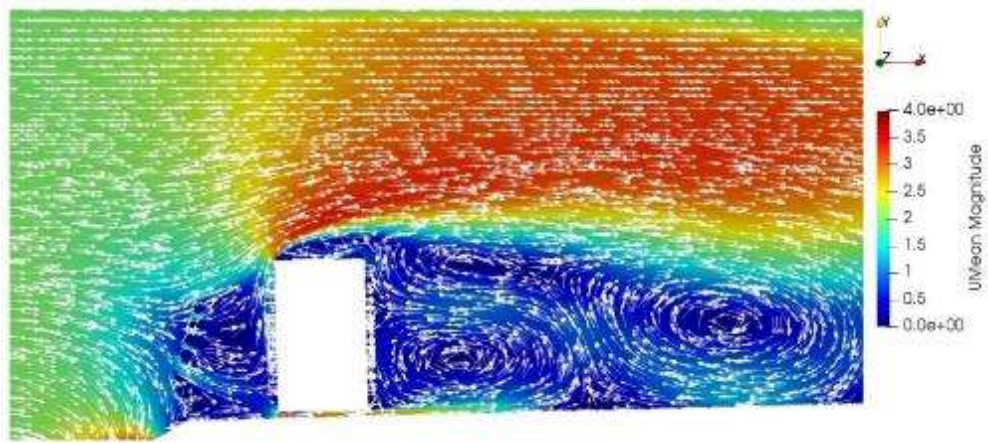


**Figure 4.16.** Contour plots of the time-averaged velocity field, comparing the flow field when the vehicle is (a) at the centre of the hard shoulder and (b) at the centre of the left lane, at the angle of attack  $4^\circ$ .

(a) Hard shoulder



(b) Left lane

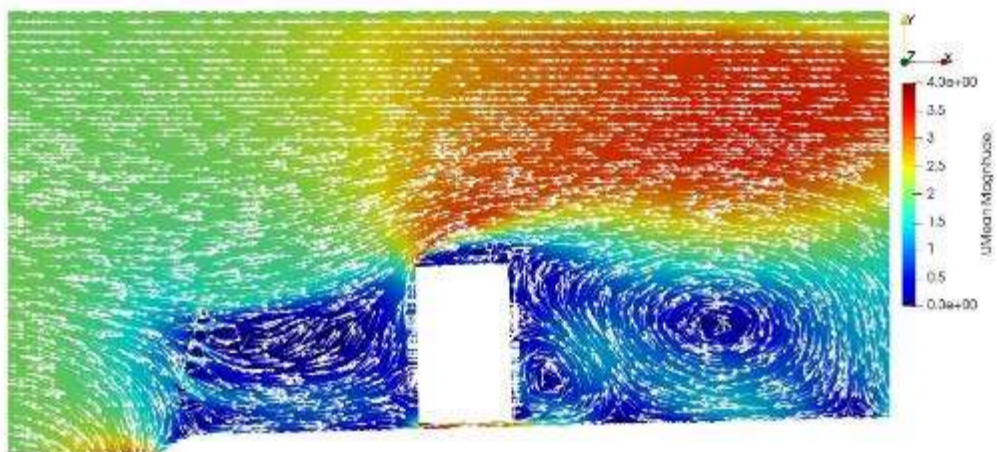


**Figure 4.17.** Contour plots of the time-averaged velocity field, comparing the flow field when the vehicle is (a) at the centre of the hard shoulder and (b) at the centre of the left lane, at the angle of attack  $-4^\circ$ .

## 4.4 Reduction factor of overturning moment

CFD simulations for the two cases where the vehicle is present on the deck were also repeated without the wind barrier. The aim of these simulations was to estimate the rolling coefficients of the reference vehicle when it was not protected by the wind barrier (hereafter referred as unshielded values) so that a reduction factor could be calculated to evaluate the performance of the barriers. Together with the shielded counterparts (i.e. when the vehicle is protected by the wind barrier), they are reported in Table 4.1 and Table 4.2 for when the vehicle is on the centre of the hard shoulder and the left lane, respectively. The reduction factor is calculated as the ratio between the shielded and unshielded rolling coefficients.

The reduction factor is seen to improve when the vehicle is moved from the centre of hard shoulder to the centre of left lane, particularly for the zero and positive angles of attack. The effect of the vehicle's position on the reduction factor is small for the negative angle of attack. In addition, when the angle of attack is negative, the shielded and unshielded rolling coefficients show very small variations between different positions of the vehicle.

Figure 4.18 compares the time-averaged velocity field across the deck at the angle of attack  $0^\circ$  when the vehicle is at the centre of the hard shoulder and the left lane. For both vehicle positions, the wake behind the vehicle is very broad, has low speed and comprises circulating flow features. The wake is trapped by a very steep shear layer originated from the top windward edge of the vehicle. A notable difference is however observed in front of the outer (side) face of the vehicle. When the vehicle is on the centre of the hard shoulder, the flow stagnates at the outer face. This is accompanied with a very small recirculation, which appears in front of the bottom windward edge, although the effect of this recirculation region on the vehicle is small. However, when the vehicle is on the centre of the left lane, the recirculation becomes significantly larger, covering the entire outer face. This leads to a change in the surface pressure distribution on this face of the vehicle and subsequently affects the rolling coefficient.

At the  $4^\circ$  angle of attack, as shown in Figure 4.19, the same behaviour is observed in the averaged flow field as the vehicle's position is changed from the hard shoulder to the left lane.

When the angle of attack is  $-4^\circ$ , Figure 4.20 shows the common characteristics of average flow fields despite the difference in the vehicle's position. There is the stagnation of the flow on the outer face and a narrow wake region behind the vehicle. These similarities lead to a very small dependence of the rolling coefficient on the vehicle's position.

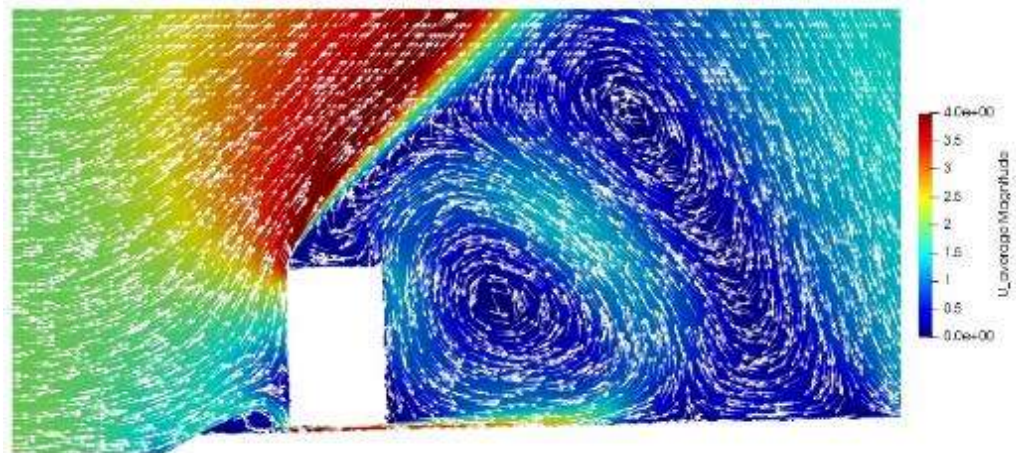
**Table 4.1.** Shielded and unshielded rolling coefficients, and associated reduction factors, when the vehicle is on the centre of the hard shoulder.

Wind speed $U$ ( $\text{ms}^{-1}$ )	Angle of attack AoA ( $^\circ$ )	Rolling coefficient		Reduction factor $R = C_{M,S}/C_{M,U}$
		Shielded, $C_{M,S}$	Unshielded, $C_{M,U}$	
2	-4	-1.36	-1.46	0.93
2	0	-1.38	-1.85	0.74
2	4	-1.33	-1.76	0.76

**Table 4.2.** Shielded and unshielded rolling coefficients, and associated reduction factors, when the vehicle is on the centre of the left lane.

Wind speed	Angle of attack	Rolling coefficient		Reduction factor
		Shield, $C_{M,S}$	Unshielded, $C_{M,U}$	
$U$ ( $\text{ms}^{-1}$ )	AoA ( $^\circ$ )			$R = C_{M,S}/C_{M,U}$
2	-4	-1.30	-1.55	0.84
2	0	-0.67	-1.00	0.67
2	4	-0.61	-0.94	0.65

(a) Hard shoulder



(b) Left lane

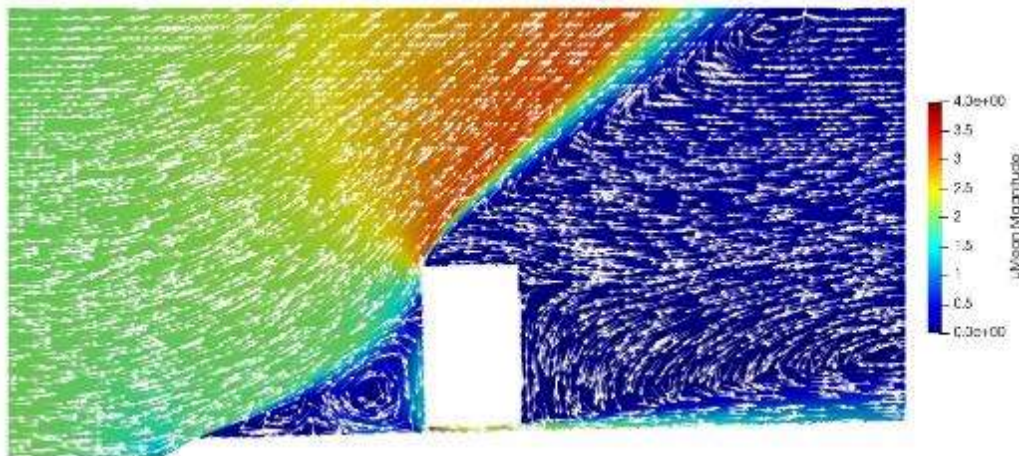
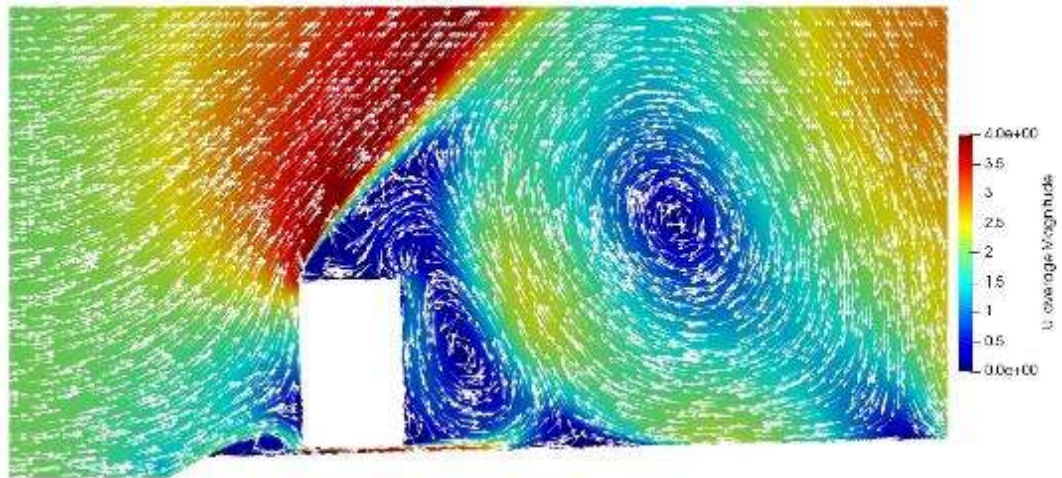


**Figure 4.18.** Contour plots of the time-averaged velocity field at the angle of attack  $0^\circ$ , when there is no wind barrier: (a) the vehicle at the centre of the hard shoulder and (b) the vehicle at the centre of the left lane,

(a) Hard shoulder



(b) Left lane

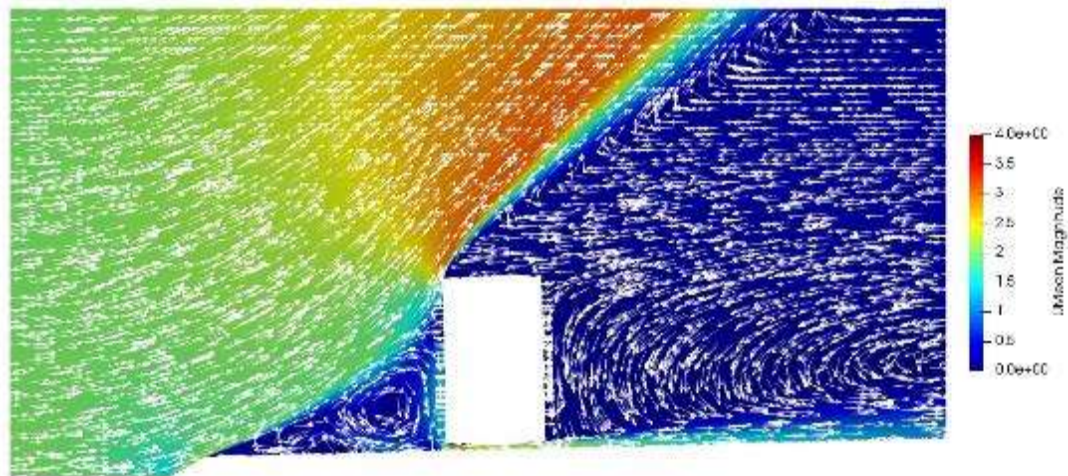
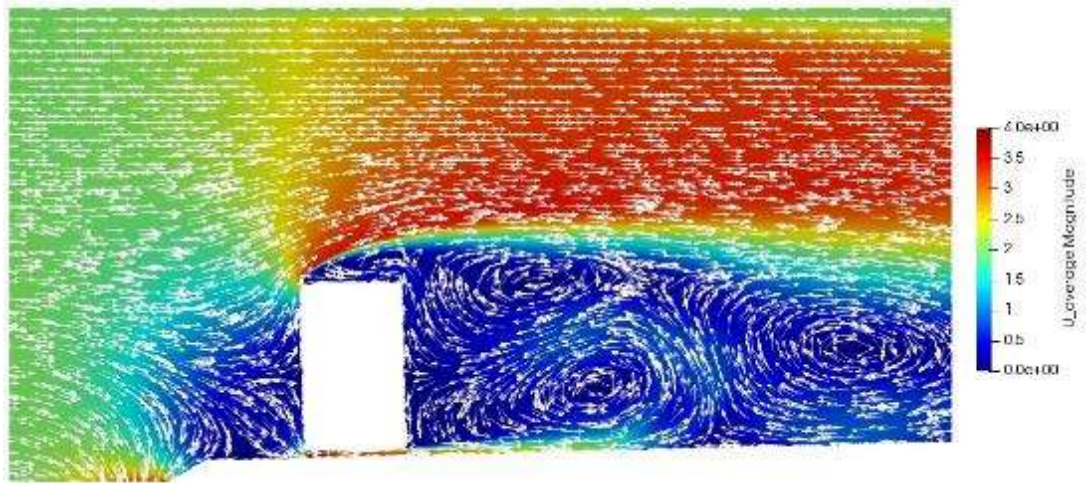


**Figure 4.19.** Contour plots of the time-averaged velocity field at the angle of attack  $4^\circ$ , when there is no wind barrier: (a) the vehicle at the centre of the hard shoulder and (b) the vehicle at the centre of the left lane.

(a) Hard shoulder



(b) Left lane

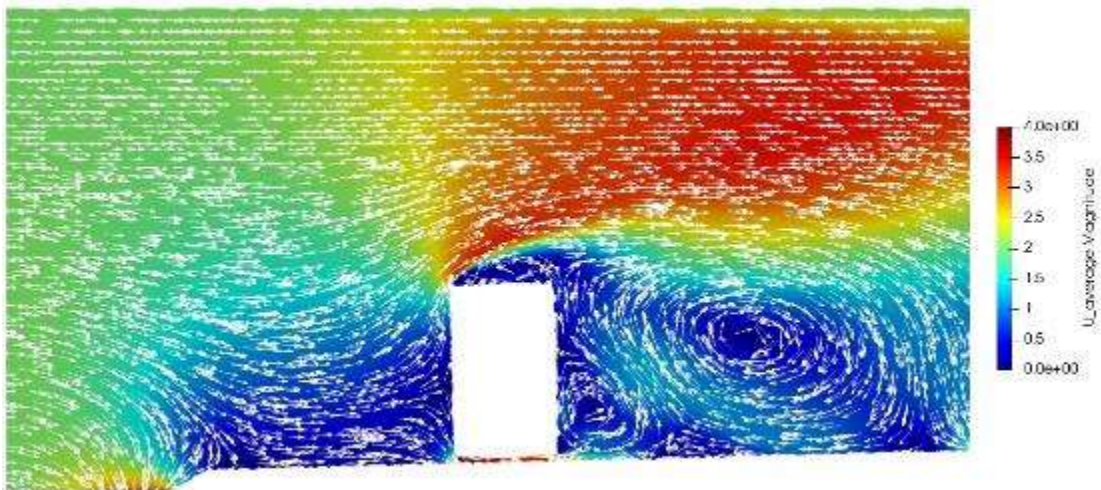


**Figure 4.20.** Contour plots of the time-averaged velocity field at the angle of attack  $-4^\circ$ , when there is no wind barrier:  
(a) the vehicle at the centre of the hard shoulder and (b) the vehicle at the centre of the left lane.

## 5 FCBC Wind Barrier

In this section, the performance of the FCBC wind barrier is compared against that of the as-built wind barrier which was discussed in Sections 3 and 4, at the wind speed of  $2\text{ms}^{-1}$  and at the angle of attack of  $0^\circ$ .

### 5.1 Empty carriageway

In Figure 5.1, the time-averaged velocity field for the case of the FCBC wind barrier is compared against that for the as-built wind barrier. The contour plot represents the magnitude of the averaged wind speed; where the red illustrates the flow speeding up while the blue illustrates slowing down. The FCBC wind barrier appears to have a greater effect on reducing the wind speed across the bridge deck. This is shown by a very dark blue region highlighted by the red rectangle in Figure 5.1b. This flow region is trapped under a shear layer originated from the top louvre. The rates at which this shear layer broadens and lifts up are higher, compared to those observed for the as-built wind barrier (shown in Figure 5.1a).

The greater shielding effect of the FCBC wind barrier can also be inferred from Figure 5.2. For the as-built wind barrier, below the wind barrier height, the reduction factor of the average wind speed varies between 0.5 to 0.75 approximately. For the FCBC wind barrier, this reduction factor is found to improve, with the lowest values of between 0.1 and 0.2 within the dark blue region (as shown by the red rectangle in Figure 5.1a). The geometry of the FCBC wind barrier appears to accelerate the flow through the gap between the bridge deck and the bottom louvre, causing a high-speed jet near the surface of the deck. This jet dissipates across the deck, accompanied with a broadening of the dark blue region where the reduction factor is found minimum.

The vector plot in Figure 5.1 also suggests there is very noticeable recirculation flow in the dark blue region mentioned above. Investigating the variation of the time-averaged flow velocity component that is parallel to the bridge deck, for the FCBC wind barrier, Figure 5.3b clearly shows the presence of reversed flow coinciding with the minimum reduction factor of the averaged wind speed. On the other hand, for the as-built wind barrier, the difference between the average flow speed and averaged flow velocity component parallel to the bridge deck is unnoticeable. The presence of recirculation and reversed flow can also be inferred from Figure 5.4 showing the variation of the averaged angle across the bridge deck. At the centre of the hard shoulder, the averaged flow angle profile exhibits a sharp change at about mid-height of the wind barrier, which is due to effects of the recirculation nearby.

In addition to the time-averaged component, the FCBC wind barrier is also found to have a greater effect on reducing the unsteadiness in the flow, which is illustrated by the turbulence intensity of the flow velocity component parallel and normal to the bridge deck and the 1-second gust factor. As shown in Figure 5.5, for the as-built wind barrier, below the wind barrier height, as the energy in the flow dissipates across the deck, the turbulence intensity of the parallel flow component (i.e. the flow component that is parallel to the bridge deck) decreases from about 20% at the centre of the hard shoulder to about 9% at the centre of the right lane. For the FCBC wind barrier, except a higher turbulence intensity closer to the bridge deck due to the hi-speed jet discussed above, the turbulence intensity at the three considered positions is found lower. Similar observations can be made when investigating the turbulence intensity of the flow component normal to the bridge deck, as shown in Figure 5.6. The dominance of the recirculation flow in the region behind the wind barrier means larger 1-second gust factors for the FBCB wind barrier, compared to the as-built wind barrier (Figure 5.7).

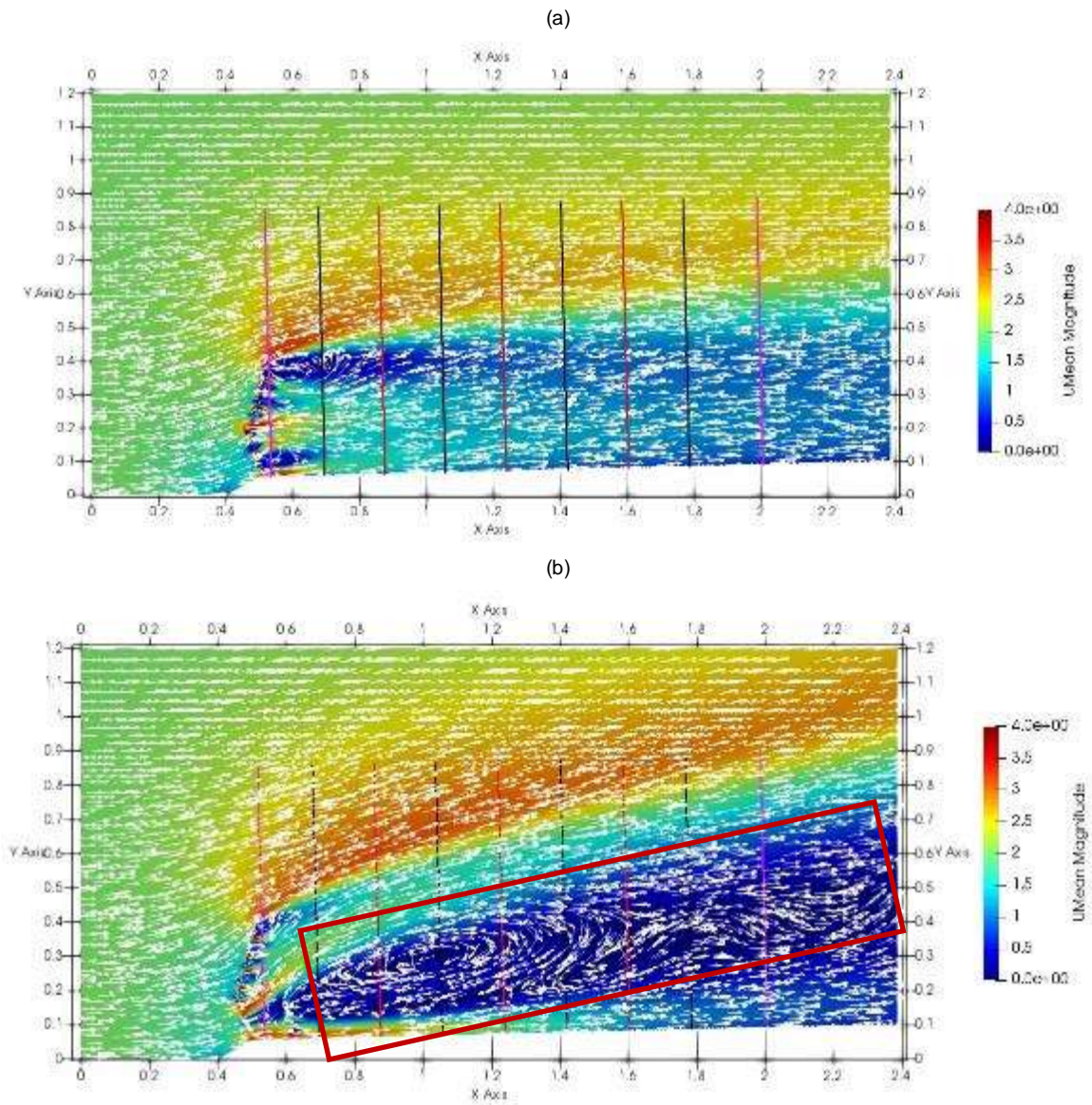


**Figure 5.1.** Contour and vector plots of the time-averaged wind speed magnitude at the wind speed of  $2 \text{ ms}^{-1}$  and the angle of attack  $0^\circ$ , for (a) the as-built wind barrier and (b) the FCBC wind barrier.

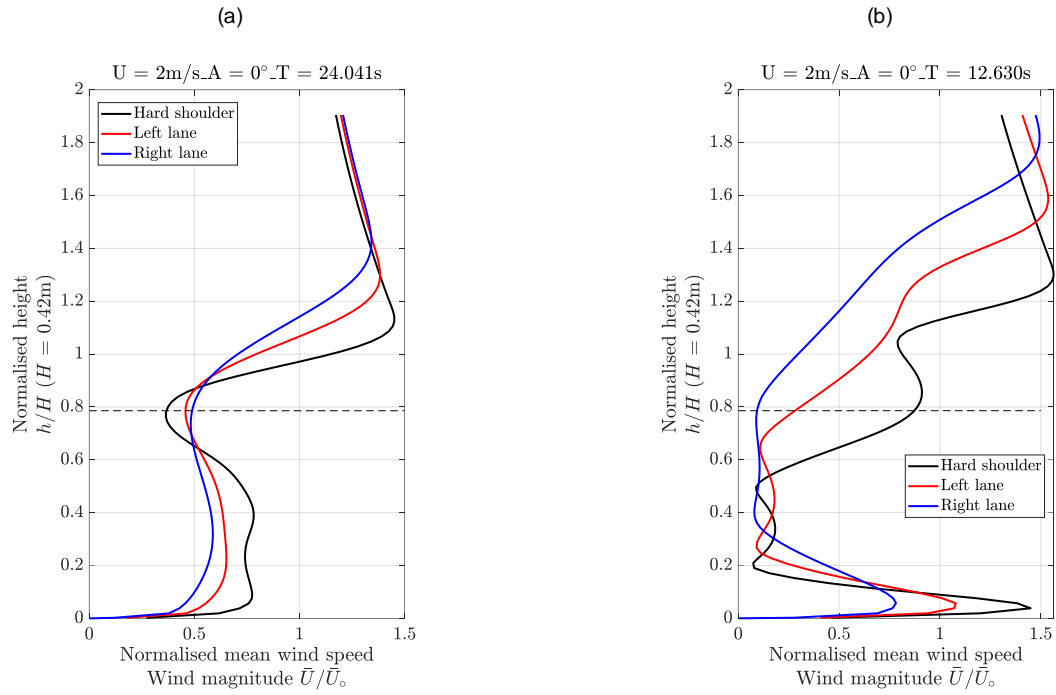


**Figure 5.2.** Variation of the profile of the normalised time-averaged wind speed magnitude, at the wind speed of  $2\text{ms}^{-1}$  and the angle of attack  $0^\circ$ , for (a) the as-built wind barrier and (b) the FCBC wind barrier. The dashed line indicates the normalised height of the wind barrier.

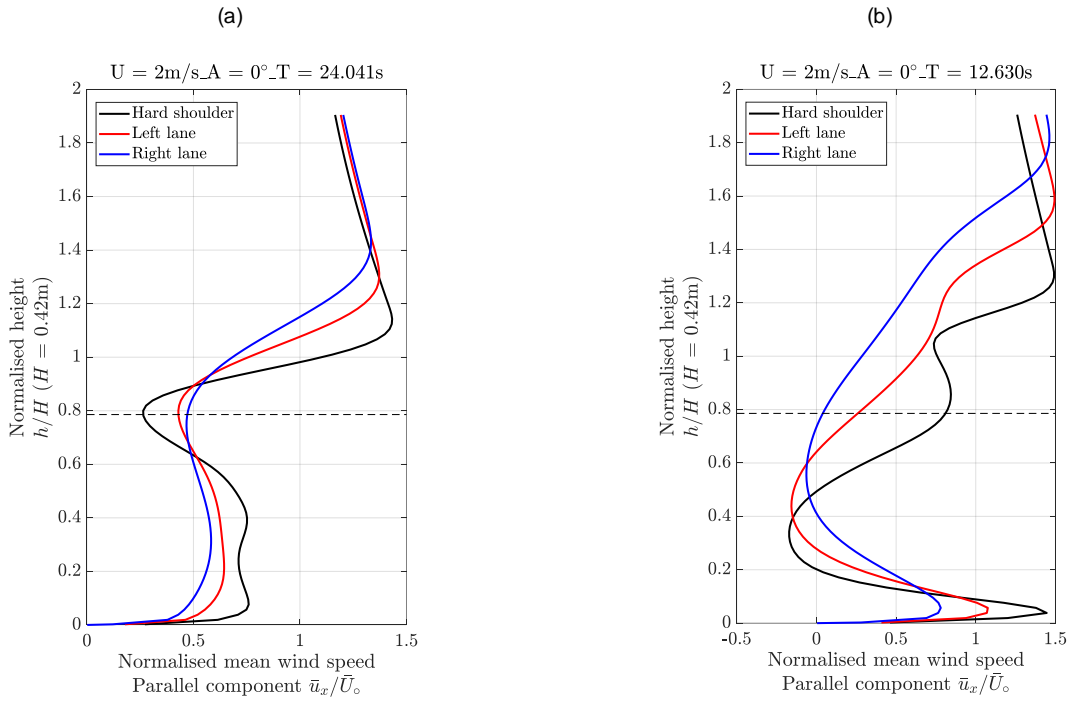


**Figure 5.3.** Variation of the profile of the wind velocity component parallel to the bridge deck, at the wind speed of  $2\text{ms}^{-1}$  and the angle of attack  $0^\circ$ , for (a) the as-built wind barrier and (b) the FCBC wind barrier. The dashed line indicates the normalised height of the wind barrier.

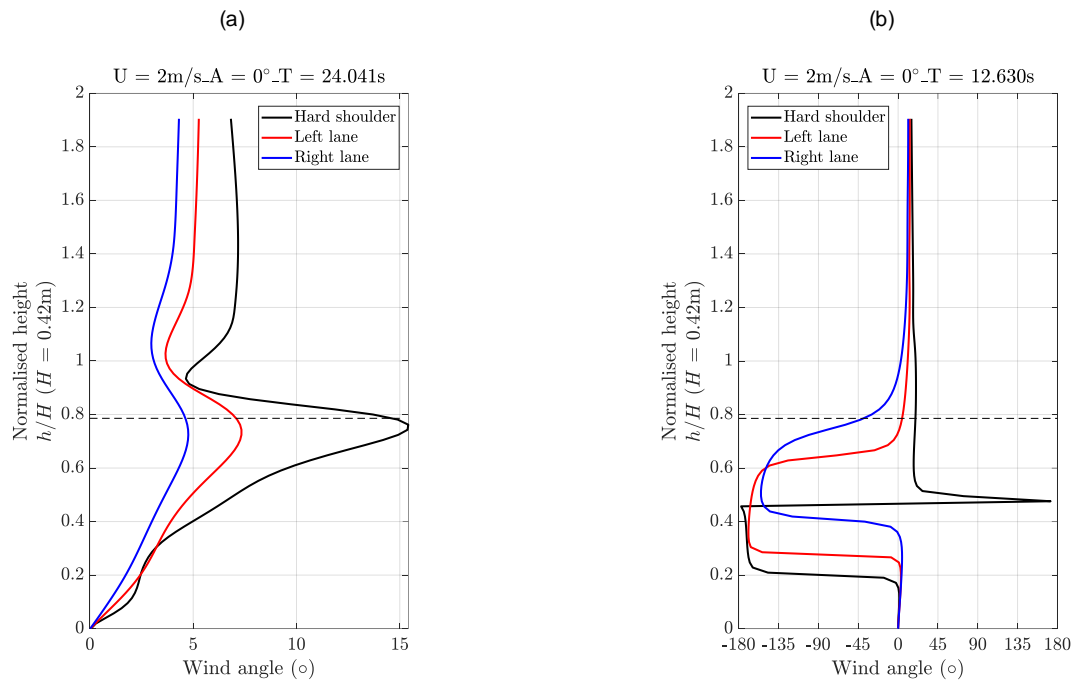


**Figure 5.4.** Variation of the profile of the time-averaged wind angle, at the wind speed of  $2m/s^{-1}$  and the angle of attack  $0^{\circ}$ , for (a) the as-built wind barrier and (b) the FCBC wind barrier. The dashed line indicates the normalised height of the wind barrier.

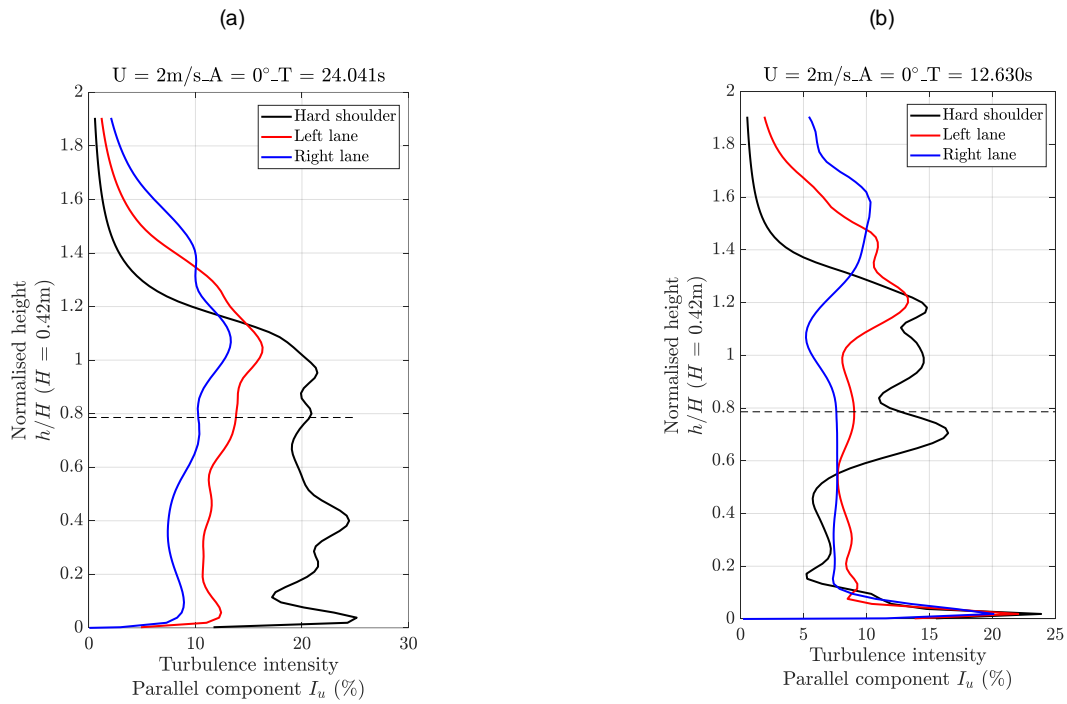


**Figure 5.5.** Variation of the profile of the turbulence intensity of the wind velocity component parallel to the bridge deck, at the wind speed of  $2m/s^{-1}$  and the angle of attack  $0^{\circ}$ , for (a) the as-built wind barrier and (b) the FCBC wind barrier. The dashed line indicates the normalised height of the wind barrier.

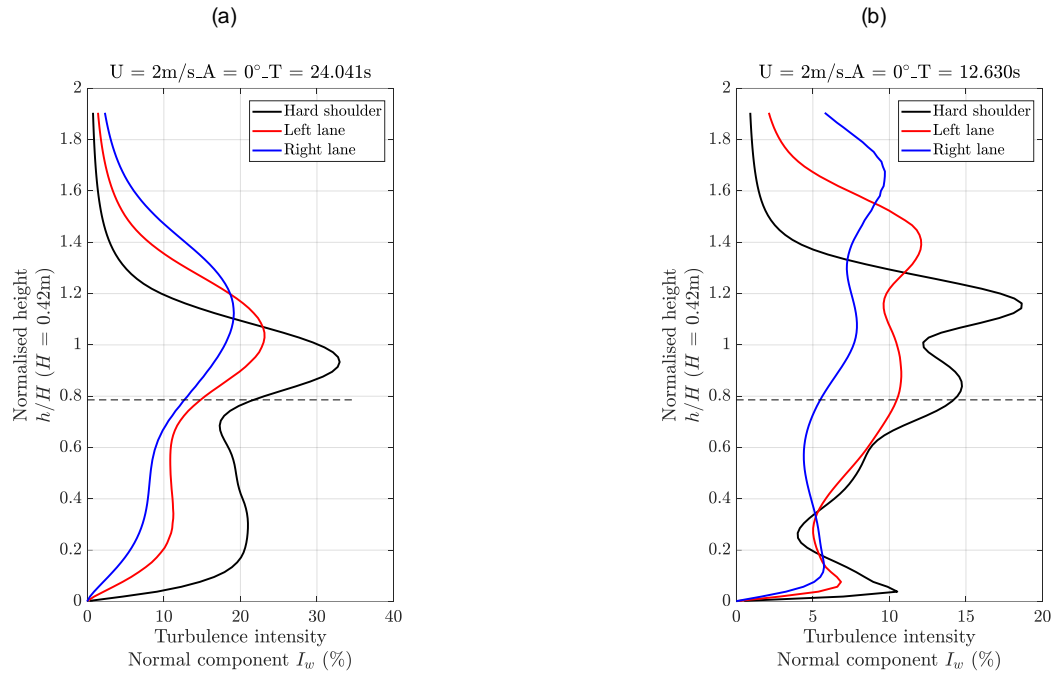


**Figure 5.6.** Variation of the profile of the turbulence intensity of the wind velocity component normal to the bridge deck, at the wind speed of  $2\text{ms}^{-1}$  and the angle of attack  $0^\circ$ , for (a) the as-built wind barrier and (b) the FCBC wind barrier. The dashed line indicates the normalised height of the wind barrier.

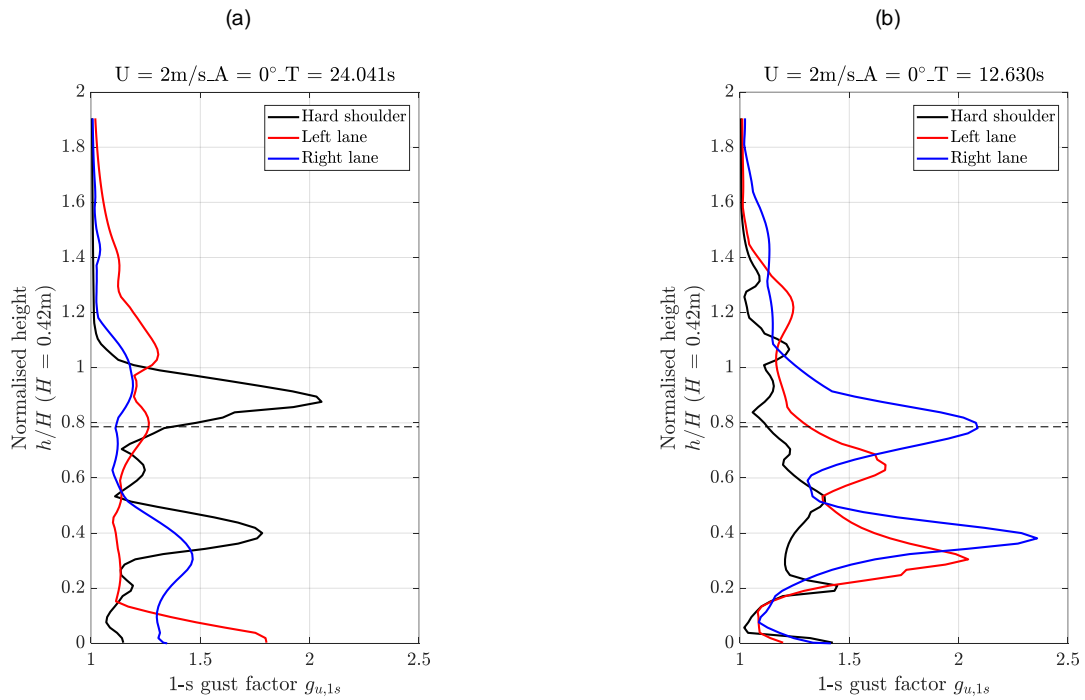


**Figure 5.7.** Variation of the profile of 1-second gust factor across the bridge deck, at the wind speed of  $2\text{ms}^{-1}$  and the angle of attack  $0^\circ$ , for (a) the as-built wind barrier and (b) the FCBC wind barrier. The dashed line indicates the normalised height of the wind barrier.

## 5.2 Vehicle on the carriageway

Figure 5.8 and Figure 5.9 show the time histories of the aerodynamic force coefficients when the vehicle is on the centre of the hard shoulder and the left lane, respectively, for the case of the FCBC wind barrier. After removing the transient parts of the time histories, which are shown by the dashed lines, the statistics of the aerodynamic coefficients are summarised in Table 5.1 and Table 5.2. Note that the duration of the records used to estimate these values is very short.

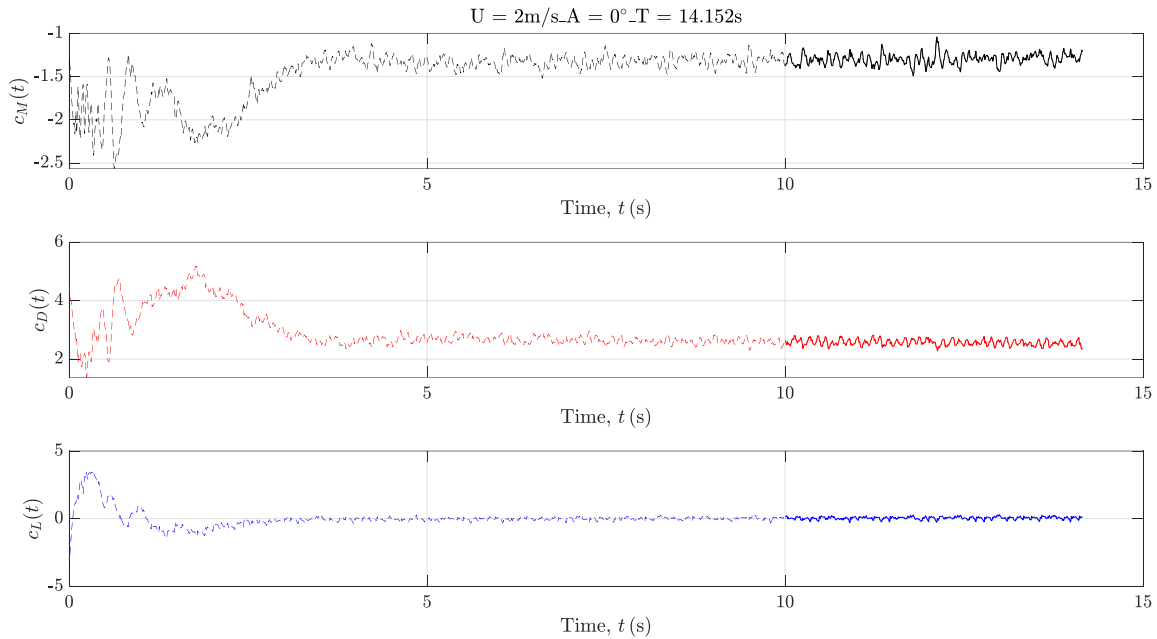


**Figure 5.8.** Time histories of rolling coefficient ( $c_M$ ), drag coefficient ( $c_D$ ) and lift coefficient ( $c_L$ ) at the angle of attack  $0^\circ$ , when the vehicle is at the centre of the hard shoulder.

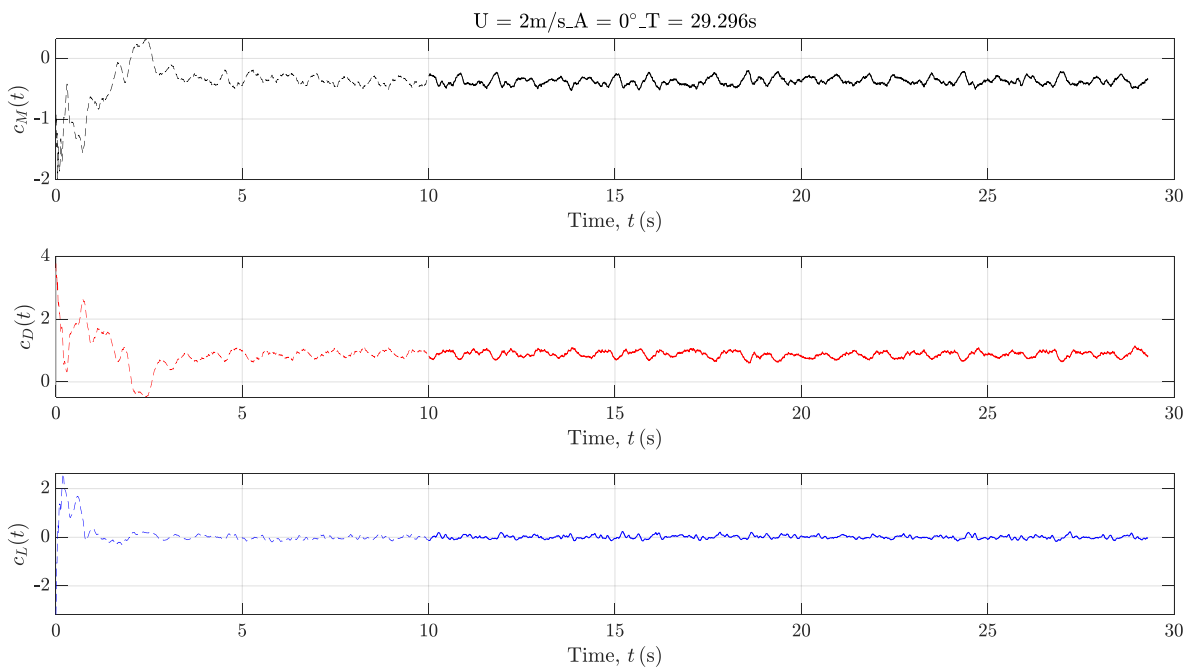


**Figure 5.9.** Time histories of rolling coefficient ( $c_M$ ), drag coefficient ( $c_D$ ) and lift coefficient ( $c_L$ ) at the angle of attack  $0^\circ$ , when the vehicle is at the centre of the left lane.

In general, the statistics (or the absolute values, for the case of the rolling coefficient) of the aerodynamic coefficients for the FCBC wind barrier are smaller than those for the as-built wind barrier. This observation is expected following the discussion in Section 5.1 where the shielding effect of the FCBC was found to be greater than the as-built wind barrier. The difference is larger when the vehicle is on the centre of the left lane, compared to when it is on the hard shoulder.

Comparing the averaged velocity field when the vehicle is at the centre of the hard shoulder, Figure 5.10 shows very small differences between the as-built and FCBC wind barrier. The average flow field behind the vehicle is dominated by two large counter-rotating vortices. There is another secondary elongated vortex sandwiched between these vortices and the shear layer originating from the top windward edge of the vehicle. The key difference between the two flow fields is the hi-speed jet close to the bridge deck generated by the flow accelerating through the gap between the deck and the bottom louvres. For the FCBC wind barrier, which has a wider gap, the hi-speed jet has a greater effect on the front face of the vehicle as well as providing more energy to the vortex right behind the vehicle.

When the vehicle is at the centre of the left lane, as shown in Figure 5.11, there are similarities in the averaged flow field in the wake of the vehicle. However, significant differences in the direction of the flow between the wind barrier and the vehicle are observed.

- The as-built wind barrier appears to deflect the flow downwards whereas this is not evident in the FCBC wind barrier. The flanges of the C-shaped louvres potentially help guide the flow downwards as it passes through the as-built wind barrier. Also, there is a smaller gap between the upper and lower parts of the as-built wind barrier; together with the presence of the UNP160 section, this prevents the flow accelerating upwards as the flow passes through the gap.
- It contrasts with the FCBC wind barrier where as shown Figure 5.11b, there is an upwards hi-speed jet passing through the gap between the upper and lower parts of the barrier. The jet deflects the flow upwards away from the VRS and the vehicle. Trapped underneath the jet is a recirculation region between the VRS and vehicle. It is suspected that the VRS may also have an impact on the recirculation. This flow feature potentially leads to smaller rolling and drag coefficients observed in the case of the FCBC wind barrier, compared to the as-built one.

In Table 5.3, the reduction factors of the overturning moment are summarised and compared between two different geometries of the wind barriers. For both wind barrier geometries, the reduction factor improves when the vehicle is moved from the centre of the hard shoulder to the centre of the left lane. Also, as expected from the flow field analysis, the reduction factors are better for the FCBC wind barrier compared with the as-built wind barrier.

**Table 5.1:** Comparison of statistics of aerodynamic coefficients when the vehicle is at the centre of the hard shoulder.

Wind barrier	Rolling coefficient			Drag coefficient			Lift coefficient		
	Mean	1-s peak	RMS	Mean	1-s peak	RMS	Mean	1-s peak	RMS
As-built	-1.38	-1.47	0.122	2.73	2.97	0.151	0.0963	0.175	0.145
FCBC	-1.30	-1.32	0.0613	2.57	2.60	0.103	0.0429	0.0718	0.100

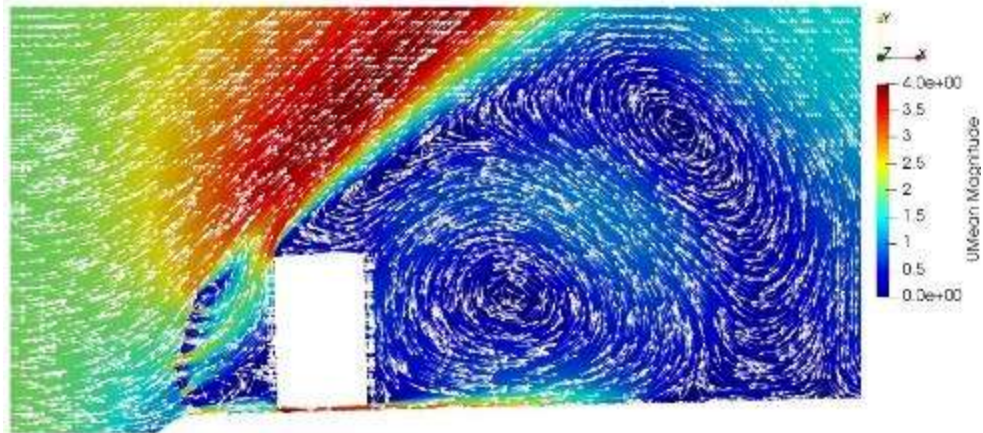
**Table 5.2:** Comparison of statistics of aerodynamic coefficients when the vehicle is at the centre of the left lane.

Wind barrier	Rolling coefficient			Drag coefficient			Lift coefficient		
	Mean	1-s peak	RMS	Mean	1-s peak	RMS	Mean	1-s peak	RMS
As-built	-0.675	-0.716	0.0947	1.32	1.40	0.126	0.0600	0.113	0.0798
FCBC	-0.376	-0.434	0.0621	0.877	0.984	0.0982	0.00897	0.0545	0.0687

**Table 5.3.** Shielded and unshielded rolling coefficients, and associated reduction factors, when the vehicle is on the centre of the hard shoulder and left lane, for the as-built and FCBC wind barrier.

Wind barrier	Location of the vehicle	Rolling coefficient		Reduction factor $R = C_{M,S}/C_{M,U}$
		Shield, $C_{M,S}$	Unshielded, $C_{M,U}$	
As-built	Hard shoulder	-1.38	-1.85	0.74
	Left lane	-0.67	-1.00	0.67
FCBC	Hard shoulder	-1.30	-1.85	0.70
	Left lane	-0.38	-1.00	0.38

(a) As-built wind barrier



(b) FCBC wind barrier

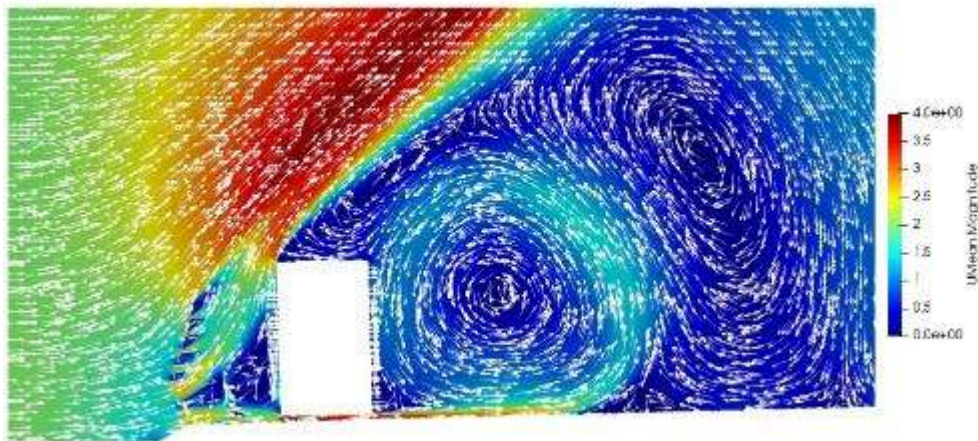
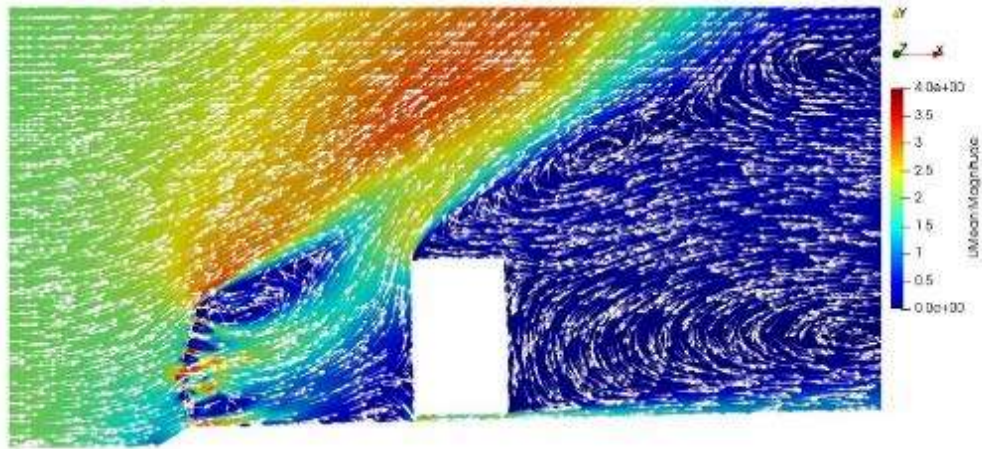


**Figure 5.10.** Contour plots of the time-averaged velocity field, comparing the flow field when the vehicle is at the centre of the hard shoulder: (a) the as-built wind barrier and (b) the FCBC wind barrier.

(a) As-built wind barrier



(b) FCBC wind barrier

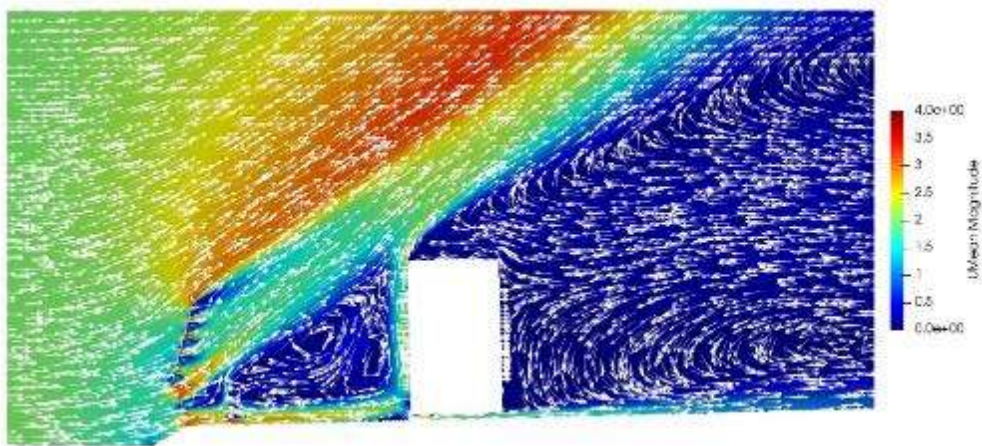


**Figure 5.11.** Contour plots of the time-averaged velocity field, comparing the flow field when the vehicle is at the centre of the left lane: (a) the as-built wind barrier and (b) the FCBC wind barrier.

## 6 Summary

This report described a CFD study where 2D URANS simulations using the SST  $k-\omega$  turbulence model were used to model the flow field on the Queensferry Crossing. The study indicated the effect of the as-built wind barrier on slowing down the wind speed and creating a more unsteady flow field across the bridge deck. Key features of the flow field such as high-speed jets through the gaps on the wind barrier and the shear layer originating from the top louvres were identified and discussed. These features of the flow field did not vary significantly as the angle of attack became positive. However, negative angles of attack led to dramatic changes to the flow field where the shear layer was found parallel to the deck and trapped underneath slowly decaying unsteady flow field.

A variation in the angle of attack also affected the aerodynamic coefficients and surface pressure distribution around the vehicle at the centre of either the hard shoulder or the left lane. At the negative angles of attack, the aerodynamic coefficients increased their RMS values and the surface pressure on the top face, bottom face and leeward (side) face of the vehicle saw an increase in both suction and fluctuation. The as-built wind barrier was found to become less effective to reduce the overturning moment when the angles of attack is negative, or when the vehicle is at the centre of the hard shoulder.

The CFD study was also extended to study the flow field in case the wind barrier had the geometry as found in the FCBC wind tunnel model. The study showed a very different flow field comprising a steeper shear layer, a large recirculation flow behind the VRS and a high-speed jet very close the bridge deck. The FCBC wind barrier was found to have greater effects on reducing wind speed, both the average and unsteady components, and reducing the overturning moment, which could be partly contributed by the VRS included in the FCBC model.

### Limitations

- The CFD study was conducted using URANS simulations where the turbulence was mathematically modelled. This has an impact on interpreting the unsteady component of the flow and the vehicle aerodynamic coefficients.
- Using a 2D model means the component of the flow in the third dimension (i.e. along the length of the bridge deck and the vehicle) is ignored. However, 3D flow features can be significant, particularly for the cases including the vehicle. Also, using a 2D model means that the study was limited to investigating effects of the vertical angle of attack, whereas horizontal skew wind can also pose large risks to the vehicle.
- The CFD study was conducted with a stationary vehicle, which did not represent the most likely scenarios on the actual bridge. A dynamic simulation with the static bridge deck and the vehicle moving along the carriageway can be advantageous, providing insights into the interaction between the 3D flow field and the moving vehicle. Such simulations will require a 3D model and the Large Eddy Simulation (LES) model, which can be very computationally expensive.
- The CFD study was conducted with smooth inflow condition. This did not represent the most likely scenarios on the actual bridge or the riskiest scenarios for the vehicle. The limitation can be improved by performing 3D LES simulation with turbulence inflow conditions derived from wind field parameters such as dominant wind direction, turbulence intensity, and turbulence length scale. The wind field parameters can be extracted from field data of anemometers installed on the Queensferry Crossing. Also, a gust can be included in the inflow condition to simulation riskier scenarios to the vehicle.
- In the CFD study, the reference vehicle, i.e. the double-decker bus, is modelled as a sharp-edge rectangular cylinder whereas the cross section of an actual bus has rounded corners and slightly tapers towards the top. The simplification can affect the flow field around the vehicle and its aerodynamics.

- The meshes were checked to ensure its suitability for the turbulence model and the aims of the CFD study. However, a detailed mesh sensitivity was not conducted due to constraints in time and issues with running simulations on the High Performance Computing system.

### **Additional Benefits**

The CFD study complemented wind tunnel experiments and full-scale measurement by providing visualisation of the flow field across the carriageway and around the vehicle. Also, from the CFD study, it was possible to extract velocity and surface pressure data at much finer spatial resolution, compared to wind tunnel experiments and full-scale measurement. The availability of such data facilitated analysis to gain insights into how the wind speed, angle of attack and wind barrier affect the flow and aerodynamics of the vehicle.

---

# Appendix C Wind Tunnel Testing



University of  
**Nottingham**  
UK | CHINA | MALAYSIA

# Report

## Investigation of Wind barriers on the Queensferry Crossing

Wind Tunnel Experiment

18 November 2020

# Change Record

---

Revision Number:

---

Reason for change	Date	Pages	Paragraph(s)
-------------------	------	-------	--------------

---

# Table of Contents

1	Introduction.....	4
2	Method.....	4
2.1	Wind tunnel model.....	4
2.2	Wind tunnel tests.....	10
3	Flow field across an empty carriageway.....	12
3.1	Angle of attack $0^\circ$ .....	12
3.2	Other angles of attack.....	19
3.3	Wind speed dependence.....	23
4	Aerodynamics of the vehicle.....	27
4.1	Without the wind barrier.....	27
4.2	With the wind barrier.....	34
5	Summary.....	38

# 1 Introduction

The wind tunnel (WT) study of the as-built wind barrier on the Queensferry Crossing (QFC) was carried out to investigate the effect the barriers have on the flow field and aerodynamics of vehicles using the bridge. This information will assist the review of the existing wind thresholds for the bridge.

## 2 Method

### 2.1 Wind tunnel model

A 1.6-m long sectional WT model of the QFC was constructed at the scale 1:50. The model not only captures the overall geometry of the cross section of the bridge deck, but also other fine details including the slope of carriageways and the geometry of wind fairings.

Supporting the main body of WT model is a wood frame made of rib plates and traverse beams which were laser-cut from 3-mm thick MDF sheets. Laser-cutting rib plates ensures the correct geometry of wind fairing and the slope of carriageways. Also, rib plates and traverse beams have pre-cut slots for an ease of assembling using wood glue.  $10 \times 10 \times 10\text{-mm}^3$  wood cubes were used to reinforced joints (Figure 2.1).

Between two adjacent rib plates, there are a central block and wind fairing blocks. Each block is made of nine exactly similar pieces which were cut from 16mm-thick plywood boards. The cutting process was done by using a CNC machine to ensure the geometry of wind fairing and the slopes of carriageways are accurately modelled. Pieces were joined using wood glue and properly aligned using 4mm-diameter dowel holes (Figure 2.2).

Dowel holes also helped properly glue central blocks and wind fairing blocks on to the frame. The result of this process is a half of the wood frame to support the main body of the WT model, as shown in Figure 2.3. The two halves were then joined using wood glue (Figure 2.4a) and the whole frame was strengthened using a 23-mm outer diameter steel tube as a spine (Figure 2.4b). Three pairs of collar clamps which were designed and manufactured in house were then used to fix the frame to the spine, at the two end of the model and at the centre where two halves of the frame were glued (Figure 2.5). There are slot cuts on the two wind fairing blocks at the centre of the model to securely mount a vehicle model and pressure tubing during WT tests (Figure 2.6).

Once the assembly of the frame had been completed, the surface finishing treatment was conducted by filling cracks with wood filler, sanding, coating central and wind fairing blocks with a number of primer and paint layers. Pre-cut 3-mm thick plywood plates were then glued to the frame to close the model (Figure 2.7). For the upwind middle section on the top surface (where a vehicle model is positioned during WT tests), the plate has pre-drilled holes to help attach it to the frame using wood screws. This design allows this plate to be removable, providing access to the void inside the model so that the vehicle and measuring instruments can be set up.

Two end plates made of 1mm-thick aluminium sheets were attached to two ends of the model using the bespoke collar clamps, wood screws and epoxy adhesive (Figure 2.9). Pre-cut holes on the end plates helped align them when mounting onto the model and provide access to the void inside. Masking tape were used to seal off any gaps between the model and the end plate, preventing disturbance to flow..

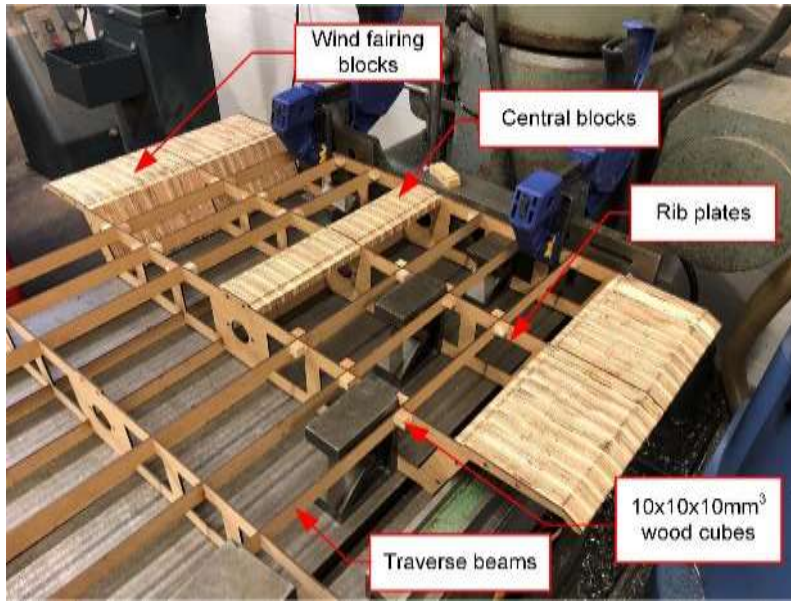


**Figure 2.1.** Assembly of rib plates and traverse beams to form a wood frame to support the main body of the WT model.

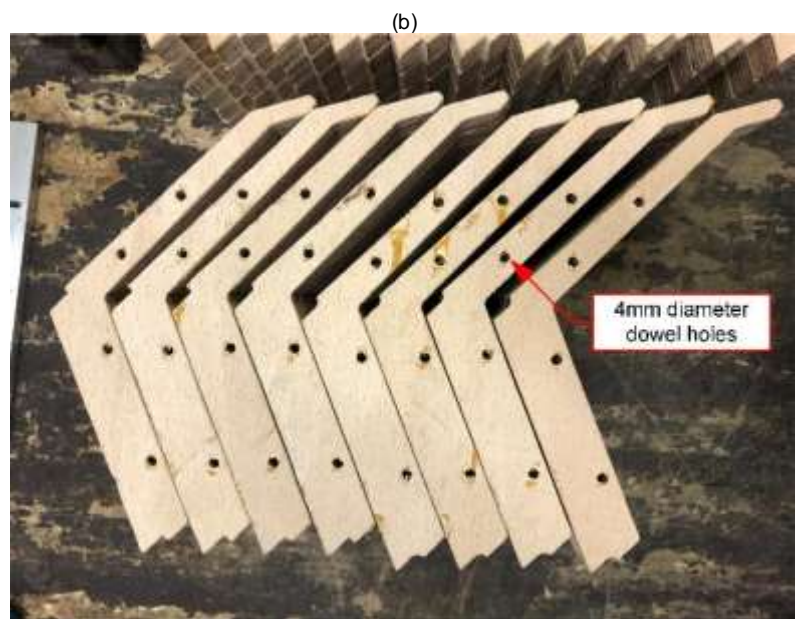


**Figure 2.2.** (a) Assembly of one wind fairing block; (b) Complete wind fairing blocks.



**Figure 2.3.** A complete half of the frame to support the main body of the WT model.



**Figure 2.4.** (a) Two halves of the frame are connected; (b) a 23mm outer diameter steel tube is used as a spine to strengthen the frame.

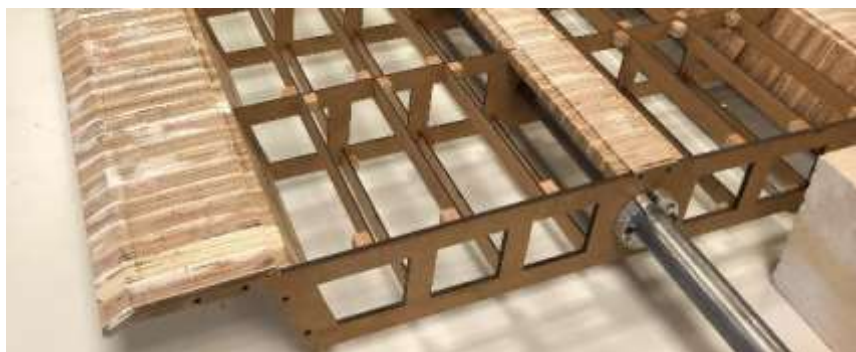


**Figure 2.5.** Three bespoke pairs of collar clamps are used to fix the frame to the steel tube. There are one pair at each end of the model and at the centre where two halves of the frame are joined.

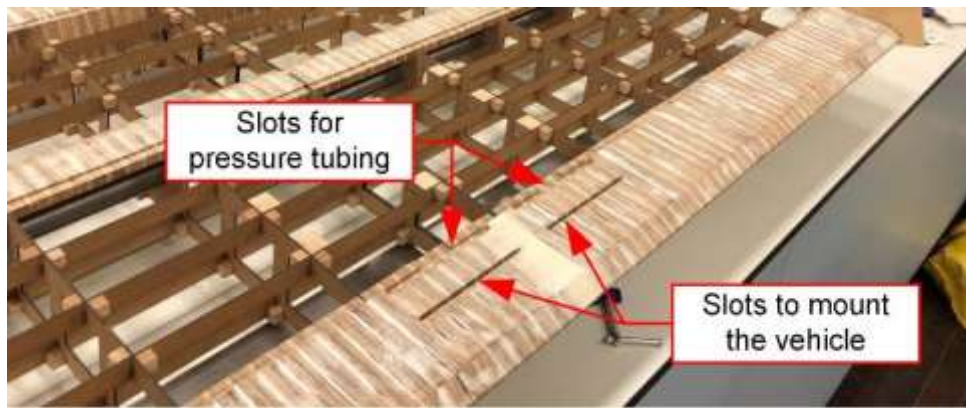


**Figure 2.6.** Slot cuts on two wind fairing blocks at the centre of the model to help securely mount the vehicle model during WT tests.



**Figure 2.7.** Pre-cut 3mm-thick plywood plates glued to the frame to close (a) the top and (b) bottom surfaces.

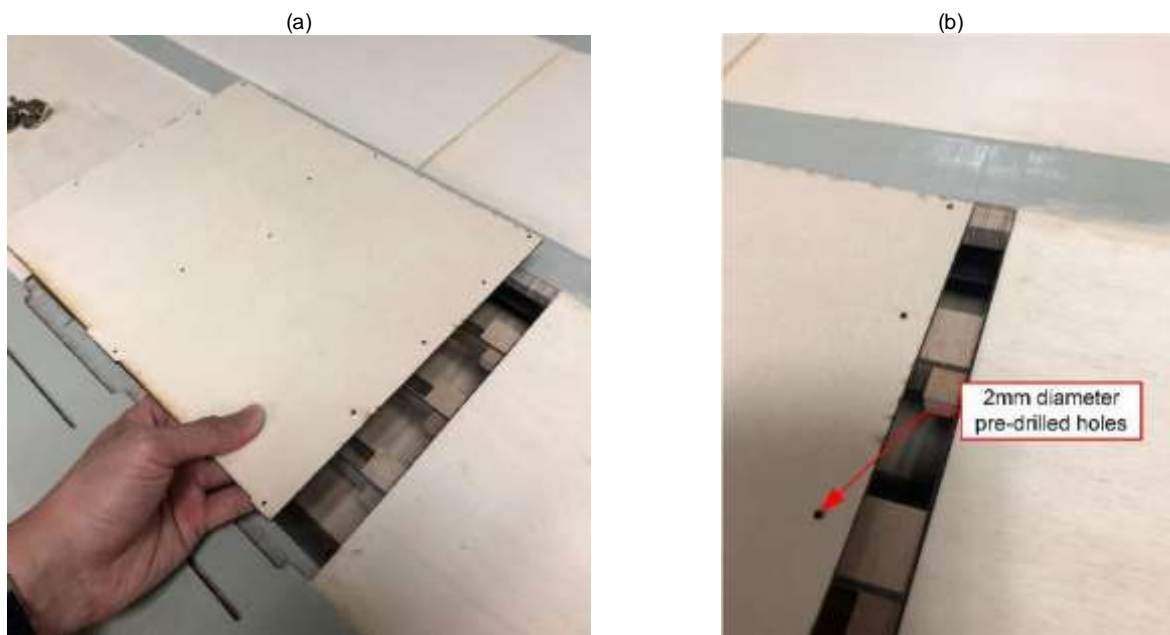


**Figure 2.8.** (a) A pre-cut 3mm-thick plywood plate used to close the upwind middle section on the top surface; (b) pre-drilled holes to help attach the plate to the frame using wood screws.



**Figure 2.9.** (a) End plates with holes to access the void of the model; (b) masking tap to seal of gaps between the model and end plates.

As-built wind barriers for the WT model were constructed panel by panel. Each panel consists of halves of two wind posts which are joined by six C-shape louvres (Figure 2.10). Wind posts were constructed using 3D plastic printing process. The same process was used to manufacture several identical pressers and moulds to create C-shape louvres from aluminium strips. There are slot cuts on wind posts that provides tight fitting to hold louvres in place. Panel of wind barriers were glued to the model (Figure 2.12). Since this process is irreversible, gluing process was conducted only when WT tests for the case without wind barriers had been completed.

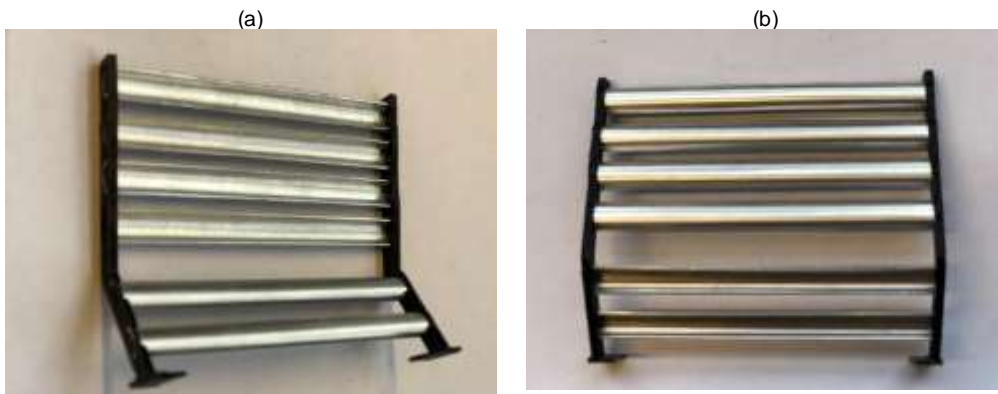


**Figure 2.10.** One panel of as-built wind barriers.

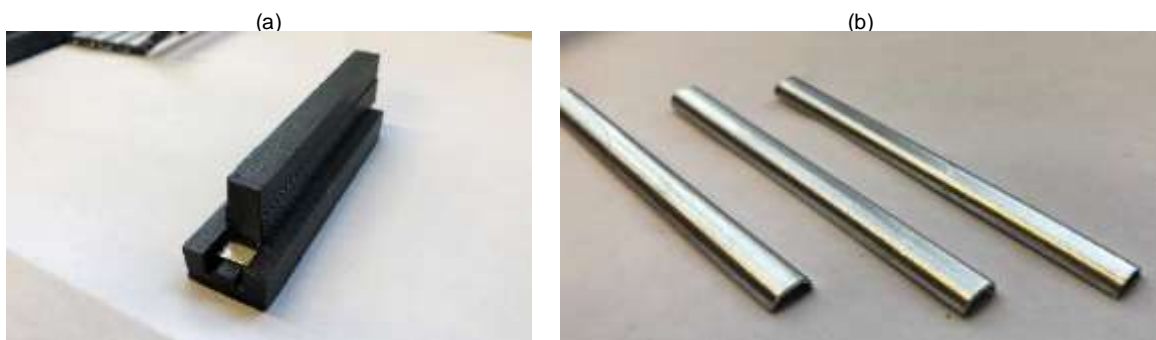


**Figure 2.11.** (a) A presser and mould used to create C-shaped louvres from aluminium strips; (b) C-shaped louvres.



**Figure 2.12.** Wind barrier along the windward edge of the model.

The reference vehicle model was a 1:50 scale double-decker bus and was modelled as a rectangular box (Figure 2.13). The top and side faces were made of 3mm thick perspex while the bottom face was made of 7mm thick aluminium plate. It was intended to use a heavy bottom to increase the stability of the model during WT test. The vehicle model is instrumented with 80 pressure taps which are distributed into five rings equally spaced along the length of the model. Wind ward wheels are extended downward so that they could be pushed into two pre-cut slots on the wind fairing blocks (as shown in Figure 2.6) to securely hold the vehicle model in place during WT tests.

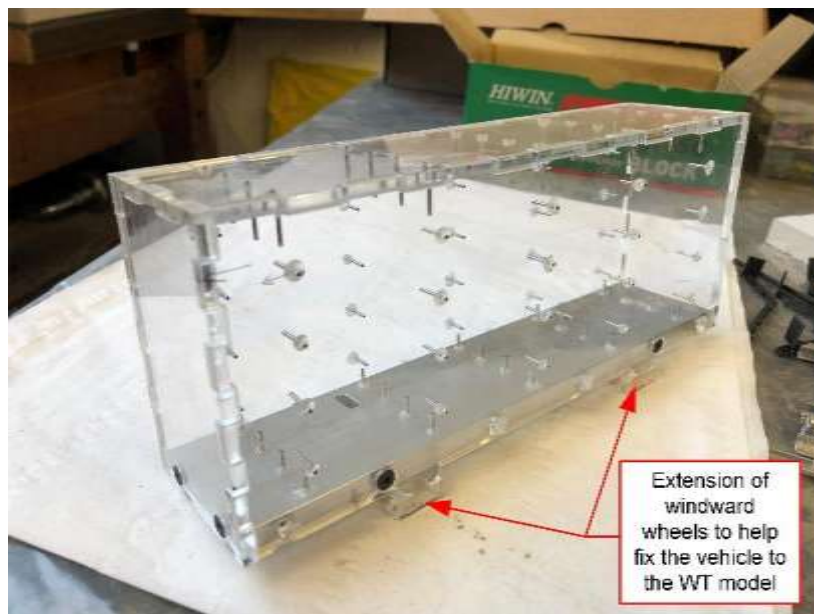


**Figure 2.13.** Model of the reference vehicle.

## 2.2 Wind tunnel tests

The WT sectional model was statically mounted onto a frame which is held rigidly inside the aerodynamic testing section of the WT (Figure 2.14). Two bespoke tube clamps are used to secure the model to the frame and provide a solution to change the angle of attack by loosening up the clamps. Dantec 55P11 single-wire probe was used to measure the component of wind velocity on the vertical plane. By mounting the probe on the traverse, the probe's position could be precisely controlled so that profiles of wind speed at three positions along the carriageway were measured (i.e. at the centre of hard shoulder, left lane and right lane). Scannivalve MPS4264 pressure scanner was used to measure the surface pressure around the vehicle which was mounted statically on the model. The pressure scanner can only support 64 channels. Therefore, for the bottom face, only four taps of the centre ring were sampled together taps on the top and vertical side faces. The sampling frequency for velocity and pressure measurement was set 2000Hz and 500Hz, respectively.

Table 2.1 describes three WT tests that were conducted in the study, using three different WT scaled wind speeds and five different angles of attack. Without any turbulence generators upstream, the flow in the WT is very close to smooth (with turbulence intensity of less than 0.5%). Positive angles of attack indicate wind coming from the underneath the section whereas negative angles of attack indicate the wind coming above. Purposes of Tests 1 and 2 are to measure wind speed profiles at three locations across the carriageway, and to investigate effects of the upstream wind speed and angle of attack on wind speed profiles. Purposes of Test 3 are to measure the surface pressure distribution around the vehicle model, perform surface integration to achieve aerodynamic coefficients and investigate effects of the upstream wind speed and angle of attack on aerodynamic coefficients.

**Table 2.1.** Matrix of WT tests.

Test ID	Description of WT model	Wind speed ( $\text{ms}^{-1}$ )			Angle of attack ( $^{\circ}$ )				
		4	6	8	-4	-2	0	2	4
1	Wind barriers No vehicle	x	x	x	x		x		x
2	Wind barriers No vehicle		x		x	x	x	x	x
3	Wind barriers Vehicle model	x	x	x	x	x	x	x	x

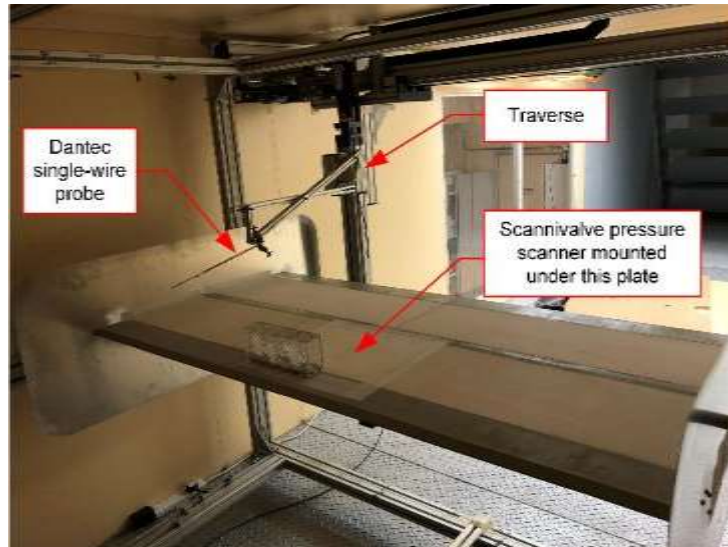


**Figure 2.14.** Wind tunnel sectional model without the wind barrier. The reference vehicle (a scaled double decker bus) is positioned at the centre of the hard shoulder



**Figure 2.15.** Wind tunnel sectional model with the wind barrier being attached along the windward edge of the cross section. The reference vehicle is positioned at the centre of the hard shoulder.

### 3 Flow field across an empty carriageway

In this section, the characteristics of the flow field behind the wind barrier across the empty section (i.e. for the case of an empty carriageway) will be described. At first, Section 3.1 will focus on analysing results where the wind speed is  $6 \text{ m s}^{-1}$  and the angle of attack is  $0^\circ$ . This will provide fundamental understandings on effects of the wind barrier on the time-averaged and unsteady components of the flow and how they develop across the section. Influence of varying the angle of attack and upstream wind speed on the flow will be discussed in Sections 3.2 and 3.3, respectively.

#### 3.1 Angle of attack $0^\circ$

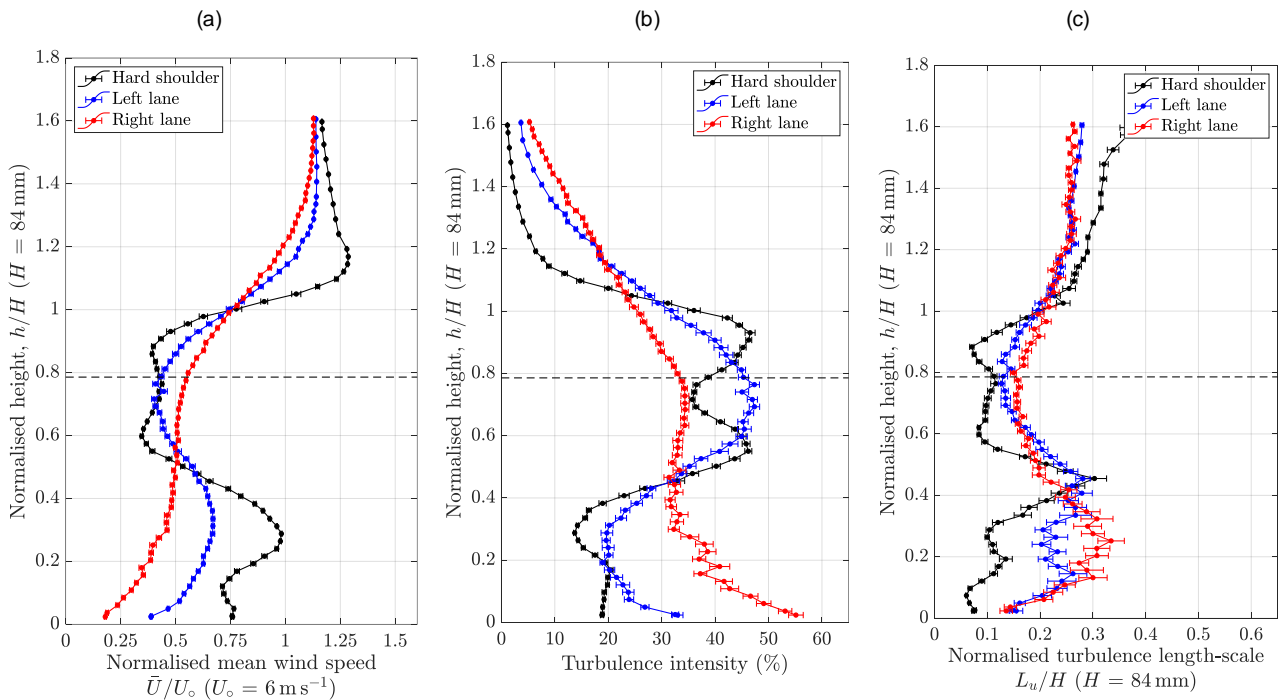


Figure 3.1 shows the variation of the profiles of the time-averaged wind speed, turbulence intensity and turbulence length scale across the section, at  $0^\circ$  angle of attack. The turbulence length scale and the height of the profiles are normalised by  $H = 84 \text{ mm}$ , which is the scaled height of a double-decker bus (i.e. the reference vehicle). The black dashed line indicates the normalised height of the wind barrier. The time-averaged wind speed is normalised by the upstream wind speed, i.e.  $6 \text{ m s}^{-1}$  in this case. Therefore, a negative normalised wind speed represents slowing down whereas a positive value represents speeding up, compared to the upstream wind.

As shown in

(a) (b) (c)

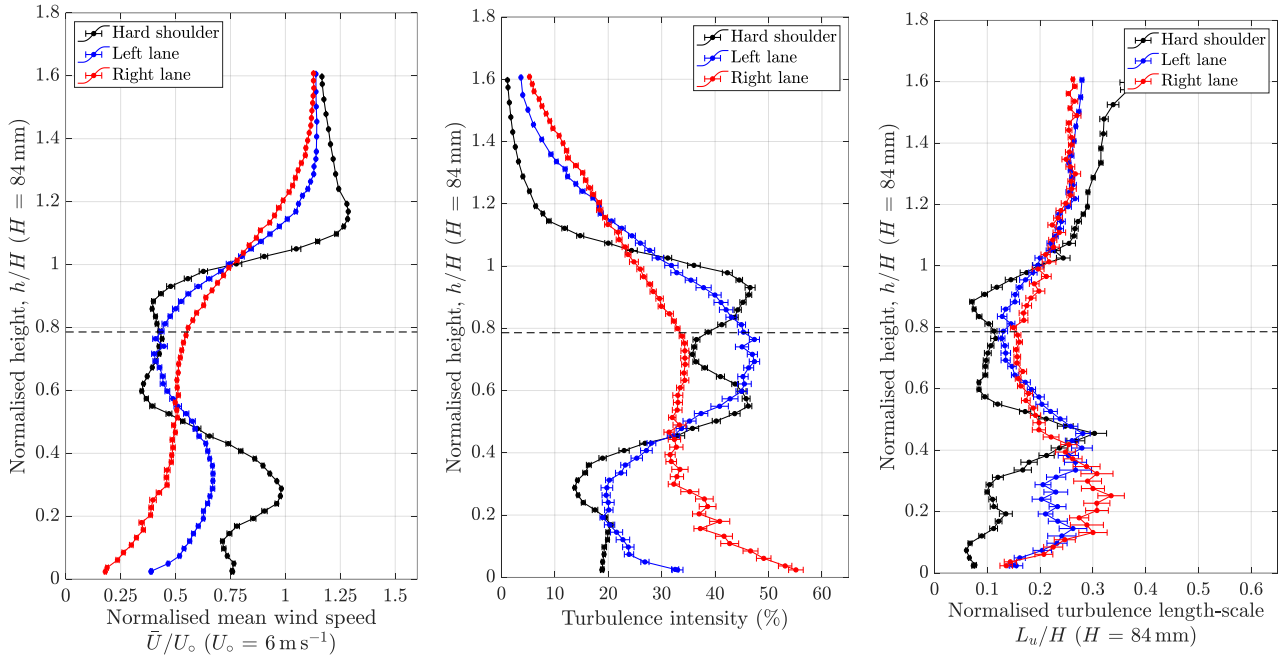


Figure 3.1a, from the normalised height of 0 to 0.5, the wind speed profile at the centre of the hard shoulder has a nose at the normalised height of 0.3 and with the value close to 1. The location of the nose is coincident with the large gap between the second and third louvres counting upwards (where the section UNP160 is located on the full-scale as-built barrier). This nose suggests fast-moving flow at the speed as high as the upstream wind, which is potentially caused by a high-speed jet as the flow accelerates through the gap. The fast-moving flow interacts with surrounding flow moving at slower speeds. This results in mixing flow phenomena which gives rise to the turbulence length scale at the normalised heights of 0.2 and 0.48 (

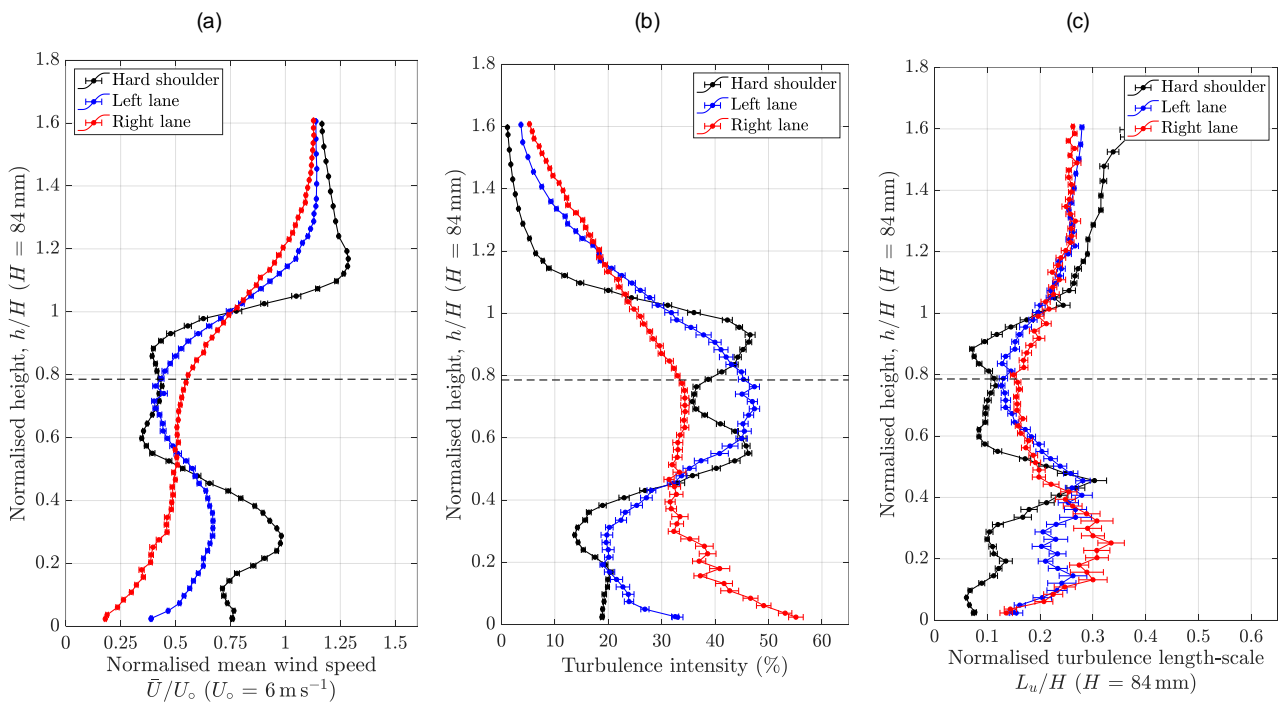


Figure 3.1c). The nose on the wind speed profile gradually dissipates across the section. At the centre of the left lane, the nose becomes much broader and the value drops to 0.65 approximately. The nose completely disappears on the

wind speed profile at the centre of the right lane. Accompanying with the reduction in the time-averaged wind speed is an increase in the turbulence intensity as shown in

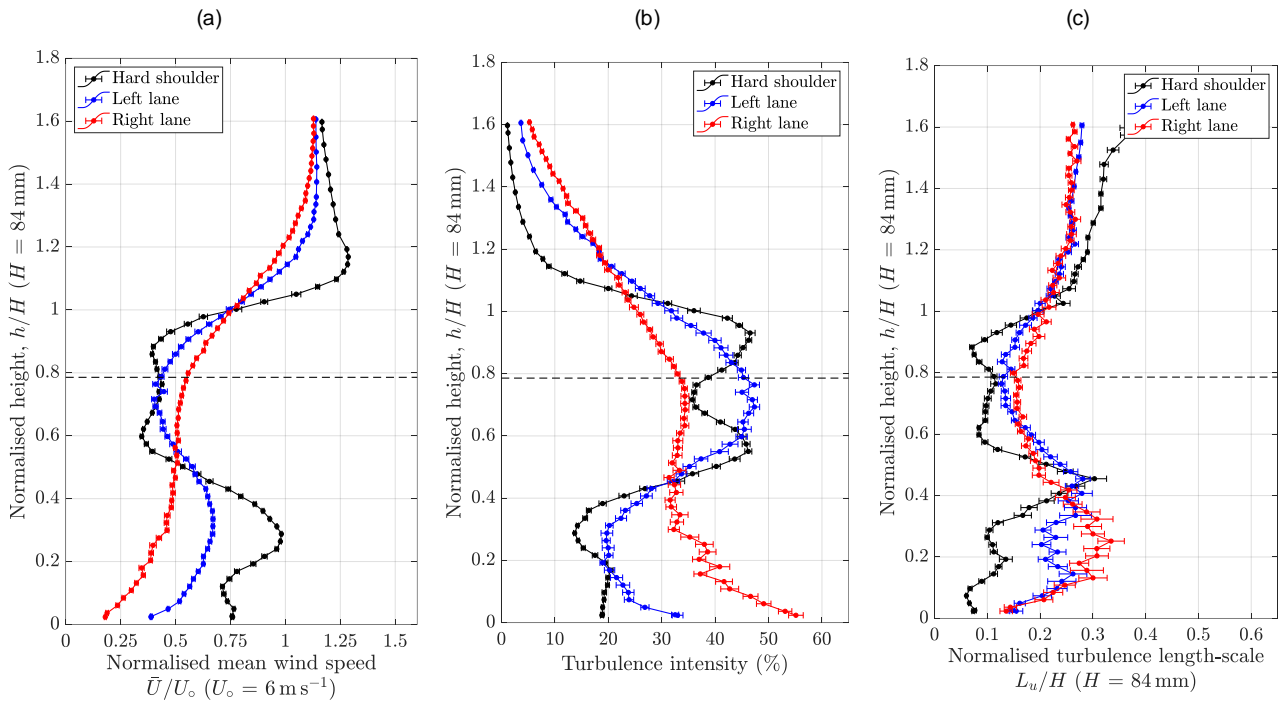


Figure 3.1b. Also,

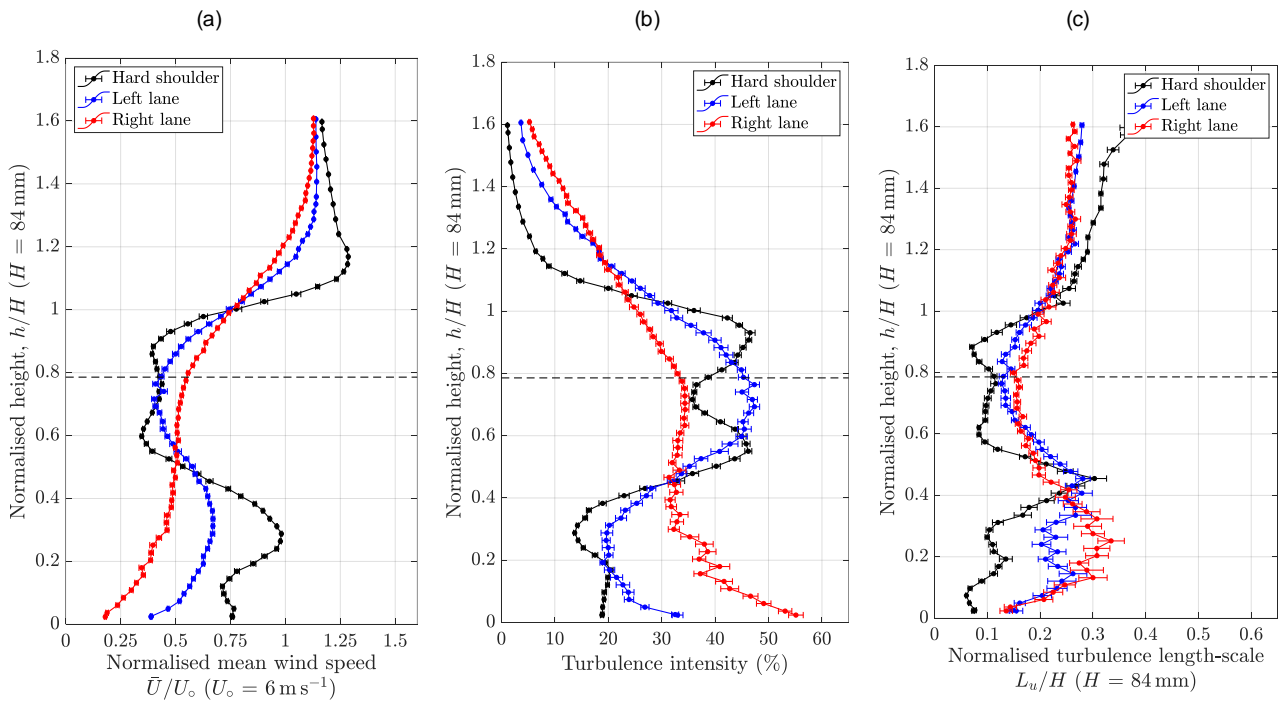


Figure 3.1c indicates there is an increase in the turbulence length scale, particularly from the hard shoulder to the left lane where the lower peak is seen to grow as large as the upper one. At the centre of the left lane, these two peaks disappear and replace by a single slight larger peak at the normalised height of about 0.25.

From the normalised height of 0.5 to 1, due to effects of the louvres on the upper part of the wind barrier, the wind speed profile at the hard shoulder shows significant slowing down. The normalised wind speed drops to about 0.4 and then

increases to about 0.65 at the centre of the right lane. The turbulence intensity exhibits significant variation within this region. The turbulence intensity profile at the centre of the hard shoulder shows the presence of two noses with the peak turbulence intensity of about 50%. At the centre of the left lane, the two noses are replaced by a single nose having the same peak turbulence intensity of 50% and at the normalise height of about 0.8. It is noted that the noses on the turbulence intensity profiles coincides with the troughs on the wind speed profiles. The turbulence intensity is found to drop to about 30% at the centre of the right lane. As for the turbulence length scale, at the centre of the hard shoulder, the normalised length scale slightly fluctuates around 0.1, and it slightly grows at the left and right lanes.

From the normalised height of 1 onwards, the flow field is dominated by the shear layer originated from the top louvre. Due to effects of the shear layer, the wind speed at the centre of the hard shoulder shows a nose having the normalised wind speed of about 1.3 and at the normalised height of 1.15. This nose is not visible at the centre of the left and right lanes. Also, the left and right lanes see an increase in the turbulence intensity and a reduction in the turbulence length scale. These indicate the broadening and lifting of the shear layer further away from the wind barrier.

In summary, at 0° angle of attack, the characteristic of the flow field is as follows:

- From the normalised height of 0 to 0.5, the flow field is driven by fast-moving flow as the flow accelerates through the big gap in the wind barrier. At the centre of the hard shoulder, this fast-moving flow is at a speed as high as the upstream wind and creates mixing phenomena creating the peaks observed in the turbulence length scale. Effects of the fast-moving flow are seen to reduce across the section and both of the turbulence intensity and length-scale increase.
- From the normalised height of 0.5 to 1, the flow field is greatly affected by the louvres on the upper part of the wind barrier. This results in a significant reduction in the wind speed, and large intensity and small scale of the turbulence. Across the section, dissipation is observed where the wind speed increases, accompanied with a reduction in the turbulence intensity and slightly growth in the turbulence length scale.
- From the normalised height of 1 onwards, the flow field is governed by the shear layer originated from the top louvre. The shear layer is found to broaden up and lift up across the section.

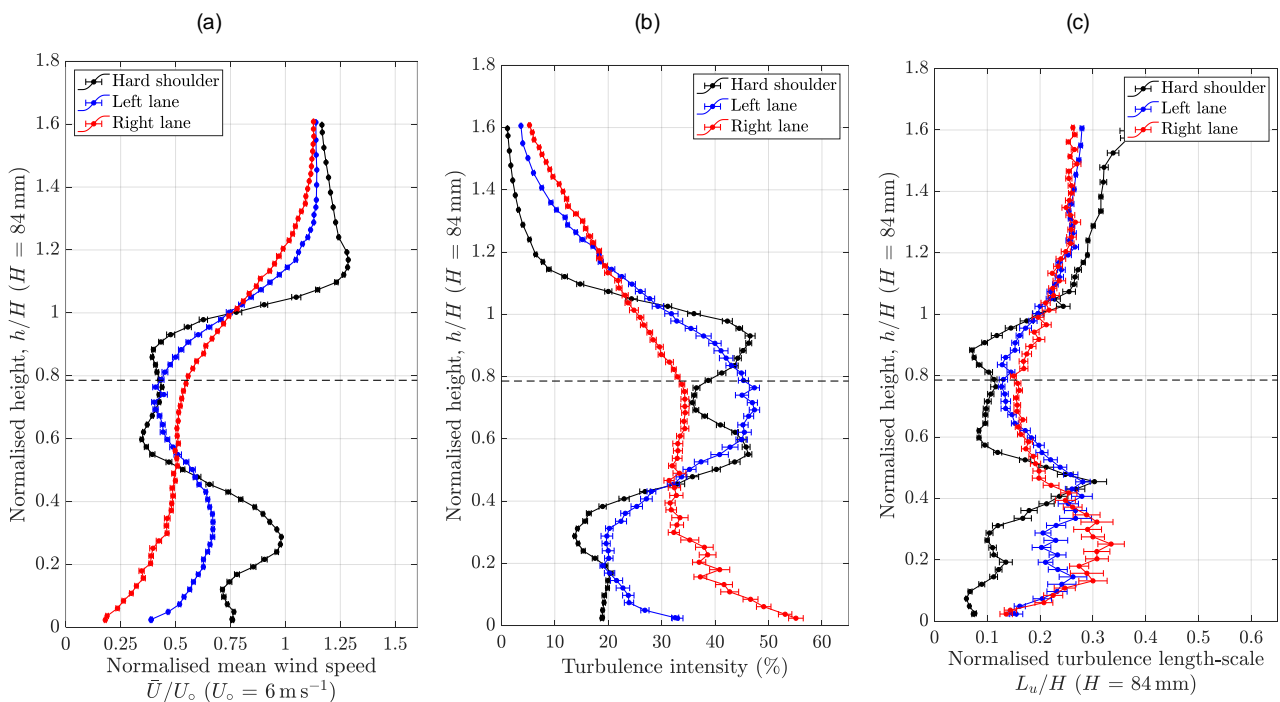


**Figure 3.1.** Variation of the profile of (a) the normalised time-averaged wind speed, (b) the turbulence intensity and (b) the normalised turbulence length scale across the carriageway, at  $0^\circ$  angle of attack and  $6 \text{ m s}^{-1}$  upstream wind speed. The black dashed line indicates the normalised height of the wind barrier.

In addition to the upstream wind speed of  $6 \text{ m s}^{-1}$ , the profiles of the wind speed, turbulence intensity and length scale were also measured at the wind speed values of 4 and  $8 \text{ m s}^{-1}$ . As shown in Figure 3.2, there is a very good agreement between the profiles of the time-averaged wind speed. For the unsteady component of the flow, Figure 3.3 and Figure 3.4 indicate a good agreement in the profile of the turbulence intensity and turbulence length scale, particularly at the centre of the hard shoulder. At the centre of the left and right lanes, the profiles measured at the wind speed of  $4 \text{ m s}^{-1}$  slightly deviate from those at the higher wind speeds. Also, it is noted that, the uncertainty associated with the estimate of turbulence intensity and turbulence length scale is higher, particularly at the centre of the left and right lanes.

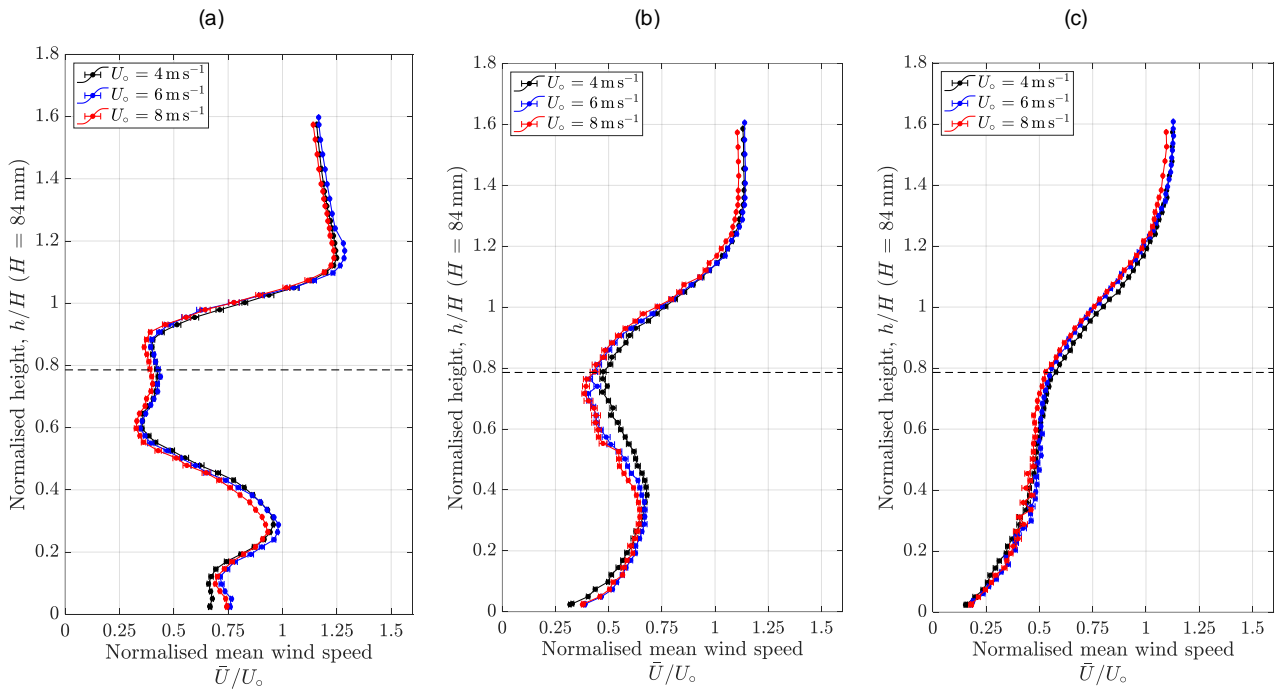


**Figure 3.2.** Profile of the normalised time-averaged wind speed magnitude at  $0^\circ$  angle of attack and different wind speeds, estimated at (a) centre of the hard shoulder, (b) centre of the left lane and (c) centre of the right lane. The black dashed line indicates the normalised height of the wind barrier.

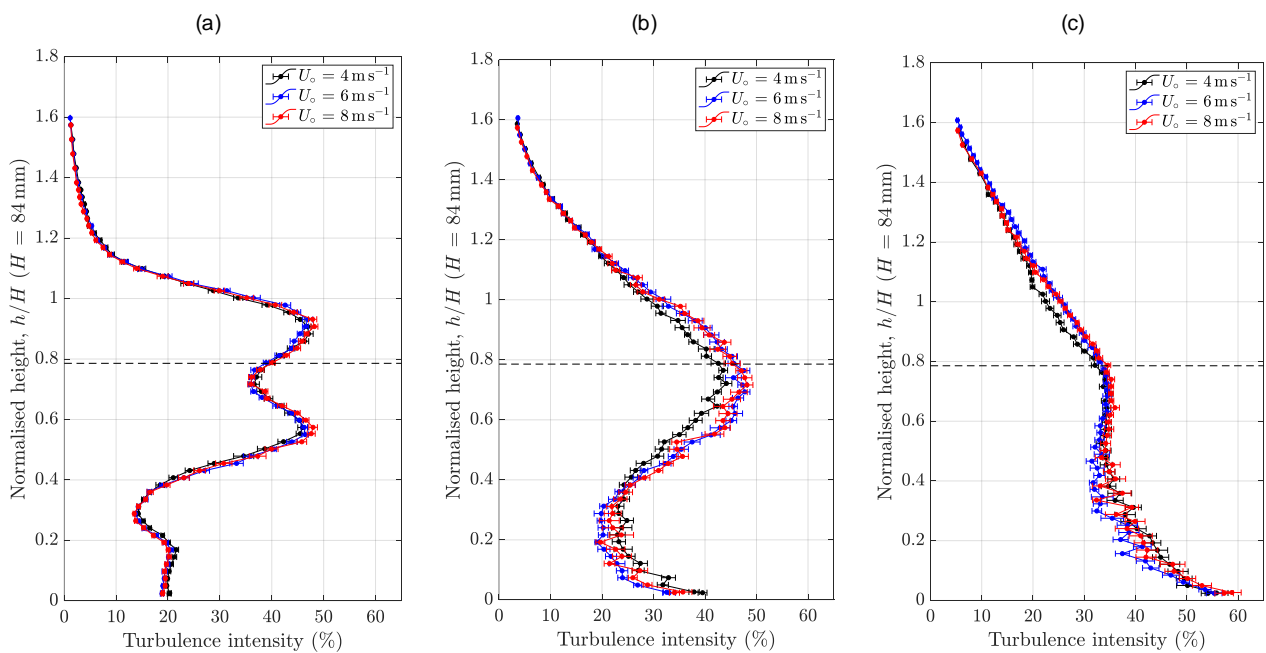


**Figure 3.3.** Profile of the turbulence intensity at  $0^\circ$  angle of attack and different wind speeds, estimated at (a) centre of the hard shoulder, (b) centre of the left lane and (c) centre of the right lane. The black dashed line indicates the normalised height of the wind barrier.

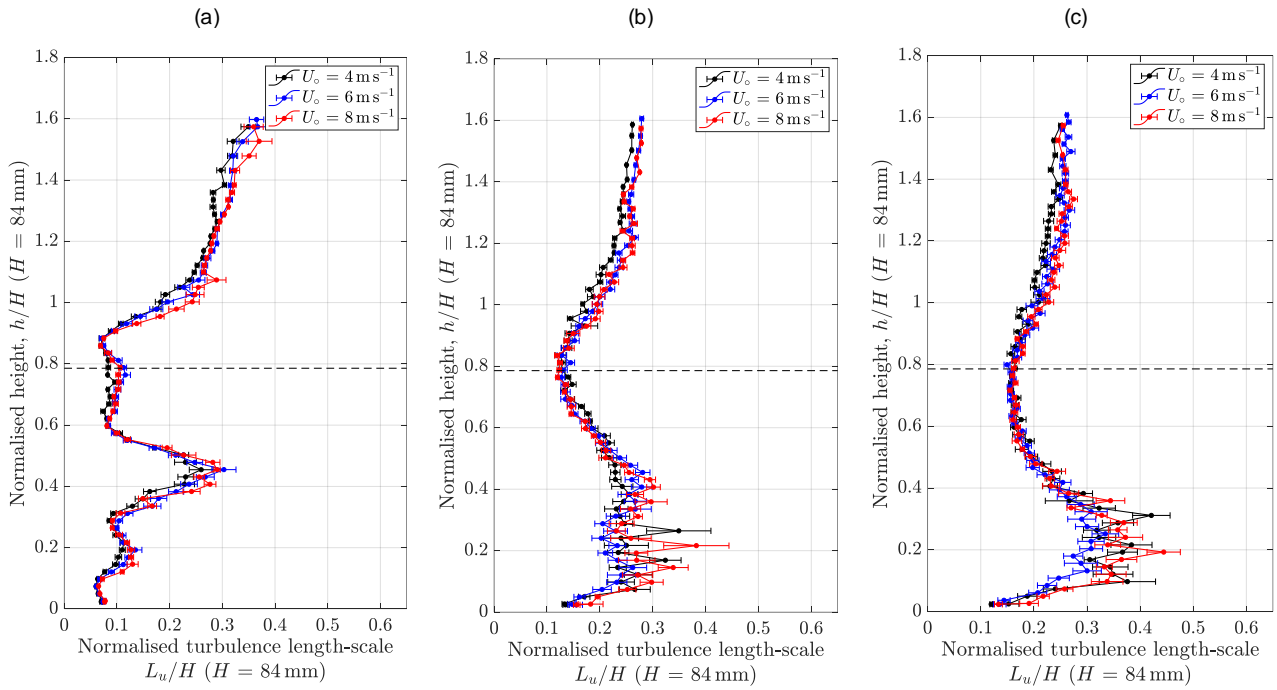


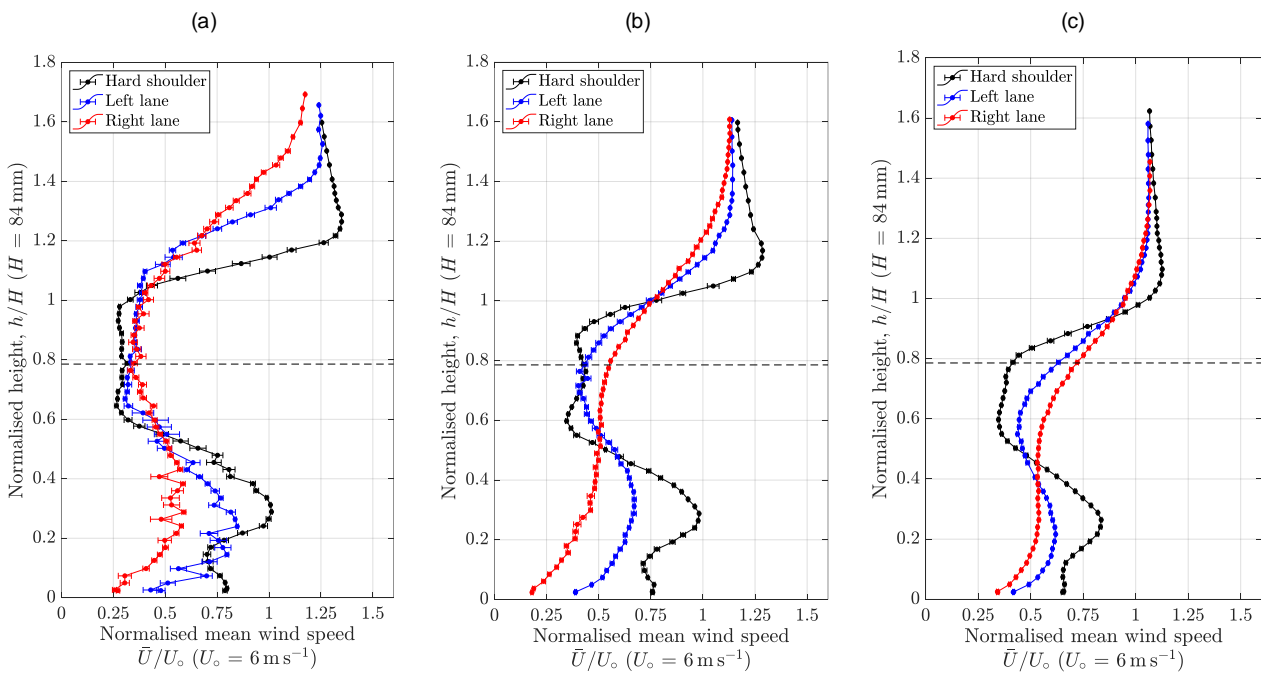
**Figure 3.4.** Profile of the normalised turbulence length scale at  $0^\circ$  angle of attack and different wind speeds, estimated at (a) centre of the hard shoulder, (b) centre of the left lane and (c) centre of the right lane. The black dashed line indicates the normalised height of the wind barrier.

### 3.2 Other angles of attack

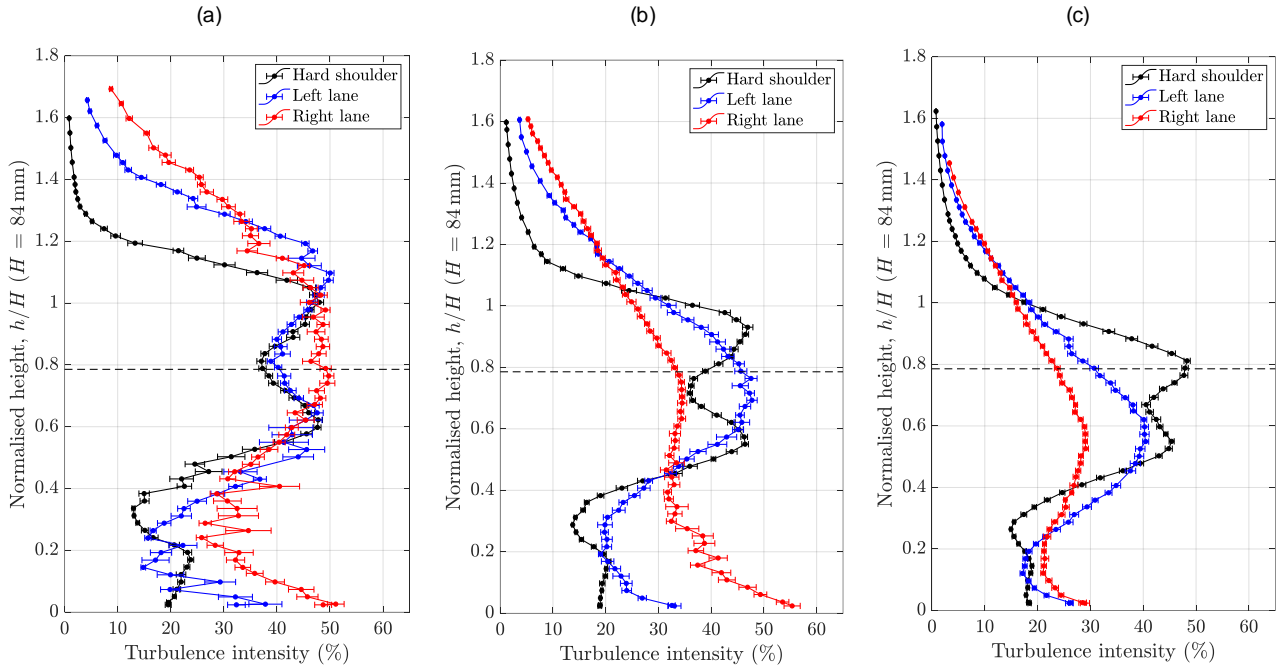
This section will discuss effects on varying the angle of attack on the flow field at the upstream wind speed of  $6 \text{ m s}^{-1}$ . In the following figures, sub-figures a and c show the profiles measured at the angles of attack  $4^\circ$  and  $-4^\circ$ , whereas the profiles at  $0^\circ$  angle of attack is shown in sub-figure b. The positive angle of attack indicates the wind coming from underneath the section, whereas the negative angle of attack indicates the wind coming from above.

Figure 3.5a, Figure 3.6a and Figure 3.7a show the variation of the profiles of the wind speed, turbulence intensity and turbulence length scale across the section at  $4^\circ$  angle of attack. As the wind comes from underneath the section, the profiles indicate, from the normalised of 0 to 1, there is a slower decay in the unsteady component of the flow, compared to that observed at  $0^\circ$  angle of attack. The wind speed profiles at the centre of the left and right lanes follow very well-defined bow shapes having larger peak values. The turbulence intensity profiles at the left and right lanes show the peaks at 50% and the length scale profiles show the presence of larger scales of turbulence across the section. From the normalised height of 1 onwards, the profiles indicate that the shear layer increases in strength and undergoes slow decay.

Figure 3.5c, Figure 3.6c and Figure 3.7c show the variation of the profiles of the wind speed, turbulence intensity and turbulence length scale across the section at  $-4^\circ$  angle of attack. The wind coming from above the section produces certain effects on the development of the flow field across the section. A significant effect can be seen on the shear layer where the nose on the wind speed profile at the centre of the hard shoulder becomes less pronounced having the value of 1.15 and occurring at a lower position of 1.05. Below the wind barrier height, the centre of the hard shoulder sees smaller wind speeds compared to  $0^\circ$  angle of attack while the wind speed at the centre of the right lane slightly increases. The peak turbulence intensity at the centre of the hard shoulder is about 50% and occurs at the normalised height of 0.8, which is lower than at  $0^\circ$  angle of attack. The peak turbulence intensity drops to 40% at the centre of the left lane and to 30% at the centre of the right lane. The location of these peaks is also lower compared to  $0^\circ$  angle of attack. The peak turbulence length scale at the hard shoulder and left lane are found smaller whereas the variation in the length scale at the left lane is very small.



**Figure 3.5.** Variation of the profile of the normalised time-averaged wind speed magnitude across the carriageway, at the wind speed of  $6 \text{ m s}^{-1}$  and at the angle of attack: (a)  $4^\circ$ , (b)  $0^\circ$  and (c)  $-4^\circ$ . The dashed line indicates the normalised height of the wind barrier.



**Figure 3.6.** Variation of the profile of the turbulence intensity across the carriageway, at the wind speed of  $6 \text{ ms}^{-1}$  and the angle of attack: (a)  $4^\circ$ , (b)  $0^\circ$  and (c)  $-4^\circ$ . The dashed line indicates the normalised height of the wind barrier.

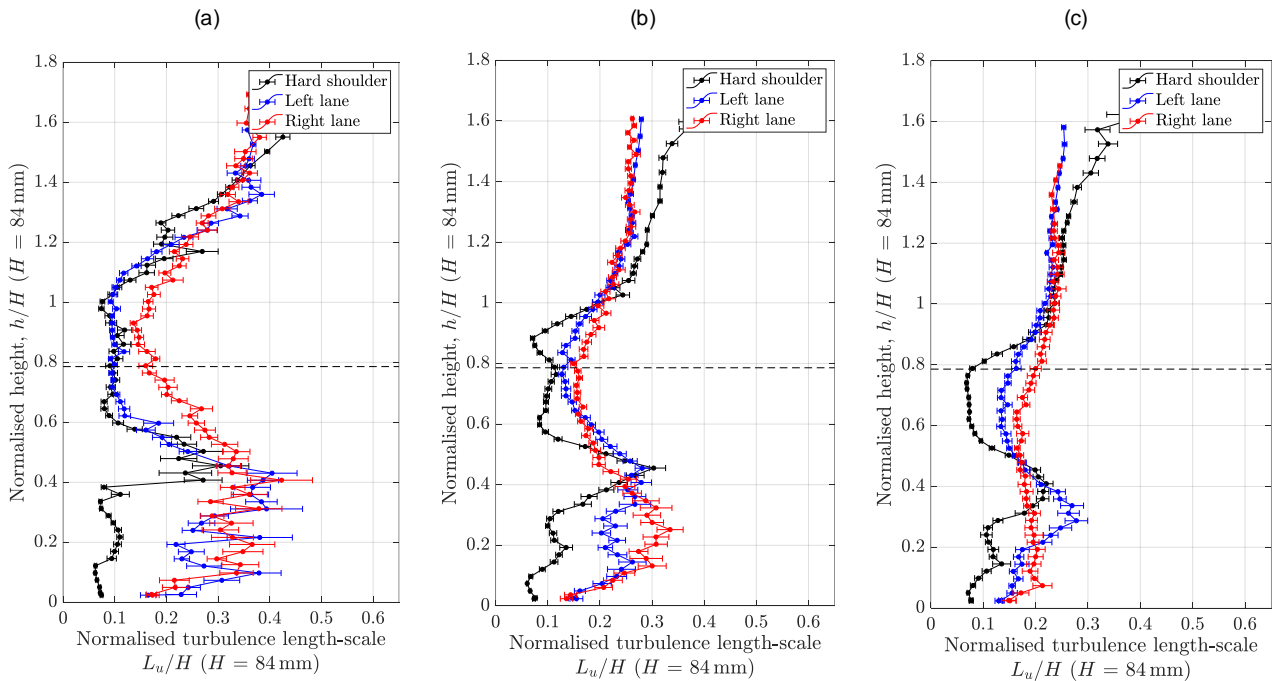


**Figure 3.7.** Variation of the profile of the normalised turbulence length scale across the carriageway, at the wind speed of  $6 \text{ ms}^{-1}$  and the angle of attack: (a)  $4^\circ$ , (b)  $0^\circ$  and (c)  $-4^\circ$ . The dashed line indicates the normalised height of the wind barrier.

In Figure 3.8, Figure 3.9 and Figure 3.10, the above comparison is extended including the angle of attack  $2^\circ$  and  $-2^\circ$ . As can be seen in sub-figures a, at the centre of the hard shoulder, there is a well-defined systematic change in the profiles when the angle of attack increases from  $-4^\circ$  to  $4^\circ$ . This includes a stronger effect of the fast-moving flow through the large gap on the wind barrier and an increase in the strength of the shear layer. A systematic change can also be seen at the centre of the left and right lanes, except at the angle of  $4^\circ$ . An analysis of time histories indicated that, at  $4^\circ$  angle of attack, the flow at the left and right lanes exhibits very different characteristics as that measured at the hard shoulder or other angles of attack. The analysis shows evidence of switching flow regimes, particular below the wind barrier height; however the cause of the phenomenon has not yet been concluded.

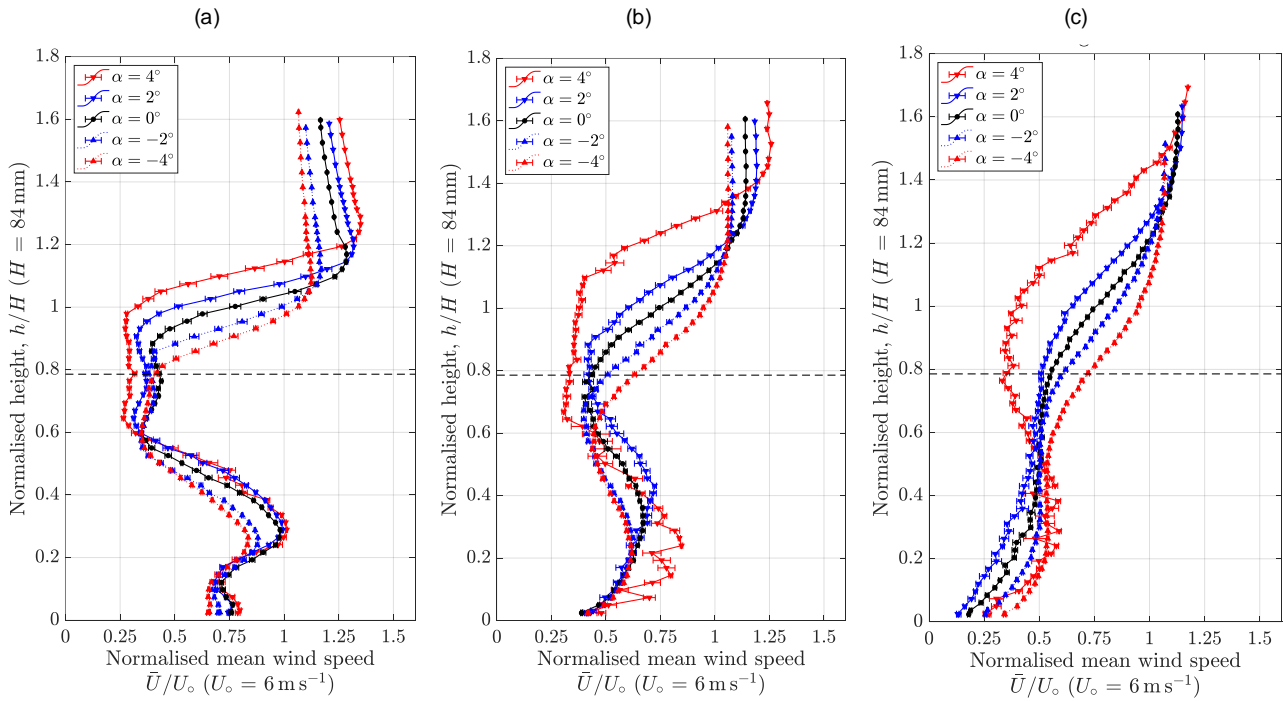


**Figure 3.8.** Profiles of the normalised time-averaged wind speed magnitude at the centre of (a) the hard shoulder, (b) left lane and (c) right lane, at the wind speed of  $6 \text{ m s}^{-1}$  and at different angles of attack. The dashed line indicates the normalised height of the wind barrier.

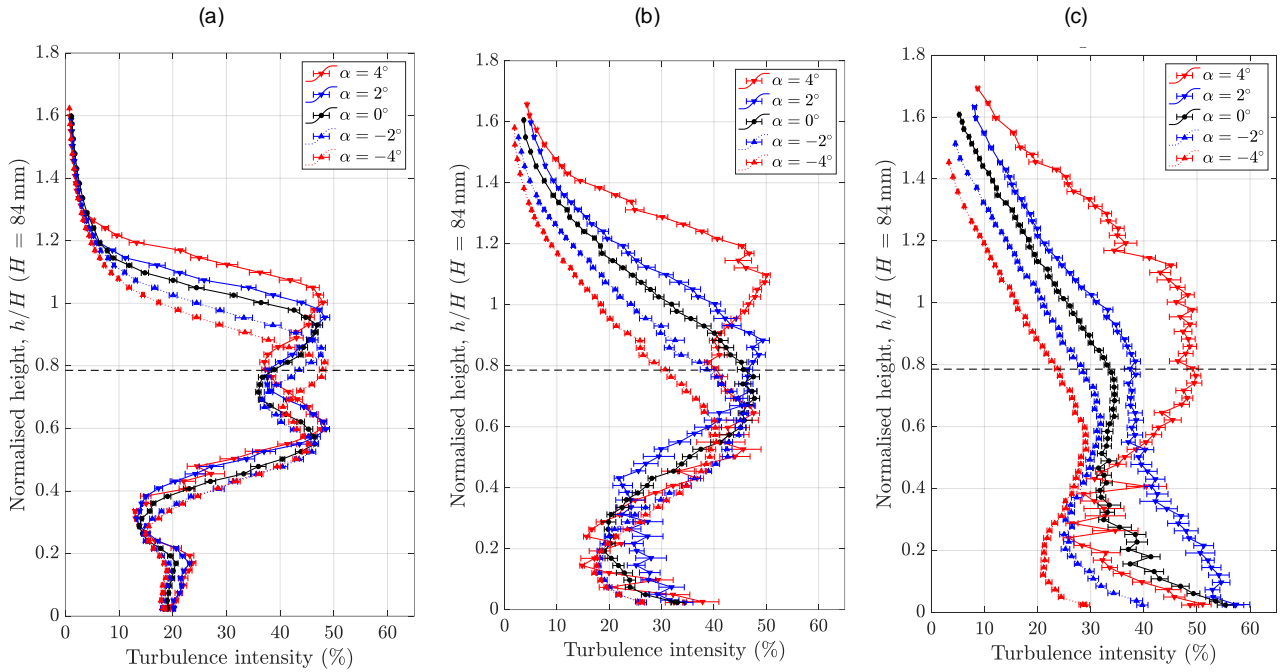


**Figure 3.9.** Profiles of the turbulence intensity at the centre of (a) the hard shoulder, (b) left lane and (c) right lane, at the wind speed of  $6 \text{ m s}^{-1}$  and at different angles of attack. The dashed line indicates the normalised height of the wind barrier.

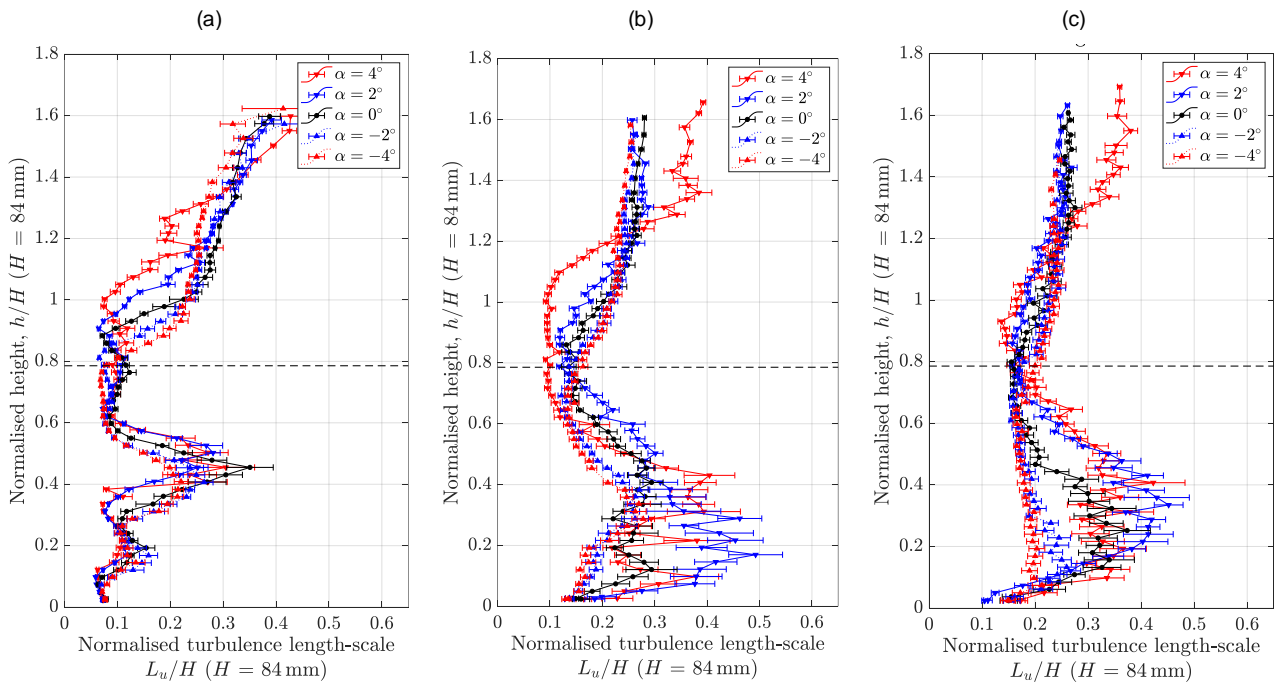


**Figure 3.10.** Profiles of the normalised turbulence length scale at the centre of (a) the hard shoulder, (b) left lane and (c) right lane, at the wind speed of  $6 \text{ m s}^{-1}$  and different angles of attack. The dashed line indicates the normalised height of the wind barrier.

### 3.3 Wind speed dependence

As discussed in Section 3.1, the flow field at  $0^\circ$  angle of attack is found independent of the upstream wind speed. As shown in Figure 3.11, Figure 3.12 and Figure 3.13, for  $4^\circ$  angle of attack, the profiles at the hard shoulder are also found independence of the upstream wind speed. However, at the centre of the left lane and right lane, the profiles at the wind speed of  $4 \text{ m s}^{-1}$  deviate significantly from those measured at higher wind speeds. This is evident particularly by looking at the profile of the wind speed and turbulence intensity. As shown Figure 3.14, Figure 3.15 and Figure 3.16, for  $-4^\circ$  angle of attack, there are good agreements between the profiles measured at different upstream wind speeds.

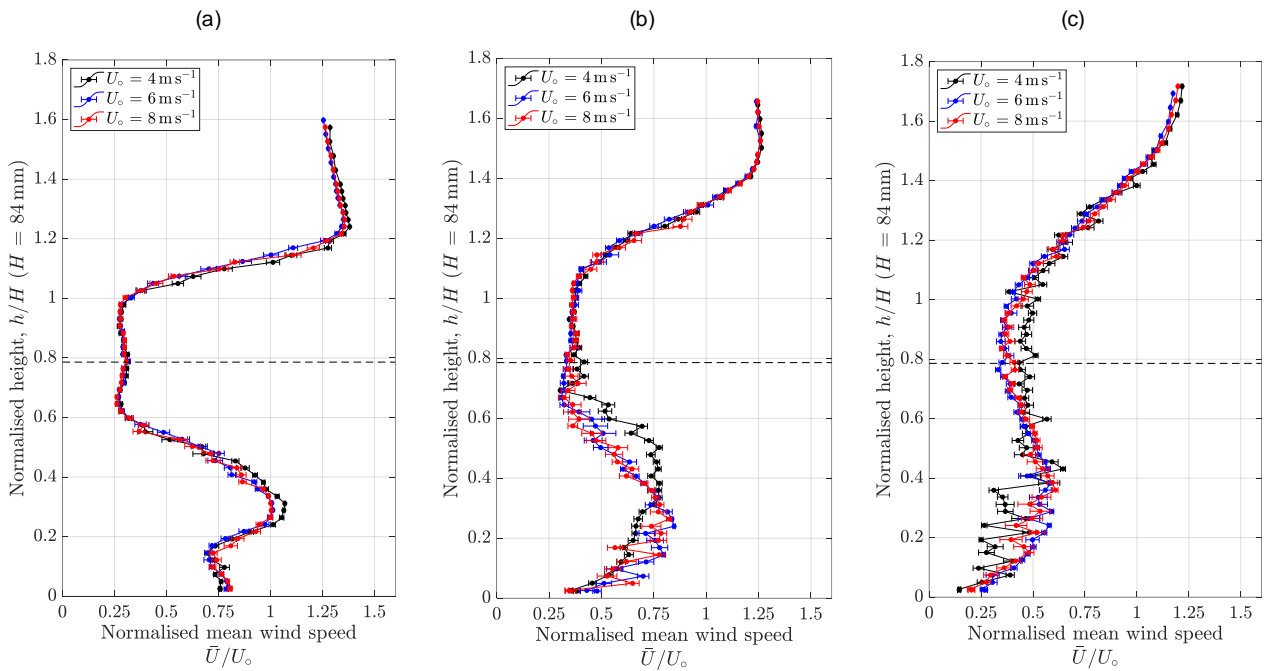


**Figure 3.11.** Profile of the normalised time-averaged wind speed magnitude at  $4^\circ$  angle of attack and different wind speeds, estimated at the centre of (a) the hard shoulder, (b) left lane and (c) right lane. The black dashed line indicates the normalised height of the wind barrier.

(a)

(b)

(c)

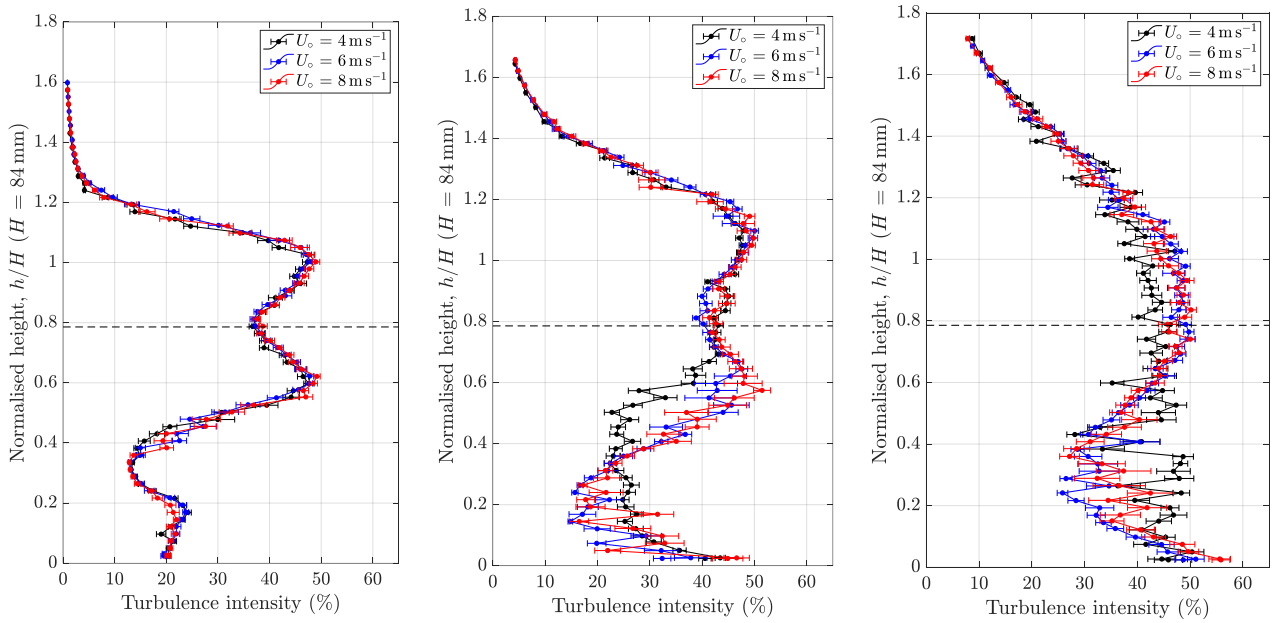


**Figure 3.12.** Profile of the turbulence intensity at  $4^\circ$  angle of attack and different wind speeds, estimated at the centre of (a) the hard shoulder, (b) left lane and (c) right lane. The black dashed line indicates the normalised height of the wind barrier.

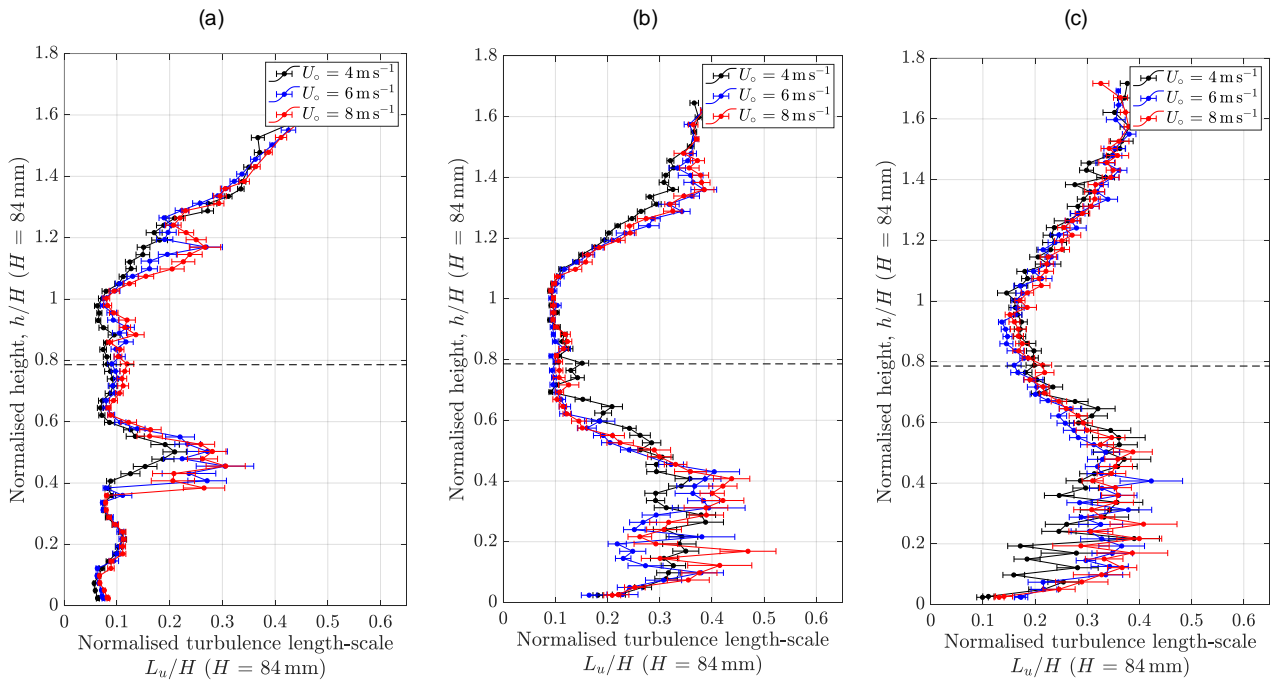


**Figure 3.13.** Profile of the normalised turbulence length scale at  $4^\circ$  angle of attack and different wind speeds, estimated at the centre of (a) the hard shoulder, (b) left lane and (c) right lane. The black dashed line indicates the normalised height of the wind barrier.

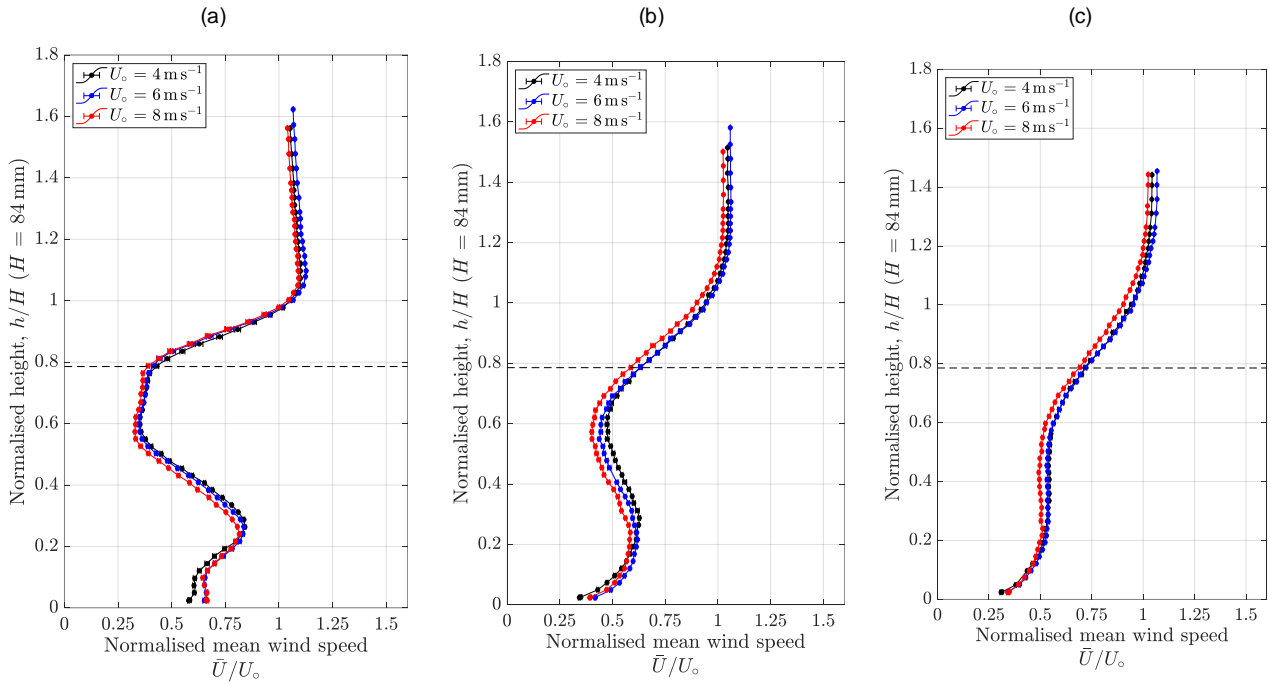


**Figure 3.14.** Profile of the normalised time-averaged wind speed magnitude at  $-4^\circ$  angle of attack and different wind speed values, estimated at the centre of (a) the hard shoulder, (b) centre of the left lane and (c) centre of the right lane. The black dashed line indicates the normalised height of the wind barrier.

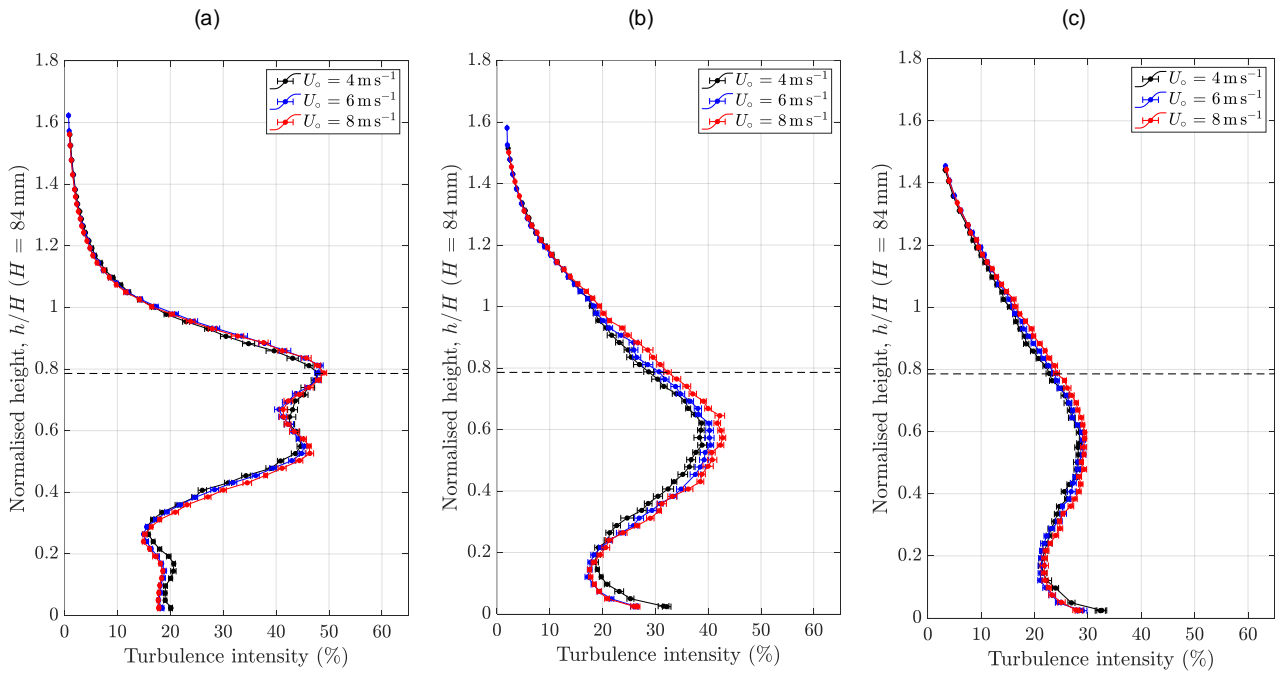


**Figure 3.15.** Profile of the turbulence intensity at  $-4^\circ$  angle of attack and different wind speed values, estimated at (a) centre of the hard shoulder, (b) centre of the left lane and (c) centre of the right lane. The black dashed line indicates the normalised height of the wind barrier.

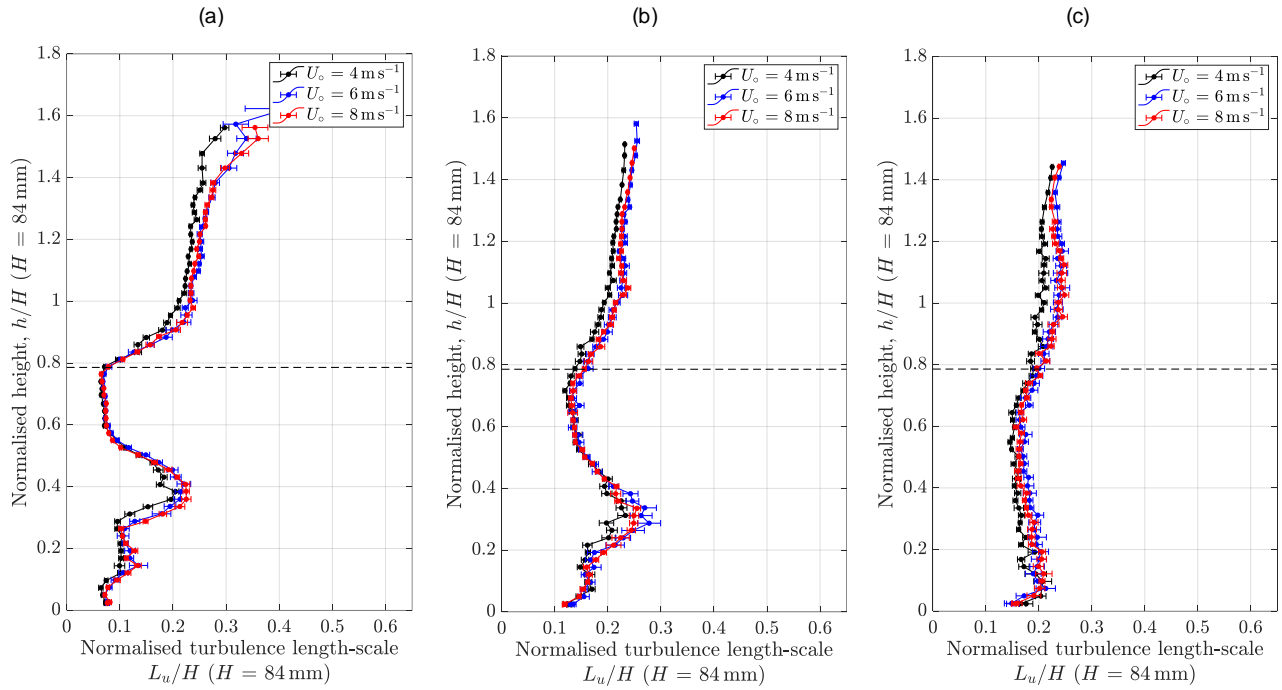


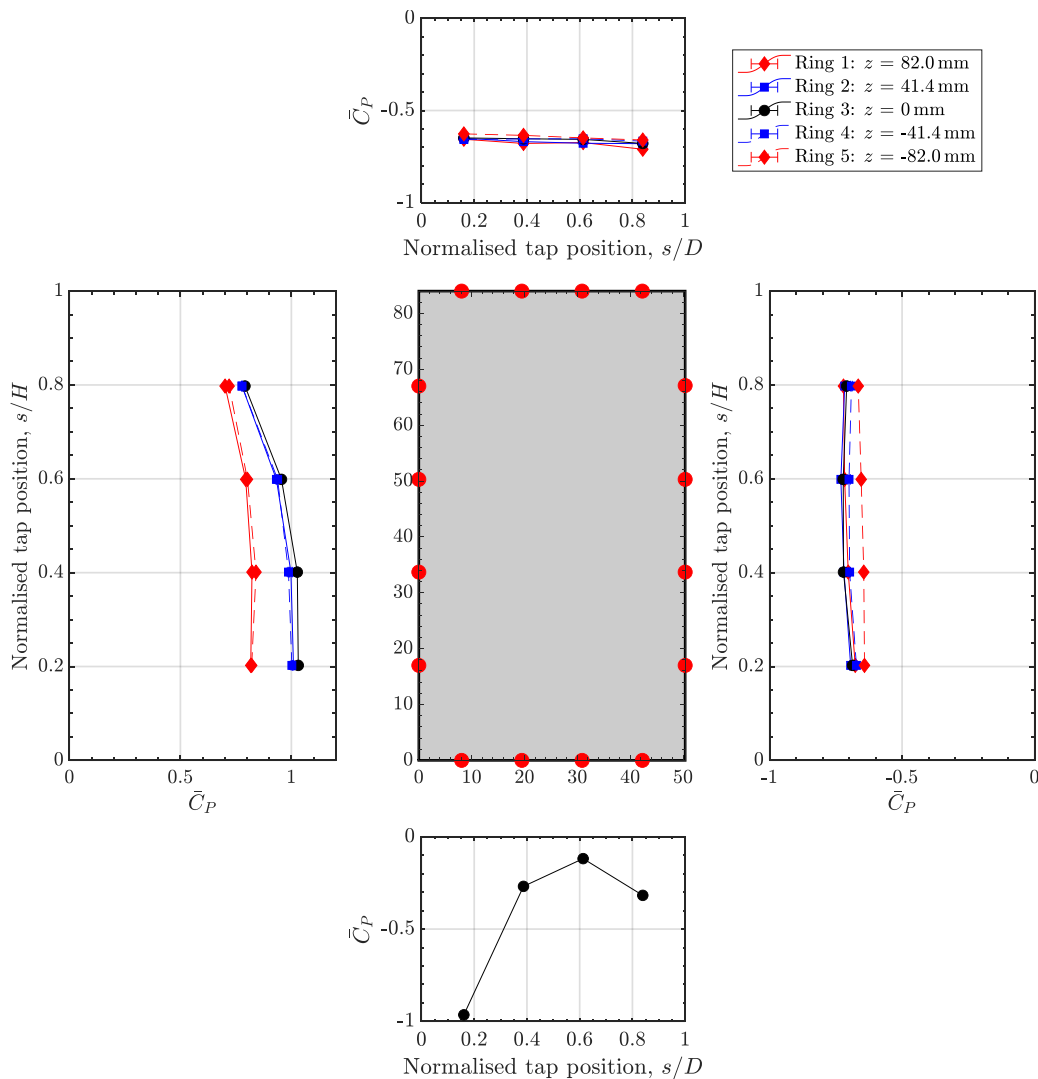
**Figure 3.16.** Profile of the normalised turbulence length scale at  $-4^\circ$  angle of attack and different wind speed values, estimated at the centre of (a) the hard shoulder, (b) left lane and (c) centre of the right lane. The black dashed line indicates the normalised height of the wind barrier.

## 4 Aerodynamics of the vehicle

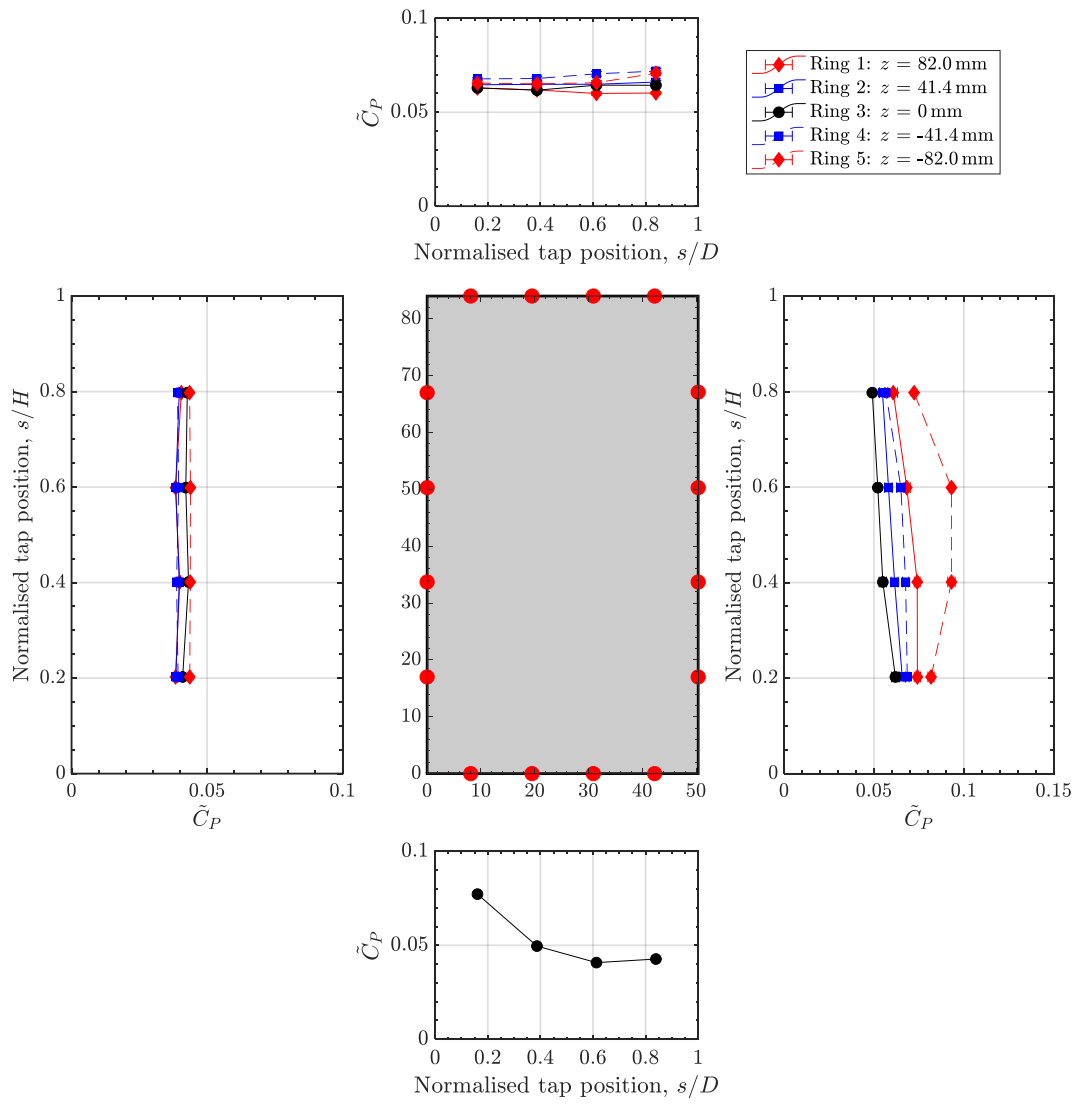
### 4.1 Without the wind barrier

Figure 4.1 and Figure 4.2 compare the distribution of the mean and root-mean-squared (RMS) pressure coefficient around the five pressure rings along the vehicle at the wind speed of  $6 \text{ m s}^{-1}$  and  $0^\circ$  angle of attack. Rings 1 and 5 are the closest to the front and back of the vehicle, respectively, while Ring 3 is the centre. On Figure 4.1 and Figure 4.2, the surface pressure distribution is plotted against the pressure tap positions which are normalised by the height  $H = 84 \text{ mm}$  or the width  $D = 50.4 \text{ mm}$  of the vehicle cross section. The dimensional position of the pressure taps around one ring is shown in the central subfigure in mm. On the bottom face, only surface pressure on the centre ring (Ring 3) was sampled.

Since Rings 1 and 5 are the closest to the front and back of the vehicle where the flow field is significantly different from the central section of the vehicle, a deviation on the pressure distribution can be seen on the outer (side) face (Figure 4.1), where the mean pressure coefficient along Rings 1 and 5 is lower than the rest. Also, on the inner (side face), surface pressure along Ring 5 shows slightly more suction and higher dynamic fluctuation than the others. The variation of the surface pressure distribution is found to be very minimal on the top surface.

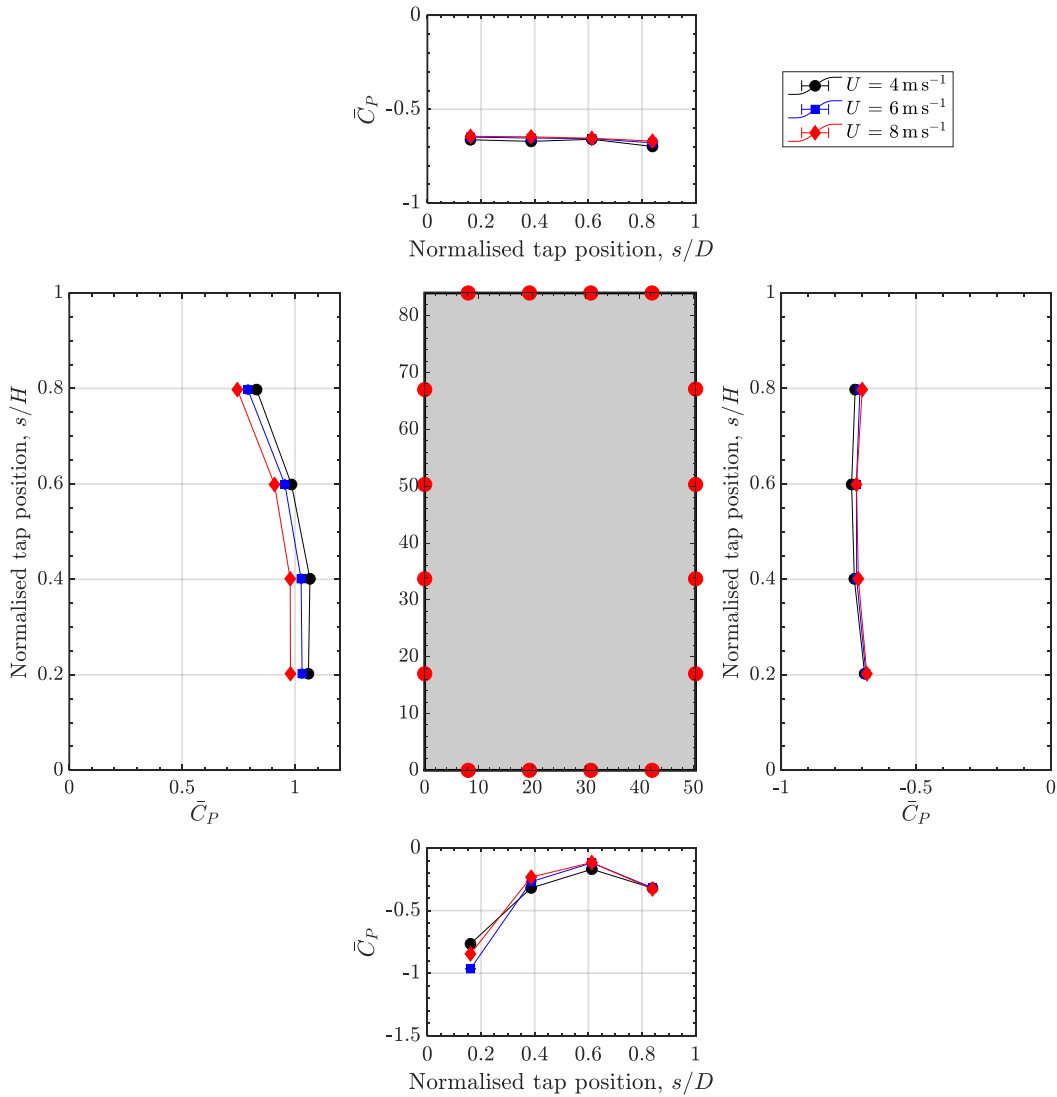


**Figure 4.1.** Distribution of the mean pressure coefficient around the five rings at the wind speed of  $6 \text{ m s}^{-1}$  and  $0^\circ$  angle of attack. Left (sub-figure) – outer (side) face; Right – inner (side) face; Top – top face; Bottom – bottom face.

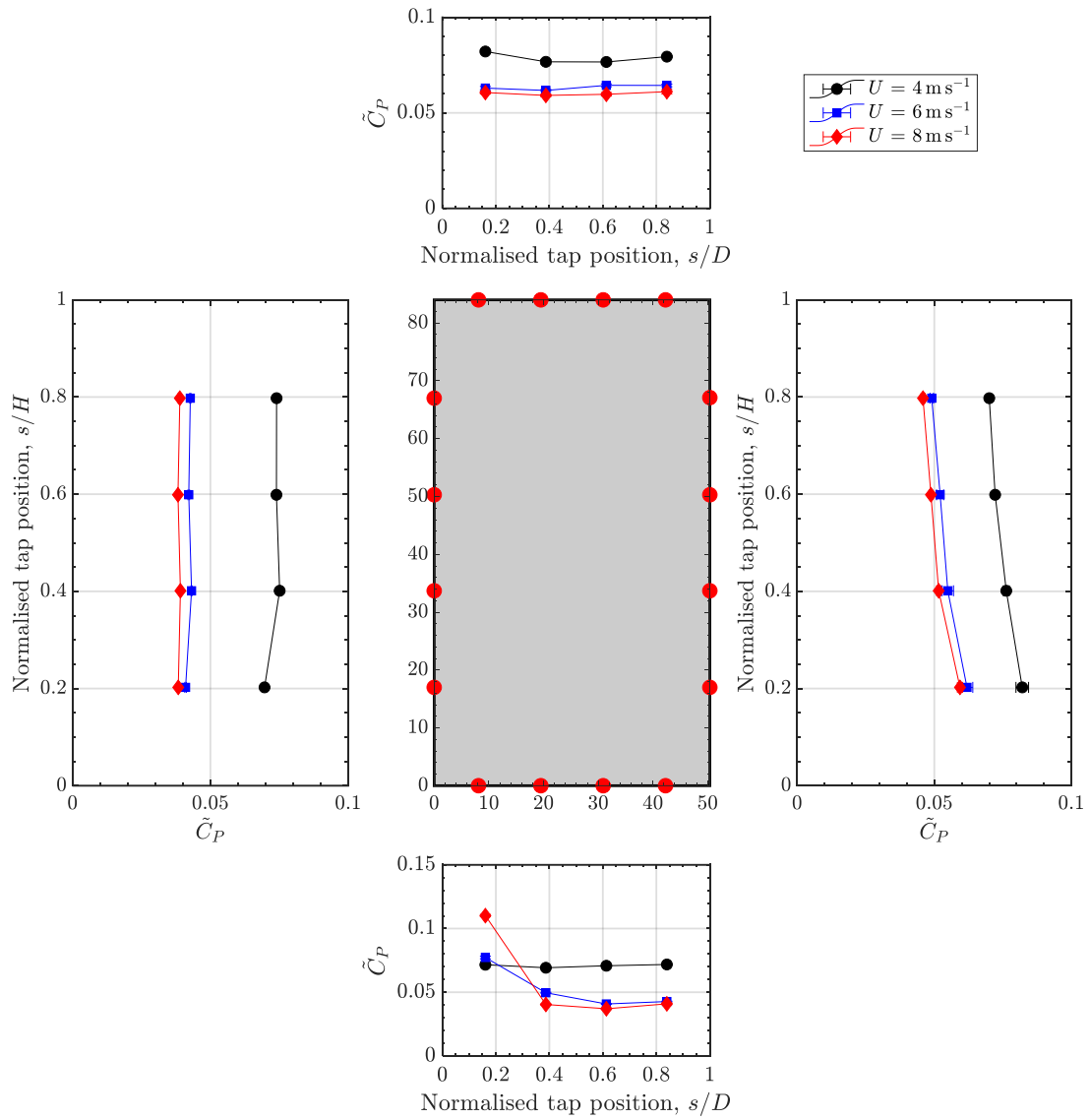


**Figure 4.2.** Distribution of the RMS pressure coefficient around the five rings at the wind speed of  $6 \text{ m s}^{-1}$  and  $0^\circ$  angle of attack. Left (sub-figure) – outer (side) face; Right – inner (side) face; Top – top face; Bottom – bottom face.

Focusing on the centre ring (Ring 3:  $z = 0\text{mm}$ ), Figure 4.3 and Figure 4.4 compare the distribution of the mean and RMS pressure coefficient around this ring at  $0^\circ$  angle of attack and the wind speed of 4, 6 and  $8\text{ m s}^{-1}$ . Effects on varying wind speeds on the mean pressure coefficient is found to very minimum (Figure 4.3), whereas the RMS pressure coefficient is found to be higher at the lower wind speed (Figure 4.4). The RMS pressure coefficients at the wind speeds of 6 and  $8\text{ m s}^{-1}$  agree well with each other, except for the bottom face, where more dynamic pressure fluctuation is found at the leading edge at a higher wind speed.



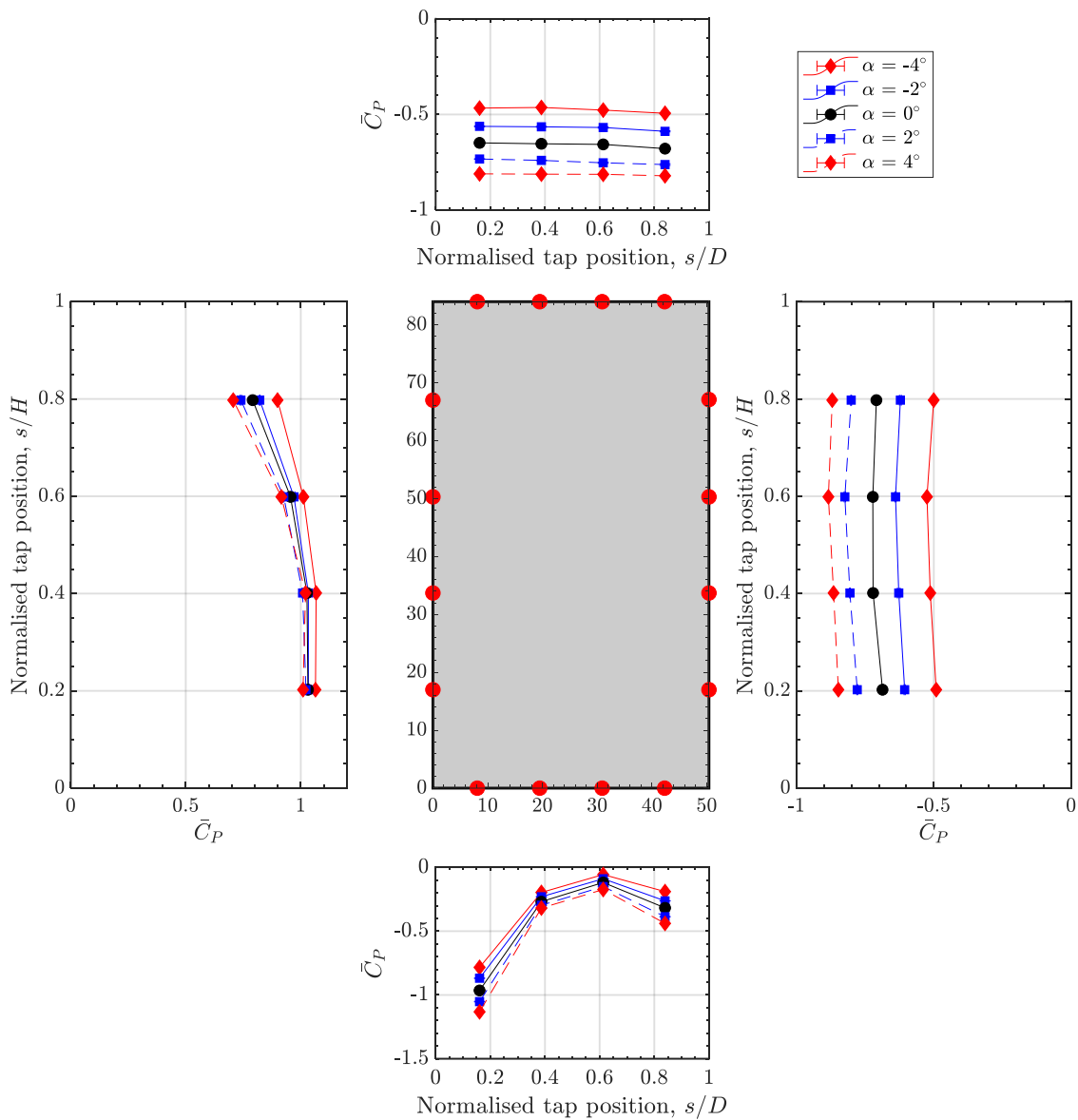
**Figure 4.3.** Distribution of the mean pressure coefficient around the centre ring (Ring 3:  $z = 0\text{mm}$ ) at the wind speed of  $6\text{ m s}^{-1}$  and  $0^\circ$  angle of attack. Left (sub-figure) – outer (side) face; Right – inner (side) face; Top – top face; Bottom – bottom face.



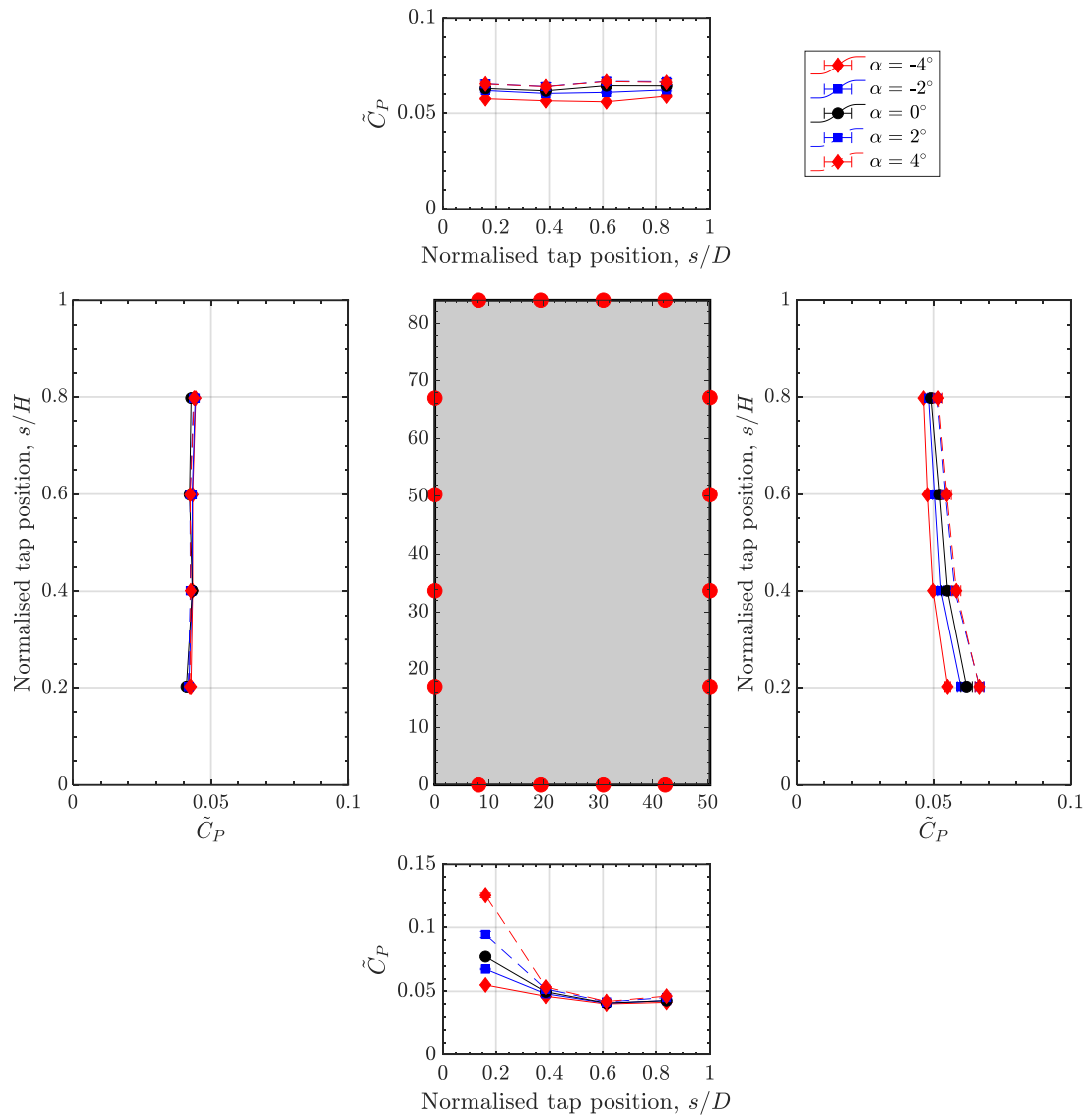
**Figure 4.4.** Distribution of the RMS pressure coefficient around the centre ring (Ring 3:  $z = 0\text{mm}$ ) at the wind speed of  $6\text{ m s}^{-1}$  and  $0^\circ$  angle of attack. Left (sub-figure) – outer (side) face; Right – inner (side) face; Top – top face; Bottom – bottom face.

Figure 4.5 and Figure 4.6 compare the distribution of the mean and RMS pressure distribution around the centre ring (Ring 3) at the wind speed of  $6 \text{ m s}^{-1}$  and five different angles of attack. On the outer (side) face, the variation of the mean pressure coefficient is found to be more significant near the top, where the flow coming above (i.e. negative angles of attack) produce higher positive pressure. The mean pressure coefficient on the top, inner (side) and bottom faces shows large dependence on the angle of attack. As the angle of attack becomes positive, there is an increase in the suction on these faces.

The dependence of the RMS pressure coefficient on the angle of attack is less pronounced. On the top and inner (side) face, when the angle of attack becomes positive, there is a slight increase in the dynamic pressure fluctuation. On the bottom face, an increase in the angle of attack leads to a significant increase in the pressure fluctuation near the leading edge.



**Figure 4.5.** Distribution of the mean pressure coefficient around the centre ring (Ring 3:  $z = 0\text{mm}$ ) at the wind speed of  $6 \text{ m s}^{-1}$  and five different angles of attack. Left (sub-figure) – outer (side) face; Right – inner (side) face; Top – top face; Bottom – bottom face.



**Figure 4.6.** Distribution of the RMS pressure coefficient around the centre ring (Ring 3:  $z = 0\text{mm}$ ) at the wind speed of  $6\text{ m s}^{-1}$  and five different angles of attack. Left (sub-figure) – outer (side) face; Right – inner (side) face; Top – top face; Bottom – bottom face.

From the surface pressure coefficient, the mean and RMS value of the vehicle aerodynamic coefficient (the drag, lift and moment coefficients) can be calculated. Their variability against the angle of attack and wind speeds are summarised in Figure 4.7. The dependence of the vehicle aerodynamic coefficient on the wind speed is small. Both the mean and RMS value of the aerodynamic coefficients get larger (in magnitude, for the case of rolling coefficients) as the angle of attack increases.

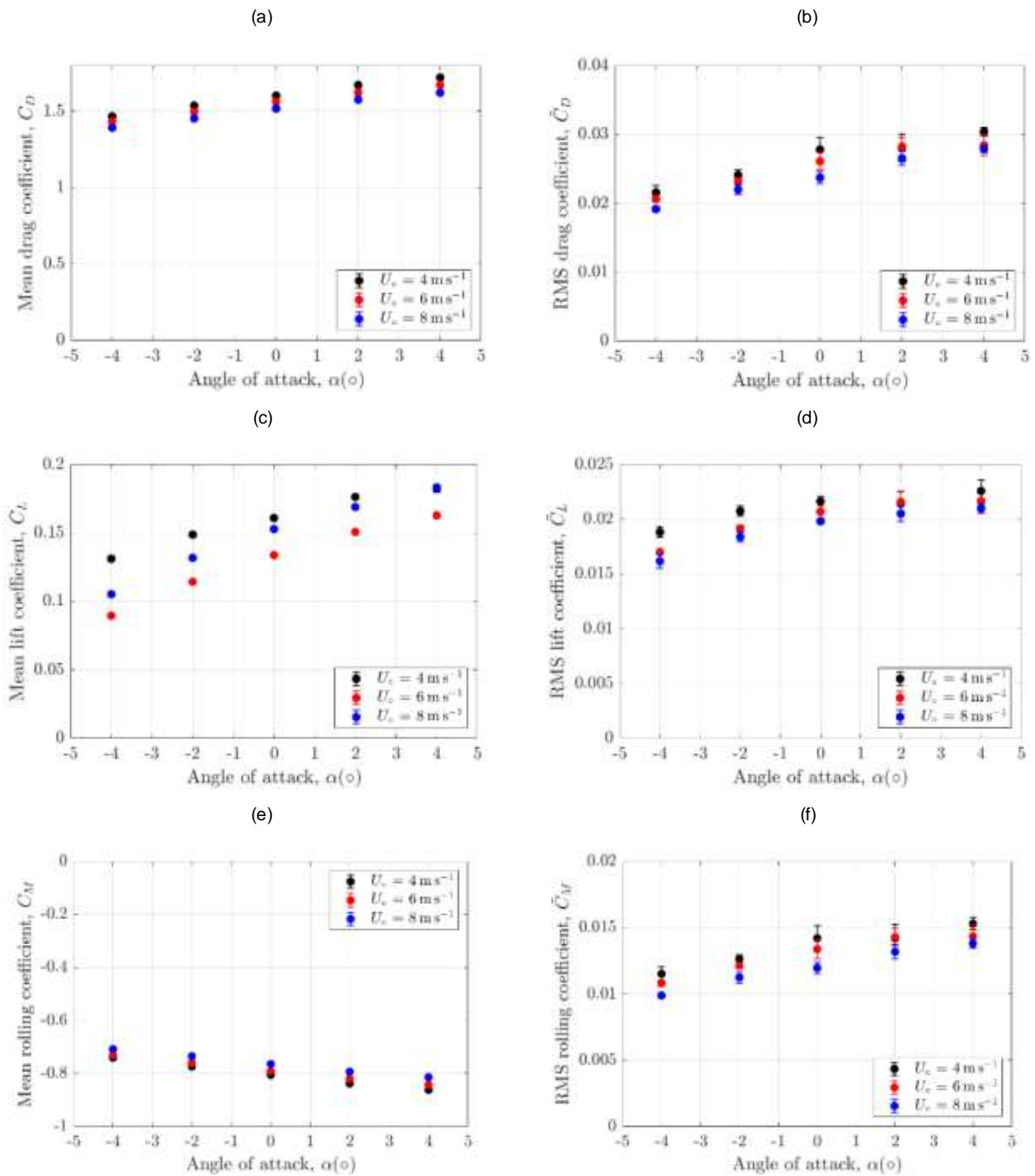


**Figure 4.7.** Variability of (a,b) the mean and RMS drag coefficient, (c,d) the mean and RMS of lift coefficient and (e,f) the rolling coefficient with respect to the angle of attack and wind speed.

## 4.2 With the wind barrier

Figure 4.8 and Figure 4.9 compares the distribution of the mean and RMS pressure coefficient at the wind speed of  $6 \text{ m s}^{-1}$  between different angles of attack, when the wind barrier is in place.

When being protected by the wind barrier, there is a significant reduction on the mean pressure coefficient on the outer (side) face whereas the RMS pressure coefficient increases. The mean pressure coefficient gets larger at the positive angle of attack while the RMS value get smaller. The inner (side) face sees a small decrease in the mean pressure coefficient and a slight increase in the RMS pressure coefficient.

The top face sees an increase in both suction and dynamic pressure fluctuation, particularly around the leading edge. There is also a significant change to the mean pressure coefficient on the bottom face. The deep suction near the leading edge (as seen in Figure 4.5) disappears and another deep suction occurs towards the trailing edge.

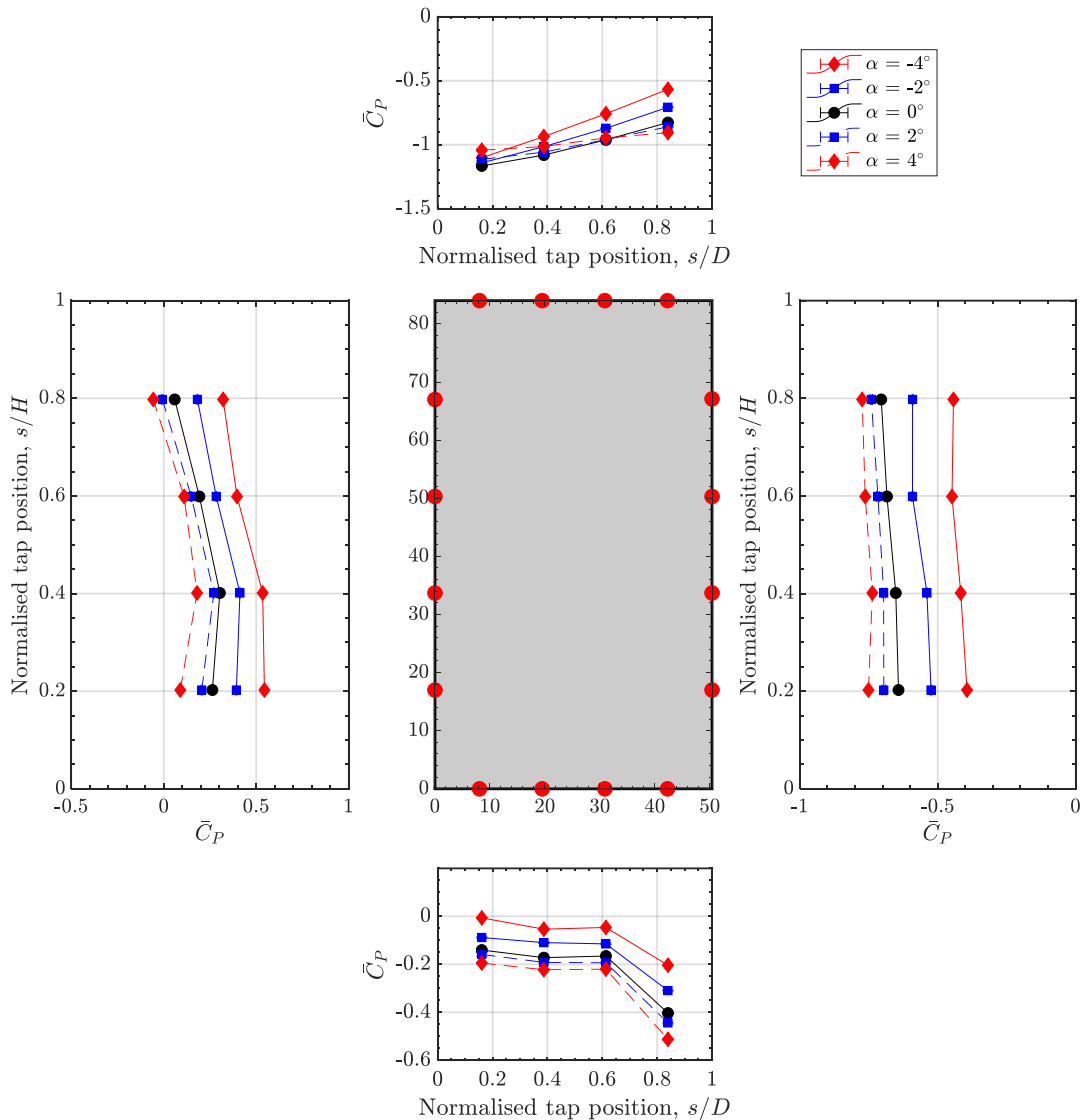


**Figure 4.8.** Distribution of the mean pressure coefficient around the centre ring (Ring 3:  $z = 0\text{mm}$ ) at the wind speed of  $6 \text{ m s}^{-1}$  and five different angles of attack. Left (sub-figure) – outer (side) face; Right – inner (side) face; Top – top face; Bottom – bottom face.

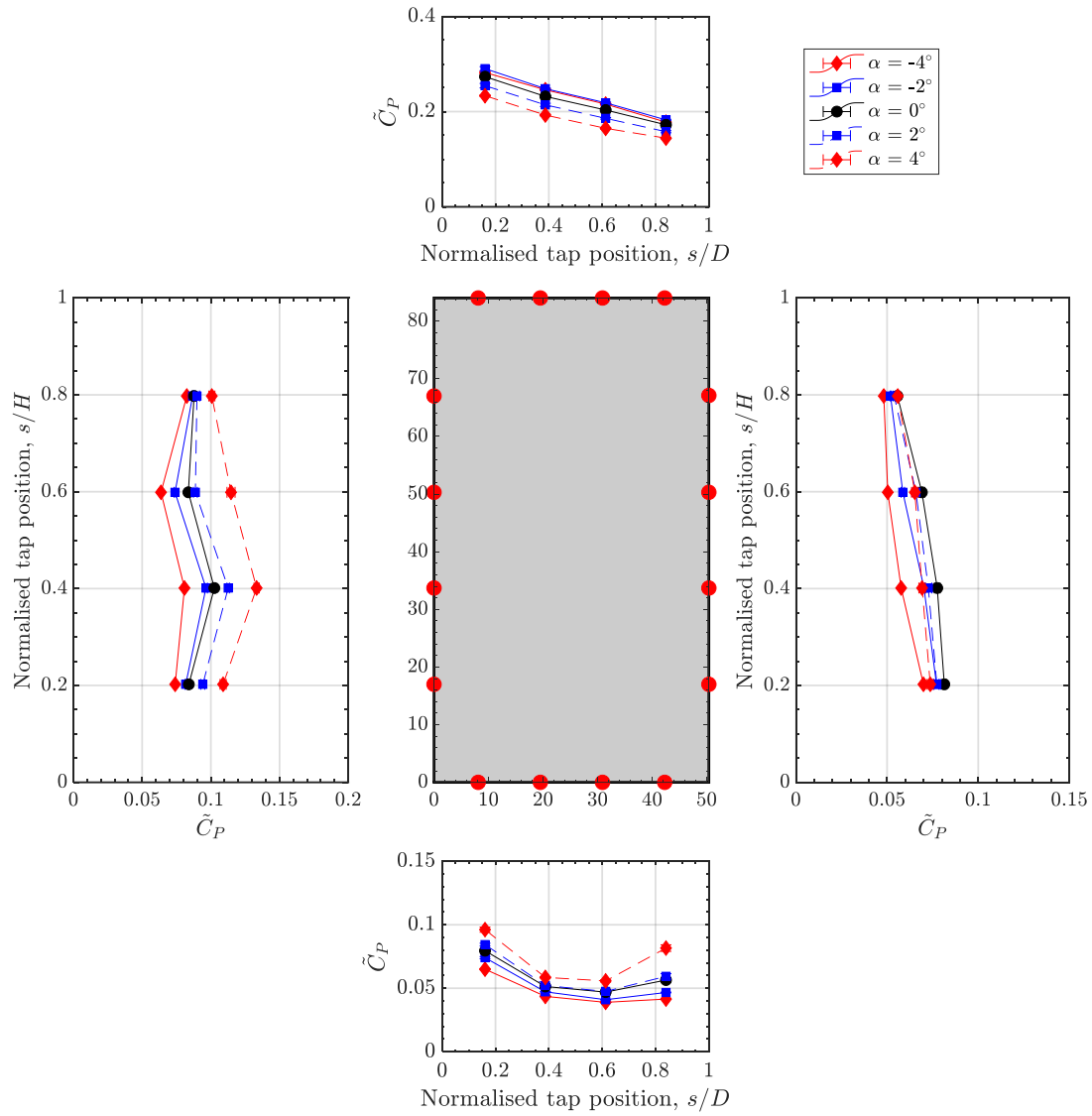


**Figure 4.9.** Distribution of the RMS pressure coefficient around the centre ring (Ring 3:  $z = 0\text{mm}$ ) at the wind speed of  $6\text{ m s}^{-1}$  and five different angles of attack. Left (sub-figure) – outer (side) face; Right – inner (side) face; Top – top face; Bottom – bottom face.

Figure 4.10 summarizes the variation of the mean and RMS of the vehicle aerodynamic coefficients with respect to the angle of attack and wind speeds when the vehicle is protected by the wind barrier.

As shown in Figure 4.10a, c and e, effects of the wind barrier lead to a decrease in the magnitude of the drag and rolling coefficient and an increase in the lift coefficient. As opposed to when the wind barrier is not in place that the mean aerodynamic coefficient increases as the angle of attack gets large, in this case, the mean drag, lift and moment coefficient remains reasonably constant from  $-4^\circ$  to  $0^\circ$  angle of attack. From  $0^\circ$  to  $4^\circ$ , the magnitude of the mean aerodynamic coefficient is found to decrease.

For the RMS aerodynamic coefficients, as shown in Figure 4.10b and f, the value of RMS drag and moment coefficient is very similar to when the wind barrier is not in place. On the other hand, the value of RMS lift coefficient is found to slightly increase. While the RMS drag coefficient increases as the angle of attack gets larger, the RMS lift and moment coefficient only increases between  $-4^\circ$  and  $0^\circ$  angle of attack and remain reasonably constant at positive angles of attack.

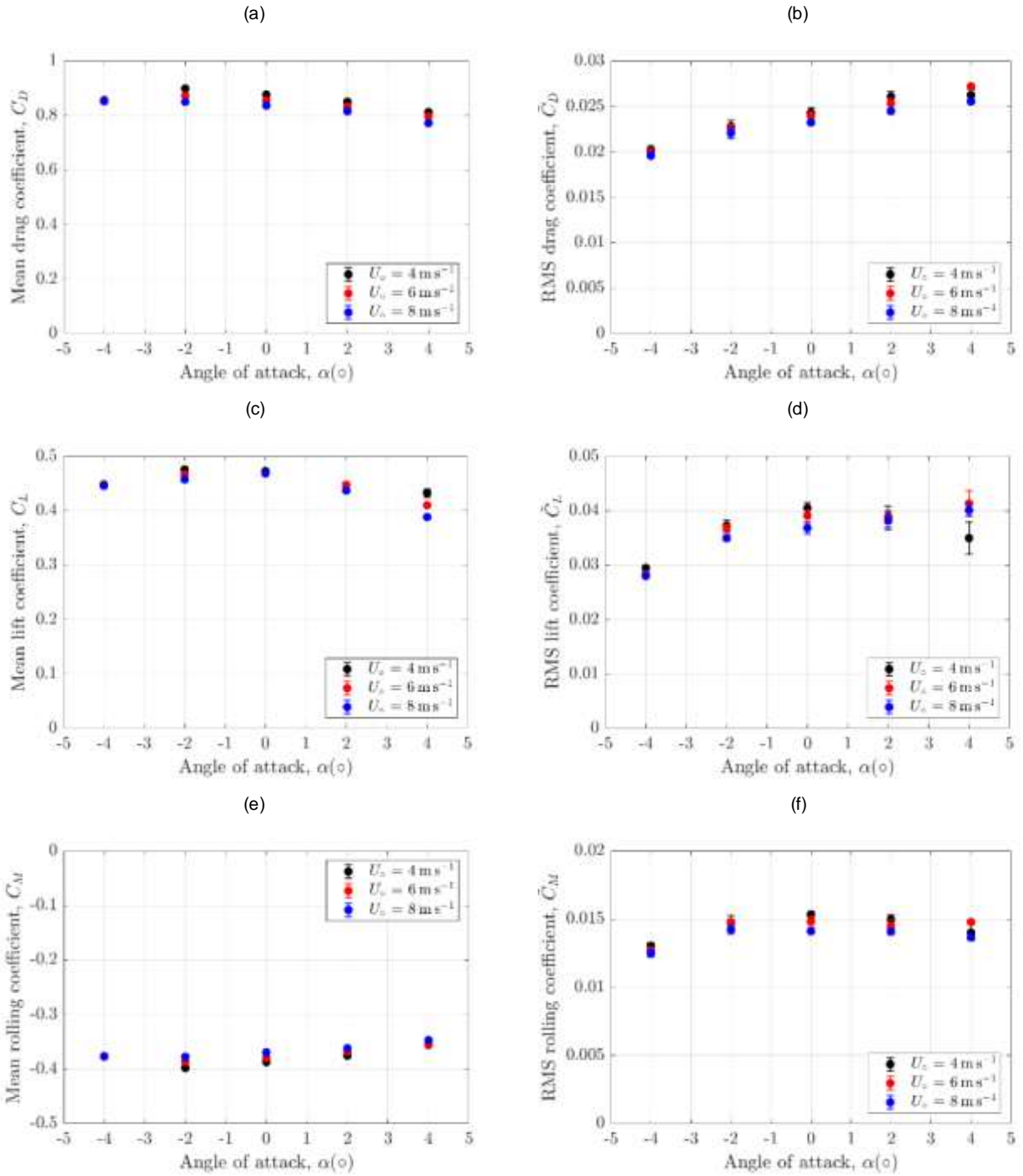


**Figure 4.10.** Variability of (a,b) the mean and RMS drag coefficient, (c,d) the mean and RMS of lift coefficient and (e,f) the rolling coefficient with respect to the angle of attack and wind speed.

Table 4.1 summaries the shield and unshielded rolling coefficient at the wind speed of  $6 \text{ m s}^{-1}$  and at the five different angles of attack. The reduction factor is reported as the ratio between the shielded and unshielded coefficients. With the higher reduction factors, the negative angles of attack appear to be vulnerable compared to zero and positive angles of attack.

**Table 4.1.** Shielded and unshielded rolling coefficients, and associated reduction factors, at the wind speed of  $6 \text{ m s}^{-1}$

Angle of attacks	Rolling coefficient		Reduction factor
	Shield, $C_{M,S}$	Unshielded, $C_{M,U}$	$R = C_{M,S}/C_{M,U}$
-4	-0.377	-0.731	51.6
-2	-0.387	-0.760	50.9
0	-0.379	-0.791	47.9
2	-0.368	-0.820	44.9
4	-0.355	-0.842	42.2

## 5 Summary

This report describes a WT study where static WT sectional model tests were conducted to investigate the flow field on the Queensferry Crossings. The study indicated the effect of the as-built wind barrier on slowing the wind speed and creating unsteady flow field across the bridge deck. Key features of the flow field were identified and discussed, including high-speed jets through gaps on the wind barrier, significant reduction in the wind speed behind the upper part of the wind barrier, and the shear layer originating from the top louvre. These features of the flow field did not vary significantly with upstream wind speed. However, a variation in the angle of attack caused dramatic changes to how the flow developed behind the wind barrier and evolved along the bridge. At negative angles of attack, the wind coming above the section created suppression effects, reducing the growth and lifting of the shear layer which trapped underneath slowly decaying unsteady flow field. At positive angles of attack, the wind coming from the underneath the section generated faster-moving flow through the large gap on the wind barrier and an increase in the strength of the shear layer. Also, at 4° angle of attack, there is evidence of switching between two flow regimes having different mean wind speeds.

A variation in the angle of attack also affected the aerodynamic coefficients and surface pressure distribution around the vehicle at the centre of the hard shoulder. In the unshielded scenario (i.e. without the barrier), as the angle of attack increased, there is an increase in both mean and RMS values of the aerodynamic coefficients. On the contrary, when being protected by the wind barrier, as the angle of attack got large, there was a reduction in mean aerodynamic coefficients. RMS values of lift and rolling coefficients remain unchanged during positive angles of attack. Comparing shielded and unshielded rolling coefficients, the as-built barrier was found to become less effective to reduce the overturning moment as the angle of attack is negative.

### Limitations

- The WT study was conducted with a stationary vehicle, which did not represent the most likely scenarios on the actual bridge. Dynamic WT tests with the static sectional model and the vehicle moving along the carriageway can be benefit, providing insights into the interaction between the flow field and the moving vehicle.
- The WT study only focused on the case where the vehicle was positioned at the centre of hard shoulder.
- The WT study was conducted with smooth flow condition. This did not represent the most likely scenarios on the actual bridge or the riskiest scenarios for the vehicle. Grids can be installed further upstream of the model to generate turbulent flow. Such grids can be designed and manufactured according wind field parameters extracted from field data of anemometers installed on the Queensferry Crossing.
- In the WT study, the reference vehicle was modelled as a rectangular box whereas the cross section of an actual bus has rounded corners and slightly tapers towards the top. The simplification adopted here can affect flow field around the vehicle and its aerodynamics.

---

## **Appendix D Lidar Survey**



# Lidar Survey

## Wind Threshold Study

### Queensferry Crossing

17 FB 1203 039 /R003 Revision 01  
January 2021



## Document Control Sheet

Project Name:	Wind Threshold Study Queensferry Crossing
Project Number:	17 FB 1203 039
Report Title:	Lidar Survey
Report Number:	R003

<b>Issue Status/Amendment</b>	<b>Prepared</b>	<b>Reviewed</b>	<b>Approved</b>
00 First Issue	Name: Patrick Madden Signature: Date: 06/01/2021	Name: Angus Bruce Signature: Date: 06/01/2021	Name: Ewan Angus Signature: Date: 06/01/2021
	Name: Signature: Date:	Name: Signature: Date:	Name: Signature: Date:
	Name: Signature: Date:	Name: Signature: Date:	Name: Signature: Date:
	Name: Signature: Date:	Name: Signature: Date:	Name: Signature: Date:

## **Executive Summary**

The Queensferry Crossing opened on the 30th August 2017 and replaces the Forth Road Bridge (FRB) as the primary carrier of road vehicles crossing the Firth of Forth between Fife to the North and Edinburgh, including links to the M8 and M9, to the south it is an important part of Scotland's infrastructure, linking important transportation routes for people, businesses and emergency services.

The bridge was built with Wind Barriers which help shelter the traffic from adverse wind conditions and allows the bridge to remain open during higher wind speed events than would otherwise be possible. The wind speed thresholds for operating the bridge were set prior to opening, and these are reviewed periodically. As part of this review Amey, the then operating company, proposed that a more detailed understanding of the performance of the as-built wind shielding needed to be confirmed with further research and on-site measurements to expand the knowledge base and further inform the review.

Part of this additional research included a Lidar survey around the bridge to record the dynamics of the wind field around the bridge and to attempt to measure the effectiveness of the wind barrier in situ. The Lidar survey, conducted between February and May 2020, was successful in providing valuable insight into the behaviour of wind around the Queensferry Crossing, and gave an indication of the performance of the wind barriers on site.

The survey provided a record of the complex nature of the wind flow across the Firth of Forth and around the bridges. Identifying the dynamic nature of gust patterns that change intensity and direction quickly with time. This makes the use of any threshold system that relies on directionality unsuitable for the operation of the bridge.

Processing the results provided an indication of the performance of the wind barrier on site. The complex nature of the flow pattern through the barrier makes it difficult to capture the exact detail on site, however it was able to confirm the general outline "S" shape pattern that was observed in greater detail in the models, and indicated a reduction in wind speed approaching that observed in greater detail in the models, providing some confidence that the models were replicating the true nature of the wind barrier.

## Contents

<b>1</b>	<b>Project Summary.....</b>	<b>4</b>
1.1	Overview .....	4
<b>2</b>	<b>Lidar Survey .....</b>	<b>5</b>
2.1	Lidar Scanner selection .....	5
2.2	How Lidar measures wind speed.....	5
2.3	Lidar Scanner positioning .....	7
2.4	Lidar Installation .....	8
2.5	Scanning scenarios .....	9
<b>3</b>	<b>Data Review .....</b>	<b>13</b>
3.1	Comparing the Lidar Data to existing sensor .....	13
3.2	Initial observations from the Lidar Survey.....	16
3.3	Obstacle identification and filtering .....	17
3.4	Wind barrier influence on wind speed.....	19
3.5	Post processing of survey data .....	20
3.6	Heat maps .....	23
3.7	Comparing site data with model results .....	24
<b>4</b>	<b>Conclusion.....</b>	<b>27</b>
<b>Appendix A</b>	<b>Leosphere Initial Site Survey Report</b>	<b>A-1</b>
<b>Appendix B</b>	<b>Leosphere Installation Report</b>	<b>B-1</b>
<b>Appendix C</b>	<b>Leosphere Final Report</b>	<b>C.1</b>

## Figures

Figure 1: Doppler effect visual.....	5
Figure 2: Schematic of the radial component measured by the Lidar. ....	6
Figure 3: Wind rose showing prevailing wind direction. ....	7
Figure 4: Gantry 08 – Lidar location relative to QC .....	8
Figure 5: Lidar in position on Gantry 08. ....	9
Figure 6: Mesoscale PPI Scan overlaid on map .....	10
Figure 7: a) PPI Microscale 0.5° b) PPI Microscale 0.6° .....	11
Figure 8: Example RHI scan visual.....	11
Figure 9: Reconstructed wind speed (m/s) and direction on 04/03/2020 .....	13
Figure 10: FRB Wind Station relative to the cluster of Lidar measurements taken for comparison. ....	14
Figure 11: Wind speed compared for Lidar and FRB Wind Station.....	15
Figure 12: Wind Direction compared for Lidar and FRB Wind Station .....	15
Figure 13: Reconstructed wind speed (m/s) and direction on 18/03/2020 at 13:00:47 – area zoomed in. ....	16
Figure 14: Tower outline and wake recorded on 22 <sup>nd</sup> Feb 2020 @ 11:59 .....	17
Figure 15: PPI scan intercepting wind barrier .....	18
Figure 16: Northbound vehicle in carriageway A and corresponding wake. ....	18
Figure 17: Scan showing location of sections through the data, scan: 04/03/2020 00:07:09 .....	19
Figure 18: Scan section data to show speeds upstream and downstream of wind barrier. ....	20
Figure 19: Close up of scan in Figure 17 showing just the northbound carriageway and upstream wind. ....	20
Figure 20: 5-minute averaged wind direction throughout the campaign, data from “FRB Wind” anemometer .....	21
Figure 21: Orientation of Queensferry Crossing and wind data ranges sampled .....	22
Figure 22: 5-minute averaged wind direction between 245° and 335°, throughout the campaign, data from “FRB Wind” anemometer .....	22
Figure 23: Heatmap visualisation of normalised radial wind speed - 0.6° PPI scan, 270° direction .....	23
Figure 24: Heatmap visualisation of normalised radial wind speed - 0.5° PPI scan, 270° direction .....	23
Figure 25: Hard shoulder normalised wind speed results compared across Lidar, CFD, and Wind Tunnel tests. ....	24

## Tables

Table 1: Survey scan summary .....	12
Table 2: Number and type of scans carried out within each scanning sequence .....	12

---

# 1 Project Summary

## 1.1 Overview

On behalf of Transport Scotland, Amey are carrying out a review of the current wind threshold for operating the Queensferry Crossing.

The current thresholds on the Queensferry Crossing are based on the wind shielding reducing the overturning potential of vehicles, induced by a wind speed, by approximately half. This is based on the results from the existing wind tunnel testing. This reduction in overturning potential is then applied to the original Forth Road Bridge thresholds, the unshielded condition, to determine the equivalent Queensferry Crossing, shielded condition, thresholds. The "Effect of High Winds on Traffic" study by Jacobs/Arup used the results from the wind tunnel testing, i.e. the reduction in overturning potential, combined with the Baker method to confirm these thresholds as suitable, based on available information. However, it suggested that the double-deck bus limit could potentially be increased from 60mph to 65mph.

Under instruction from Transport Scotland Amey progressed with a study of the effectiveness of the wind barriers as built. This included

- Computational Fluid Dynamics (CFD) Modelling of the As Built wind barrier condition
- Wind Tunnel Testing of the As Build wind barrier condition
- Lidar survey of the bridge to record wind behaviour on site.

This report focuses on the output from the Lidar Survey, which was used to record the dynamics of the wind field around the bridge and to try to measure the effectiveness of the wind barrier in situ. The Lidar survey, conducted between February and May 2020, was successful in providing valuable insight into the behaviour of wind around the Queensferry Crossing, and gave an indication of the performance of the wind barriers on site.

---

## 2 Lidar Survey

### 2.1 Lidar Scanner selection

The initial proposal outlined a method of recording the change in wind speed on approach to, and in the wake of the wind shielding using Lidar technology using 2 No. Lidar sensors installed on the Queensferry Crossing. One on a Northbound tower gantry and one on a Southbound tower gantry. This was based on using the ZX TM Lidar from ZXLidars. A Lidar scanner would allow us to record the wind speed remotely at different locations along the bridge, a process that could not be carried out by traditional means without closing the bridge. The limitations of using the ZX TM Lidar were in its single scanning mode, and its predefined scanning cone arrangement, which would have resulted in large amounts of data being located out with the critical window, i.e. the wake behind the barrier. It also would have meant that upstream and downstream wind speeds would be recorded at different sections across the bridge and, due to the observed complicity of the wind field around the bridge during the survey, may not have provided directly comparable results. From ongoing discussions with industry suppliers an alternative, more accurate Lidar was selected for use for this study.

The Windcube 100S scanning wind Doppler Lidar system was selected as an alternative, more effective system. Its multi scanning mode, and controllable scanning profile, allowed better control in directing the scans on the bridge. It facilitated the collection of more data from critical areas and helped build a better picture of the wind field. It also allowed more comparable upstream and downstream record of the wind relative to the wind barrier, compared to alternative systems.

### 2.2 How Lidar measures wind speed

The Lidar scanner uses Doppler pulsed LiDAR to work out if aerosols in the wind are moving towards or away from it, and at what speed. Consider a siren passing with noise/frequency change, this is the doppler effect.

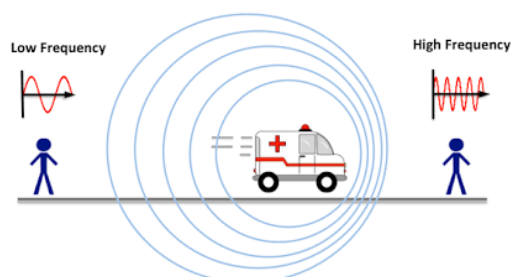


**Figure 1: Doppler effect visual**

---

To record the doppler shift the sensor needs three things:

- Transmitter
- Receiver
- Relative motion

The LiDAR emits pulses (100,000 pulses per second) which interact with minute aerosols in the air (water vapour, dust, smoke etc.). The pulses emit secondary emissions when they reflect off aerosols, and a minute amount of these secondary emissions are reflected back to the LiDAR. Therefore, in our case:

- The transmitter is the reflected secondary emission reflected off the aerosol,
- The receiver is the Lidar scanner
- The relative motion is between the aerosol and the LiDAR.

As a result the Lidar system records the Radial component of the wind. If the aerosol is moving towards the Lidar it will "squash" the frequency on a minute scale, if it is moving away it will elongate the frequency on a minute scale, this shift in frequency can be used to determine the radial speed component of the wind, see Figure 2. This is carried out at multiple locations along each Lidar beam and gives a reading almost instantaneously.

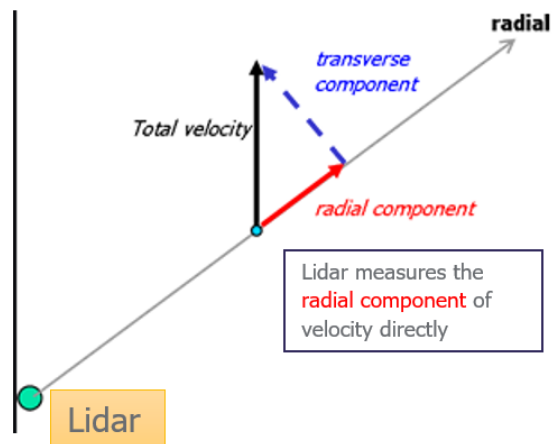


**Figure 2: Schematic of the radial component measured by the Lidar.**

If enough radial wind speed components are recorded, in a wide enough azimuth, then the software is able determine the actual direction and wind speed of each individual component.

## 2.3 Lidar Scanner positioning

Initial results from the CFD modelling indicated that the area of most interest is close to the barrier (hard shoulder and lane 1). As the prevailing wind comes from the South West, see Figure 3, the most valuable data was deemed to be on the Northbound hard shoulder and lane 1. Locating the Lidar with sight along the Northbound carriageway, monitoring the west wind barrier which interacts with the prevailing wind, ensured we collected the most valuable data.

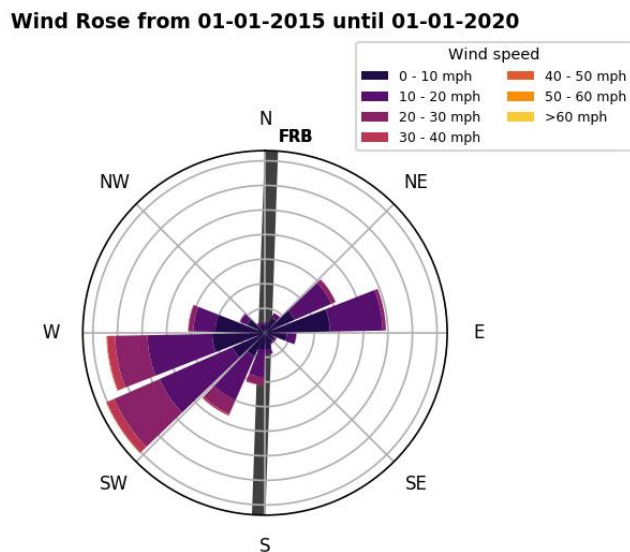


**Figure 3: Wind rose showing prevailing wind direction.**

A site survey, including line of site checks, was undertaken, with Leosphere, to identify the most suitable location for the equipment. Appendix A – Site Survey report outlines the different locations considered. Gantry 08, located at the southern end of the Queensferry Crossing see Figure 4, was considered the most suitable location. This position gave a superior line of sight along the bridge, compared to the other locations, and provided a better view of the wind approaching the bridge, helping us understand the base condition prior to interference from the bridge and wind barriers. Leosphere identified this position as their preferred position to obtain the most useful data set.



**Figure 4: Gantry 08 – Lidar location relative to QC**

## **2.4 Lidar Installation**

To install the Lidar into Gantry 08 required some modifications to allow the survey to take place while minimising the impact to the gantry itself.

A support platform was installed to ensure that the Lidar was supported on the main steelwork of the Gantry, and not the mesh flooring. New mesh panels with a view port allowing the survey to take place were installed on the Gantry for the duration of the survey. A dedicated power supply was designed and installed to provide power to the equipment for the duration of the survey.

The Lidar was lifted into position under Traffic Management. The system was commissioned, and the initial scans progressed. The initial scans identified the Main Towers of the Queensferry Crossing, allowing a reference point for the remainder of the scans to be programmed. A detailed account of the installation is available in Appendix B – Installation Report.

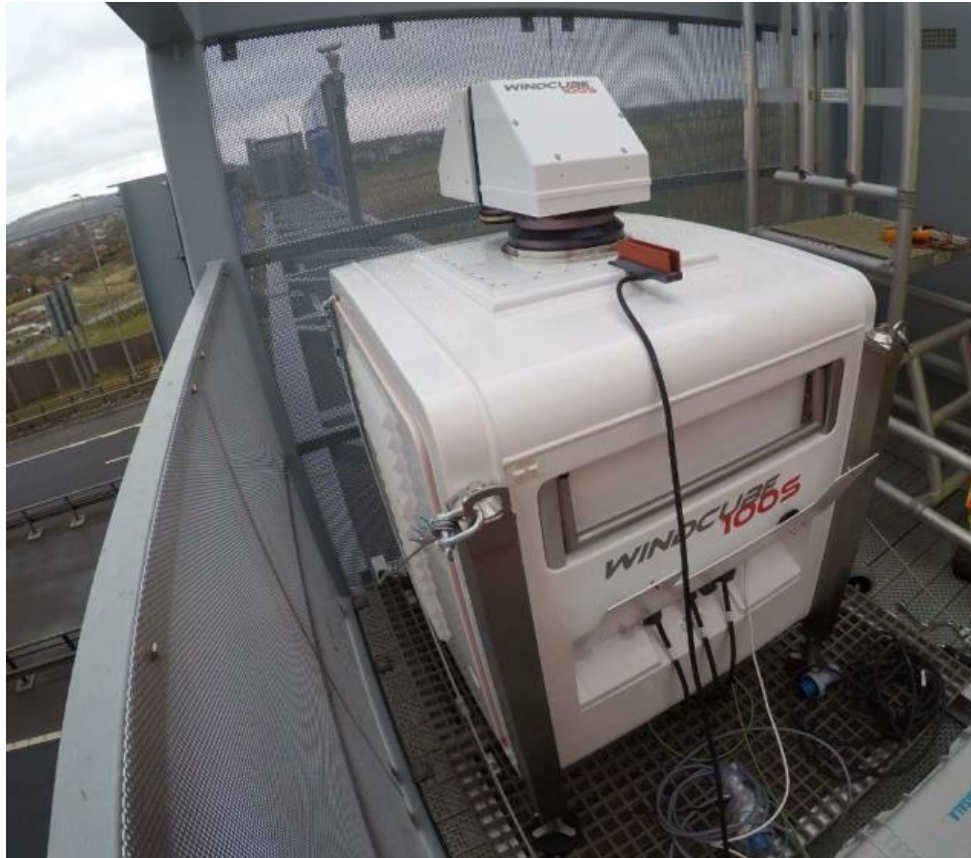


**Figure 5: Lidar in position on Gantry 08.**

## **2.5 Scanning scenarios**

Following the initial test scans a programme of scanning was developed to best capture the information on site. Two main types of scan were programmed:

- PPI mode (Plan Position Indicator): constant elevation angle scenario
- RHI mode (Range Height Indicator): constant azimuthal angle scenario

A wide view PPI scan, referred to as PPI mesoscale, gave an understanding of the characteristics of the wind surrounding the bridges. This scan was angled at an elevation of  $0.55^\circ$  to better align with the bridge and had a resolution of 25m along the sight of the scan. It covered a range of up to 3000m and gave an overview of the wind upstream and downstream of the bridge, see Figure 6. The outline of the three bridges can be observed in the data where the scan is interrupted by the structures. This gives an understanding of the large-scale behaviour of the wind field around the bridge. Larger wind structures, gusts, and turbulence around the southern end of the bridge can be observed within the data.

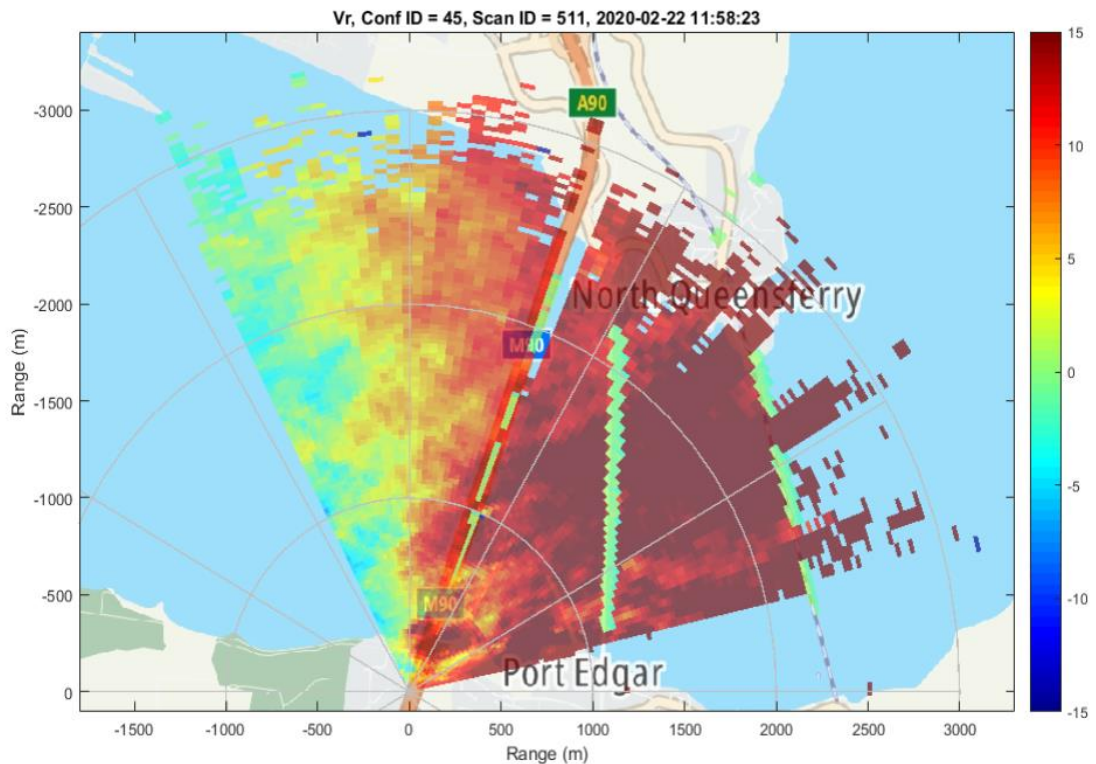


**Figure 6: Mesoscale PPI Scan overlaid on map**

Two more refined PPI scans were also carried out.

- PPI Microscale 0.5°
- PPI Microscale 0.6°

These scans targeted the area closer to the bridge and the refined area allowed a more detailed resolution to be achieved. The higher resolution allowed the smaller wind structures near the windshield to be identified, see Figure 7. A horizontal angular resolution of 0.06° converts to a wind speed reading every 1m across the bridge, at a distance of 1000m from the Lidar, the approximate distance of the South Tower. These scans had a resolution of 5m along the line of sight. The different angles of the two PPI Microscale scans allowed them to intersect the bridge at different locations.

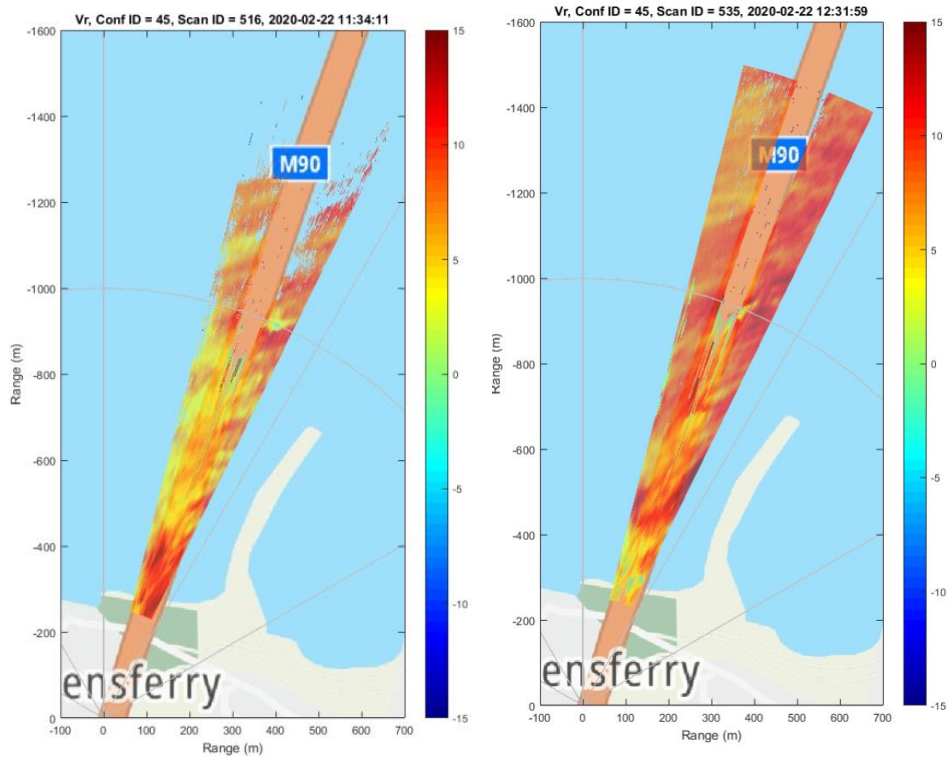


**Figure 7: a) PPI Microscale 0.5° b) PPI Microscale 0.6°**

A series of two RHI scans were also carried out, in an attempt to provide a better understanding of the 3D effect of the wind. Figure 8 gives an impression of what these scans look like in relation to the bridge. They were taken at the following angles:

- 19.8° to measure a cross section of the wind aligned with the zone between the windshield and the middle of the bridge
- 19.9° to measure the wind adjacent to the tower



**Figure 8: Example RHI scan visual**

Table 1: Survey scan summary provides a summary of the parameters of the scans carried out during the survey.

**Table 1: Survey scan summary by Leosphere**

Scan parameter	PPI Mesoscale	PPI Microscale	RHI
Azimuth angle (°)	120	6	19.8 – 19.9
Elevation angle (°)	0.55	0.5 – 0.6	3
Accumulation time per line of sight (ms)	500	100	100
Angular resolution (°)	1.5	0.06	0.02
Rotation speed (°/s)	3	0.6	0.2
Range gate length (m)	25	25	25
Number of gates	129	259	250
Minimum range (m)	100	255	250
Display resolution (m)	25	5	5
Max range (m)	3300	1545	1495

Each scanning sequence lasted approximately one hour. Table 2 summaries the number and types of scans that were undertaken during each sequence.

**Table 2: Number and type of scans carried out within each scanning sequence**

Number of scans	Type of scan	Angle of scan
120	PPI Microscale	0.5°
120	PPI Microscale	0.6°
15	PPI Mesoscale	0.55°
18	RHI	19.8°
18	RHI	19.9°

### 3 Data Review

A detailed description of the data processing carried out by Leosphere can be found in their project report, Appendix C. An overview of the process, including highlights of relevant findings, coupled with description of further processing of the data carried out by Amey, and subsequent findings area also presented in this section.

#### 3.1 Comparing the Lidar Data to existing sensor

Lidar technology as a technique of recording wind speed and direction is well established, and commonly used within the wind power industry to monitor local wind speeds and directions. Comparison can be made to existing sensors on the FRB to confirm accuracy. The scans record radial wind speed, however when a scan is large enough, i.e. covers a significant azimuth, the data can be post processed to provide an accurate actual wind speed value. While the microscale scans cover too narrow an azimuth, only 6°, the mesoscale scan covers 120°, which is sufficient to facilitate the conversion. An example of this is shown in Figure 9 overlain on a map of the area.

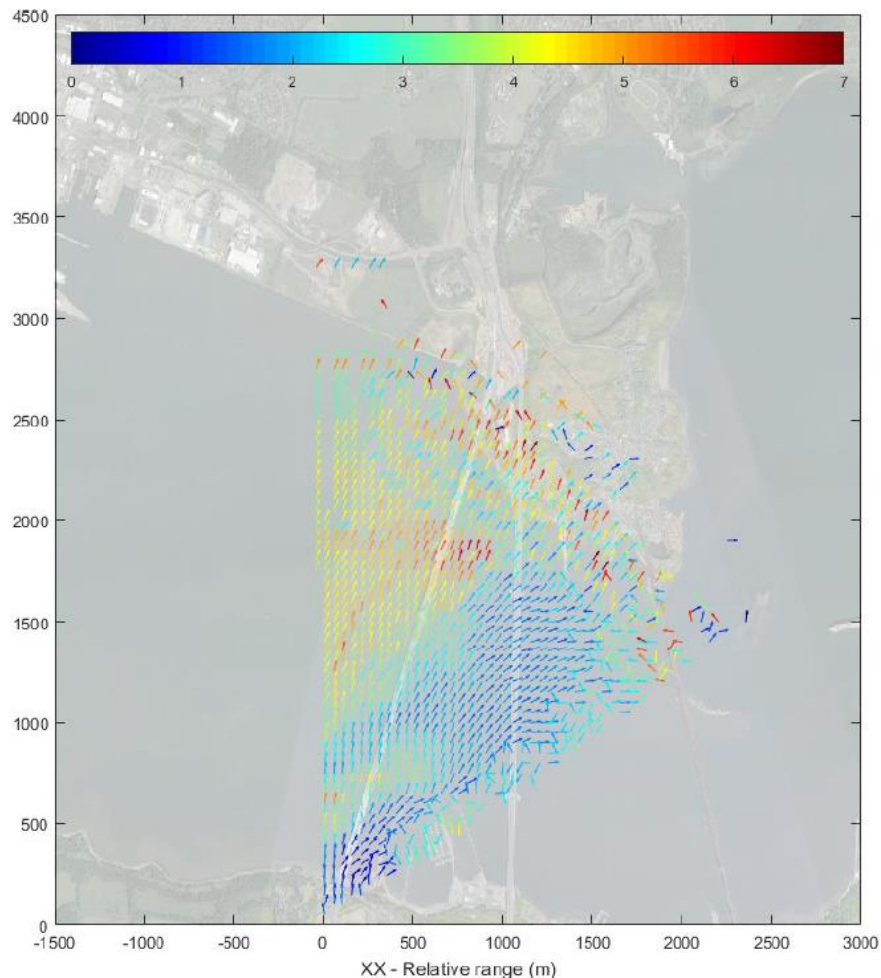


**Figure 9: Reconstructed wind speed (m/s) and direction on 04/03/2020**

The position of each wind record relative to the Lidar sensor is also recorded which allows the positions to be mapped with reasonable accuracy, as seen in Figure 9. The height of each of these positions above sea level is also recorded. The FRB Wind sensor is installed at mid-span on the Forth Road Bridge, the co-ordinate position of this sensor can be approximated with reasonable accuracy. It is worth noting that the Lidar data is recorded at approximately 25m a.m.s.l., whereas the FRB Wind Sensor is located at approximately 65m a.m.s.l. therefore, throughout the campaign, some discrepancy in wind speed will be recorded between the two sensors due to the elevation difference.

To allow a comparison to be made between the Lidar sensor record and the FRB Wind sensor record a cluster of Lidar measurements were taken. There is no Lidar record at the exact position of the FRB wind sensor, so capturing the data recorded in a 150m radius around the position ensures we capture a reasonable sample around the sensor and consider all directions of wind. The cluster of sampled Lidar data relative to the FRB Wind sensor is shown in Figure 10

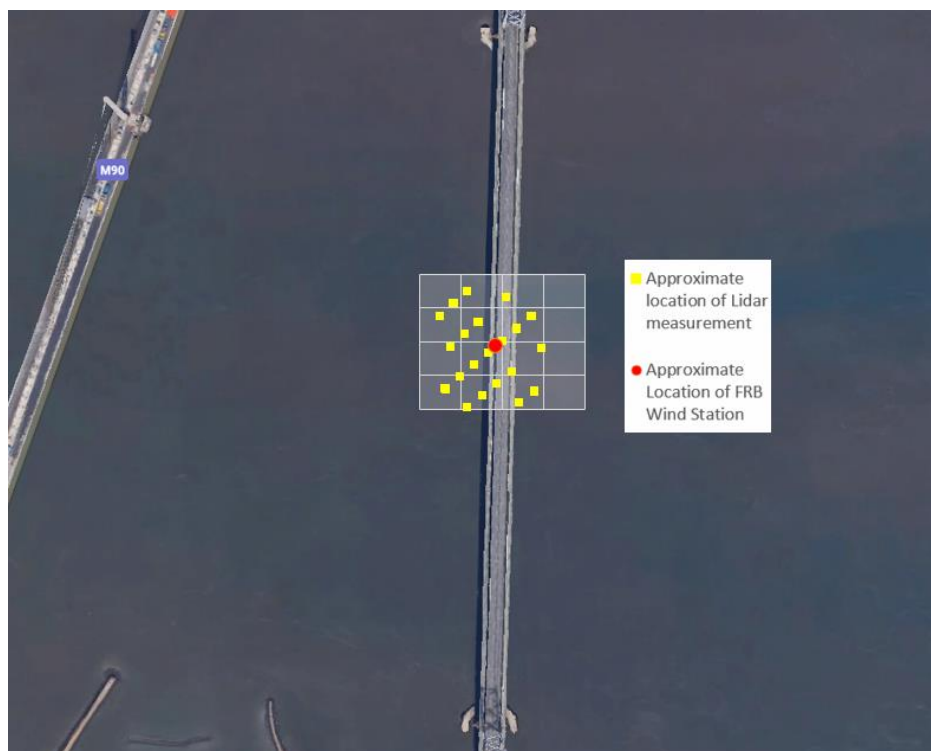


**Figure 10: FRB Wind Station relative to the cluster of Lidar measurements taken for comparison.**

The record from the cluster sample of Lidar data recorded on the 12/03/2020 between 01:00:00 and 01:05:00 is presented in Figure 11 and Figure 12 and compared to the 5minute data recorded at the FRB Wind station. All available data from the cluster is shown, as well as the average value. The FRB Wind station records data at 5-minute intervals, therefore only the average and max value is available for the start and end of the sample time from FRB Wind station.

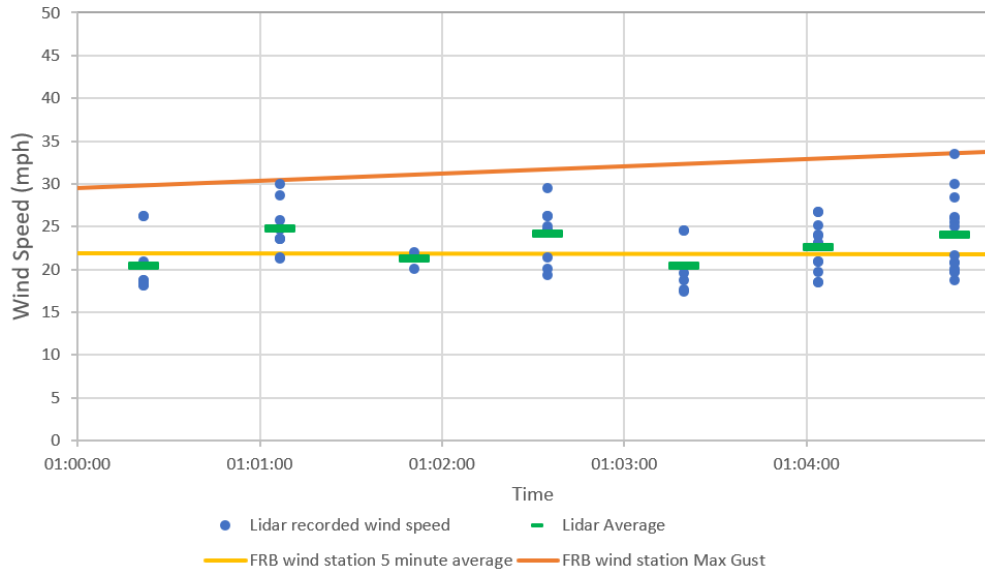


**Figure 11: Wind speed compared for Lidar and FRB Wind Station**

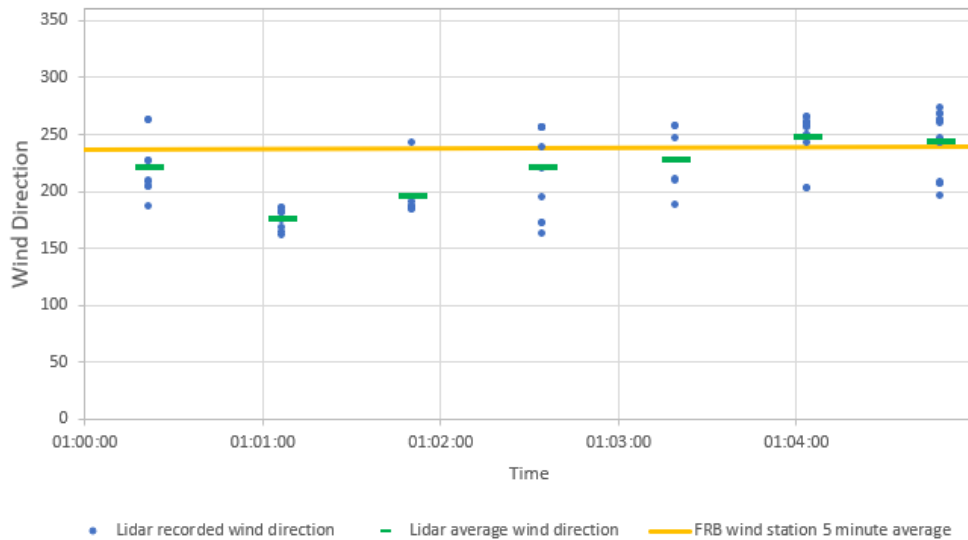


**Figure 12: Wind Direction compared for Lidar and FRB Wind Station**

Both parameters, wind speed and direction, show reasonable correlation, despite the difference in elevation of the record, confirming confidence in the Lidar output.

### 3.2 Initial observations from the Lidar Survey

The Mesoscale scans give a good overview of the complexity of the wind around the QC and FRB. In a previous review of the wind speed thresholds for QC, undertaken by Jacobs and Arup, they reviewed the possibility of considering directionality as part of the QC wind thresholds. This is not currently implemented in the operational thresholds for the QC as the wind direction is known to change quite quickly in the Forth and therefore difficult to manage from an operational point of view, however it remains an approach that may be considered again in the future.

The Lidar study observed that not only does wind direction change quickly with time, it is not uniform across the bridge at any one time, making it even more difficult to manage a system that considers directionality. The direction recorded at a stationary point, i.e. a weather station, may not be the same as the wind direction across the length of the bridge. See Figure 13 as an example of the fluctuating behaviour.

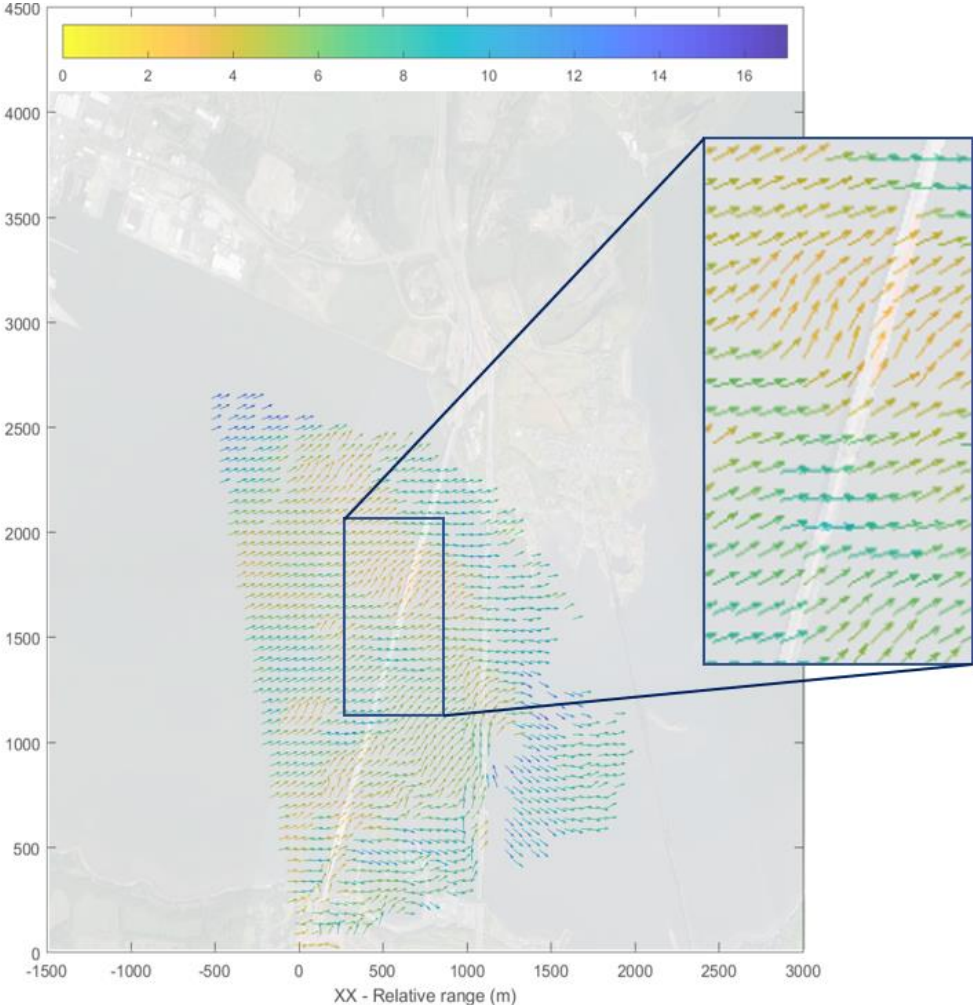


**Figure 13: Reconstructed wind speed (m/s) and direction on 18/03/2020 at 13:00:47 – area zoomed in for clarity.**

At the start of the scanning campaign some additional scans were undertaken to pinpoint certain targets such as the QC towers. During these initial scans some interesting behaviour was observed around the towers, see Figure 14. While not the focus of the campaign, the wake from the tower is clearly visible, this corresponds to anecdotal reports of drivers experience when driving southbound past the towers during high winds and feeling the wake/shelter from the towers.

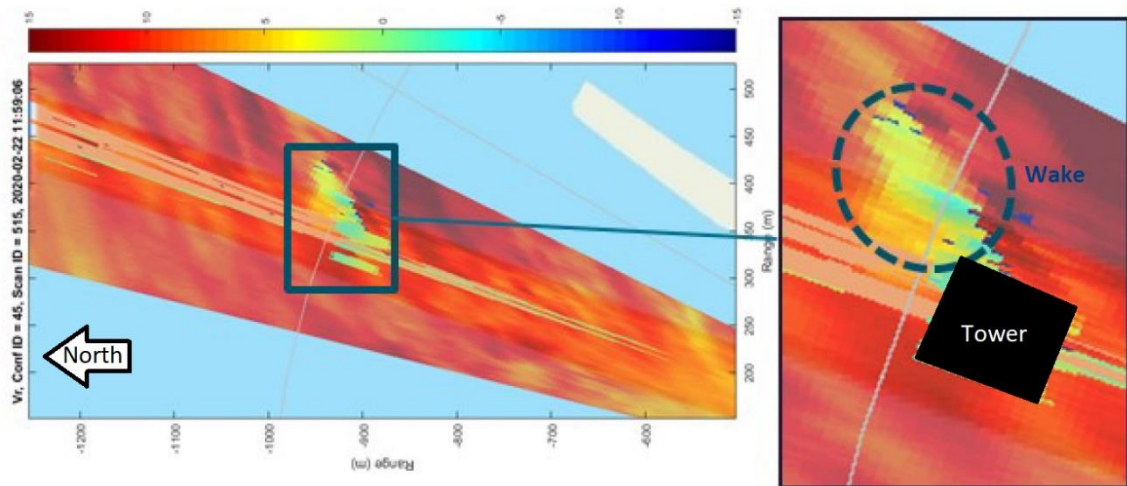


**Figure 14: Tower outline and wake recorded on 22<sup>nd</sup> Feb 2020 @ 11:59**

### **3.3 Obstacle identification and filtering**

As the PPI scans cross the bridge, they intercept the wind barrier and carriageway. The angle at which they intercept is a product of both the angle of the scan and the rise of the bridge deck at that section of the bridge. Identifying the wind barrier in the scan data was important to allow us to detect exactly where the scan dipped below the barrier, which will in turn allow a comparison of upstream and downstream wind speeds to be carried out. Figure 15 illustrates the identification of the wind barrier, and other bridge elements such as the cables and bridge deck, within the scan.

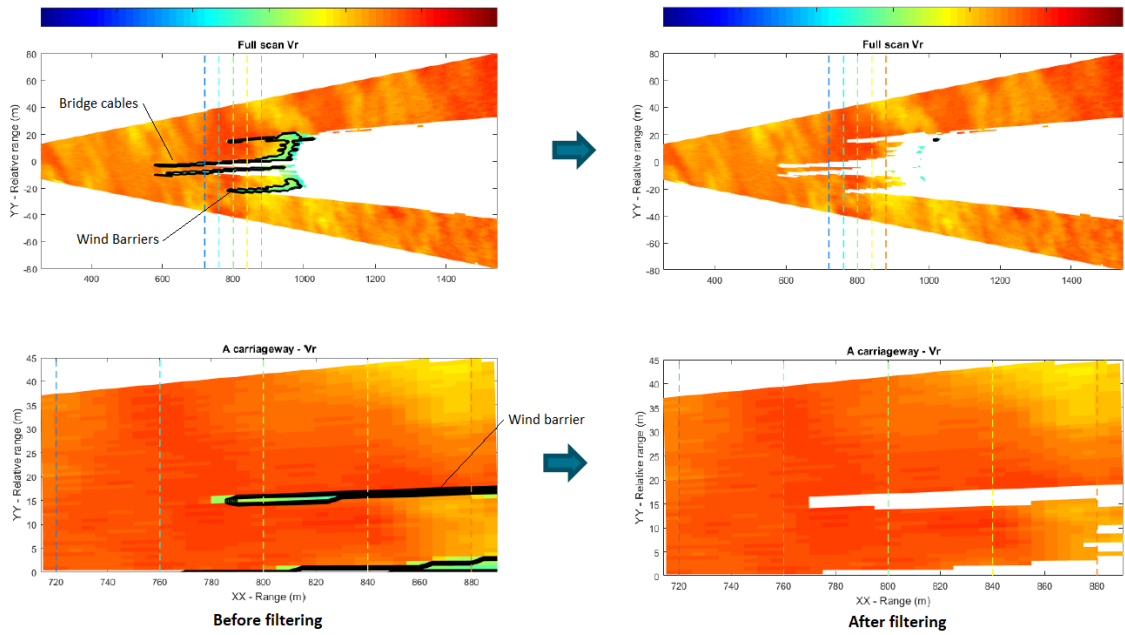


**Figure 15: PPI scan intercepting wind barrier**

The data points close to these bridge elements will suffer significant interference and therefore the elements and the area of interference is filtered out of the data, see right hand side images in Figure 15 showing the data post filter.

Within the data set it was also noted that traffic, both physical vehicles, and the wake generated by the vehicles, can have a significant influence on the data. There are many examples of this in the data set, and example of which is shown in Figure 16 . This cannot easily be filtered out, and therefore must be considered in any interpretation of the data.

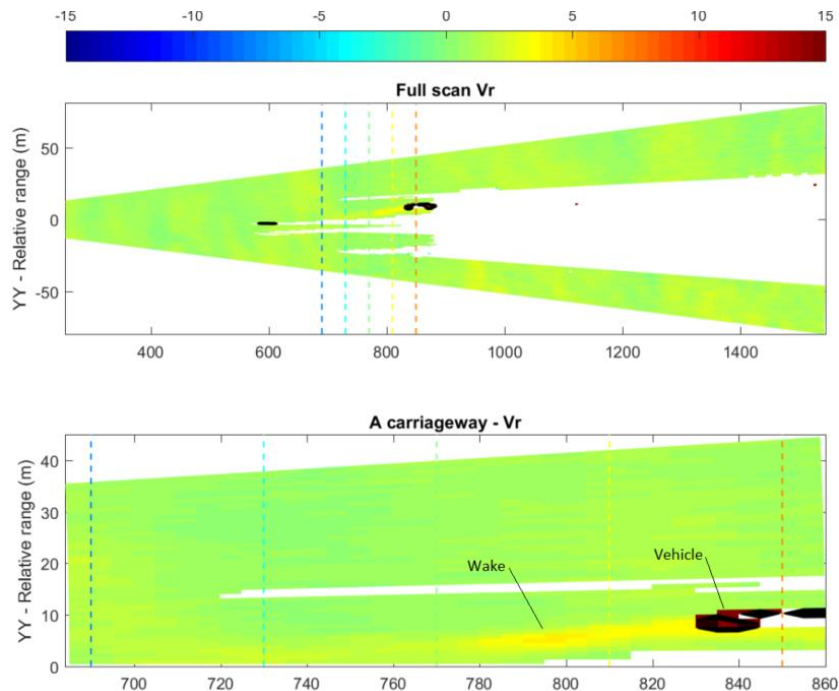


**Figure 16: Northbound vehicle in carriageway A and corresponding wake.**

### 3.4 Wind barrier influence on wind speed

Visually comparing the scans can give an indication of the influence of the wind barrier but it does not provide a quantitative measurement. To compare data upstream and downstream of the wind barriers sections are taken through the scan data. The positions of these sections, Figure 17, were defined to provide information above and below the wind barrier height.

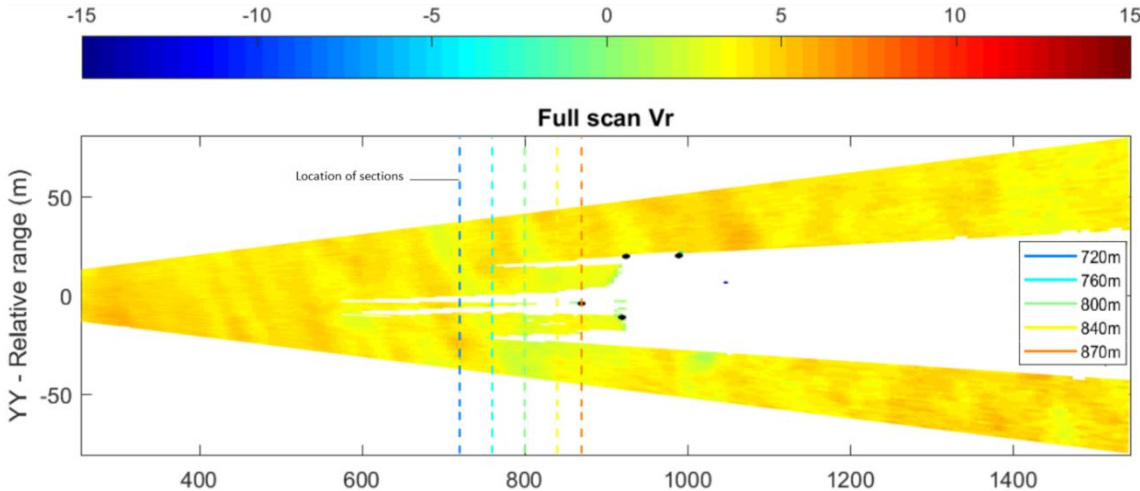


**Figure 17: Scan showing location of sections through the data, scan: 04/03/2020 00:07:09**

Taking individual sections through the data provides a record of the upstream and downstream radial wind speed. Normalising the radial wind speed in the sections by a value upstream of the wind barrier gives a clearer indication of the influence of the wind barrier. The position at which the wind speeds are normalised, for westerly wind direction, is taken at chainage 25m, which is approximately 11m upstream of the westerly wind barrier. The dynamic nature of the wind around the Queensferry Crossing means that considering individual scans in isolation may not be sufficient to gain a clear insight into the effect of the wind barrier.

Differences in wind speeds across the scan, observed as diagonal stripes in the colour gradient of Figure 17, coupled with wind directions not aligned perpendicular with the bridge result in the upstream and downstream values of a section not always aligning with the same wind gust. An example of this issue can be seen in Figure 18. The reduction in wind speed at section 840m and 870m is clearly evident, however section 800m appears to show an increase in wind speed, and the two sections above the barrier, sections at 720m and 760m, appear to show a decrease.

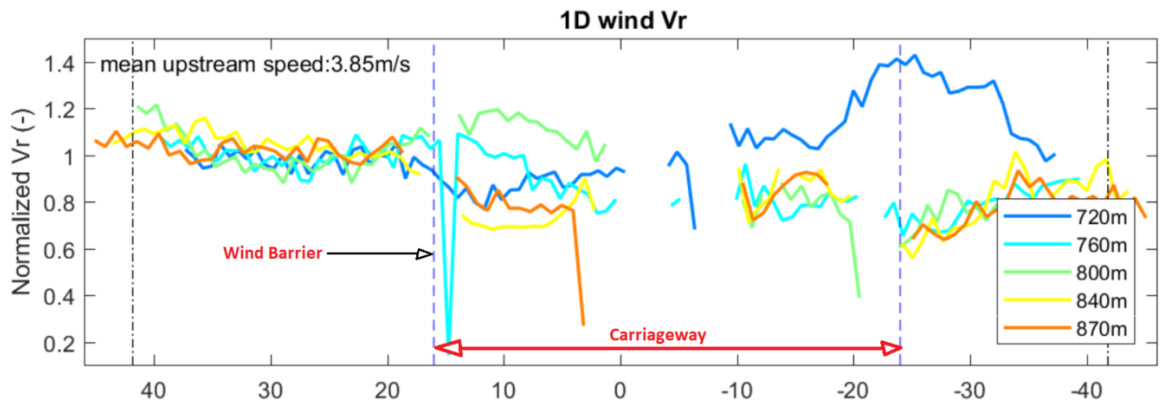


**Figure 18: Scan section data to show speeds upstream and downstream of wind barrier.**

If we look in detail at Section 800m, Figure 19, we can see that the point of normalisation upstream of the barrier is in a zone of very low radial wind speed. The wind direction is moving at an angle non-parallel to the section, therefore the wind speed behind the barrier for this section is not directly comparable to the speed at normalisation.

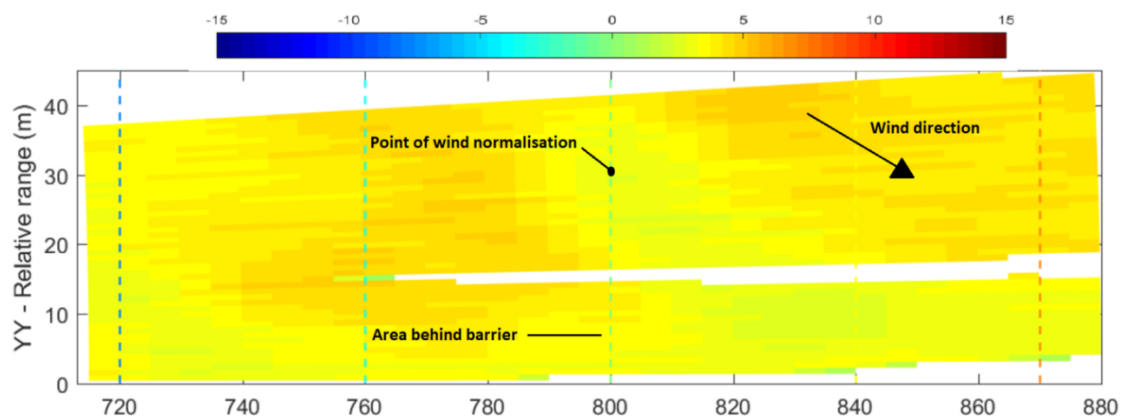


**Figure 19: Close up of scan in Figure 17 showing just the northbound carriageway and upstream wind.**

Wind direction and flow dynamics continually change during a scan, and between subsequent scans, making extracting definitive conclusions from individual scan sections very difficult. Additional batching and processing of the full data set can help assist in obtaining a more representative data set.

### 3.5 Post processing of survey data

During the campaign West/South Westerly, and North Easterly winds were the most common, providing the largest data base, see Figure 21.

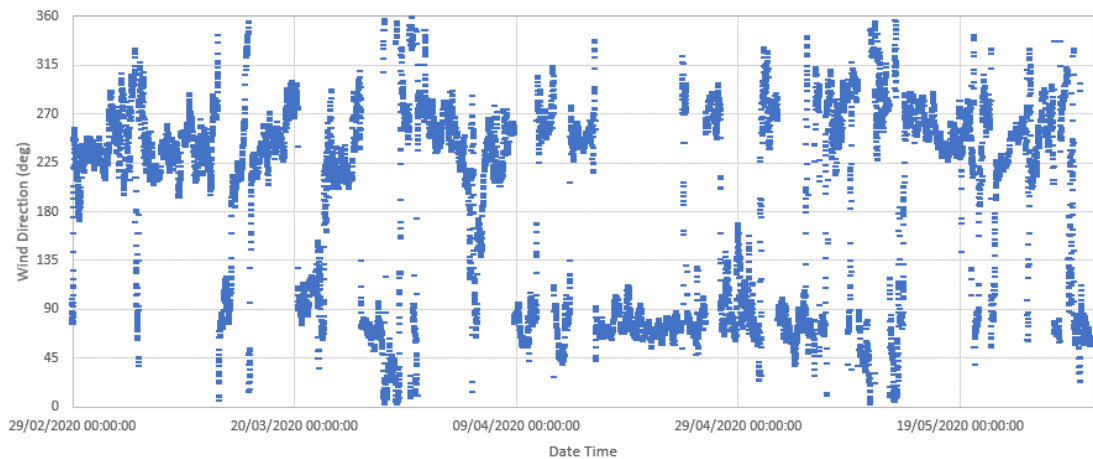


**Figure 20: 5-minute averaged wind direction throughout the campaign, data from “FRB Wind” anemometer**

Easterly and westerly winds interact with different wind barriers on the bridge therefore need to be considered separately in any analysis. The position of the Lidar provided a better line of sight for the west side barrier providing a cleaner and more complete set of scan data, therefore comparative results will focus on westerly winds only. A full 180° range was considered too broad a range to average the data across to obtain representative comparisons, therefore the data set was divided into smaller 45° range sets, to provide more representative behaviour while still retaining a significant number of samples. As noted in Section 3.2 the wind direction across the bridge is not uniform, and can change quickly both with position and with time, therefore the data batches are based on the average wind direction over a 5minute period as recorded by the wind station located at mid-span on the Forth Road Bridge. This was the closest available sensor and fell within the range of the wider scans.

Ideally only winds at exactly 90° to the barrier would be considered, as this is most comparable with the CFD and wind tunnel modelling. Perpendicular westerly wind to the QC is from a 290° direction. Throughout the campaign only 5% of the data recorded was within 5° of this direction (within a range of 285° and 295°). As noted in Leosphere’s report, the data from this direction, close to perpendicular to the wind barriers were recorded primarily during periods of low wind speed, less than 10mph, making the radial component significantly distorted by vehicle wake interference and therefore not suitable for direct analysis. Two of the 45° range sets straddle the 290° direction, 245° to 290°, and 290° to 335°, as indicated by the orange quadrant in Figure 21.

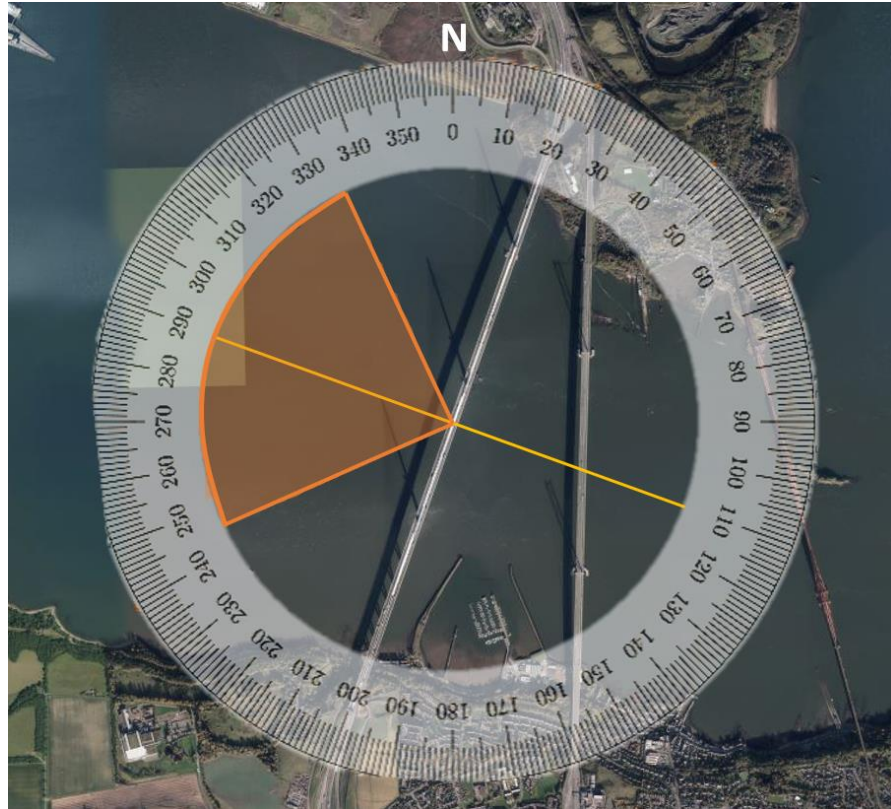


**Figure 21: Orientation of Queensferry Crossing and wind data ranges sampled**

A closer look the data from this quadrant, Figure 22, reveals that the majority of the recorded data falls into the 245° to 290° range direction, with a reasonable number of samples, equivalent to 37% of the total data sampled during the campaign. Data from 290° to 335° is infrequent, accounting for only 6% of the full campaign data set. Closer inspection of the 290° to 335° data set revealed that a significant proportion of this small data set contained “NUL” values in the region where the sections were taken. “NUL” values occur when the scanner is unable to record a specific data point, over large data sets this is usually insignificant, however in smaller data sets this can prove an issue.

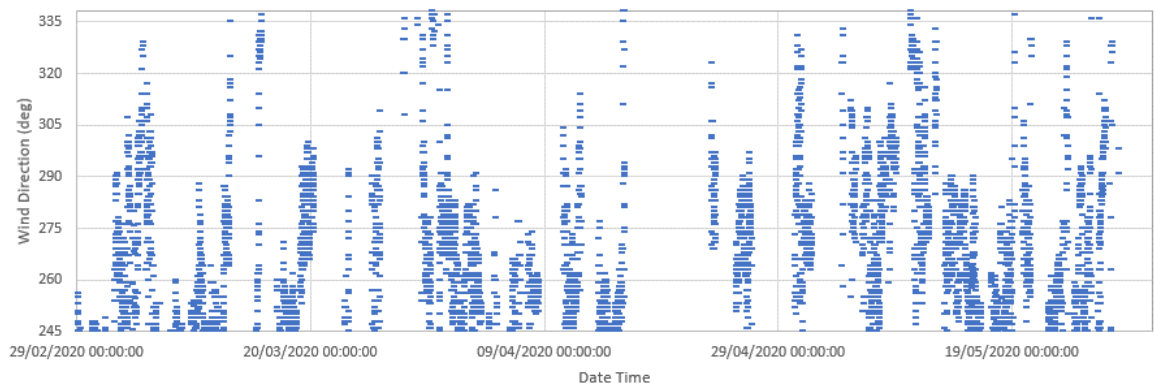


**Figure 22: 5-minute averaged wind direction between 245° and 335°, throughout the campaign, data from “FRB Wind” anemometer**

Considering the above, the data from the 245° to 290° direction only is used for further analysis. In the following sections any data referred to as the "270° direction" represents data averaged across the 245° to 290° direction.

### 3.6 Heat maps

To assist with visualising the impact of the wind barrier and identify other obstacles within the scan the normalised radial wind speed, averaged across the 45° direction range, is presented in heat maps overlain on a section of the bridge. For the purposes of the heatmaps the 0.5° PPI and 0.6° PPI scans are kept separate, see Figure 23 and Figure 24.

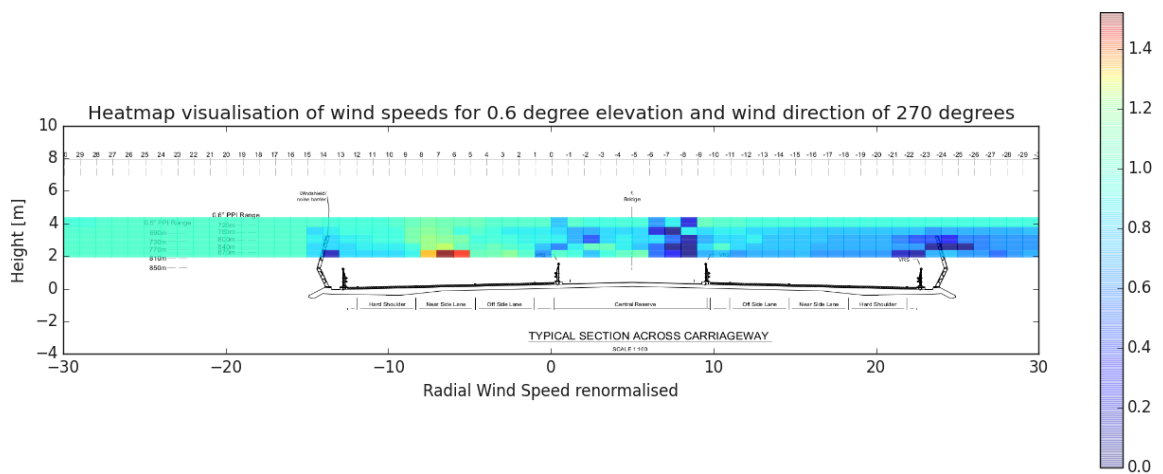


**Figure 23: Heatmap visualisation of normalised radial wind speed - 0.6° PPI scan, 270° direction**

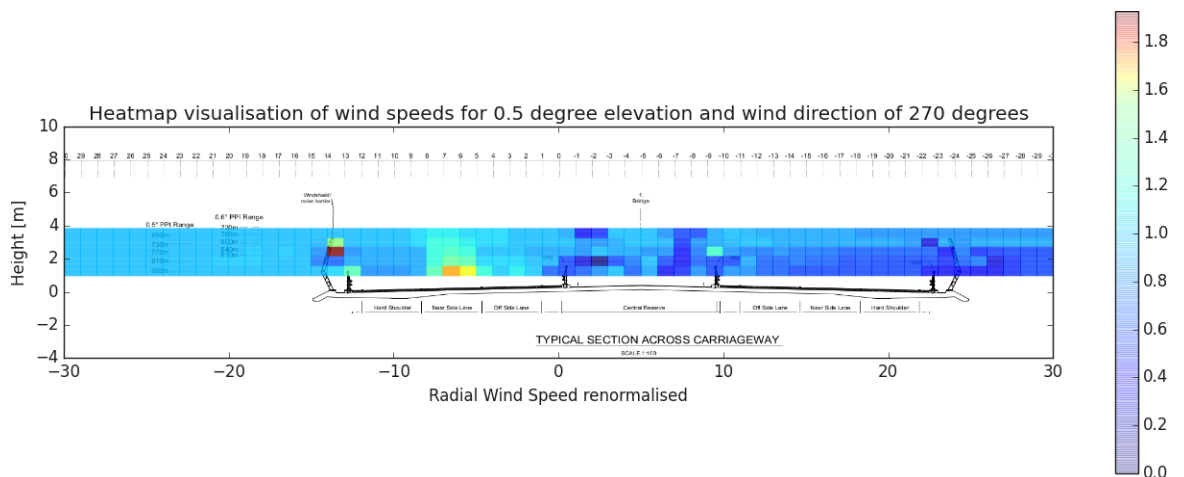


**Figure 24: Heatmap visualisation of normalised radial wind speed - 0.5° PPI scan, 270° direction**

The 0.6° scan, and the corresponding sections through the data, sit higher relative to the bridge barrier and carriageway than the 0.5° scan. Both scans identify the wind barriers on both sides of the bridge, and the cables in the central reserve. The area very close to these points is slightly distorted by the filtering process.

In both scans the presence of vehicles in Lane 1 and their subsequent wake, extending above the vehicle, is observed. This indicates that wind recorded in this area is heavily influenced by these vehicles. Vehicles in Lane 2 are not as obvious, as fewer vehicles use this lane and the averaging may be slightly masking the influence. As expected, the area around the hard shoulder does not appear to show any influence from vehicles. This provides a relatively clean data set in this area which can be further analysed.

### 3.7 Comparing site data with model results

The CFD and Wind Tunnel results, for wind speed reduction behind the wind barrier, recorded in the hard shoulder, are in broad agreement with each another, see Figure 25.

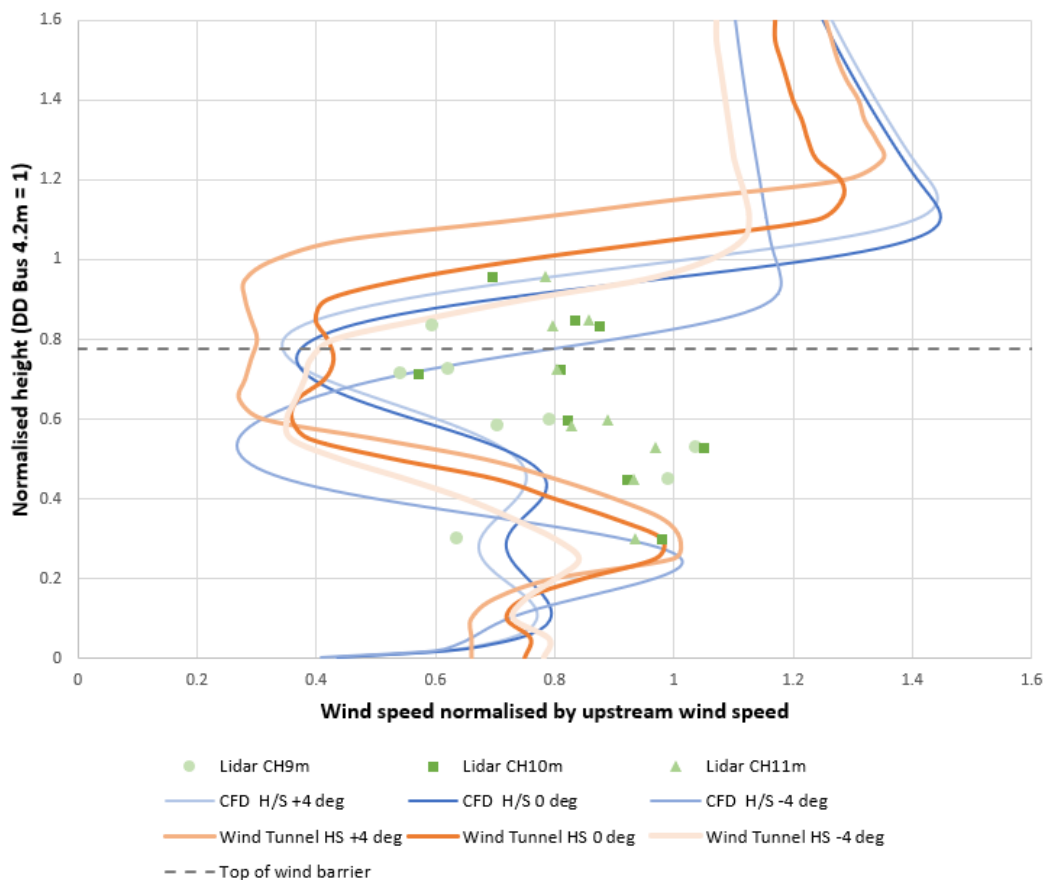


**Figure 25: Hard shoulder normalised wind speed results compared across Lidar, CFD, and Wind Tunnel tests.**

---

In all cases in Figure 25 the wind speed is normalised by a wind speed upstream of the wind barriers, and the height is normalised by the height of a double deck bus, approximated to be 4.2m. The differences in the model results can be accounted for by the 2D nature of the CFD modelling compared to the 3D wind tunnel, and the variance between a computer simulation and physical model. Both model simulations identify a change in the profile of the normalised wind speed behind the barrier when different angles of attack are considered, but while multiple wind speeds were tested only the maximum wind speed, 6m/s, for each of these models are presented as wind speed did not have a significant effect on the profile shape. Therefore, the results for the CFD and Wind Tunnel modelling include the extreme vertical angles of attack that were considered, +/- 4°, alongside the neutral 0° angle of attack results, to show the variance in the response when vertical angle of attack is modified. Figure 25 also includes the normalised site data recorded by the Lidar survey, green data points, for comparison.

The CFD and Wind Tunnel models both use a uniform upstream wind profile from a direction exactly perpendicular to the wind barrier. These controlled simulations allow detailed results to be extracted, and therefore show more refined profile shapes for the downstream normalised wind. The Lidar results are coarser sampled data, compared to the controlled model data, and are therefore shown as individual points on the graph, rather than a line.

There is broad general agreement in the simulations and site data, but there are some notable differences. In all three cases, CFD, wind tunnel test, and lidar data, a distinctive "S" shape is noted. In general, the wind speed behind the barrier for the models averages around 0.6 of the upstream wind, whereas for the Lidar data it averages around 0.8 of the upstream wind. The lower "nose" of the "S" shape for the model data aligns well with the gap in the wind barrier, which equates to approximately 1.3m above the carriageway, whereas for the Lidar data the "nose" sits higher up, at around 2.1m above the carriageway.

There are a number of factors that could explain the discrepancy between the models and the site data:

- The models allow a greater number of positions to be recorded, in a more controlled setting, with greater precision, providing a clearer, more accurate profile of wind barrier performance than can be achieved on site.

- 
- Vertical angle component of the wind on site is not known – the models show that this can have a significant effect, however this parameter is not recorded on site.
  - VRS, this is not modelled in CFD or Wind Tunnel models, as it is not part of the wind barrier. However, the VRS may be acting to deflect wind gusts coming through the gap in the barrier upwards. A similar effect was noted in the CFD modelling when the FCBC wind tunnel model barrier was modelled for general comparison, this single simulation included the VRS (as it was included in the FCBC wind tunnel model) and a hi-speed jet was observed deflecting the flow upwards, See Figure 5.11 in the *Investigation of Wind barriers on the Queensferry Crossing Computational Fluid Dynamics Study* report. The as-built VRS is not as dense as the one modelled in that CFD simulation, so it is not expected to produce the exact same result, but it may still have an effect.
  - The exact position of the lidar data point relative to the wind barrier. A lot of care was taken to align the Lidar data results with the bridge and wind barrier, however pinpointing a singly 3D point in a large (1km) scan relative to a comparatively small stationary object (wind barrier is approx. 3.26m high) is challenging. Small discrepancies in this alignment could move the position of this point and explain a 1m difference in position.
  - Interference from traffic in Lane 1 – both the turbulence caused by vehicles in Lane 1, and the traffic flow influencing the direction of the wind as opposed to the speed, subsequently changing the radial component of the wind, which the Lidar measures.
  - Averaging of data not sufficient to fully account for the alignment of the gusts affecting the data.

---

## 4 Conclusion

The Lidar survey, conducted between February and May 2020, was successful in providing valuable insight into the behaviour of wind around the Queensferry Crossing, and gave an indication of the performance of the wind barriers on site.

The survey provided a record of the complex nature of the wind flow across the Firth of Forth and around the bridges. Identifying the dynamic nature of gust patterns that change intensity and direction quickly with time. This makes the use of any threshold system that considers directionality but is based on the direction recorded at a stationary point averaged over a period of time, i.e. a weather station, unsuitable.

Batching the recorded scan data into directional ranges, taking sections through the data, and averaging the results across the data set, provided an indication of the performance of the wind barrier on site. The complex nature of the flow pattern through the barrier makes it difficult to capture the exact detail on site, however it was able to confirm the general outline "S" shape pattern that was observed in greater detail in the models, and indicated a reduction in wind speed approaching that observed in greater detail in the models, providing some confidence that the models were replicating the true nature of the wind barrier.

---

## **Appendix A Leosphere Initial Site Survey Report**

# SITE SURVEY REPORT

## WLS100S

### QUEENSFERRY CROSSING

#### AMEY

Confidential



**Leosphere**  
A VAISALA COMPANY



# Summary

<b>1.</b>	<b>Overview .....</b>	<b>3</b>
<b>2.</b>	<b>Site Description.....</b>	<b>5</b>
2.1.	Site Layout.....	6
2.2.	Environmental condition.....	7
2.2.1.	Weather condition .....	7
2.2.2.	Wind condition .....	7
2.3.	Site access and restrictions .....	9
<b>3.</b>	<b>Candidate Location .....</b>	<b>10</b>
3.1.	Candidate Location#1: Glass House .....	11
3.1.1.	Localization.....	11
3.1.2.	Obstacles .....	12
3.1.3.	Electrical power supply .....	13
3.1.4.	Network.....	13
3.1.5.	Site constraints .....	13
3.2.	Candidate Location#2: South Tower .....	14
3.2.1.	Localization.....	14
3.2.2.	Obstacles .....	15
3.2.3.	Site constraints .....	15
3.3.	Candidate Location#3: Gantry 8.....	16
3.3.1.	Localization.....	16
3.3.2.	Structure Description .....	17
3.3.3.	Obstacles .....	18
3.3.4.	Electrical power supply .....	19
3.3.5.	Network.....	19
3.3.6.	Site constraints .....	19
<b>4.</b>	<b>Evaluation of candidate location.....</b>	<b>20</b>
<b>5.</b>	<b>Conclusion .....</b>	<b>22</b>



# 1. Overview

<b>Site survey date</b>	20 <sup>th</sup> November 2019
-------------------------	--------------------------------

<b>Client</b>	AMEY
<b>Supplier</b>	Leosphere / Vaisala
<b>Instructions</b>	AMEY Subcontractors Instruction, FB/VAI/014, JSFDW1900613
<b>Date of Instructions</b>	13th November 2019

<b>Context</b>	<p>This project is led by Amey who is renting a Windcube 100S with PPI mapping post processing service to verify the effect of the wind shielding on the Queensferry crossing bridge.</p> <p>Further information is provided in the document “Technical proposal v2 of 5th September 2019 included in the VAISALA offer dated 19th September 2019.”</p>
----------------	---

<b>Site location</b>	Queensferry Crossing road bridge, Edingburgh, United-Kingdom
<b>Client attendees</b>	<ul style="list-style-type: none"> <li>Patrick MADDEN, Assistant Engineer, AMEY</li> </ul>
<b>Supplier attendees</b>	<ul style="list-style-type: none"> <li>Ameya PASEBAND, Service Field Engineer, LEOSPHERE</li> <li>Gerry SHARP, Field Engineer, Vaisala UK</li> </ul>

<b>Version history</b>			
Rev	Author	Date	Description
00	Ameya Paseband Jerome Southammakosane	10-Dec-2019	Initial version



## 2. Site Description

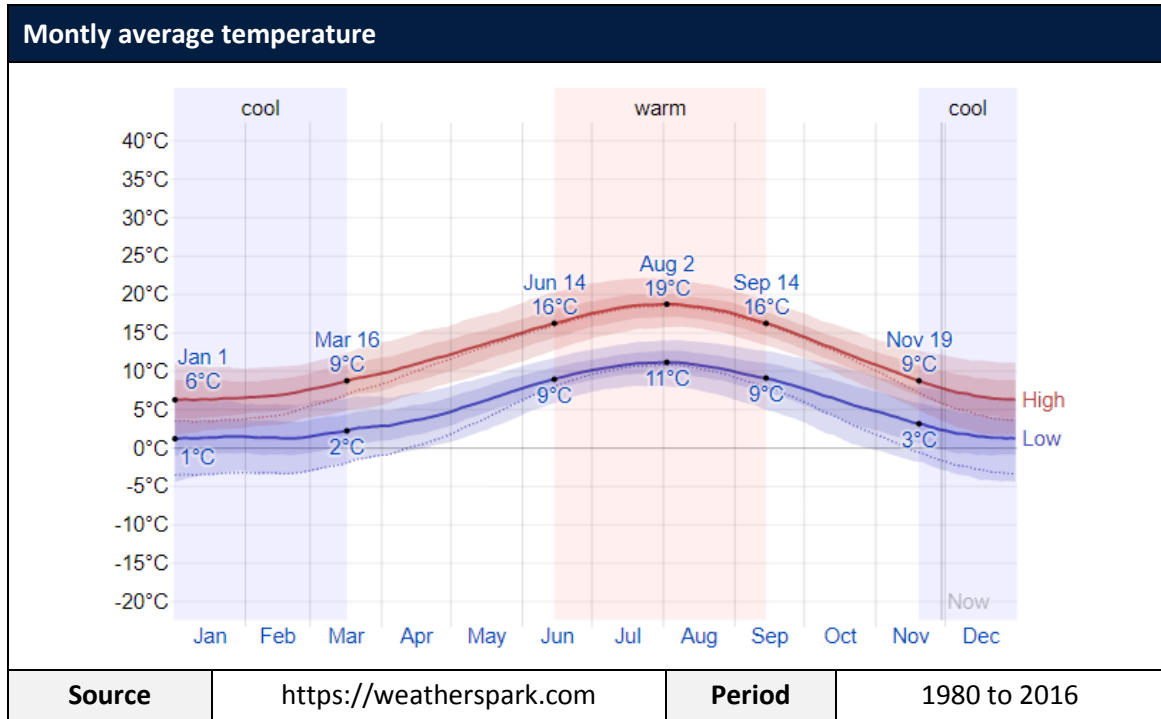


## 2.1. Site Layout

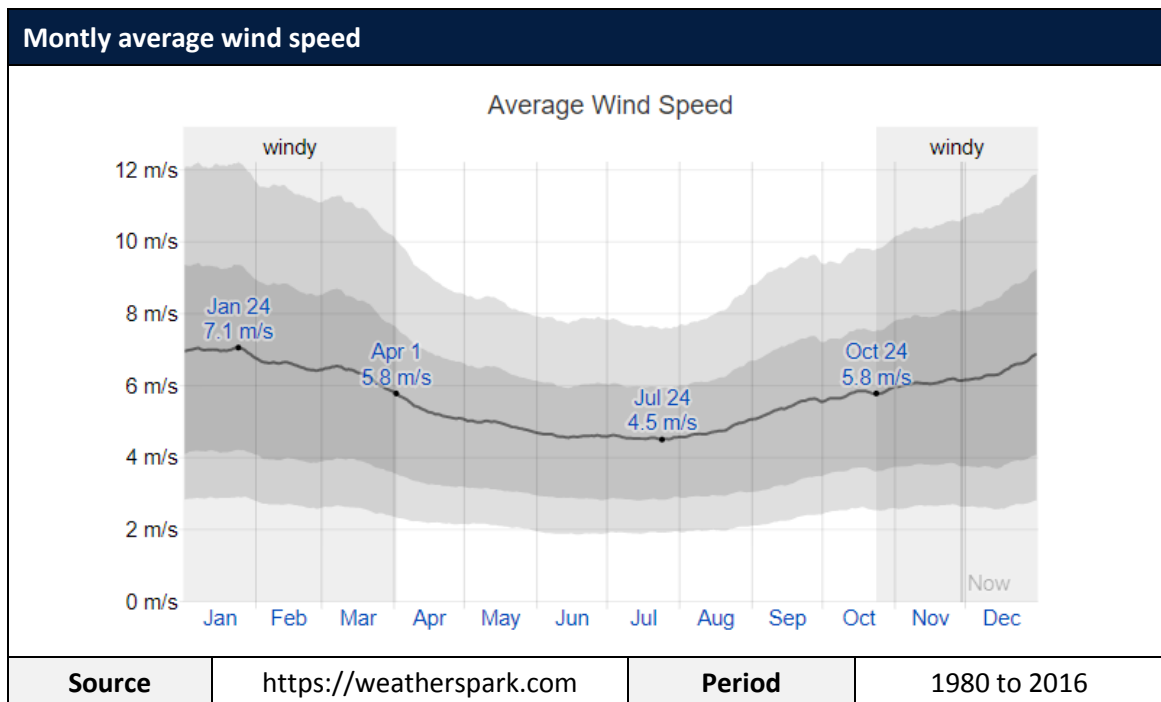
<b>Site Name</b>	Queensferry Crossing
<b>Site GPS Coordinates</b>	55.987476, -3.425377
Point of Measurement	Description
<b>Wind Shield</b>	<p>Along the bridge from the location where the barrier transitions from solid noise barrier to porous wind barrier to the hump of the bridge: 200m to 1560m from glass house.</p> <p>The highest elevation of bridge deck is at the central tower: 63.717m from road design level. The RDL at the glass house is 40.137m. Therefore the difference between road level at the glasshouse and the central tower is approximately 23.58m</p>
Candidate Location	Description
<b>Location #1</b>	Glass House (55.991619, -3.420843)
<b>Location #2</b>	South Tower (55.999328, -3.416188)
<b>Location #3</b>	Gantry 8 (55.991280, -3.421332)

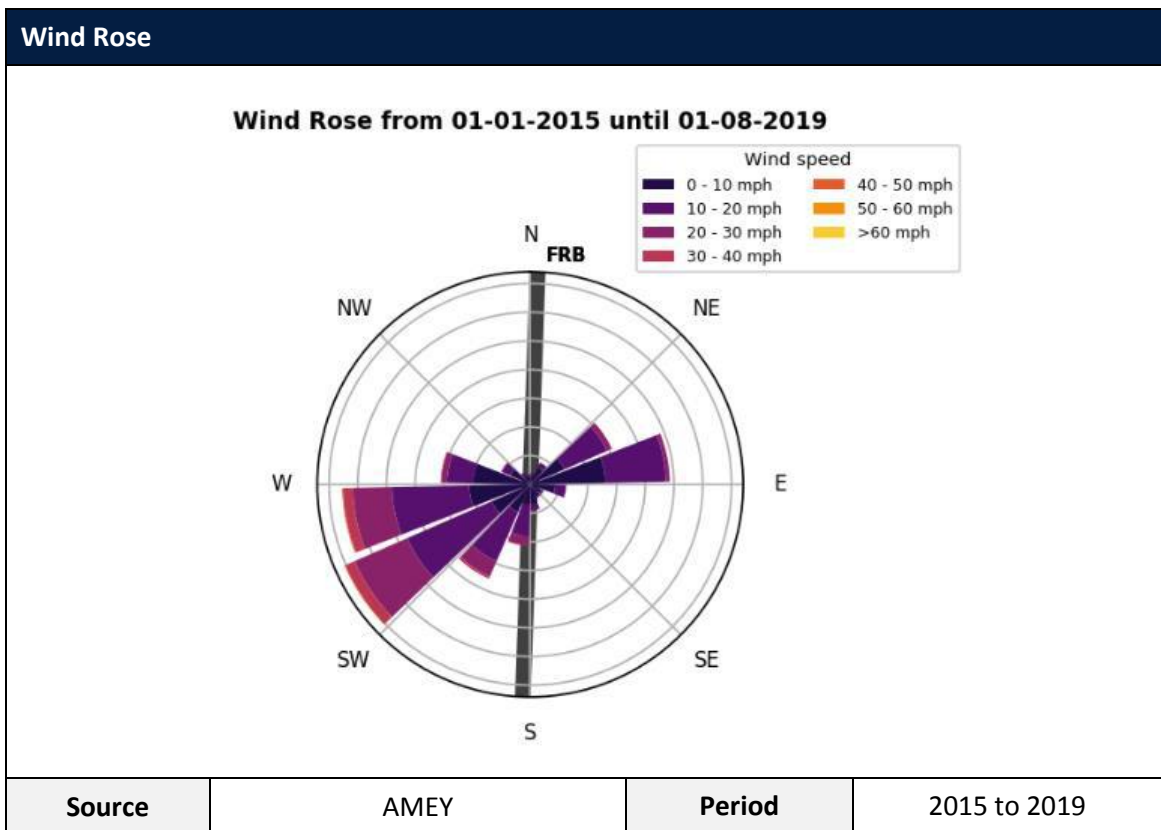
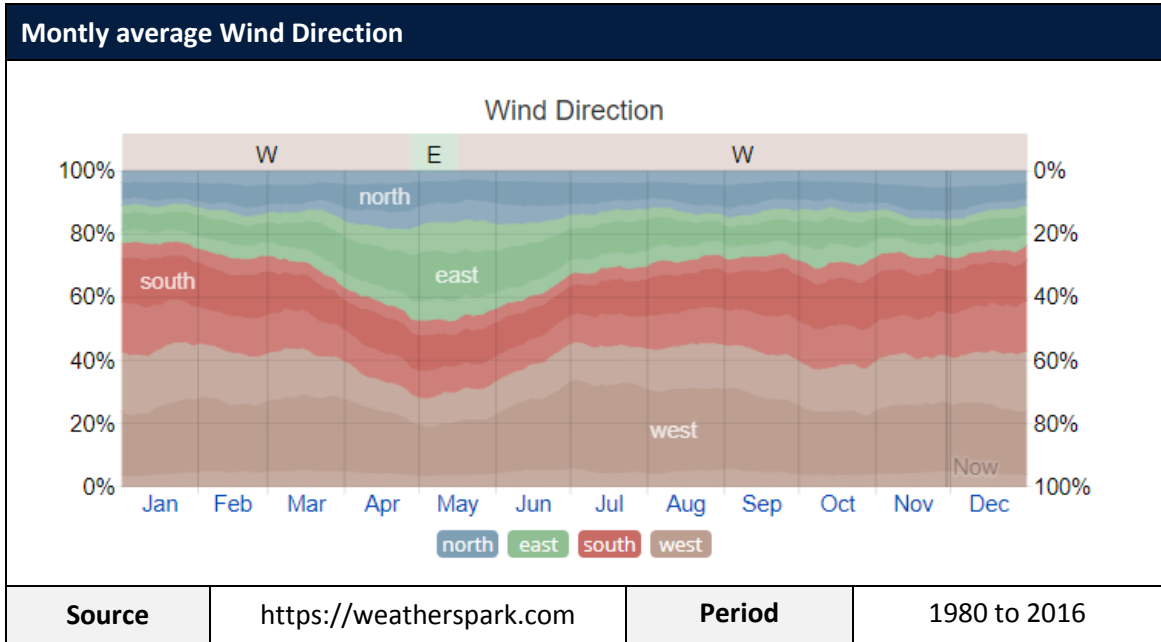
## 2.2. Environmental condition

### 2.2.1. Weather condition



### 2.2.2. Wind condition





## 2.3. Site access and restrictions

Limited access area	<input checked="" type="checkbox"/> Yes	<input type="checkbox"/> No
	<b>Comment:</b> Permit access required before site visit. Administrative procedure takes usually 0.5 day. Requires passport and portrait photo.	
Safety course required	<input checked="" type="checkbox"/> Yes	<input type="checkbox"/> No
	<b>Comment:</b> 1 hour on site safety induction course is mandatory. Drug and Alcohol test to be taken on site, prior to site visit. Process takes up to 4 hours in total.	
Risk and method assessment required	<input type="checkbox"/> Yes	<input checked="" type="checkbox"/> No
	<b>Comment:</b>	
Personal safety certification	<input type="checkbox"/> Yes	<input checked="" type="checkbox"/> No
	<b>Comment:</b>	
Personal protective equipment required	<input checked="" type="checkbox"/> Yes	<input type="checkbox"/> No
	<b>Comment:</b> Each visitor must have his own safety shoes and hard hat. Hi-vis jackets and pants.	
Personal IT equipment authorized	<input checked="" type="checkbox"/> Yes	<input type="checkbox"/> No
	<b>Comment:</b> Visitors are allowed to bring camera, mobile phone and computer.	
Specific tools authorized	<input checked="" type="checkbox"/> Yes	<input type="checkbox"/> No
	<b>Comment:</b>	
Others	<input type="checkbox"/> Yes	<input checked="" type="checkbox"/> No
	<b>Comment:</b>	



## 3. Candidate Location

### 3.1. Candidate Location#1: Glass House

#### 3.1.1. Localization

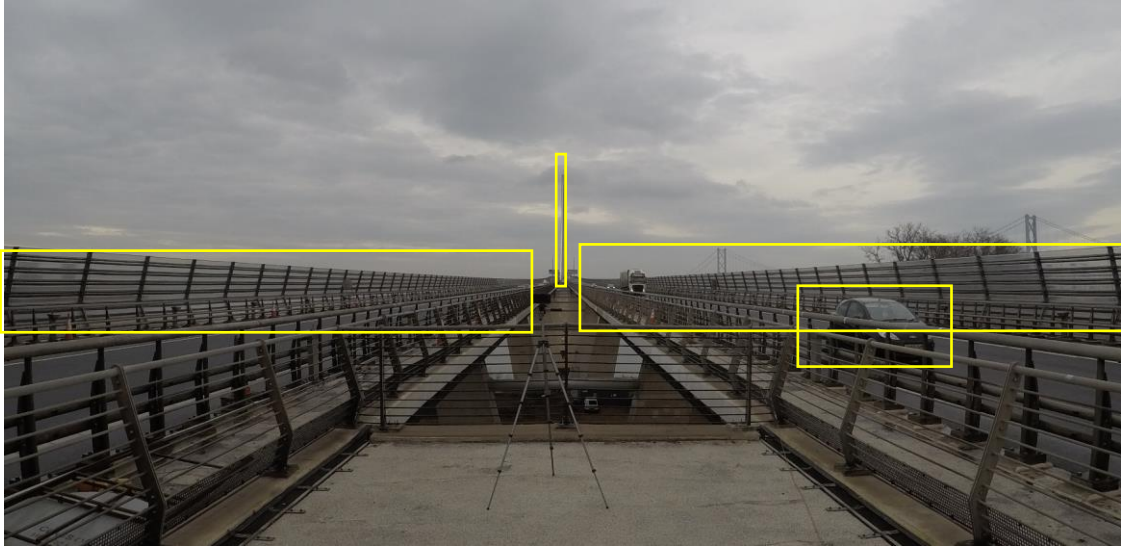


<b>GPS Coordinates</b>	55.991619, -3.420843	
<b>Platform material</b>	Concrete surface	
<b>Available space around the Lidar</b>	4m x 5m.	
<b>Maximum weight</b>	Sufficient to withstand more than the weight of LiDAR + 2 operators.	
<b>Access by car/truck</b>	<input checked="" type="checkbox"/> Yes	<input type="checkbox"/> No
<b>Site secured</b>	<input type="checkbox"/> Yes	<input checked="" type="checkbox"/> No
<b>Crane Required</b>	<input checked="" type="checkbox"/> Yes	<input type="checkbox"/> No
<b>Others</b>	Two lane closures would be required. One to construct the scaffolding (if any). The Second to lift and install the lidar on the scaffolding.	

3.1.2. Obstacles

**Obstacles location**

**North View: Obstructions in Yellow: Wind Shield, South tower, Traffic**



**South View: Obstructions in Yellow: Gantry8, Traffic, Glass House**



**Infrastructure required to avoid obstacles**

<b>Platform/Tower required?</b>	<input checked="" type="checkbox"/> Yes	<input type="checkbox"/> No
<b>Minimum height</b>	At least 4m (To avoid the traffic)	

**3.1.3. Electrical power supply**

<b>Power supply available</b>	<input type="checkbox"/> Yes	<input checked="" type="checkbox"/> No
<b>Maximum power available</b>	N/A	
<b>Electrical ground available</b>	<input type="checkbox"/> Yes	<input checked="" type="checkbox"/> No
<b>Lightning protection available</b>	<input type="checkbox"/> Yes	<input checked="" type="checkbox"/> No

**3.1.4. Network**

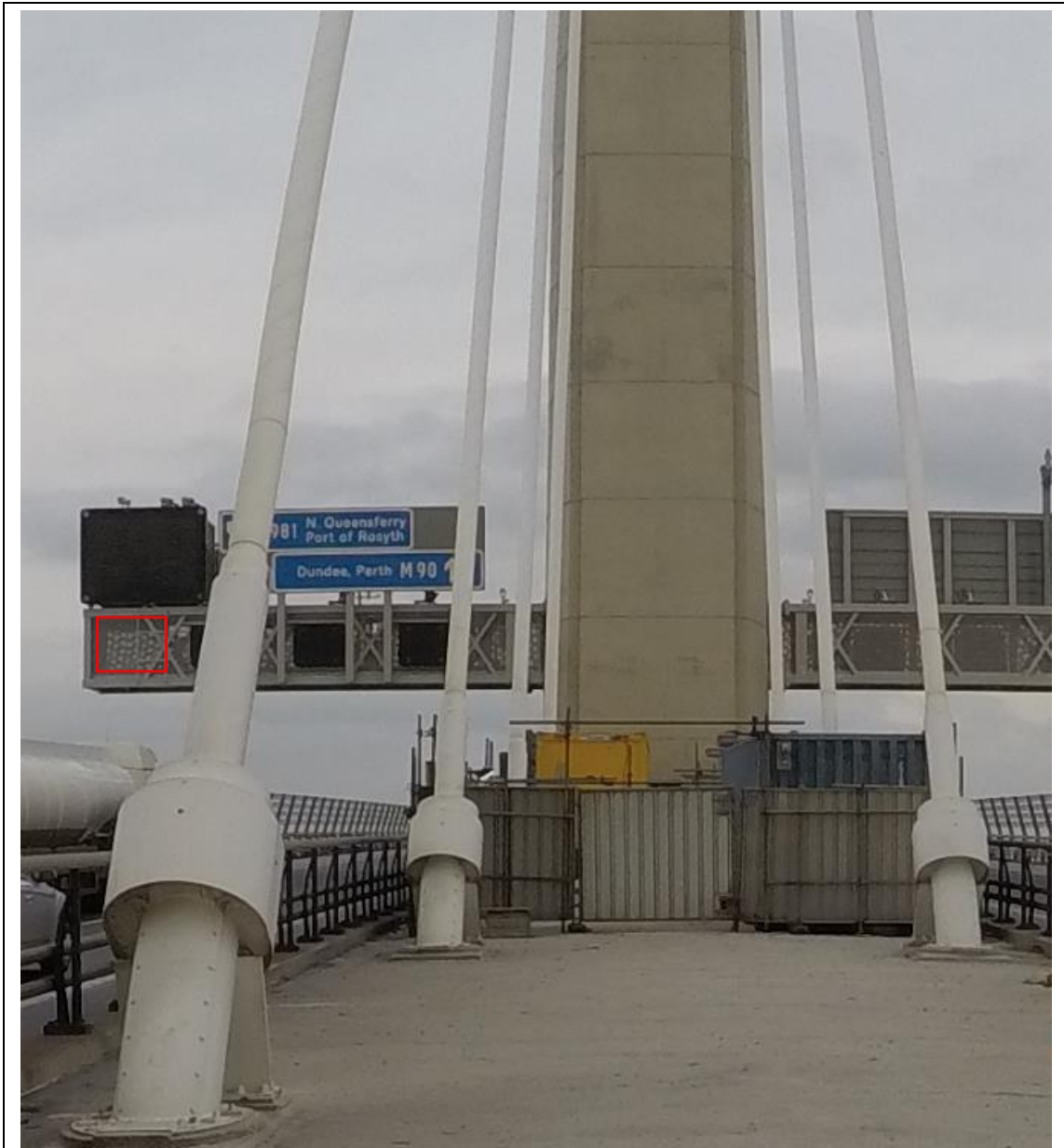
<b>Network available on site</b>	<input type="checkbox"/> Yes	<input checked="" type="checkbox"/> No	
<b>Interface type is RJ45</b>	<input type="checkbox"/> Yes	<input checked="" type="checkbox"/> No	
<b>Network type</b>	<input type="checkbox"/> LAN cable	<input type="checkbox"/> Optical fiber	<input type="checkbox"/> Wireless
<b>Maximum baud rate</b>	Not applicable		

**3.1.5. Site constraints**

- None reported by the client during the site survey.

### 3.2. Candidate Location#2: South Tower

#### 3.2.1. Localization



<b>GPS Coordinates</b>	55.999328, -3.416188	
<b>Height above bridge deck (m)</b>	10m	
<b>Platform material</b>	Metal truss structure	
<b>Available space around the Lidar</b>	More than 1m space around the Lidar	
<b>Maximum weight</b>	Sufficient to withstand more than the weight of LiDAR + 2 operators.	
<b>Access by car/truck</b>	<input checked="" type="checkbox"/> Yes	<input type="checkbox"/> No
<b>Site secured</b>	<input checked="" type="checkbox"/> Yes	<input type="checkbox"/> No

### 3.2.2. Obstacles

#### Obstacles location

The south tower installation site is very difficult to access- the structure above and below both prevent the lidar from being lifted into place. As a result this site is a No-Go.



### 3.2.3. Site constraints

- None reported by the client during the site survey

### 3.3. Candidate Location#3: Gantry 8

#### 3.3.1. Localization



<b>GPS Coordinates</b>	55.991280, -3.421332	
<b>Height above bridge deck (m)</b>	Approx. 8m	
<b>Platform material</b>	Metal Truss Structure	
<b>Available space around the Lidar</b>	More than 1m space buildable around the Lidar	
<b>Maximum weight</b>	Sufficient to withstand more than the weight of LiDAR + 2 operators.	
<b>Access by car/truck</b>	<input checked="" type="checkbox"/> Yes	<input type="checkbox"/> No
<b>Site secured</b>	<input checked="" type="checkbox"/> Yes	<input type="checkbox"/> No

### 3.3.2. Structure Description

The lidar will be positioned in the spot here :



The mesh ahead of the lidar position will be removed :



<b>Crane required</b>	<input checked="" type="checkbox"/> Yes	<input type="checkbox"/> No	
<b>Physical access to the roof/platform?</b>	<input checked="" type="checkbox"/> Yes	<input type="checkbox"/> No	Ladders

### 3.3.3. Obstacles

#### Obstacles location

North View: Obstructions in Yellow: South Tower



Obstructions: The surroundings of the lidar, except for the removed part of the mesh



#### Infrastructure required to avoid obstacles

<b>Platform/Tower required?</b>	<input type="checkbox"/> Yes	<input checked="" type="checkbox"/> No
<b>Minimum height</b>	Not required	

### 3.3.4. Electrical power supply

<b>Power supply available</b>	<input type="checkbox"/> Yes	<input checked="" type="checkbox"/> No
<b>Maximum power available</b>	0W	
<b>Electrical ground available</b>	<input type="checkbox"/> Yes	<input checked="" type="checkbox"/> No
<b>Lightning protection available</b>	<input type="checkbox"/> Yes	<input checked="" type="checkbox"/> No

### 3.3.5. Network

<b>Network available on site</b>	<input type="checkbox"/> Yes	<input checked="" type="checkbox"/> No	
<b>Interface type is RJ45</b>	<input type="checkbox"/> Yes	<input checked="" type="checkbox"/> No	
<b>Network type</b>	<input type="checkbox"/> LAN cable	<input type="checkbox"/> Optical fiber	<input type="checkbox"/> Wireless
<b>Maximum baud rate</b>	Not applicable		

### 3.3.6. Site constraints

- None reported by the client during the site survey.

## 4. Evaluation of candidate location

Each candidate location is evaluated following the amount of additional work required in order to make it compliant with the Lidar operation. Here after the evaluation criteria.

- No additional work required
- Some works required
- Not available during site survey. Under customer’s responsibility
- Heavy works required
- No-Go / No reasonable solution

Candidate location		#1: Glass House	#2: South Tower	#3: Gantry 8
<b>Coverage area</b> Sector of interest / Obstacles		Many obstacles, requires at least a 4m scaffolding to avoid the traffic. Good visibility along the bridge for objective 1 and 2 with the scaffolding	Line of sights blocked by the structure walls for objective 1 (no solution) Acceptable visibility along the bridge for objective 2	Good visibility along the bridge for objective 2 without additional structure. Sight blocked by the gantry walls for objective 1. Requires adding a structure on the gantry to raise the Lidar above the walls.
<b>Site access</b>	<b>Transport case</b>	Ok for truck access	Ok for truck access	Ok for truck access
	<b>Equipment installation</b>	Crane required to install the Lidar on the foreseen scaffolding	External crane required but no access available	Crane required to install the Lidar on the gantry
		Unpacking space required is 3 x 4m. It can be done on the bridge as the traffic will be shut down for the installation		
	<b>Staff access</b>	<ul style="list-style-type: none"> <li>Stairs or Ladder available</li> <li>Permit access required before site visit</li> <li>Induction and drug/alcohol tests on site (4 hours)</li> <li>Safety shoes, hard hat, hi-vis jackets and pants required</li> </ul>		
<b>Installation location</b>	<b>Installation location</b>	Platform hard material, Space around Lidar > 1m, Maximum load OK, No exposure to contaminants, Anchorage points available		
	<b>Electrical power supply and protection</b>	Power outlet available but connection to be made. Requirements: <ul style="list-style-type: none"> <li>Connector type</li> <li>Max power &gt; 1.6kW</li> <li>Ground available</li> <li>Distance to Lidar &lt; 10m</li> </ul>		
	<b>Lightning protection</b>			
	<b>Network</b>	Not available. To be designed. 4G or WIFI connection foreseen. Requirements: <ul style="list-style-type: none"> <li>Remote access for scan optimization and monitoring</li> <li>Data download for post processing</li> <li>50Gb / day for radial wind data and spectrum data</li> </ul>		



## 5. Conclusion

## Conclusion

The Location#3: Gantry#8 is the preferred location for the purpose of fulfilling the objective 1 and objective 2 described in the “Technical proposal v2 of 5th September 2019 included in the VAISALA offer dated 19th September 2019.”

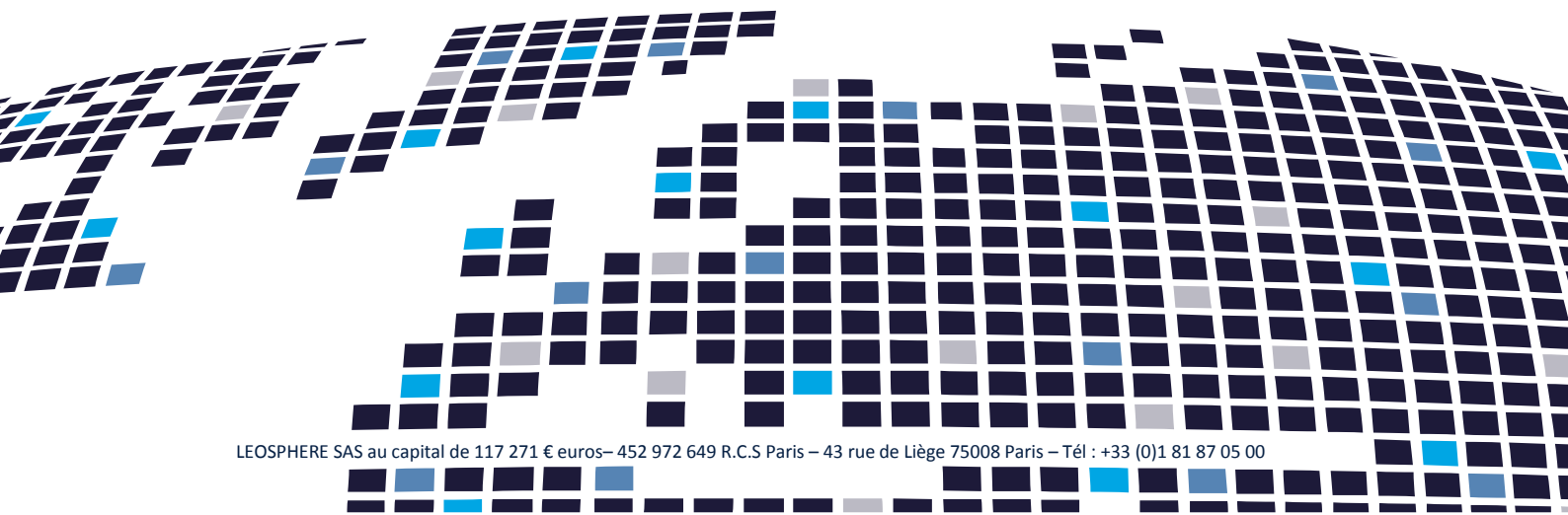
The objective 2 can be achieved from this location without additional civil work.

However, it is noted that objective 1 will require an additional structure on the gantry to raise the Lidar above the walls and enable the 180° to 360° PPI scan.

The proposed horizontal scan (PPI) would be with a positive elevation angle so to scan above the highest point of the bridge. This scan will be above but very close to the traffic, this latter may disturb the wind flow and hence, the Lidar measurement.



**LEOSPHERE**  
A VAISALA COMPANY



---

## **Appendix B Leosphere Installation Report**

AMEY Consulting

# INSTALLATION REPORT

30<sup>th</sup> January 2020

Confidential



**LEOSPHERE**  
A VAISALA COMPANY



# Summary

1. Overview .....	3
2. Service performed.....	5
3. Final Result .....	8
4. Comments .....	13



# 1. Overview

Start Date: 2020-01-28

End Date: 2020-01-30

Client	
AMEY	
System model	Serial number
WLS100S	WLS100S-134
Client attendees	
<ul style="list-style-type: none"> <li>Patrick MADDEN</li> <li>Dan</li> </ul>	
LEOSPHERE / EKO attendees	
Ameya PASEBAND, Field Engineer, Leosphere Gerry SHARP, Field Engineer, Vaisala	

Site	
55°59'28.6"N 3°25'16.8"W (55.991280, -3.421332) Office: Amey FBU, Queensferry, South Queensferry EH30 9SF	
Service performed	
<input type="checkbox"/> Training	<input checked="" type="checkbox"/> Installation
<input type="checkbox"/> FAT	<input type="checkbox"/> SAT
<input checked="" type="checkbox"/> Other: Hard target	

#### Context

- Site survey was performed in November 2019.
- Installation of the WLS100S-134 at Gantry#8 was planned as per the site survey document.

## 2. Service performed

# Installation

## Comments:

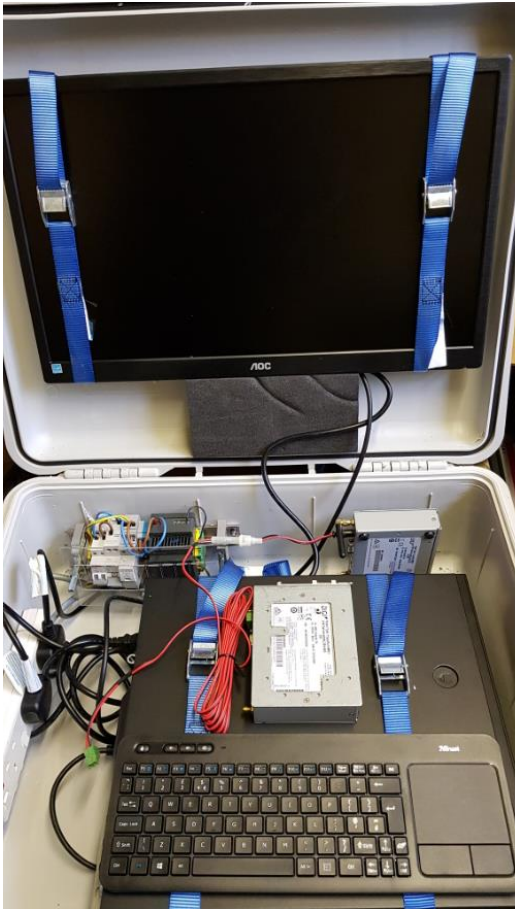
### 1. Lidar mock deployment



2. Lidar Lifted Overnight. Installation



3. Vaisala Cabinet installed next to LiDAR



### 3. Final Result

# ACCEPTANCE TEST

Designation	Conformity	Results			Decision
System cleaning	System is clean inside and outside				<input checked="" type="checkbox"/> OK <input type="checkbox"/> NOK
External condition	White shockwatch, Casing, Wiper Window, Doors Locks, Feet				<input checked="" type="checkbox"/> OK <input type="checkbox"/> NOK
Accessories condition	Power supply converter, Power cables LAN cable, Ground cable, 2 cranks				<input checked="" type="checkbox"/> OK <input type="checkbox"/> NOK
Protective caps	All trapdoor not-cabled-connectors have a caps and they are all plugged				<input checked="" type="checkbox"/> OK <input type="checkbox"/> NOK
S/N and IP stickers	S/N and IP visible on casing stickers	S/N = WLS100S-134			<input checked="" type="checkbox"/> OK <input type="checkbox"/> NOK
Internal condition	Door seal, Connectors tightened No moving parts, Desiccant, Optical fibers				<input checked="" type="checkbox"/> OK <input type="checkbox"/> NOK
Laser beam locked	XY screws, Emission Module screws and Focal screw are locked				<input checked="" type="checkbox"/> OK <input type="checkbox"/> NOK
Warranty Void stickers	4 stickers in good conditions				<input checked="" type="checkbox"/> OK <input type="checkbox"/> NOK
Power supply	100Vac < VAC < 240Vac VDC > 25.5VDC (3 cables)	VAC = 232V	VDC = 26.11V		<input checked="" type="checkbox"/> OK <input type="checkbox"/> NOK
Condensation pump	Start after power up				<input checked="" type="checkbox"/> OK <input type="checkbox"/> NOK
LEDs	LEDs of Power converter, Trapdoor, PC and Optical rack are ON after power up				<input checked="" type="checkbox"/> OK <input type="checkbox"/> NOK
Fans	Peltiers (x4), EDFA, PC Optical rack fans are ON after power up				<input checked="" type="checkbox"/> OK <input type="checkbox"/> NOK
Peltiers test	Air flow correct when Peltiers active				<input checked="" type="checkbox"/> OK <input type="checkbox"/> NOK
Internal battery	LED is green, no error wiring (red)				<input checked="" type="checkbox"/> OK <input type="checkbox"/> NOK
Internal Desiccant	Desiccant indicator is orange				<input checked="" type="checkbox"/> OK <input type="checkbox"/> NOK
System closing	4 locks are locked				<input checked="" type="checkbox"/> OK <input type="checkbox"/> NOK
Scanner head start	Scanner head homing after system start				<input checked="" type="checkbox"/> OK <input type="checkbox"/> NOK
Server start	Successful connection with GUI	IP = 192.168.15.15	Server Version = 3.1.1		<input checked="" type="checkbox"/> OK <input type="checkbox"/> NOK
Lidar status	No persistent critical status in real time				<input checked="" type="checkbox"/> OK <input type="checkbox"/> NOK
Export Client configuration	Resolution, Setting, Scans				<input checked="" type="checkbox"/> OK <input type="checkbox"/> NOK
Automatic restart	Measurement start automatically after power cut (min. 10min)				<input checked="" type="checkbox"/> OK <input type="checkbox"/> NOK
Acquisition signal	Pulse available				<input checked="" type="checkbox"/> OK <input type="checkbox"/> NOK
Spectrum	No HF oscillation, No abnormal peaks, Fitting MLE				<input checked="" type="checkbox"/> OK <input type="checkbox"/> NOK
CNR	CNR > Noise level No peaks when window is blocked				<input checked="" type="checkbox"/> OK <input type="checkbox"/> NOK
Laser output power	100S: 350mW ± 50mW 200S: 700mW ± 100mW 400S: 1400mW ± 200mW	Output power= Not measured due to difficult weather conditions			<input type="checkbox"/> OK <input type="checkbox"/> NOK
Range and Focal distance	Range, Focal (1km) and CNR are consistent with weather condition.	Max Range= 3000 m	Focal= 1000 m	CNR= -15 db	<input checked="" type="checkbox"/> OK <input type="checkbox"/> NOK
Time synchronization	GPS status is OK, Lidar time is correct				<input checked="" type="checkbox"/> OK <input type="checkbox"/> NOK
Wiper pump	Wipe and pump function properly Water tank level				<input checked="" type="checkbox"/> OK <input type="checkbox"/> NOK
Scanner head movement	Noise at acceptable level, no vibrations or shock, smooth and continuous movement				<input checked="" type="checkbox"/> OK <input type="checkbox"/> NOK
Scanner head shutdown	Parking position is correct				<input checked="" type="checkbox"/> OK <input type="checkbox"/> NOK
Tradoor closing	2 screws are locked				<input checked="" type="checkbox"/> OK <input type="checkbox"/> NOK

## LIDAR INFORMATION (1/2)

Software version	V.3.1.1
FTP connection	ID: Not set.
IP Configuration	Static IP: 192.168.15.15
	Dynamic IP:

### Installation



#### Results

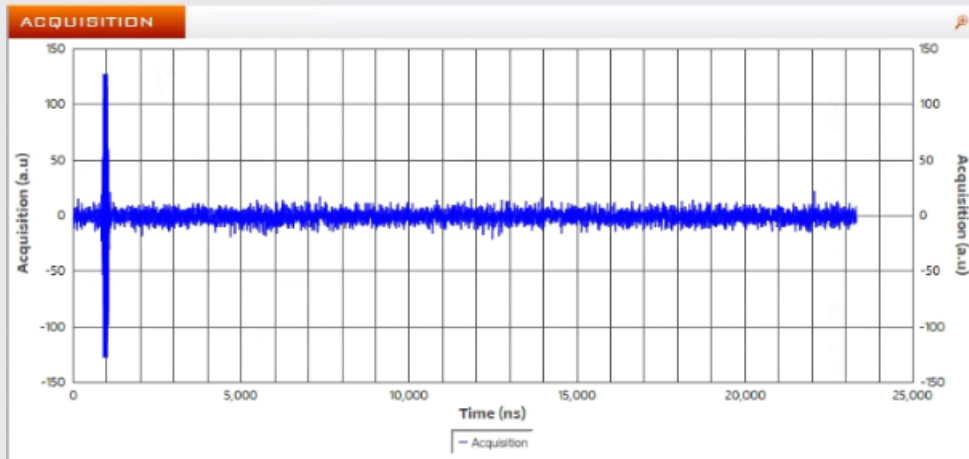
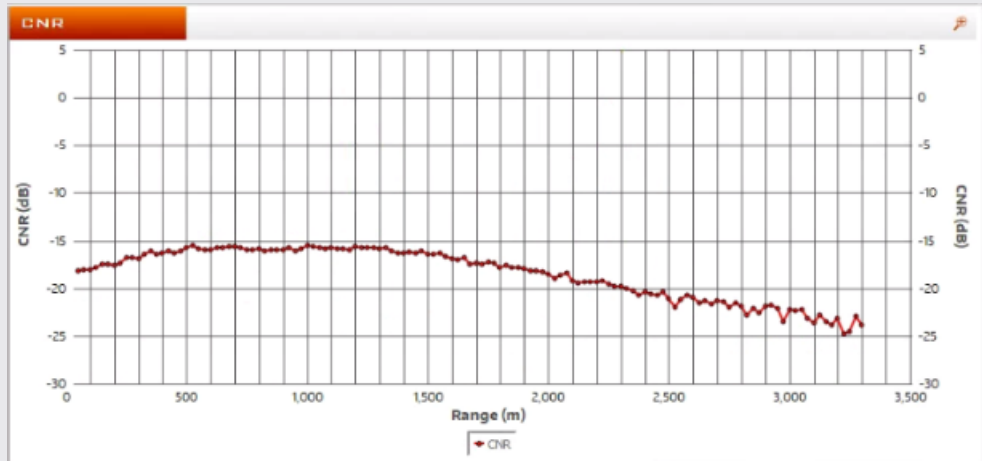
OK  NOK

#### Comments

Lidar wheels need to be stored indoors.

## LIDAR INFORMATION (2/2)

### Processing signals



#### Results

OK  NOK

#### Comments

CNR was lower than expected.

**Lidar Status**

DEVICE	STATUS	EXPLANATION	CODE	
Water pump	OK	Device OK	11	2020/01/30 23:27:02
Time synchronization	OK	Last synchronization date and time : 2020-01-30 23:26:46 Source: GPS	7	2020/01/30 23:27:02
Scanner	OK	Azimuth: 21.040 ° Elevation: -2.781 ° Counter: 0.001 % Last lubrication date and time: 2020-01-30 00:00:04	0	2020/01/30 23:27:03
Lidar 3.1.1 [192.168.3.134]	OK	LIDAR STATE: ACQUIRING	59	2020/01/30 23:27:00
Internal temperature	OK	Internal temperature: 19.3 °C	0	2020/01/30 23:26:58
Internal T° and RH sensor	OK	Device OK	7	2020/01/30 23:26:59
Internal RH	OK	Internal RH: 26 %	0	2020/01/30 23:26:53
Inclinometer	OK	Device OK	7	2020/01/30 23:27:02
Inclination	OK	Pitch: -0.012 ° Roll: -0.018 °	0	2020/01/30 23:27:02
Hard disk	OK	Device OK	7	2020/01/30 23:26:57
GPS receiver	OK	UTC date and time: 2020-01-30 23:27:01.000 Longitude: -3.421358 Latitude: 55.991333 GPS time updated GPS Position updated	7	2020/01/30 23:27:01
FTP 2	OK	Device OK	7	2020/01/30 23:27:01
FTP 1	OK	Device OK	7	2020/01/30 23:27:01
Edfa	OK	VER: K3SA3.7.L Laser: ON	0	2020/01/30 23:27:02
Disk occupation	OK	/dev/mapper/d-root: 1.2 %	0	2020/01/30 23:26:57
CPU load	OK	CPU load: 5 %	0	2020/01/30 23:27:01
Acquisition Loop	OK	Time of processing : 22 ms	0	2020/01/30 23:27:03
Acquisition board	OK	VER: 0004, 0005, 64 Acquisition board works normally	7	2020/01/30 23:26:57

Status screenshot

Results	Comments
<input checked="" type="checkbox"/> OK <input type="checkbox"/> NOK	

## 4. Comments

## Comments

Comments:

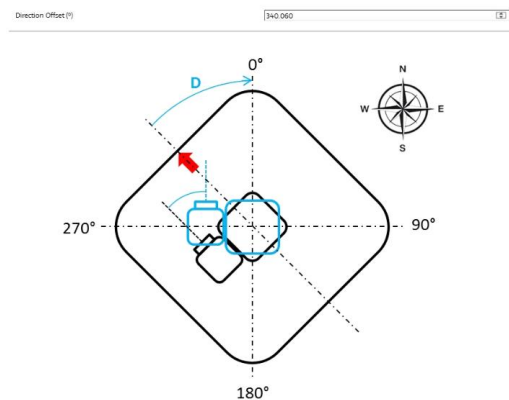
1. Hard Target Calculation as below.

USER INPUT VALUES				HARD TARGET		
<b>Items</b>	<b>Description</b>	<b>GPS DD</b>		<b>Lidar Hit Azimuth</b>		
		<b>Lat</b>	<b>Long</b>			
Scanning Lidar	Lidar 134	55,991303	-3,42138		NA	
Hard Target 1	Bridge 2 55.996957, -3.404476	55,996957	-3,404476			
Hard Target 2	QFC 55.999309, -3.415985	55,999309	-3,415985		1,1	
Hard Target 3	FR Bridge 56.005994, -3.404035	56,005994	-3,4040350		34	
Hard Target 4						
Hard Target 5						
CALCULATED RESULTS				OFFSETS MEASURED		
<b>Items</b>	<b>Description</b>	<b>Distance HT &lt;&gt; Lidar (m)</b>	<b>True Azimuth Angle</b>		<b>Azimuth Offset if Arrow on North's right</b>	<b>Azimuth Offset if Arrow on North's left</b>
Hard Target 1	dge 2 55.996957, -3.404476	1228	59,51		300,49	59,51
Hard Target 2	QFC 55.999309, -3.415985	952	21,04		340,06	19,94
Hard Target 3	Bridge 56.005994, -3.404035	1961	33,83		360,17	-0,17
Hard Target 4	0	6212816	182,84		177,16	182,84
Hard Target 5	0	6212816	182,84		177,16	182,84

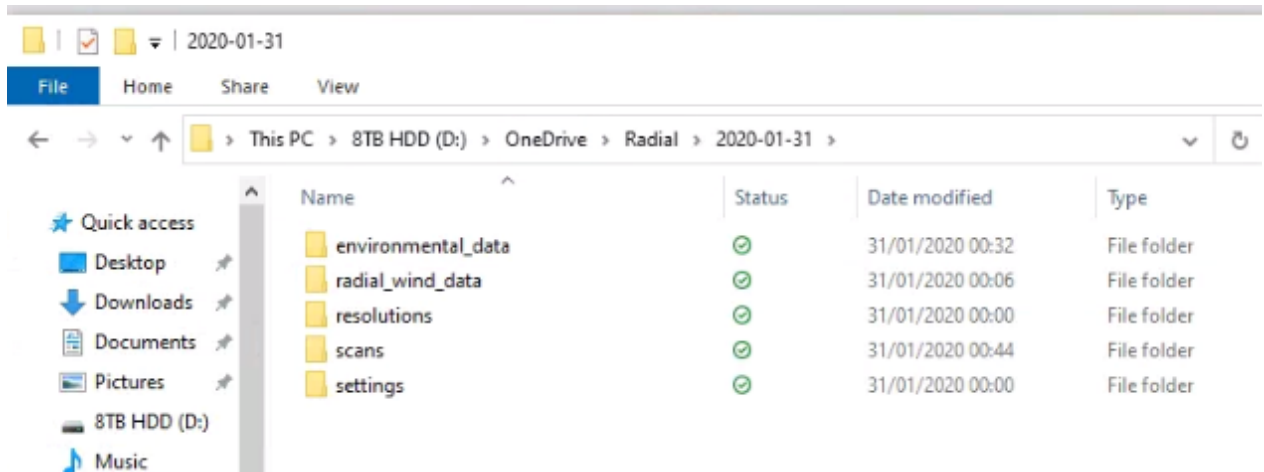
2. Hard Target detected at 1.1 degree azimuth



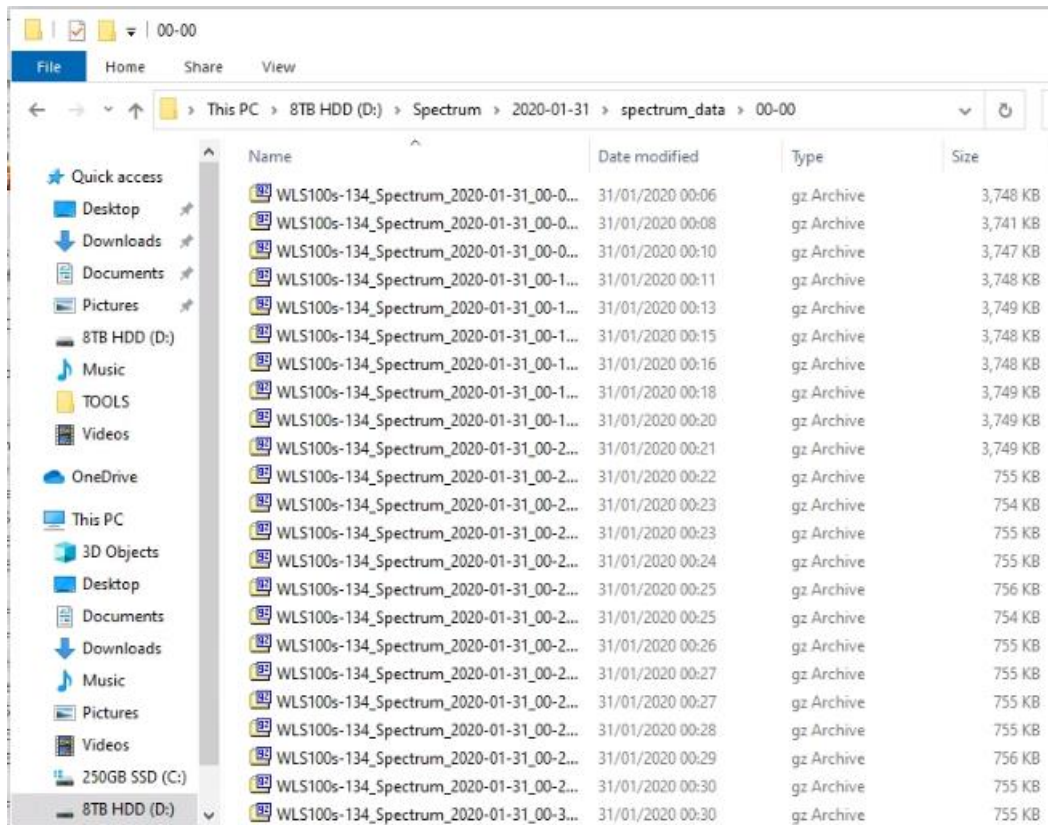
3. Offset of 340.06 degrees:



OneDrive folder: D:\OneDrive\

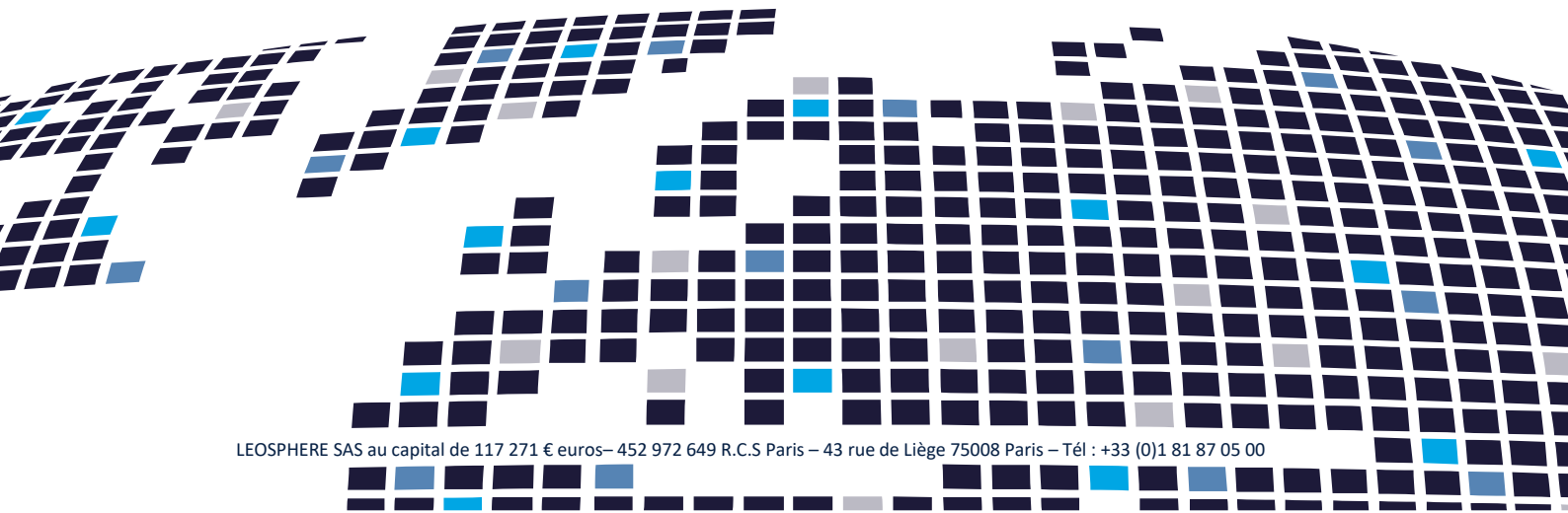


Spectrum Data Folder : D:\Spectrum





**LEOSPHERE**  
A VAISALA COMPANY



---

# Appendix C Leosphere Final Report

# Assessment of the impact of windshields on Queensferry bridge with Windcube 100S

---

	<b>Name</b>	<b>Date</b>
<b>Written by</b>	THOBOIS Ludovic TROIVILLE Anselme	05/21/2019
<b>Final version by</b>	THOBOIS Ludovic TROIVILLE Anselme	06/08/2019

<b>1.</b>	<b>Introduction</b>	<b>4</b>
1.1.	Presentation of Queensferry Crossing	4
1.2.	Problematic	4
<b>2.</b>	<b>Description of the study</b>	<b>7</b>
2.1.	Objectives	7
2.2.	Timeline	7
<b>3.</b>	<b>Installation</b>	<b>9</b>
3.1.	Lidar installation	9
3.2.	Description of scenarios	10
3.2.1.	PPI mesoscale	12
3.2.2.	PPI microscale	13
3.2.3.	RHI	13
3.2.4.	Table	14
3.3.	Scenarios time repartition	15
<b>4.</b>	<b>Lidar Monitoring &amp; operation</b>	<b>17</b>
4.1.	Remote monitoring	17
4.2.	Connection issue	18
4.3.	Synchronization delay	18
4.4.	Database overloading	19
<b>5.</b>	<b>Lidar data workflow</b>	<b>20</b>
<b>6.</b>	<b>Reconstructed wind – PPI Mesoscale</b>	<b>23</b>
6.1.	3D wind	23
6.2.	Results	23
<b>7.</b>	<b>PPI microscale preliminary observations</b>	<b>28</b>
7.1.	Data visualization	28
7.2.	Obstacles	30
7.2.1.	Tower effect	30
7.2.2.	Traffic – vehicles	31
7.3.	Filtering process	33
<b>8.</b>	<b>Wind shield effect</b>	<b>35</b>
8.1.	Primary observations	35
8.1.1.	Upstream vs downstream wind	35
8.1.2.	Gust	35
8.2.	Influence of Wind speeds	38
8.2.1.	Moderate winds (<8m/s) – Example of the 8 <sup>th</sup> of March	38
8.2.2.	Strong winds (>8m/s) - Example of 1st of March 2020	41
8.3.	Influence of wind direction	44
8.3.1.	South-East wind	44

*Assessment of the impact of windshields on Queensferry bridge with Windcube 100S*

8.3.2.	Wind direction perpendicular to bridge .....	44
<b>9.</b>	<b>Analysis – RHI .....</b>	<b>47</b>
9.1.1.	Tower and Gantry effect .....	47
9.1.2.	Complex wind .....	49
9.1.3.	Rain.....	49
<b>10.</b>	<b>Some limitations of the dataset .....</b>	<b>51</b>
10.1.	Radial issue .....	51
10.2.	Backlash .....	52
10.3.	Difference in obstacle detection at same elevation.....	53
<b>11.</b>	<b>Summary and Perspectives .....</b>	<b>55</b>
11.1.	Summary .....	55
11.1.1.	Achievements .....	55
11.1.2.	Main technical results .....	55
11.2.	Recommendations / Suggestions for future work .....	56

# 1. Introduction

## 1.1. Presentation of Queensferry Crossing

The Queensferry crossing is a 2.7km cable-stayed and long bridge opened in August 2017 close to Edinburgh with three towers of 207m high. It is the longest triple tower cable-stayed bridge in the world. Opened to traffic in August 2017, this bridge was built to smooth the road traffic in that region close to Edinburgh. It can handle more than 90,000 journeys a day.



Figure 1 – The Queensferry crossing

## 1.2. Problematic

As for many bridges around the world, local regulations commit the operator of the bridge to close the traffic in case of adverse and extreme weather conditions especially the wind conditions. More specifically, some procedures have been put in place as shown by the table below to ensure safety to road traffic, but this limit the use of the bridge.

The region where the bridge was built is frequently affected by high winds as shown by the wind rose below. Prevailing wind direction is South West to West whereas averaged wind speeds is usually around 20 mph and a significant part of the year wind speeds can reach 40 to 60 mph. Due to the prevailing winds, the effect on road traffic is stronger on Western side of the bridge, called the “A” carriageway.

During the design of the bridge, wind shields have been developed to reduce the impact of crosswinds effect in case of strong winds. The high wind procedures are significantly different between Queensferry crossing and the older Forth Road bridge located very close.

### High wind procedures: Queensferry Crossing

Wind Speed	Restrictions
Gusts > 50 mph ●	40mph speed limit on bridge
Gusts > 60 mph ●	Closed to double-deck buses
Gusts > 70 mph ●	Closed to: - All high-sided vehicles - Transit van style with modification - Vehicles with trailers or caravans - Vehicles with roof boxes or wind-susceptible roof rack items - Motorcycles - Three-wheeled cars - Any other vehicle which appears, in the judgement of bridge staff or the police, to be clearly at risk
Gusts > 90 mph ●	Closed to all vehicles except cars 30mph speed limit on bridge
Gusts > 100 mph ●	Closed to all traffic

### High wind procedures: Forth Road Bridge

Wind Speed	Restrictions
Gusts > 35 mph	40mph speed limit on bridge
Gusts > 45 mph	Closed to double-deck buses
Gusts > 50 mph	Closed to: - Motorcycles - Bicycles - Pedestrians
Gusts > 65 mph	Closed to all traffic

Figure 2 – Procedures in case of high winds

Wind Rose from 01-01-2015 until 01-08-2019

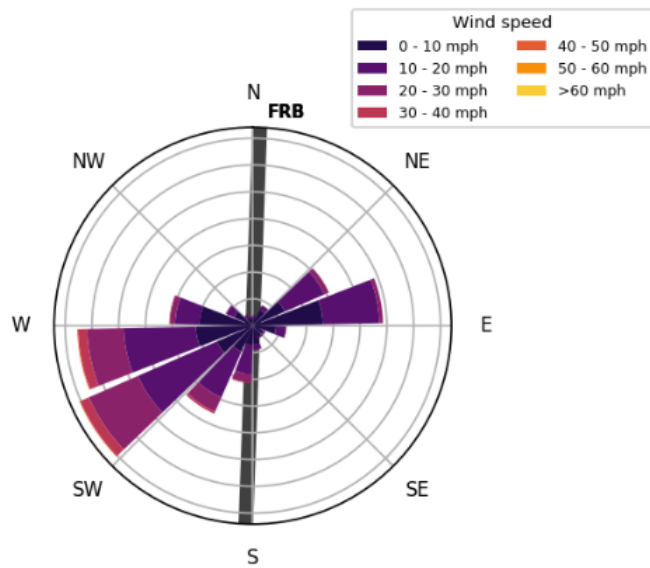


Figure 3 – Wind rose at Forth Road Bridge from 2015 to 2019

Assessment of the impact of windshields on Queensferry bridge with Windcube 100S



Figure 4 – Picture showing the wind shields and area of interest for the present study

## 2. Description of the study

### 2.1. Objectives

The objectives of the study are:

- To characterize the potential horizontal variations of wind around the bridge
- To collect relevant data for the study of the “positive” effect of wind shields on downstream winds with real scale wind measurements

With the deployment of a scanning Lidar Windcube100S during four months from February to May 2020. The Windcube100S provides real scale wind measurements by emitting pulses of light in the Infrared wavelength, backscattered by atmospheric particles and whose the frequency is shifted proportionally to the wind speed (motion of the particles in the atmosphere).

For the study, the Lidar measurements were focused on the area of interest length of about 1500m from Gantry to South Tower. Moreover, the objective is to characterize the wind fluctuations downstream the wind shields from the bridge deck to the top of the shields thus over a height of 4m and along the width of the bridge deck of about 40m (see Figure 4).

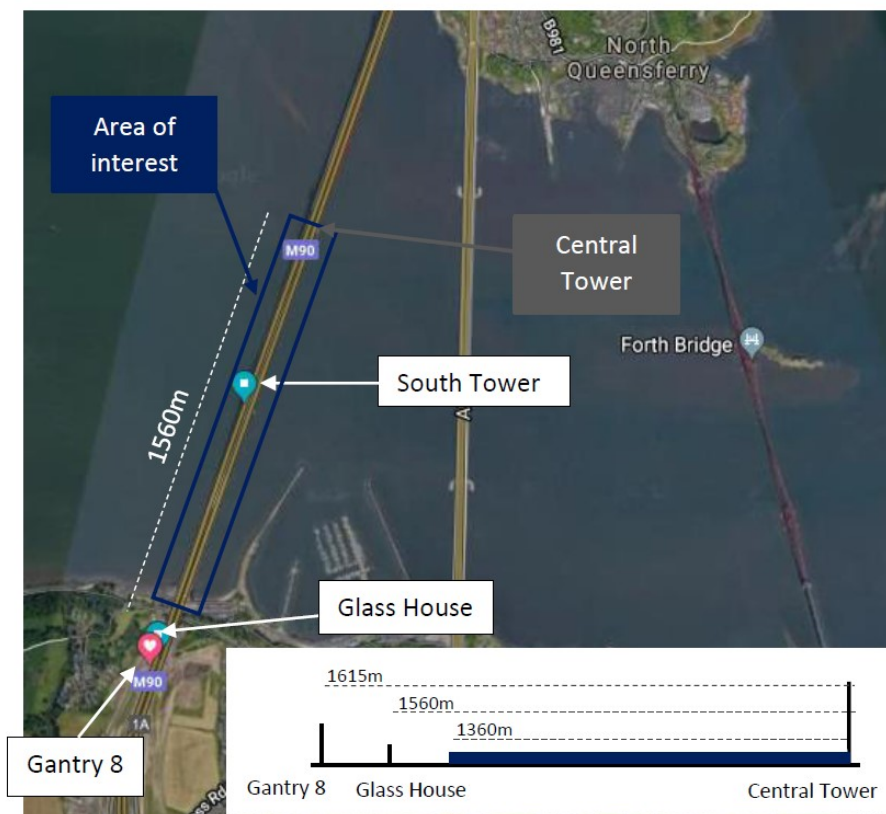


Figure 5 – Area of interest

### 2.2. Timeline

Assessment of the impact of windshields on Queensferry bridge with Windcube 100S

Tasks	LIDAR Project	Work load (Man Day)	M-2	M-1	M1	M2	M3	M4	M5	M6	M7	M8
WP1	2 months Campaign with potential extensions	-			█	█	█	█	█	█	█	█
WP2.1	Site survey	1	█									
WP2.2	Installation & Quick start	1		█								
WP2.3	Daily monitoring of Lidar	2		█	█	█	█	█	█	█		
WP3.1	Validation of Lidar configuration and scenarios	1		█								
WP3.2	Post-processing with PPI Mapping Tool	5			█	█	█	█	█			
WP3.3	Adaptation of EAV Tool	15				█	█	█	█	█	█	█
WP3.4	Post-processing with adapted EAV Tool	10					█	█	█	█	█	█
WP3.5	Data analysis	10						█	█	█	█	█
WP3.6	Delivery of data packages	2								█	█	
WP3.7	Delivery of technical report	2									█	█
WP4	Project management	5	█	█	█	█	█	█	█	█	█	█

The period from M3 to M4 corresponds to the extension linked to the Coronavirus outbreak.

## 3. Installation

### 3.1. Lidar installation

Prior to the installation, a site survey was performed in November 2019 to determine the best location for the system. Two sites with similar scanning potential were proposed for the Lidar installation: Glass House and Gantry 8. After deliberations, the gantry #8 was chosen.

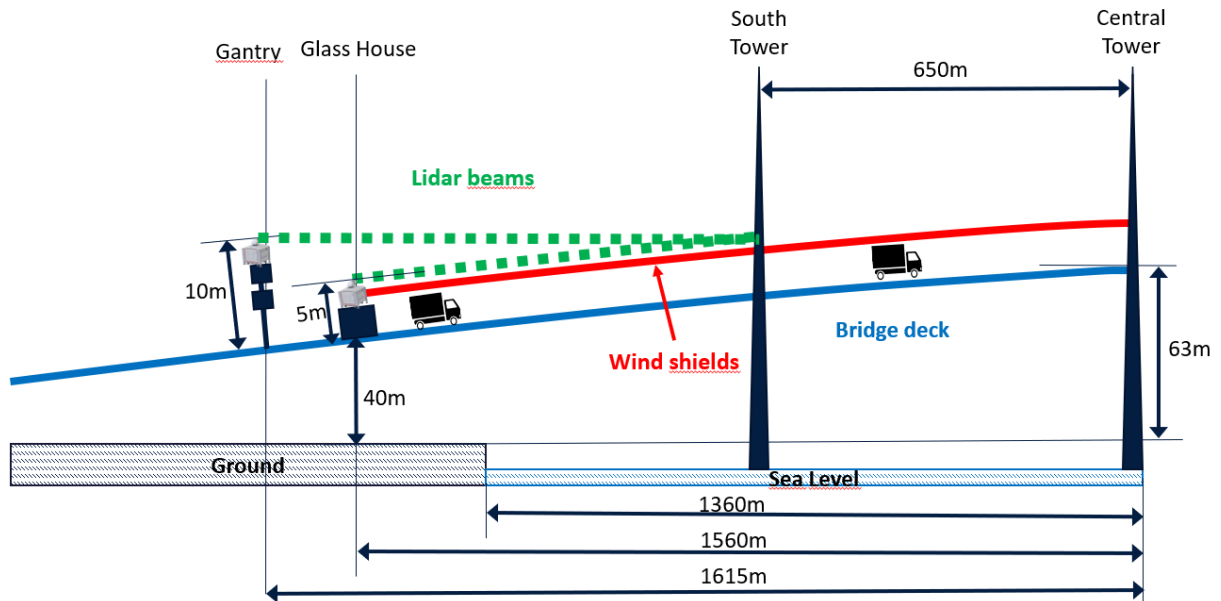


Figure 6: Layout of the bridge, wind shields and potential Lidar installation sites

The Lidar system was installed the 27th January 2020 at the GPS coordinates 55.991280° / - 3.421332°



Figure 7: Lidar installed on gantry #8

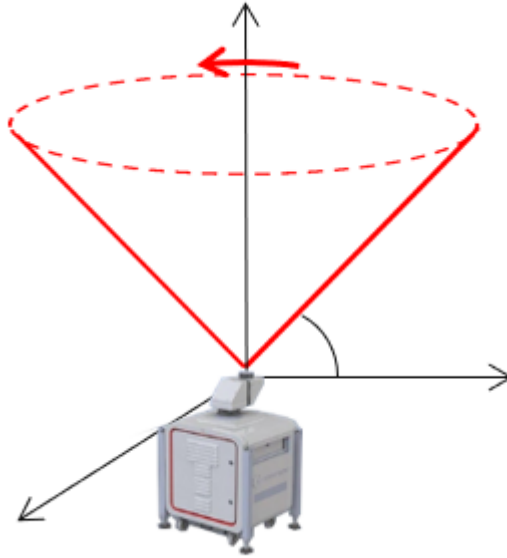
After 3 days of test, the Lidar system was deemed operational and started its measurements the 30<sup>th</sup> January in the evening.

A network connection was added to allow data transfer to a shared repertory.

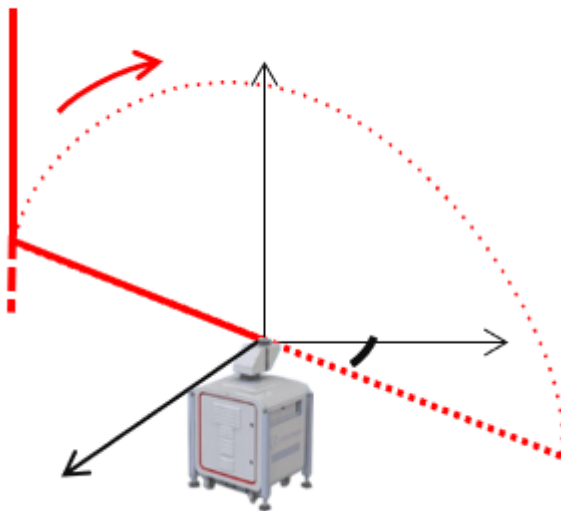
### 3.2. Description of scenarios

The definition of scenario was an essential part of the project to ensure the quantity and the quality of data generated. Many different scenarios were tested the first month. The Windcube scanning Lidar can perform measurements in four different modes:

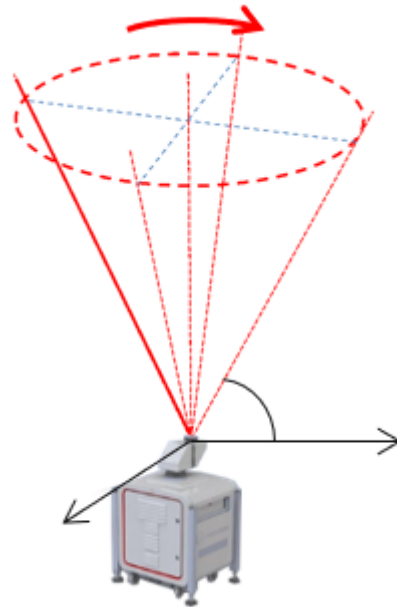
- LOS mode (Line of sight): fixed line of sight scenario with fixed elevation and azimuthal angles
- PPI mode (Plan Position Indicator): constant elevation angle scenario



- RHI mode (Range Height Indicator): constant azimuthal angle scenario



- DBS mode (Doppler Beam Swinging): vertical profile wind reconstruction which consists in four tilted beams oriented to the four cardinal points and one vertical line of sight.



The final scenarios chosen the 28<sup>th</sup> of February are described in section 0. A excel file gathers all the information about all the scenarios used from the beginning to the end of the campaign.

### 3.2.1. PPI mesoscale

As the goal of mesoscale PPI is to characterize the synoptic wind and give a global wind mapping, the azimuth angle was chosen to cover a wide area before and after the bridge.

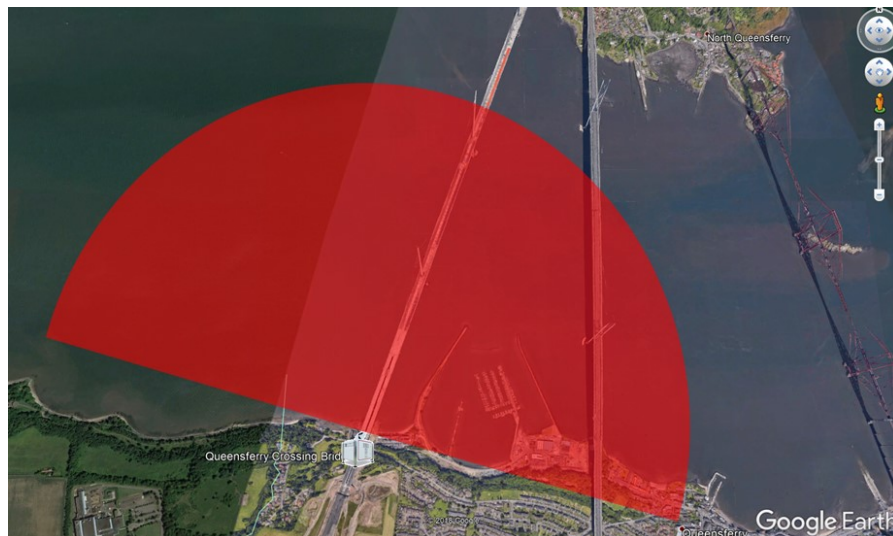


Figure 8 – Scheme of Mesoscale PPI scan over Queensferry bridge

Measuring up to 3300m, with a resolution of 25m along line of sight, data provide an overview of large scale wind behavior.

The elevation angle of  $0.55^\circ$  was kept as an average between the two types of PPI microscale used.

### 3.2.2. PPI microscale

Focused on high resolution to see the small wind structures near the windshield, the parameter of the PPI microscale were chosen to bring the highest resolved wind data as possible.



Figure 9 – Scheme of Microscale PPI scan over Queensferry bridge

With an angular resolution of  $0.06^\circ$ , the Lidar system was able to measure 1m width wind formation at a distance of 1000m.

Several tests were needed to determine the best elevation to keep. As the bridge inclination is not constant, the Lidar scan had to find an angle to maximize parallelism with the windshields. After analysis, two elevation angles were kept:

- $0.5^\circ$  which is near enough the bridge to observed desired wind behavior;
- $0.6^\circ$  which is less affected by traffic during peak hour.

### 3.2.3. RHI

To have a better understanding of the 3D effect of the wind, two RHI were used.

- $19.8^\circ$  to measure a cross section of the wind aligned with the zone between the windshield and the middle of the bridge
- $19.9^\circ$  to measure the wind just adjacent to the tower

### 3.2.4. Table

This table summarizes the definitive parameters for each type of scan

Scan parameter	PPI Mesoscale	PPI Microscale	RHI
Azimuth angle (°)	120	6	19.8 – 19.9
Elevation angle (°)	0.55	0.5 – 0.6	3
Accumulation time per line of sight (ms)	500	100	100
Angular resolution (°)	1.5	0.06	0.02
Rotation speed (°/s)	3	0.6	0.2
Range gate length (m)	25	25	25
Number of gates	129	259	250
Minimum range (m)	100	255	250
Display resolution (m)	25	5	5
Max range (m)	3300	1545	1495

Those were used from the 28<sup>th</sup> of February up to the latest data.

The scheme below illustrates the different parameters of a PPI scan

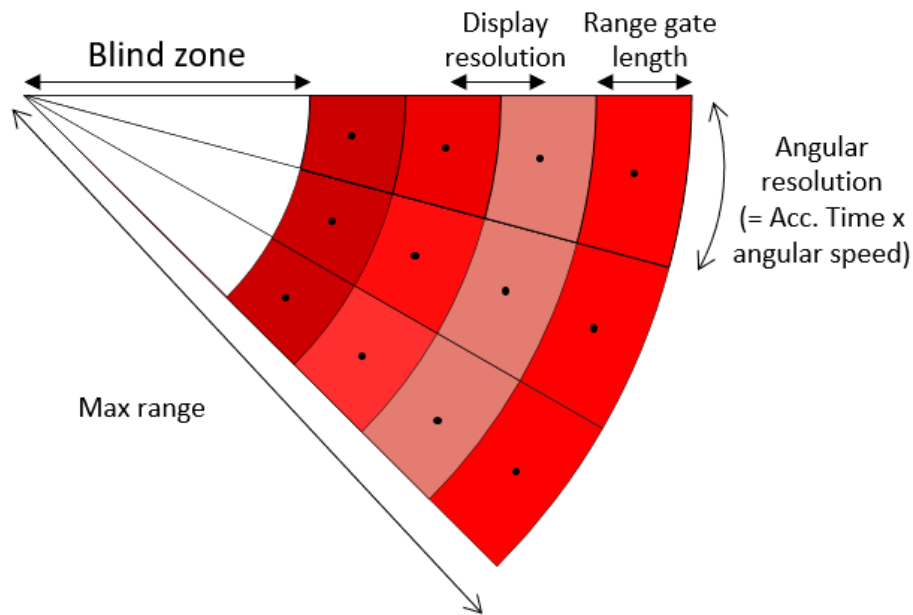


Figure 10 – Scheme of the main parameters to define a PPI scan

### 3.3. Scenarios time repartition

To maximize the quantity of PPI microscale scenarios, an alternation of clockwise and anticlockwise rotation was used, saving few seconds per rotation, leading to additional data in the long term. In average, 120 scans per hour were captured for each elevation.

PPI mesoscale scenarios were configured for a duration of 10 minutes every hour, allowing to perform 15 scans per hour.

Throughout the day, each RHI scan was configured for a duration of 4:30minutes each (9min total), with 18 scans performed per hour. The RHI scenarios are replaced by maintenance scenarios (lubrication and wipe) at midnight

Throughout the day, the percentages of time spent for the different types of scenarios is displayed in the pie chart below.

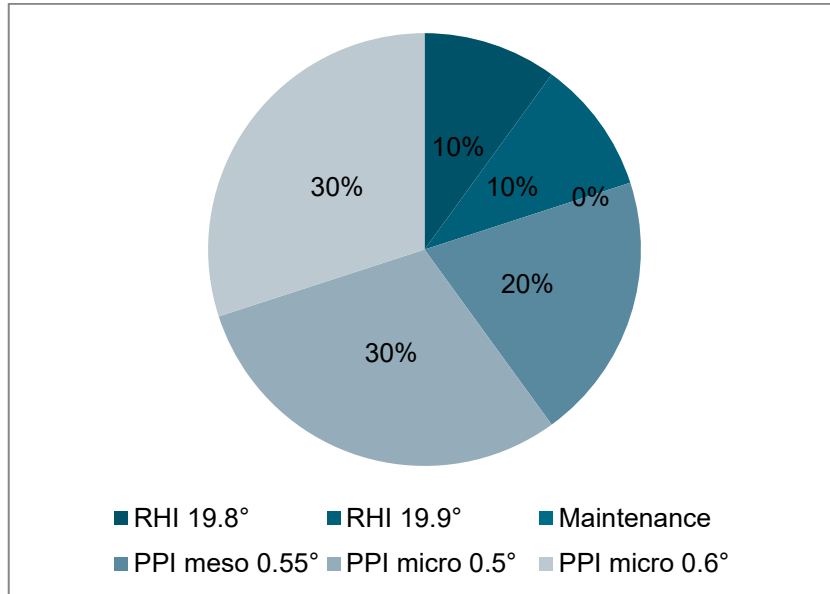


Figure 11 – Pie chart of the different scans performed each day by the Windcube100S

## 4. Lidar Monitoring & operation

### 4.1. Remote monitoring

A daily monitoring was put in place in Leosphere.

The goal was to make a regular check of the Lidar system to ensure the data generation and data quality. Data transfer from local computer to One Drive database was also monitored, to ensure the regular access of data.

A summary of events of the week with a global view of the status of processes was presented/send weekly to Amey Consulting.

Date	Lidar Status	Spectra generated	Radial generated	Reconstructed wind	Data recuperation
...					
09/03/2020	OK	OK	OK		OK
10/03/2020	OK	OK	OK		OK
11/03/2020	OK	OK	OK		OK
12/03/2020	OK	OK	OK		OK
13/03/2020	OK	OK	OK		OK
14/03/2020	OK	OK	OK		OK
15/03/2020	OK	OK	OK		OK
16/03/2020	OK	OK	OK		OK
17/03/2020	OK	OK	OK		OK
18/03/2020	OK	OK	OK		OK
19/03/2020	OK	OK	OK		OK
20/03/2020	OK	OK	OK		OK

Example of status table in monitoring report

During the entire duration of the campaign, no issue was found with the Lidar status and spectra generated (raw data) except the 15<sup>th</sup> of May where a low signal has been observed. The lidar signal came back to normal the 18<sup>th</sup> of May. The lower signal was due to the very clear air conditions occurred at that time in Scotland. Indeed, the aerosol optical depth (AOD)

which means the opacity of the atmosphere was very low. A normal AOD (visibility close to 10km) is close to 0.1.

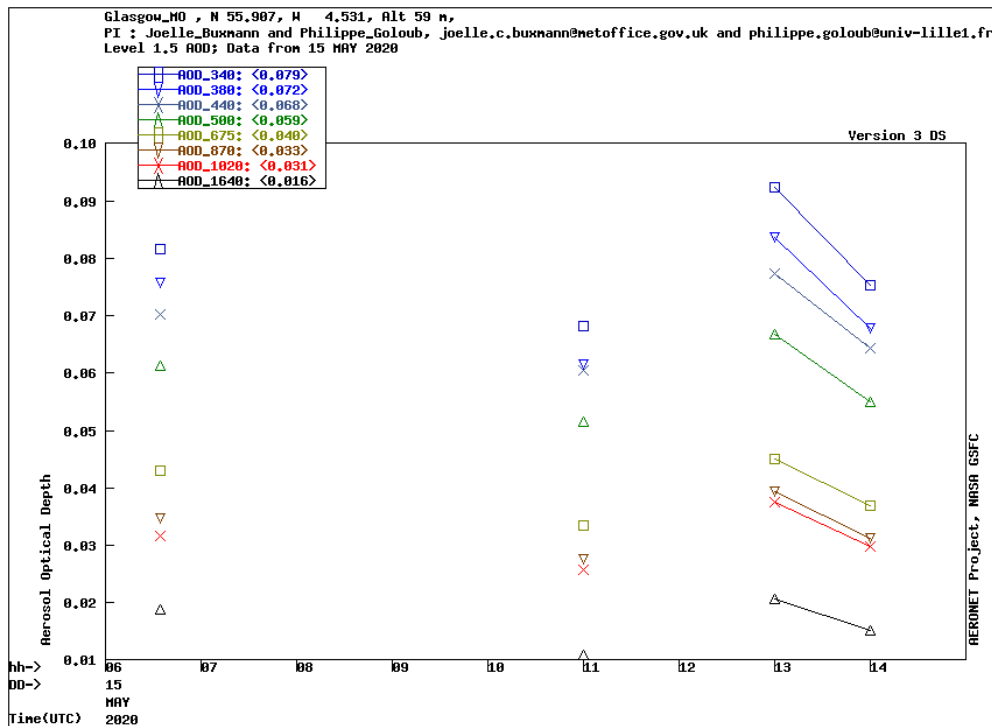


Figure 12 – Aerosol Optical Depth at Glasgow the 15<sup>th</sup> of May

## 4.2. Connection issue

Temporary disconnection from Lidar occurred the 05/03/2020. The cause seems to be license expiration on the computer where data are processed.

Thanks to quick intervention of Amey team and Gerry Sharp (Vaisala), the problem was solved before the 06/03/2020 and hasn't reappeared since then.

## 4.3. Synchronization delay

On several occasions, because of an update freezing, the One Drive had to be relaunched manually. While being more a constraint than an issue, this induced noticeable delay in the transmission of data (up to two weeks).

The variable quality of the connection to network coupled with large amount of data send might have been at the origin of the difficulty sending the new data batch to Amey (.mat files, pictures, filtered scans, etc.).

A bi-daily check of the one drive update was added to the monitoring process to ensure data transmission.

#### **4.4. Database overloading**

Overloading of Lidar database leads to an automatic stop of the measurements and then leads to subsequent loss of data. It happened the weekend of the 21<sup>st</sup> and 22<sup>nd</sup> of March 2020. Investigation showed that the space taken by file was much higher than expected and needed thus to be cleaned regularly.

A regular cleaning of the database was instituted monthly. Since then, no similar issue occurred.

## 5. Lidar data workflow

To have a better overview of the different deliverables expected, as well as their position in the workflow, one can use the following visualization:

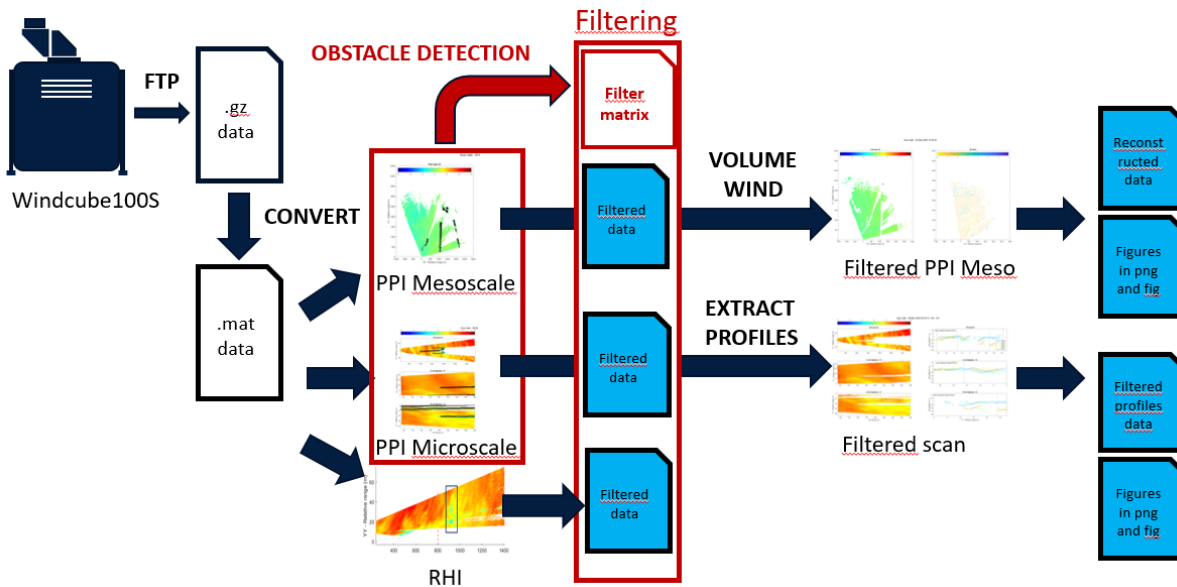


Figure 13 – Data workflow

Raw data, consisting of spectra and radials are generated by the Lidar system and send to the computer installed nearby. Radial data (.gz) are automatically updated on oneDrive.

The radial data contain:

- Radial Wind Speed noted VR [m/s]: Wind speed projected along the current line of sight at the current range gate.
- Dispersion Radial Wind Speed [m/s]: Full width at half maximum of the spectrum at the current range gate
- CNR [dB]: Carrier to noise ratio at the current range gate which corresponds to the number of photons received on the detector for each range gate

With the MATLAB script provided to Amey, radial are converted and indexed in .mat format to create a database that will allow the generation of scans. Display of RHI and PPI can thus be created.

Reconstructed data (.txt), provided by Leosphere, can be used to plot the 3D wind in complement of the PPI mesoscale.

An advanced filter of fixed obstacles is possible through the filter matrix, given with the scripts. This option will gives access not only to filtered scans, but also to filtered data (.mat & .csv), which can be used to plot directly the filtered scans without the filtering process.

<b>.gz data</b>	radial data produced by the Lidar system
<b>.mat data</b>	radial data converted to .mat
<b>index data</b>	index of .mat radial data (used to read data)
<b>raw scans .png</b>	scan picture obtained from .mat radial data
<b>reconstructed data</b>	data used to plot reconstructed wind in PPI mesoscale (in .txt)
<b>raw PPI meso scans .png</b>	PPI mesoscale scan picture, obtained from .mat radial data and reconstructed wind data
<b>filtered scans</b>	scan figure obtained from radial data after obstacle filtering process
<b>filtered PPI meso scans .png</b>	PPI mesoscale scan picture, obtained from .mat radial data and reconstructed wind data, after obstacle filtering process
<b>filtered data</b>	<ul style="list-style-type: none"> <li>- radial data obtained after filtering process (in .mat &amp; .csv)</li> <li>- used to obtain filtered scan picture</li> </ul>

**Table 1 - File format and explanation**

To ensure that all data could be reused and analyzed, a table was constituted to track the different scenarios from the first day of measurement. This table is contained in the excel file delivered in the project data files. For each day, there is one column indicating all the different scenarios used. The numbers in the table correspond to the scan "ID". The scan ID allows to easily retrieved all the parameters of all scans thanks to the .xscan files.

	21/02/2020	22/02/2020	23/02/2020	24/02/2020	25/02/2020	26/02/2020	27/02/2020	28/02/2020	29/02/2020	01/03/2020	02/03/2020	03/03/2020	04/03/2020	05/03/2020
535	535	535	535	535	535	535	535							
536	536	536	536	536	536	536	536							
537	537	537	537	537	537	537	537							
538	538	538	538	538	538	538	538							
550	550	550	550	550	550	550	550							
551	551	551	551	551	551	551	551							
552	552	552	552	552	552	552	552							
553	553	553	553	553	553	553	553							
							557	557	557	557	557	557	557	557
							558	558	558	558	558	558	558	558
								561	561	561	561	561	561	561
								562	562	562	562	562	562	562
								564	564	564	564	564	564	564
								566	566	566	566	566	566	566
								567	567	567	567	567	567	567

**Table 2 – Extract from scenarios table (full table in annex)**

## *Assessment of the impact of windshields on Queensferry bridge with Windcube 100S*

In the example above, we can see the implementation of the newest scenarios the 27<sup>th</sup> of February, which contains both older and newer parameter.

Combined with the parameter list in WindForge software, it is possible to find which type of scan was used for a given day without having to open each file.

## 6. Reconstructed wind – PPI Mesoscale

### 6.1. 3D wind

The goal of reconstructed wind is to understand the synoptic wind and the wind upstream and downstream the bridge. Studying the evolution of wind barbs on a map can give some insights about the characteristics of gusts and the structures of the wind.

To apply the reconstructed scan algorithm called “Volume Wind”, the wind must be considered locally as a homogeneous flow.

Generation of reconstructed wind data was done via the Volume Wind processing tool developed by Leosphere. Reconstructed data for all the campaign are sent to Amey.

### 6.2. Results

On PPI mesoscale scan, several longitudinal obstacles were observed.

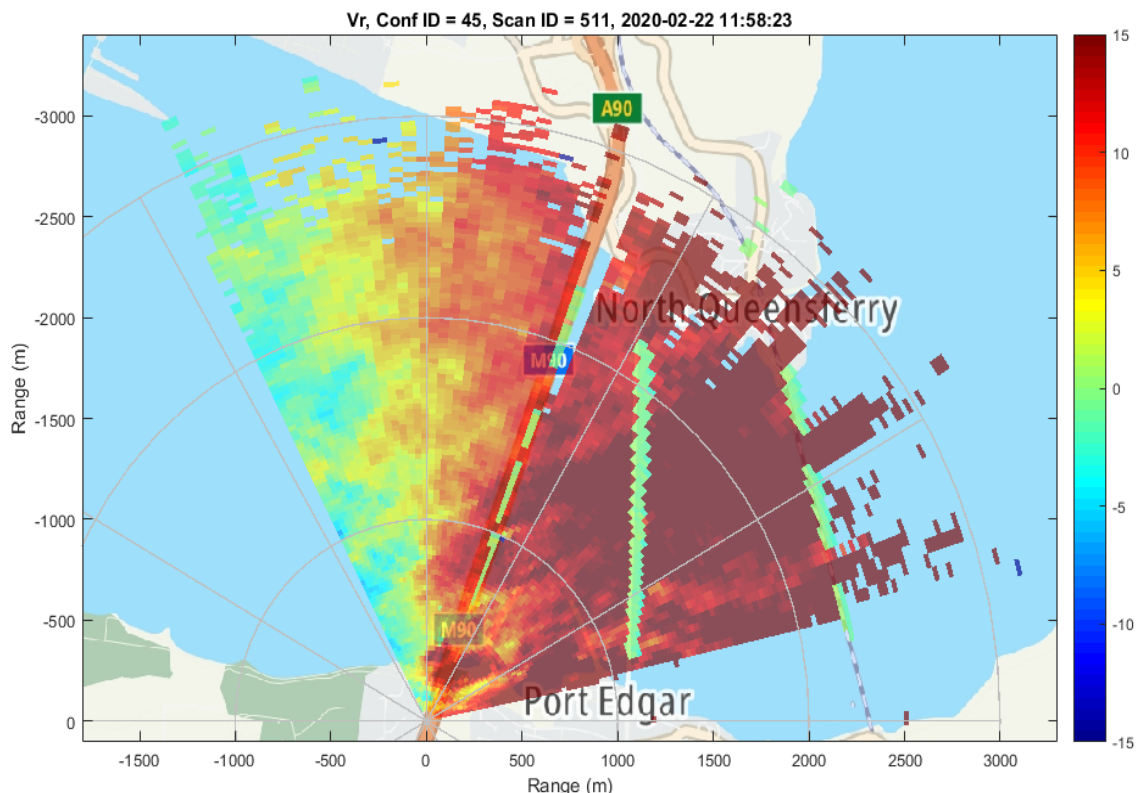
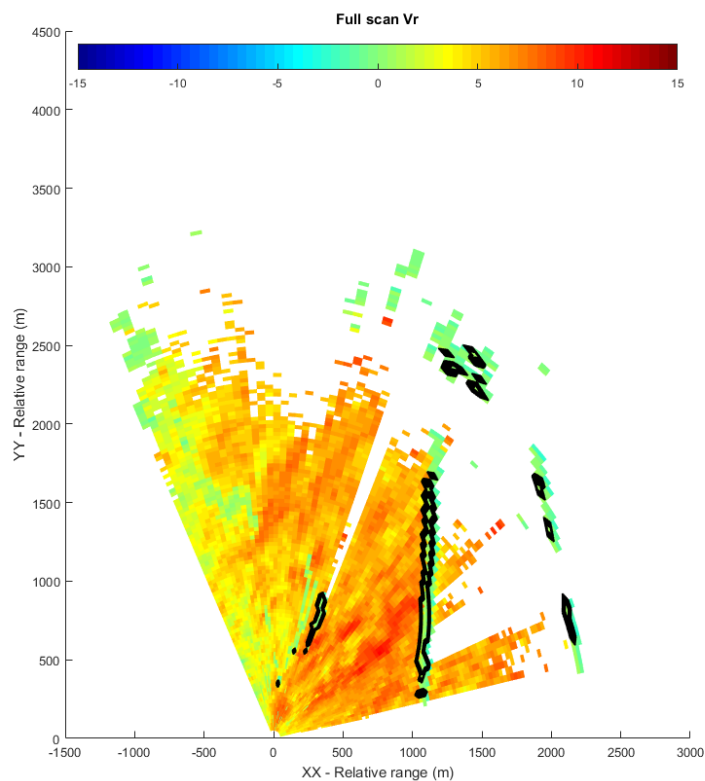


Figure 14 - PPI scan 0.55° measuring up to 3000m

Along the length of the bridge, the first gap is due to the hit of cables linked to the South tower, happening around 600m. On the east side of the Queensferry Crossing, the two semi-parallel long gaps in data are caused by the Forth Road Bridge and the Forth Bridge.

As the wind is mainly coming from South West, the Queensferry Crossing is hit the first, and thus doesn't suffer the possible deviation generated by the two other bridges.

After filtering the obstacles, puzzled data were observed a few kilometers from the Lidar. Those data were associated with high CNR. These are linked to physical obstacles, probably several hills located at approximately 20km away from the Lidar. Their measurements at closer ranges can be explained by the phenomena of range ambiguity, corresponding to the backscattering of the previous pulse. The graph shows the radial wind speeds measured the 29<sup>th</sup> of February 2020 at 12:00:02 UTC. The values of radial wind speed equal to zero correspond to obstacles. On the eastern side of the Queensferry crossing, the Forth Road Bridge and Forth Bridge can be clearly observed. On the Western side, some pockets of zero wind speeds (zero) can also be observed whereas they of course don't correspond to any obstacle at that location (1.5km away) since there is no fixed obstacle there. They correspond to hills located much further at about 20km whose the echoes are so strong that they are present during the acquisition of the next pulse as shown by the figure of google earth.



**Figure 15 - Unfiltered mesoscale PPI scan measured the 29<sup>th</sup> of February at 12:00:02 UTC**

# Assessment of the impact of windshields on Queensferry bridge with Windcube 100S



Figure 16 - View of Google Earth with enhanced topography by a factor 3 to better see the hills on the North West that can create sometimes range ambiguities

Scan date : 04-Mar-2020 01:07:26

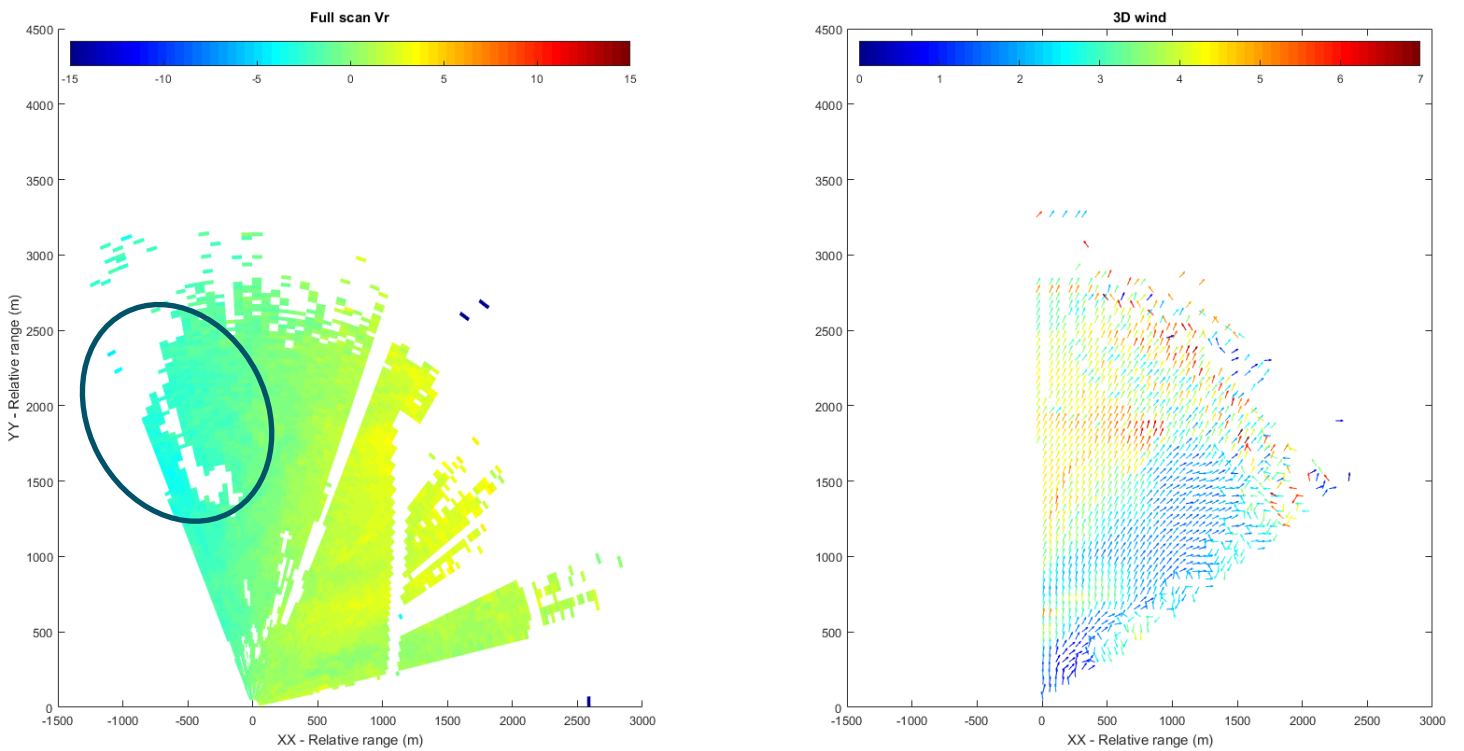


Figure 17 - On the left: the Vr scan; on the right: the reconstructed wind scan, with obstacle filtering applied

## Assessment of the impact of windshields on Queensferry bridge with Windcube 100S

As the wind reconstruction algorithm needs a minimum of 30 degree angle to reconstruct the wind in a given point, the left and right sides of the scan angle are truncated.

As data are reconstructed over the whole scan, holes that were previously caused by missing data (due to the bridge hit) are patched. This can be understood as an interpolation of wind data.

Scan date : 04-Mar-2020 01:07:26

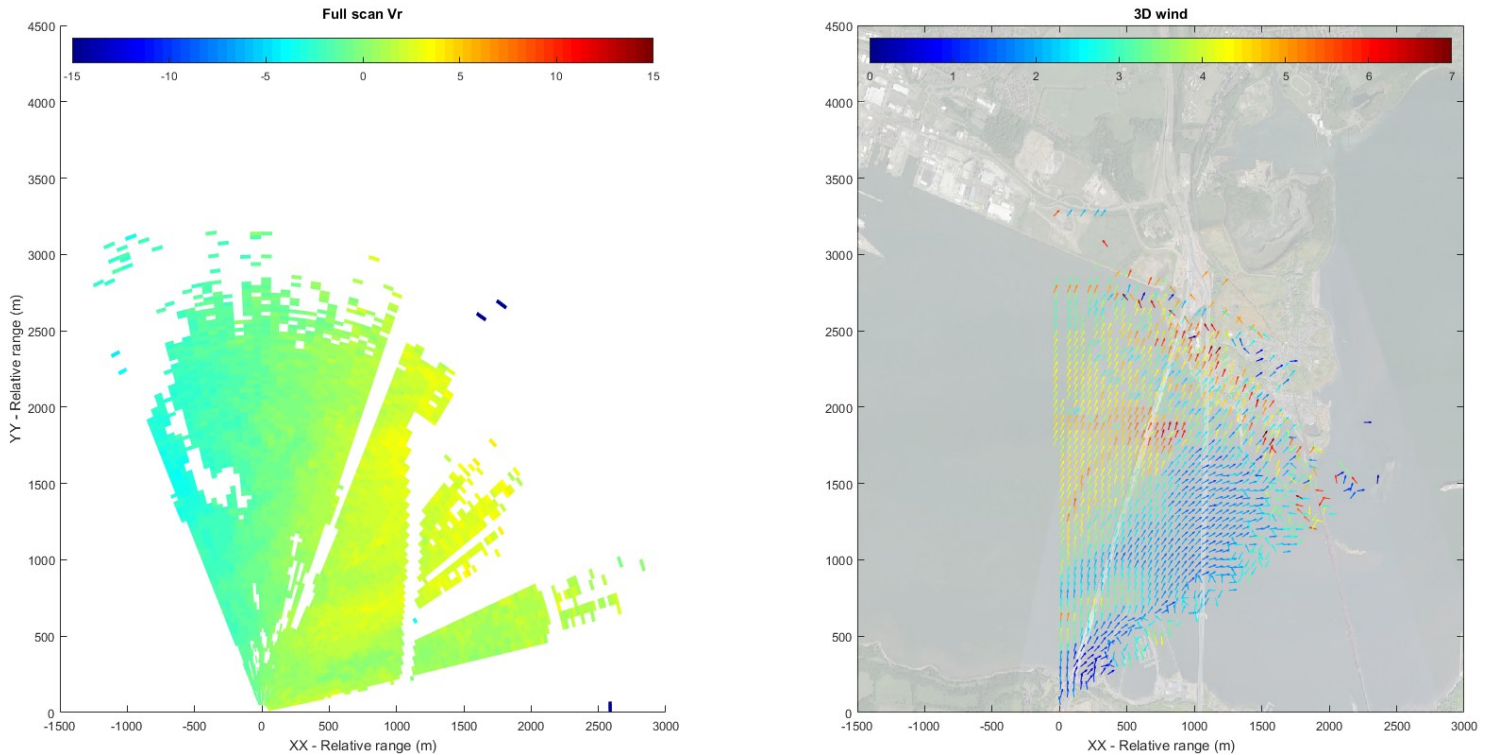


Figure 18 - Bridge display activated on reconstructed wind

After revision of color to clarify the independent plot scale, we have the final display available:

Scan date : 12-Mar-2020 13:51:31

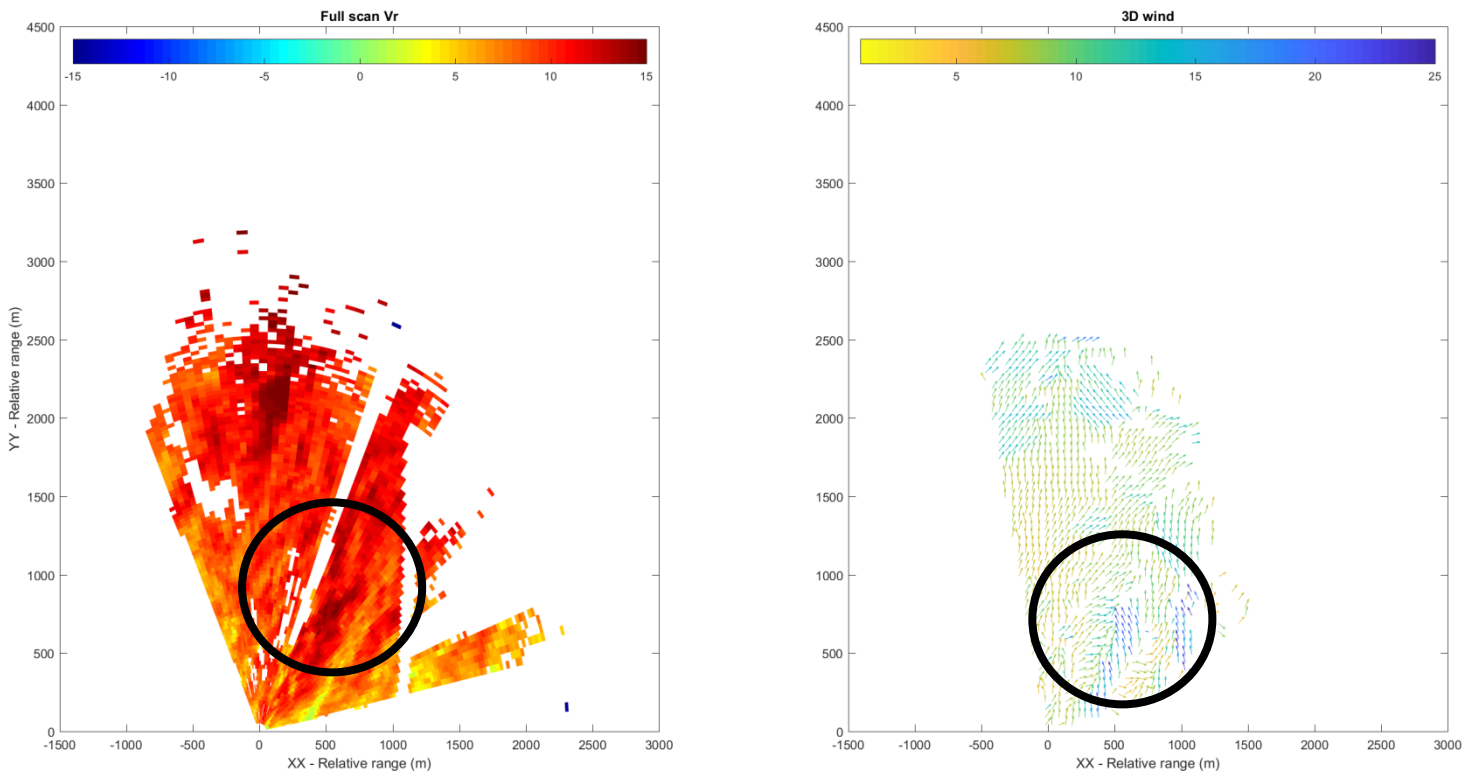


Figure 19 - Strong wind case of Vr wind

Here, it is possible to see the presence of strong gust after the bridge on both graphs (circled on the Figure above on the maps of radial wind speeds and reconstructed wind).

## 7. PPI microscale preliminary observations

### 7.1. Data visualization

A specific visualization tool has been developed for the project to have a better understanding of the wind structures relative to the bridge and the wind shields. Hereafter are the first types of display used:

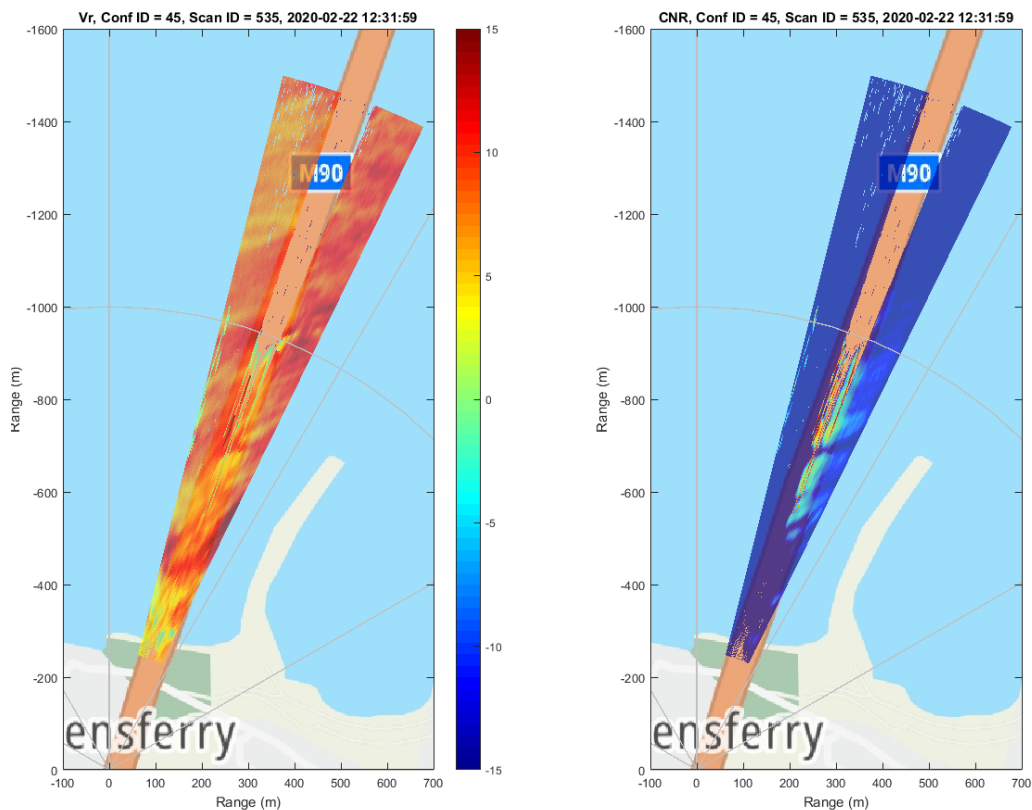


Figure 20 - VR and CNR scan display of 0.6° elevation scan (microscale)

Analyses of scans were done on the same visualization, but centered around the bridge, allowing zooming on more detailed aspect of the scan.

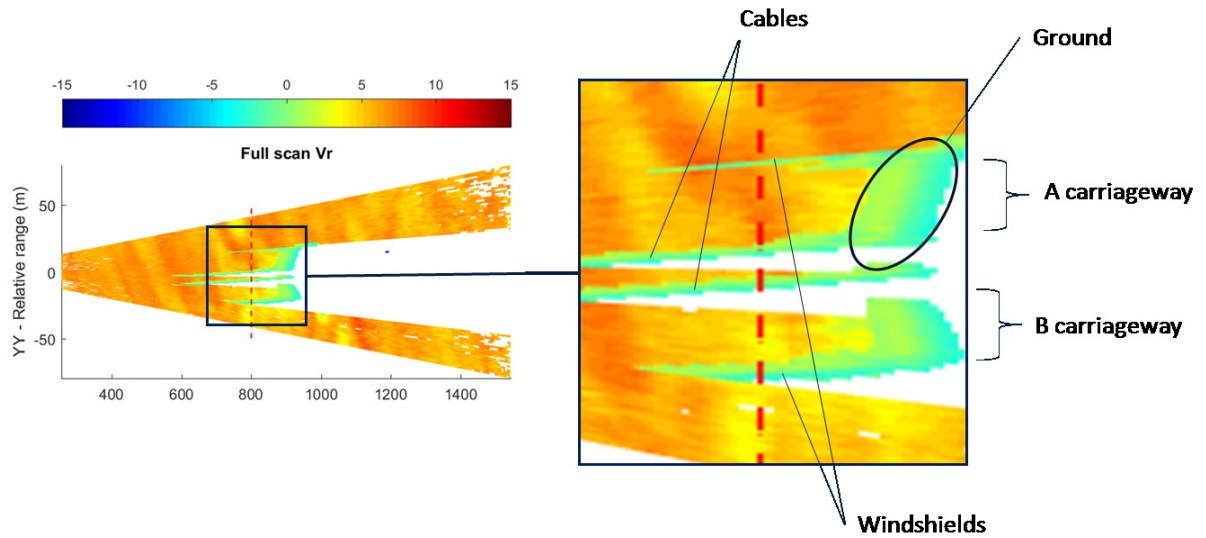


Figure 21 - Example of scan and obstacles

The two carriageways are here visible, separated by the cables of the south tower. Windshields are delimiting the bridge border.

As the Lidar is directly aligned with the A carriageway, some data of the B carriageway are missing, as they are occulted by the cables. To highlight those obstacles, the strong CNR was displayed in black outlines in the next scans.

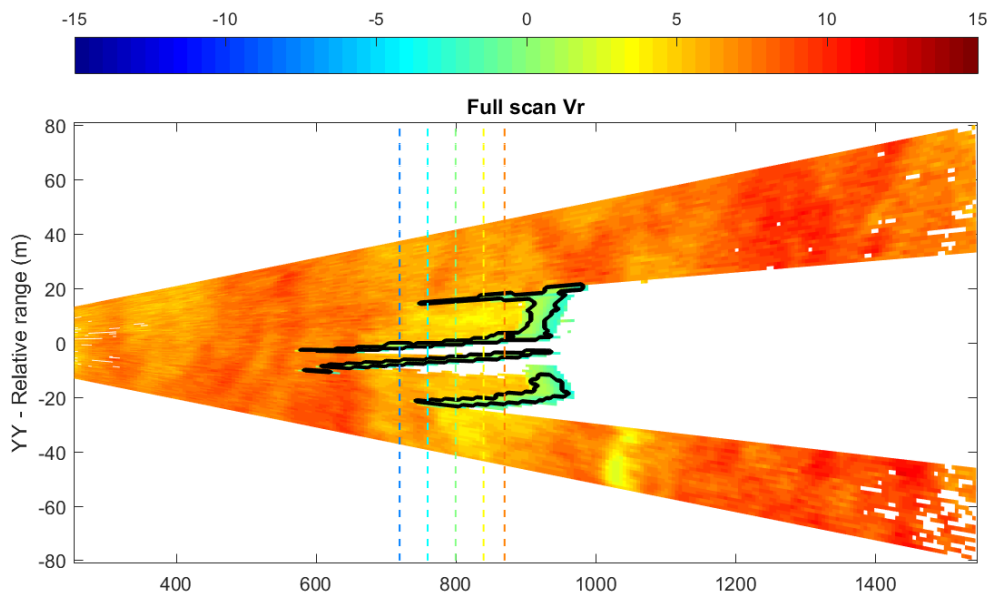


Figure 22 - 11-03-2020 - 00:05:57 (0.6°)

To have access to the profiles of wind across the bridge, the Doppler speed profiles at five ranges both for PPI microscale and RHI are gathered to create a profile of the wind perpendicular to the bridge. For example, as in the previous scan, the ranges selected are at the distances 720, 760, 800, 840, and 870m to give an overview of wind behavior before the windshield area and inside it.

The winds speed measured along the different colored axes can then be presented in a complementary plot:

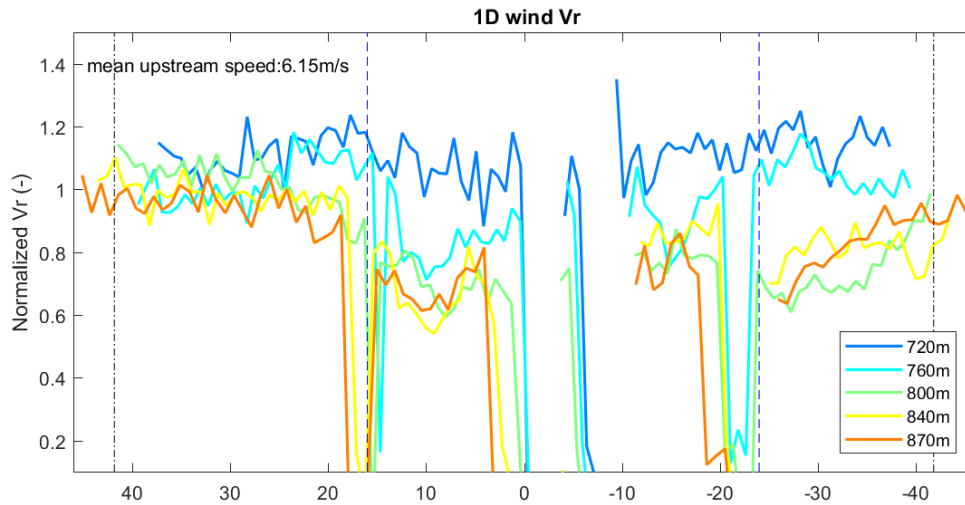


Figure 23 - Doppler speed for each range – lines shown in the previous graph

With a normalized Vr speed in Y-axis (normalized by the upstream mean speed), and the range in X-axis centered on the bridge, this visualization makes possible the comparison of wind speed from different timestamps. At the upper left of the graph, the mean upstream wind used for the normalization is displayed.

As obstacle hit is characterized by a zero wind speed, it is possible to deduce the position of each windshield at 17m and -21m, similarly to what is seen on the scan display.

## 7.2. Obstacles

### 7.2.1. Tower effect

Some highly distinguishable obstacles were used as marker to position the Lidar azimuth angle relatively to the bridge. Positioned at a little more than 1000m from the Lidar, this high elevation scan shows the impact of the South tower on the scan.

It is possible to see not only the tower hit, but also the wake generated.

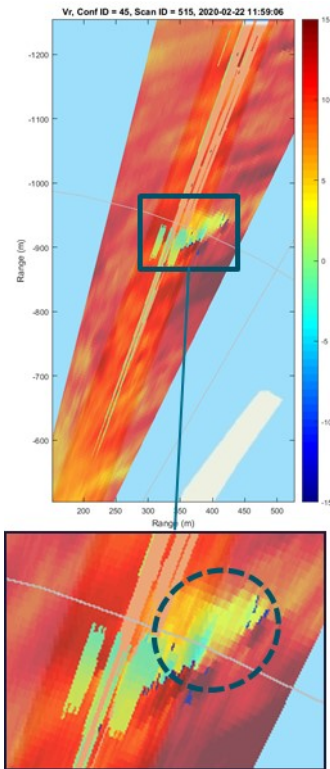


Figure 24 - Tower hit and wake as measured by the Windcube100S with a PPI microscale at 1° of elevation

### 7.2.2. Traffic – vehicles

Traffic was a concern from the beginning of the study. As passing vehicles might obstruct the Lidar beam, lower data availability would have been expected during rush hours.

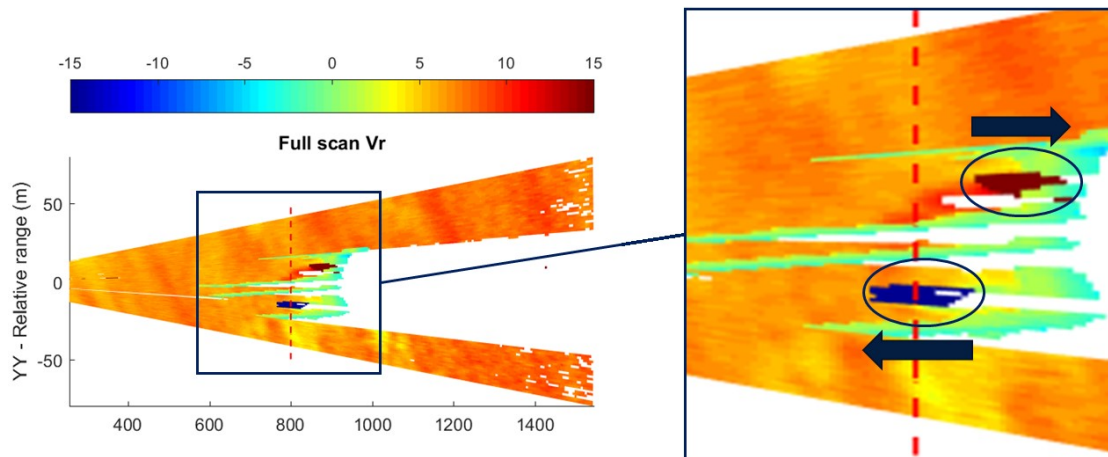


Figure 25 - 09-03-2020 – 05:28:58 (0.5°) – Indicate the PPI scan and the elevation angle

On the graph above, the rectangles observed of positive for the A carriageway and negative for the B carriageway correspond to road traffic, probably trucks. Velocities of cars or trucks can be observed on several scans, mostly lower elevation (0.5). As a reminder of the meaning of Doppler velocities: red for vehicles travelling away from the Lidar and blue when they are coming toward the Lidar.

As seen in the previous scan, those vehicles are blocking part of the Lidar measurement and thus limit the study when present.

More than just the vehicles, their wake might alter the interpretation of the results.

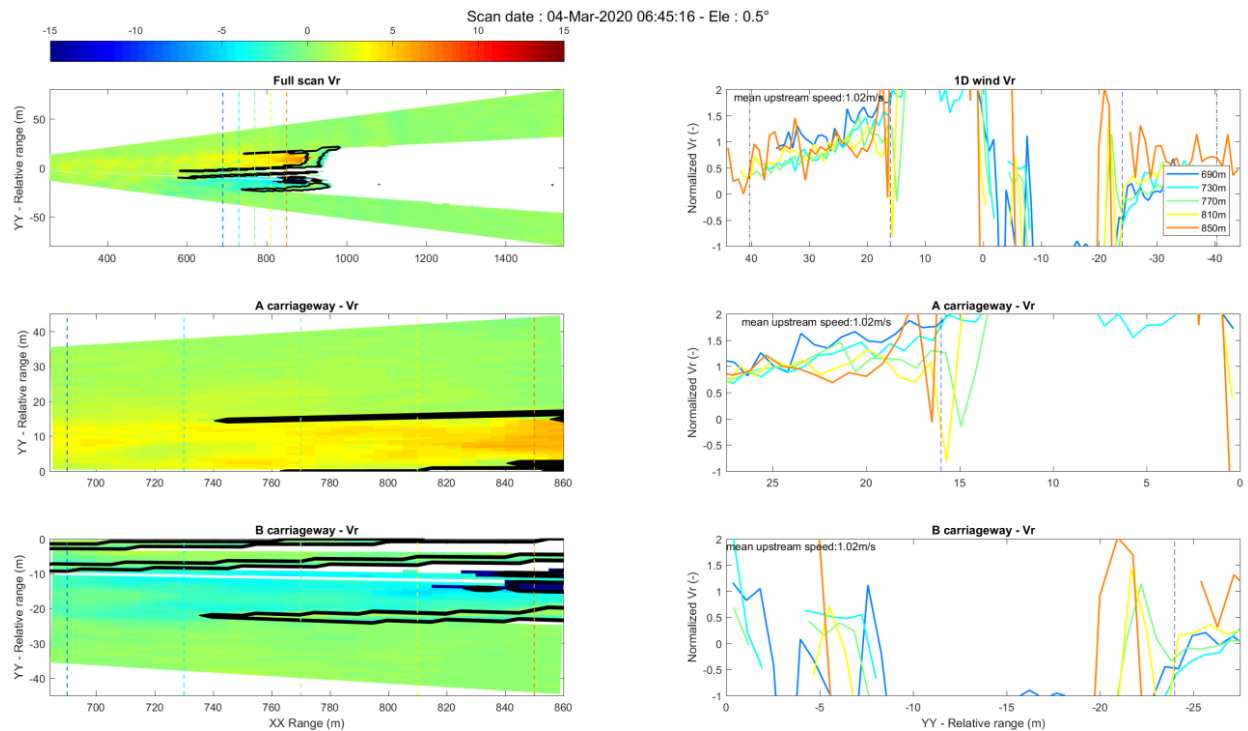
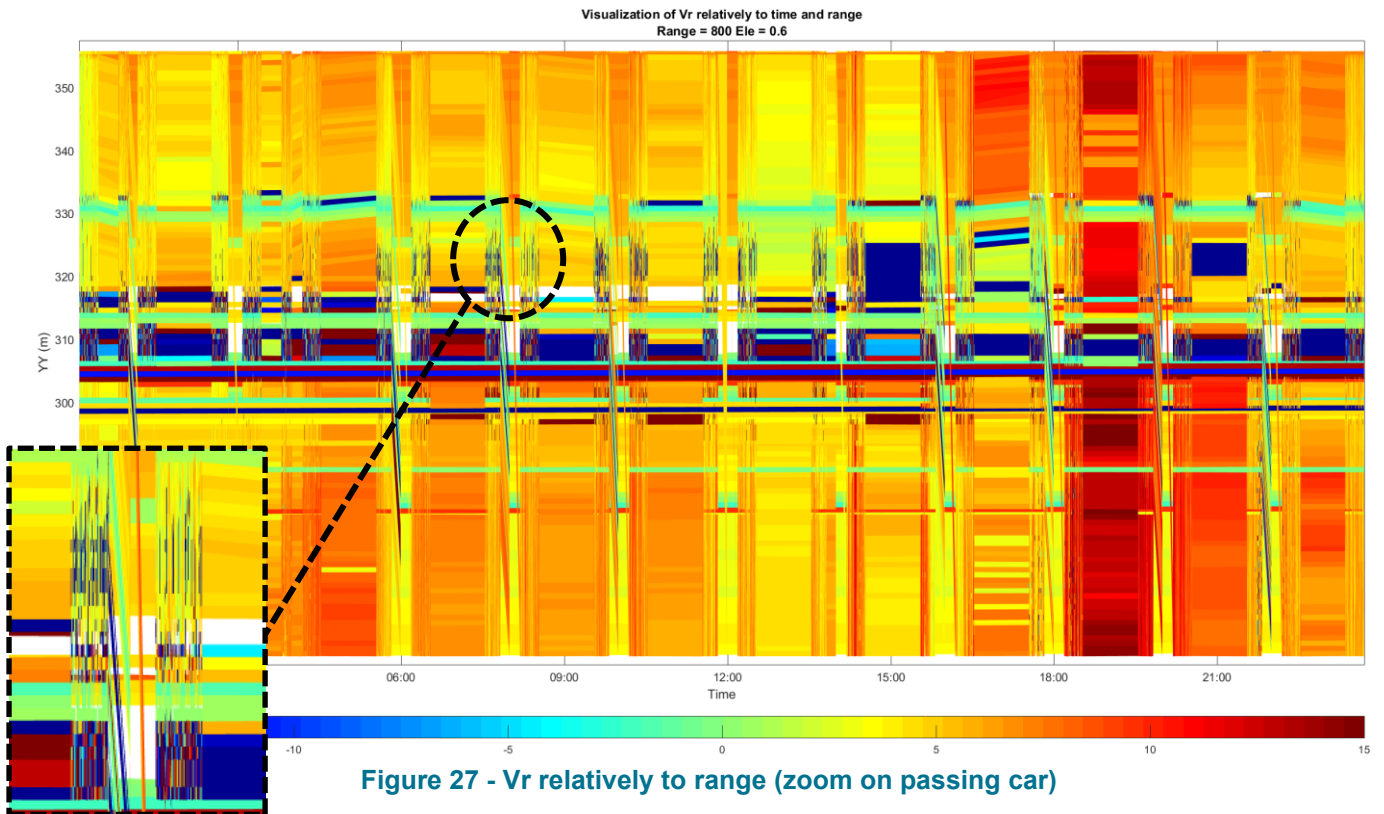


Figure 26 - 04/03/2020-06/45/16 (0.5°)

In those scans, we can see that while the wind is very low outside the bridge limit, it tends to be up to 5m/s between the windshield and the cables. The wakes generated by moving vehicles combined with the windshield geometry tend to create a tunnel effect for each carriageway which might be not observable under stronger wind, but can still affect results.

### Time distance profile

By concentrating all Doppler velocities of a day on a single graph, with Time in X-axis and position in Y, we were able to pinpoint the impact of road traffic on the radial data



The center of the bridge is shown here by the thin green line, and the quantity of traffic by the number of cars.

High density of traffic can be observed as thick colour bands through its wake during rush hour, between 7:30 and 9:30am and later during 5:30 to 6:30 pm.

On the graph above, the dark blue points and the dark red points are "markers" or "indicators" of vehicles.

A special attention needs to be put on the data used for analyzing wind measurements behind wind shields in order to select only data not affected by the road traffic.

### 7.3. Filtering process

A rough filtering is automatically applied by removing data identified as having a too low dispersion and CNR. This filter gets rid of bad data, such as one that appear where part of the Lidar is occulted.

However, it can't remove perturbation caused by obstacles.

Fixed obstacle filtering was a solution implemented to solve this issue. By identifying the zone with wrong data which is common to several scans, a matrix is generated determining data usable or not.

# Assessment of the impact of windshields on Queensferry bridge with Windcube 100S

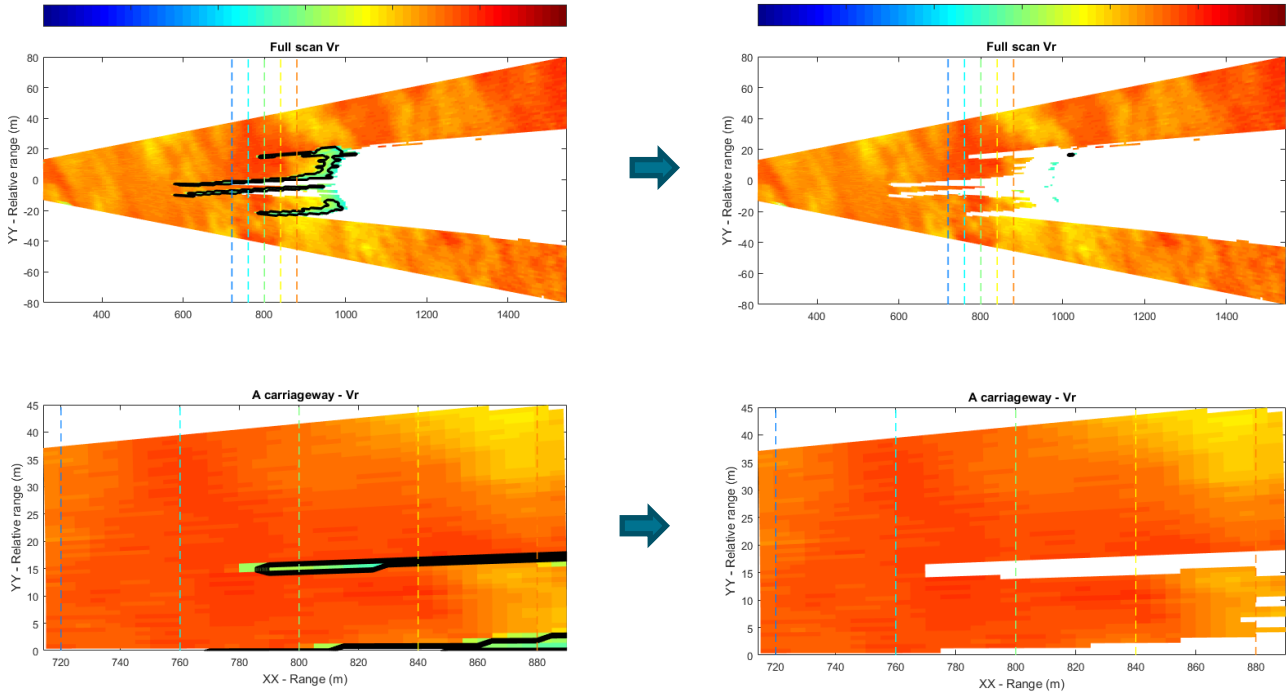


Figure 28 - Before and after obstacle filtering (Vr scan)

This type of filtering is useful to have a better view of the Doppler wind speed, as the huge peaks are removed from the graph, keeping only wind measurements behind wind shields.

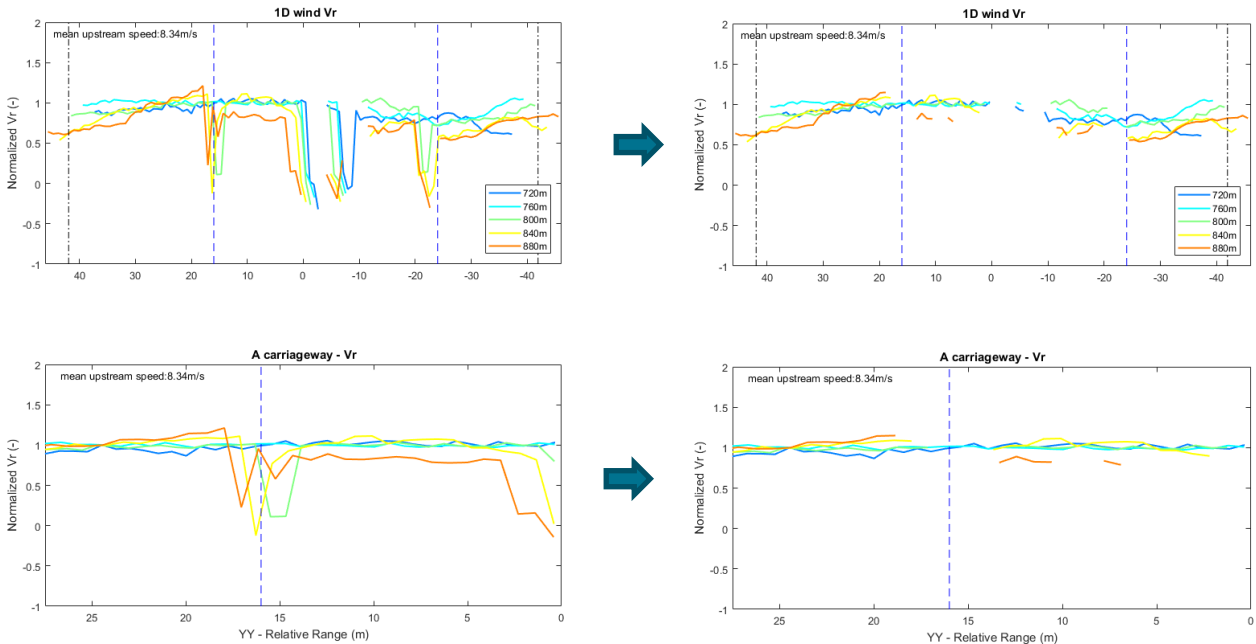


Figure 29 - Before and after obstacle filtering (Doppler wind scan)

## 8. Wind shield effect

As discussed during the project, understanding the effect of wind shields with the Windcube100S is the primary objective. Ideally, the final objective is to determine the impact of wind shields with heights above the ground but the resolution available could be too limited. Another objective is to determine the effect of wind shields with wind speeds and wind directions.

### 8.1. Primary observations

#### 8.1.1. Upstream vs downstream wind

In most of the cases, upstream wind (wind before windshield) seems to be different than downstream wind. Below is one example of moderate winds where wind behind wind shields is a little bit lower than upstream wind.

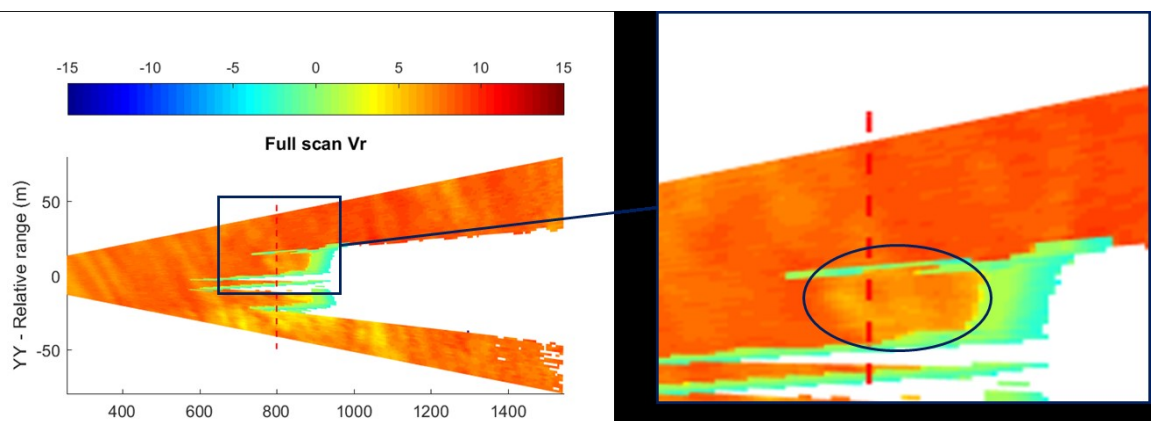


Figure 30 – Microscale PPI scan performed the 9<sup>th</sup> of March 2020 at 04:34:41

#### 8.1.2. Gust

Local gust can be observed behind and before windshield, making it sometime tricky to correctly interpret data.

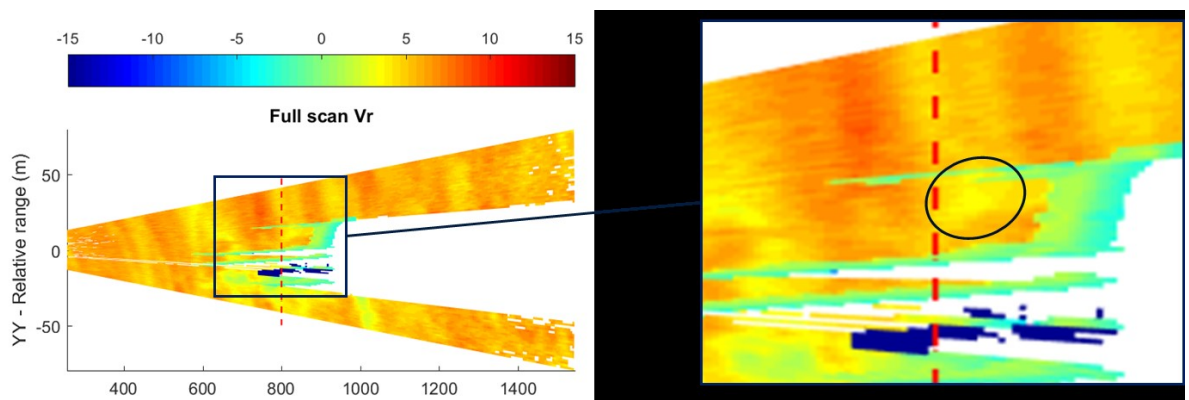
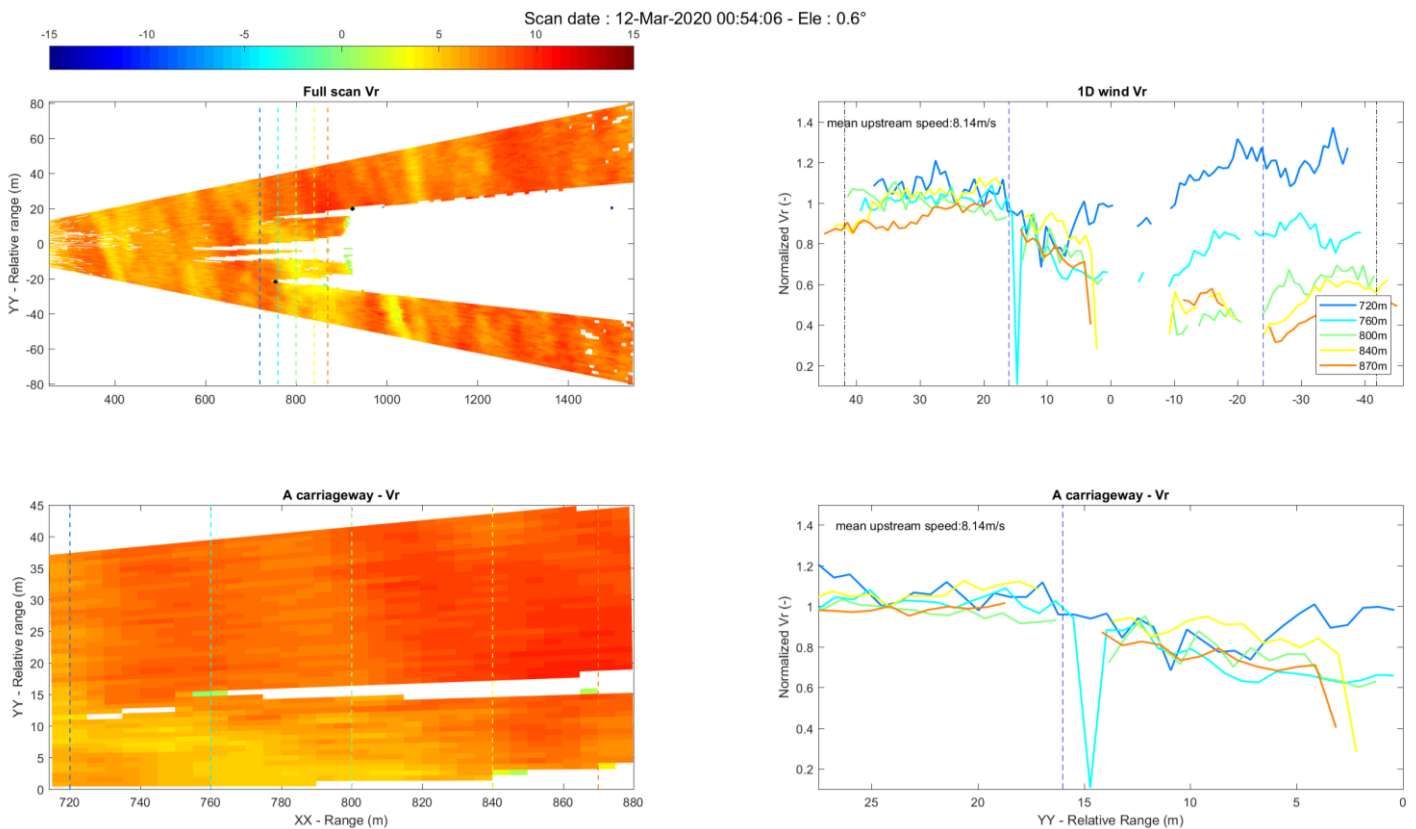


Figure 31 – Microscale PPI at 0.5° of elevation the 9<sup>th</sup> of March 2020 at

On the example above, a small structure is observed behind windshield, caused by a gust.

Here after another example of a gust::



**Figure 32 – Example of a gust as seen on the microscale PPI at 0.6° the 12<sup>th</sup> of March 2020 at 00:54:06**

On the zoomed part of the scan, focusing on the A carriageway, we can see on the Vr plot that the wind speed is weaker after the windshield (in the lower part) than before. This is confirmed by the Doppler speed, where the decline seemingly affects all ranges.

Because the first range (at 720m, in dark-blue) is following the same tendencies as the range that intersects with the windshield, we probably have here a common phenomenon, linked to a gust.

Following the same reasoning with the graph below, we can see on the Doppler speed of the A carriageway that all but the first range are decreasing after the windshield hit.

# Assessment of the impact of windshields on Queensferry bridge with Windcube 100S

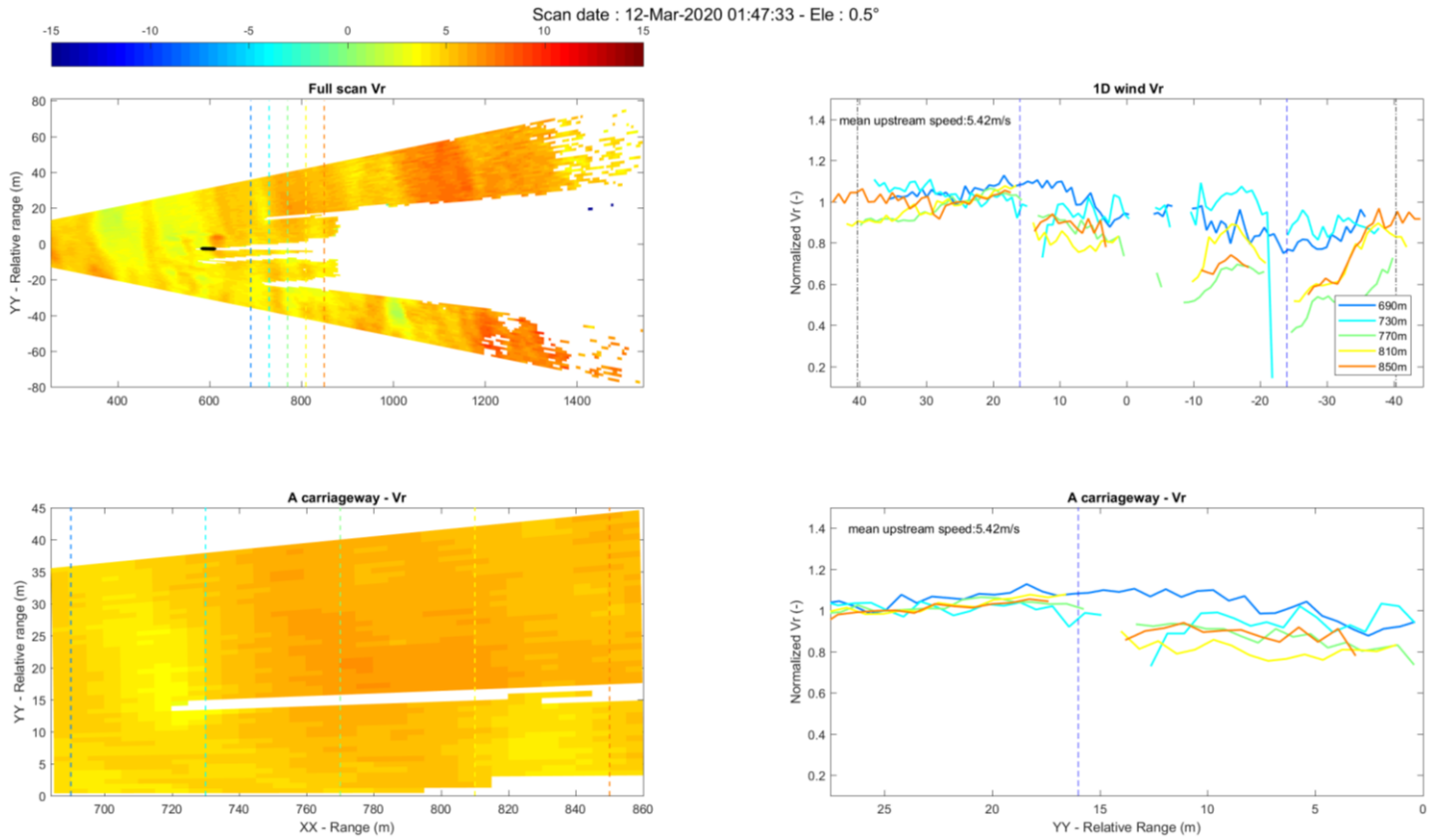


Figure 33 – Microscale PPI scan of the 12<sup>th</sup> of March 2020 at 01:47:33

Effect of strong gust can be better seen when observed on a sequence of scans.

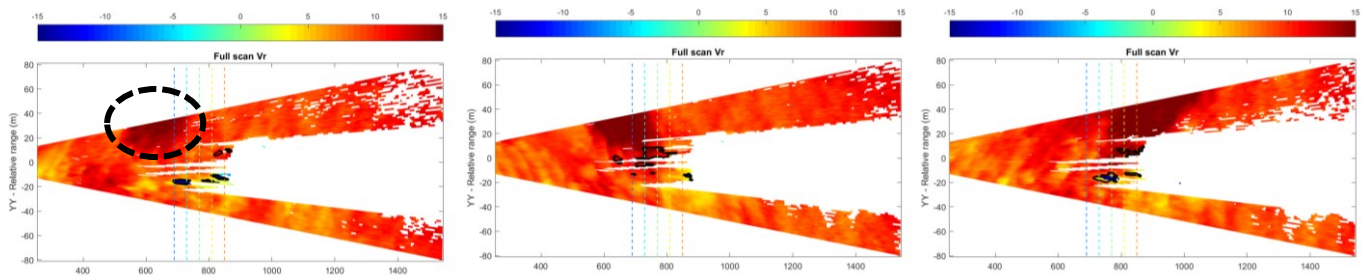
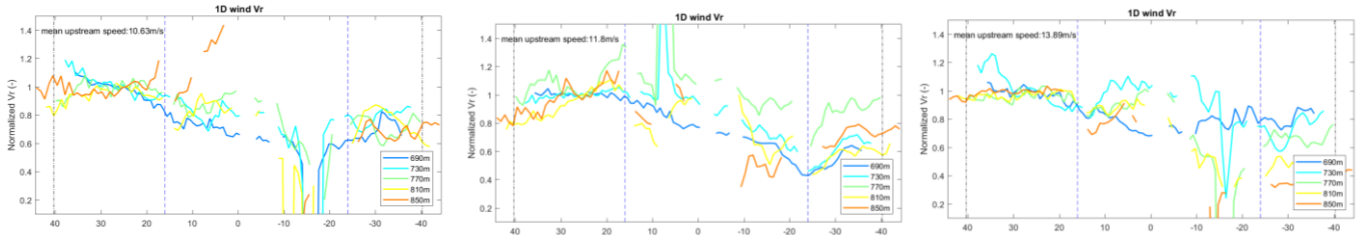


Figure 34 - Scans at 0.5° elevation, 12/03/2020 14:16

Circled in the example above, localized strong winds are travelling parallel to the bridge, and can be seen entering the windshield on the second scans.



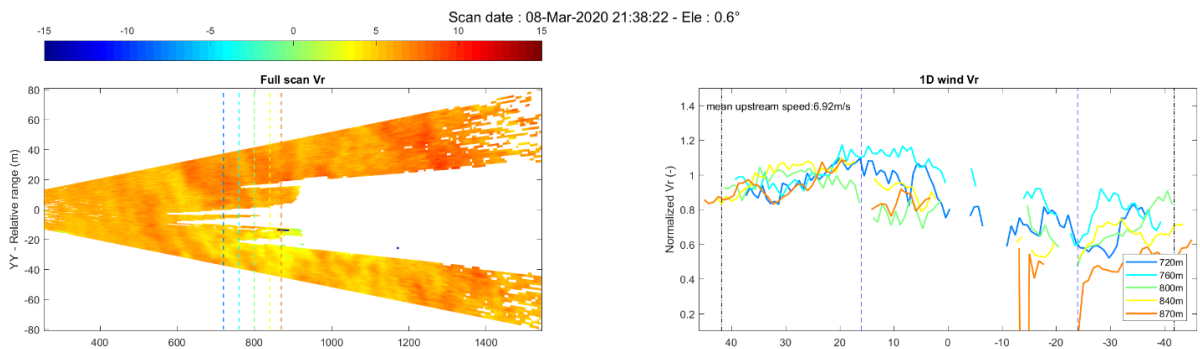
This makes analysis with turbulent wind somewhat tricky to interpret when looked at a fixed timestamp.

## 8.2. Influence of Wind speeds

The effect of wind shields has been studied for moderate and strong wind conditions.

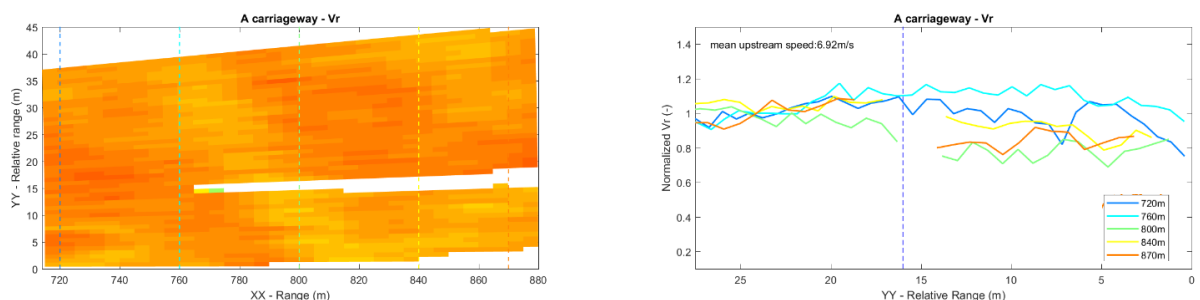
### 8.2.1. Moderate winds (<8m/s) – Example of the 8<sup>th</sup> of March

First of all, strong fluctuations of the upstream wind 7m/s and variations of +/- 2-3m/s can be observed along the bridge deck on the PPI microscale. As these wind measurements are performed on the same line of sight and at the same time (+/- few microseconds), it means that those fluctuations reveal the spatial heterogeneities of the upstream wind. Downstream winds are lower than upstream winds due to the blockage effect of the bridge as expected in stationary conditions.



The wind profiles across bridge confirm variations of upstream wind of about 20% (1.4m/s)

Strong reductions of wind can be observed behind wind shields with a linear decrease of 10% to 20% at the end of A carriageway and of about 30 to 40% of reduction at the end of the deck.



In zooming in to the A carriageway, fluctuations of upstream can be observed clearly as well as their continuation directly behind wind shields. The differences of wind profiles for the different distances 720, 760, 800, 840 and 870m can be explained by multiple factors:

- Usually, wind profiles at 720m and 760m can look like a Bell curve with a maximum above the bridge. Our understanding is that at this distance, the Lidar measures wind above the wind shield. In this case, at 760m only a slight decrease of wind across A carriageway can be observed and with sometimes a maximum above A carriageway.
- Understanding the other profiles is also quite complex. Indeed, as the wind direction is titled compared to the bridge, higher upstream winds at a given distance (in this case at 760m) can induce higher winds behind shields at another distance (in this case 800m).
- But, in this case as for many cases in moderate wind conditions, a significant decrease of the wind behind the shields is observed of about 10 to 20%.
- Thus the differences of the wind profiles across carriageway cannot be attributed to the wind shields only and to the height above the deck. In this case, the differences of wind just behind the shields between the profiles at 800, 840 and 870m are of about 1.6 to 2m/s.

10 seconds before or after, the microscale PPI scans look very different compared to the previous scan. The patterns observed that could have been interpreted as atmospheric waves are in fact the follow-up of the same wind during the azimuthal scanning of the Lidar. Indeed, the scan sweeps a distance at 800m of 80m in 10s. For PPI scanning clockwise, in this case in the same orientation than the wind, the scanning head and the wind move at similar wind speeds for wind speeds of approx. 8m/s. The clockwise scan follows the same gust for example which induce the longitudinal patterns at 9:38:22 and 9:32:44. The anticlockwise scans don't reveal such patterns as their motion is totally desynchronized to westerly winds. This is important to mention that this effect will be less predominant for lower or higher wind speeds than 8m/s.

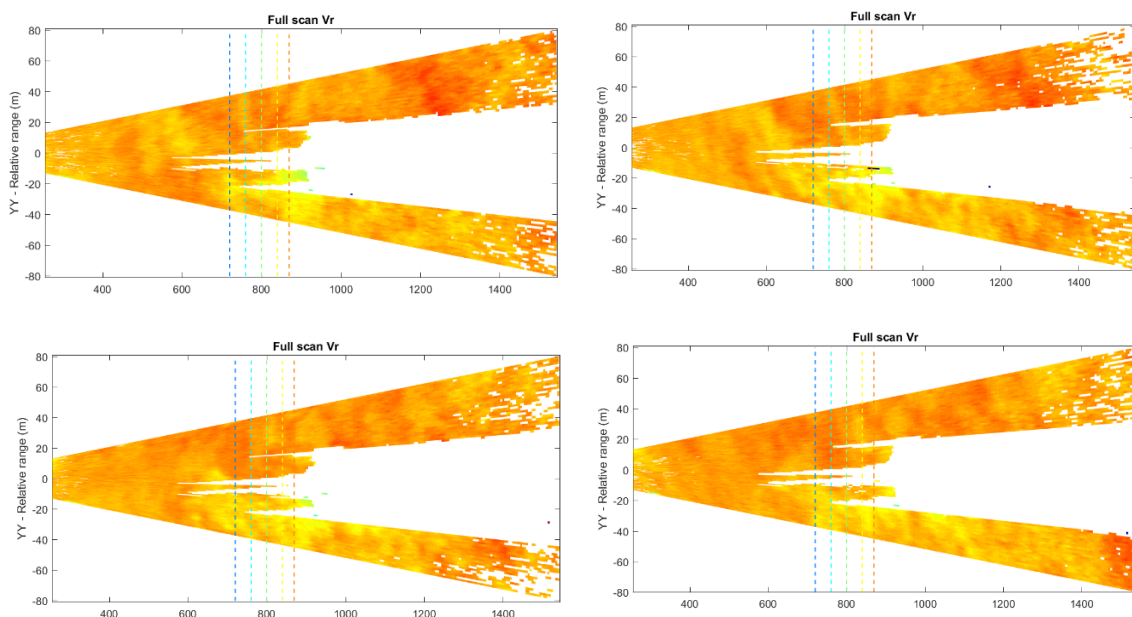
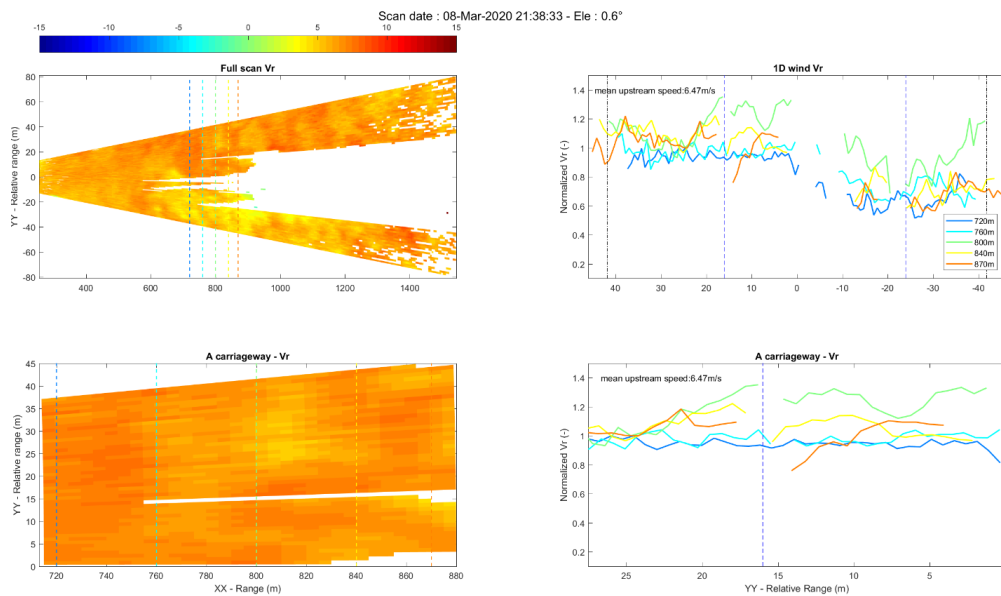


Figure 35 - Microscale PPI scans at 0.6° of elevation the 8th of March at 9:38:12, 9:38:22, 9:38:33, 9:38:44 (from Top Left to Bottom Right)

## Assessment of the impact of windshields on Queensferry bridge with Windcube 100S

The measurements performed by anticlockwise scans are therefore of interest since they measure better wind fluctuations and their structures. The differences between the wind profiles across the bridge do agree with the previous observations made on clockwise PPI scans:

- The profiles at 720 and 760m are very different from the others. They don't show any slowdown of the wind above the A carriageway. This absence of slowdown needs to be further investigated since it could come from the synchronization between the wind fields and the scanning (clockwise or anticlockwise). A temporal analysis at those particular points behind the wind shields will help to conclude on the behaviors between wind shields depending on the distance. A decrease of wind can be observed nevertheless above B carriageway.
- Upstream winds vary a lot in this case with fluctuations up to 40% between the different profiles
- The wind slowdown just behind the wind shields is much lower for the profile at 800m (about 10%) than the one at 840m (20%) and the last one at 870m (30%). It seems that the same conclusion is reached for that day with a moderate wind.
- But when looking at the wind profiles across the A-carriageway at the three distances 800, 840 and 870m, the wind accelerates 5m after the wind shields. This increase of wind speed can't be fully explained. It may be partially explained by wind gusts as wind speed varies in time of about 20% in this case.



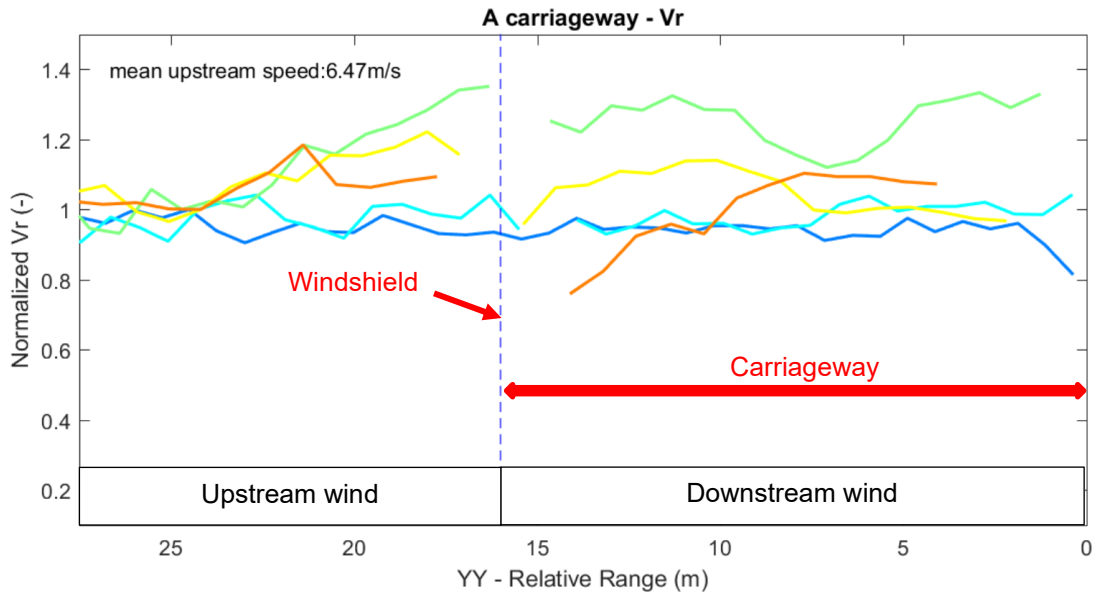
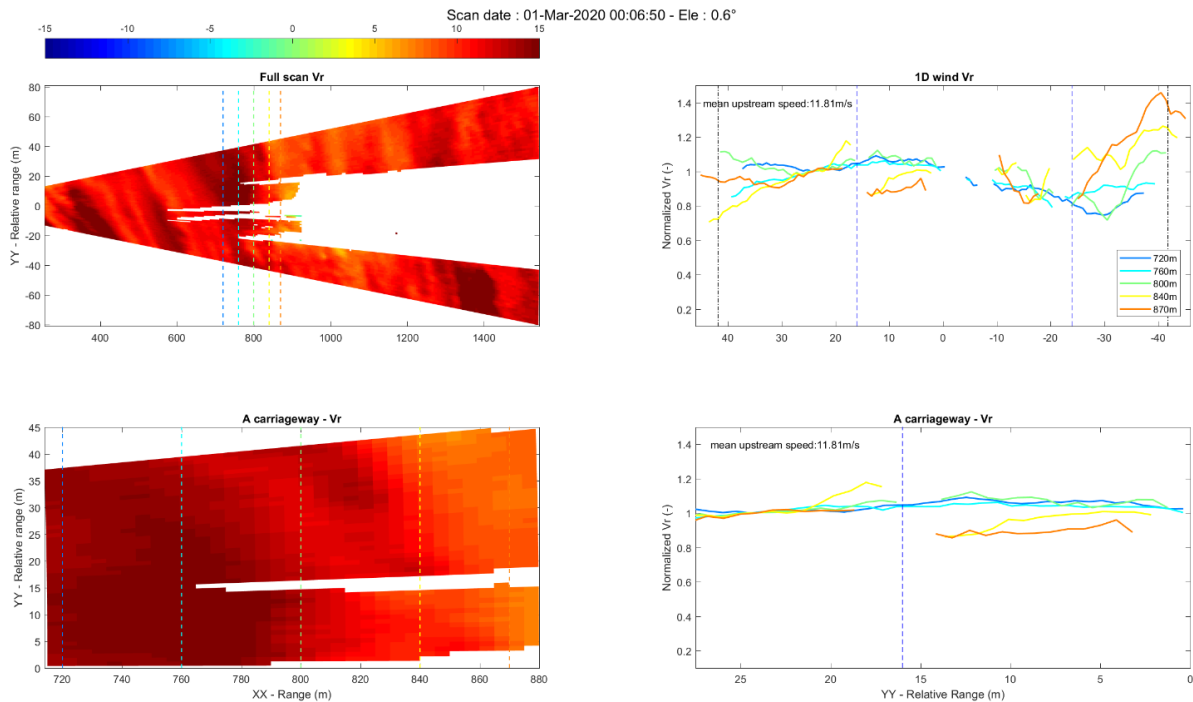


Figure 36 - Microscale PPI scans the 8th of March at 0.6° of elevation at 9:38:33 (bottom -Zoom of the profiles across A-carriageway)

### 8.2.2. Strong winds (>8m/s) - Example of 1st of March 2020

In this example, wind speeds before wind shields reached 11.81m/s. As for the moderate winds, the wind varied in space and in time but less in proportion with 10% of fluctuations. As mentioned previously, the waves observed are linked to the synchronization of the scan with the wind speed. What is different compared to moderate winds, it seems that only profiles at 840 and 870m are affected by the wind shields. In those profiles, a significant slowdown of the wind of about 10% to 30% is observed. The profiles at 720, 760 and 800m behave similarly whereas at moderate wind speeds, only the first two profiles share the same behavior. This can be explained by the higher wind speeds, inducing more flow detachment especially at the top of the wind shields leading to less reduction of wind at 800m. In addition, the slowdown of the wind is higher at 870m than 840m whereas it was the opposite at moderate wind speeds. No explanation has been found here.

# Assessment of the impact of windshields on Queensferry bridge with Windcube 100S



**Figure 37 – Microscale PPI at elevation of 0.6° the 1<sup>st</sup> of March 2020 at 00:06:50**

When analyzing the anti-clockwise scan just after, observations significantly different can be performed. The decrease of the wind speed behind wind shields is also observed but also for the profiles at 800, 840 and 870m. This can be due to the slight variations of the elevation angles leading to a shift in the position of the wind shields on the scan. Therefore, at 760m the lidar measures the wind below the top of the wind shields. The slowdown is of 10%, <10%, 20% and 25% for the profiles at 760m, 800m, 840m and 870m. As for the clockwise scan, a non-linearity of the wind speed reduction can be observed.

# Assessment of the impact of windshields on Queensferry bridge with Windcube 100S

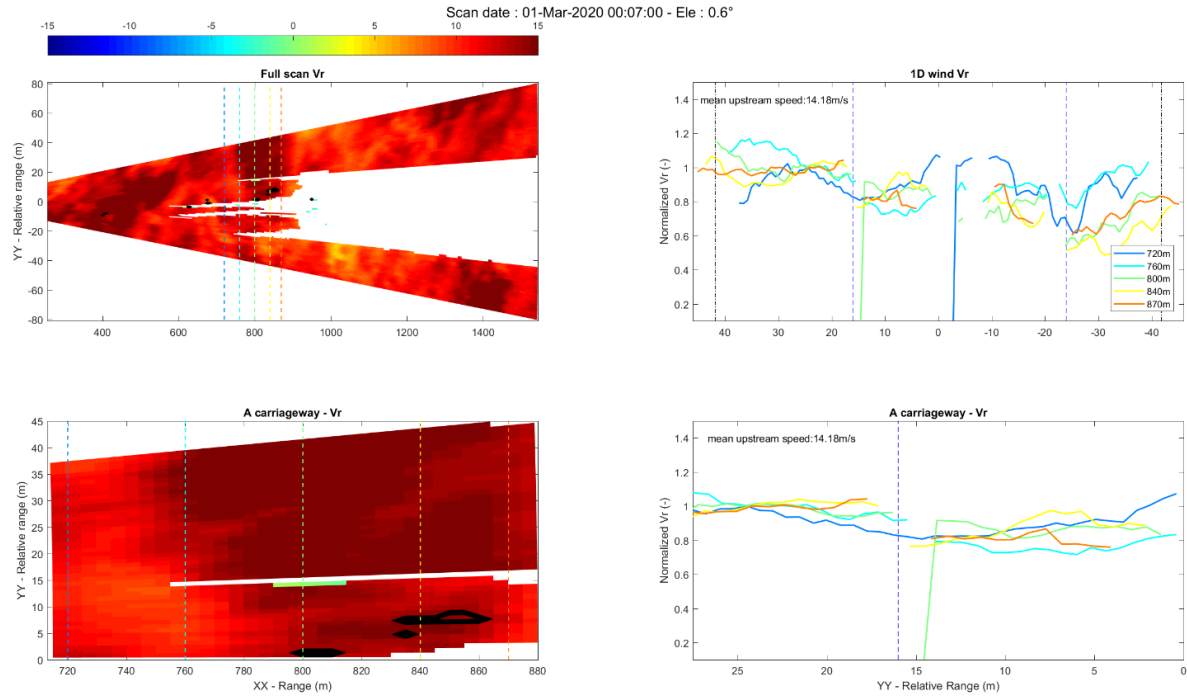


Figure 38 – Microscale PPI scan at 0.6° elevation the 1<sup>st</sup> of March 2020 at 00:07:00 UTC

### 8.3. Influence of wind direction

Most of the time, wind is coming from West or South-West. Timestamps and wind direction were obtained via the wind sensor table provided by Amey group.

#### 8.3.1. South-East wind

Because windshields were installed on both sides of the bridge, when the wind direction is opposed to its most frequent pattern, the same behavior is expected to appear on the B carriageway than on the A.

The 13/03/2020 is a day composed mostly of opposite wind direction:

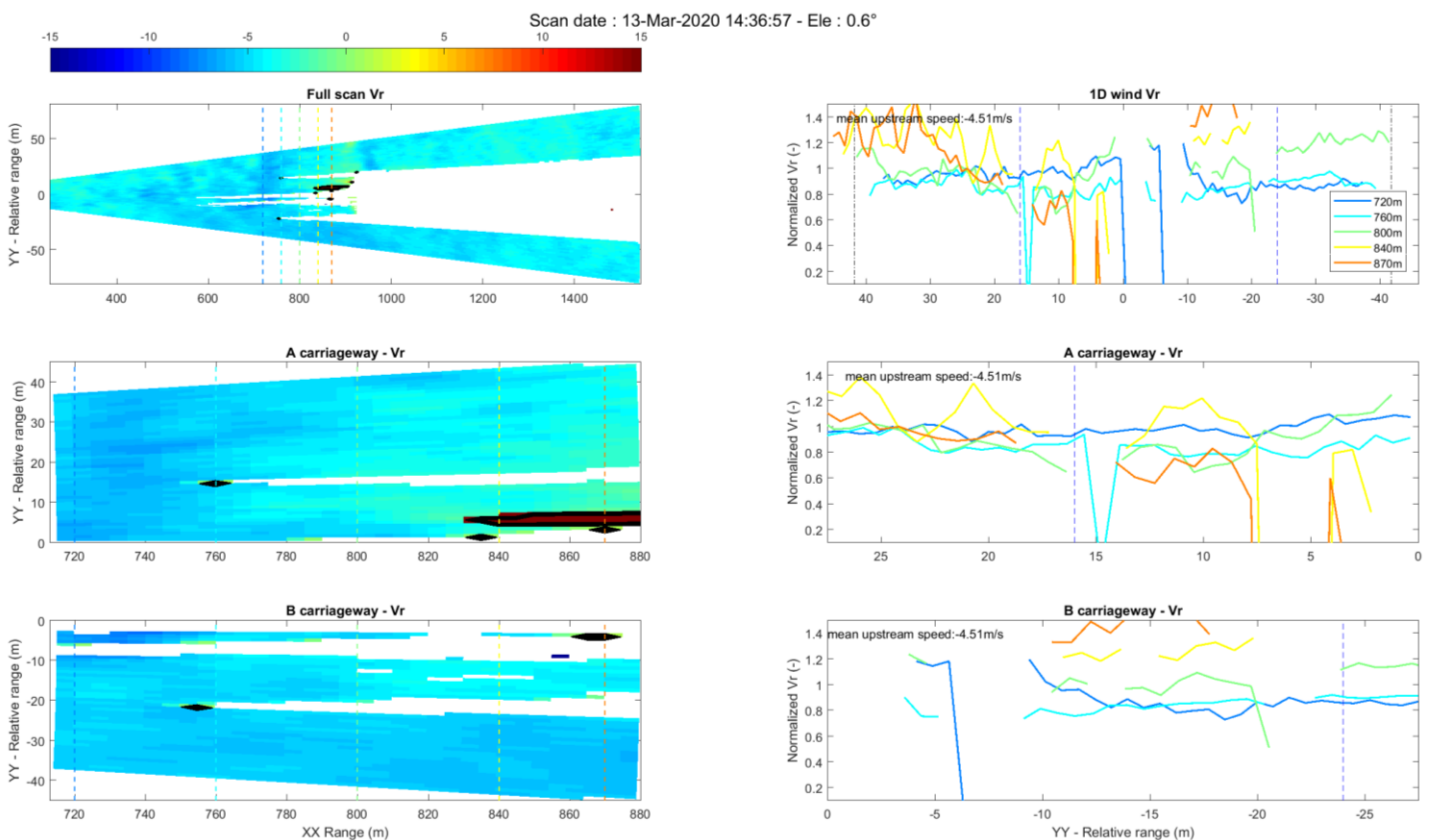


Figure 39 - 13/04/2020 – 14:36:57 (0.6°)

On B carriageway, it is possible to distinguish a decrease of wind speed just after the windshield (Doppler speed graph, on lower right).

Of course, as similar behaviors are expected, the same limitations have to be applied regarding gusts and wake effect.

#### 8.3.2. Wind direction perpendicular to bridge

## Assessment of the impact of windshields on Queensferry bridge with Windcube 100S

When the wind is weak (approx.  $<5\text{m/s}$ ) and perpendicular to the bridge, radial wind speeds are very low and noisy and no impact of wind shields can be observed. In those cases, during rush hours, the Lidar measures mostly the turbulence and the wakes behind vehicles. In addition, we recommend in such cases not to use the normalized wind profiles which are too noisy due to the very low upstream wind. The wind profiles should be plotted directly in order to be able to see the wind structures as it can be observed on the PPI scans.

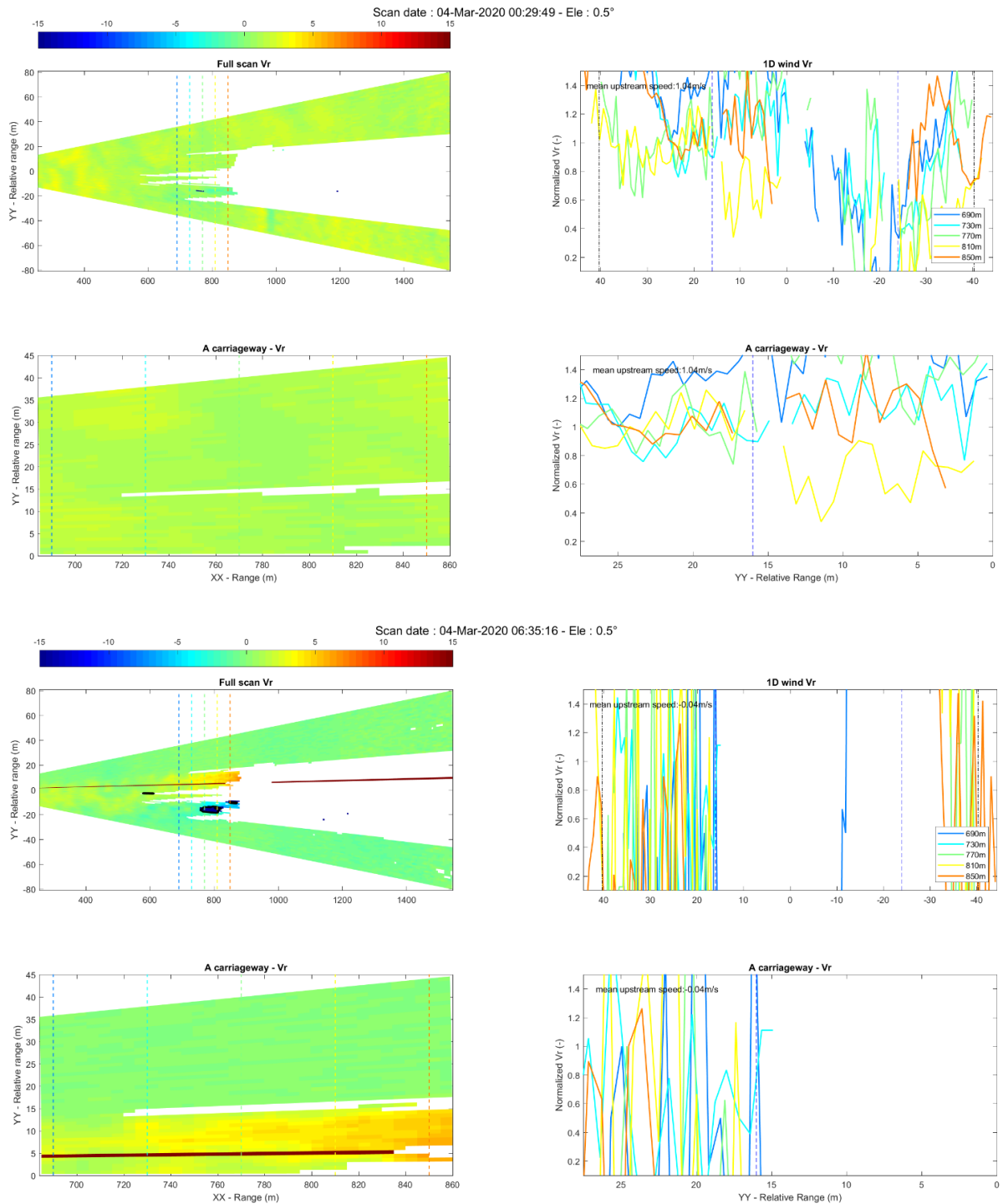


Figure 40 – 3th of March 2020 – 00:29:49:57 (0.5°) (Top) and 06:35:16 (0.5°) (Bottom)

## Assessment of the impact of windshields on Queensferry bridge with Windcube 100S

When the wind increases, similar wind decreases behind wind shields and similar behaviors with height can be observed. No wind slowdown can be observed on the first profile at 720 and 760m which remain above wind shields. Going lower, with profiles at 800, 840 and 870m, the wind slowdown is more and more important.

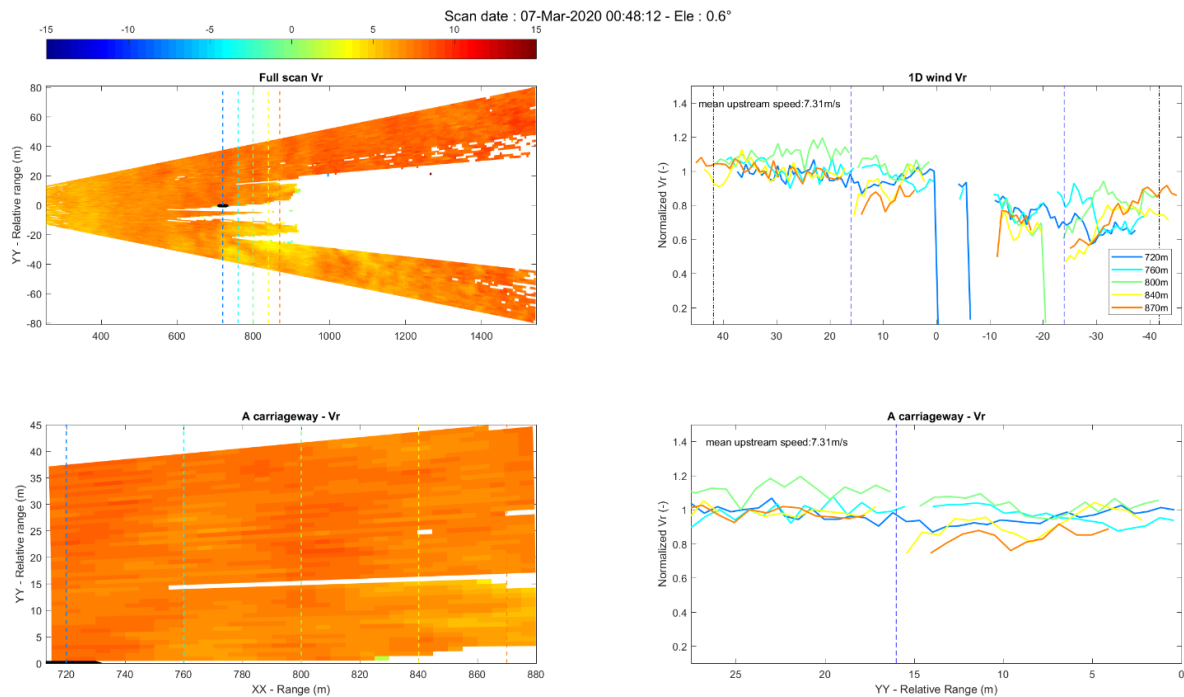


Figure 41 – 7th of March 2020 – 00:48:12 (0.6°)

When the upstream wind increases the same day, the same behaviors can be observed as the scan below but more chaotic as instantaneous wind profiles are analyzed only.

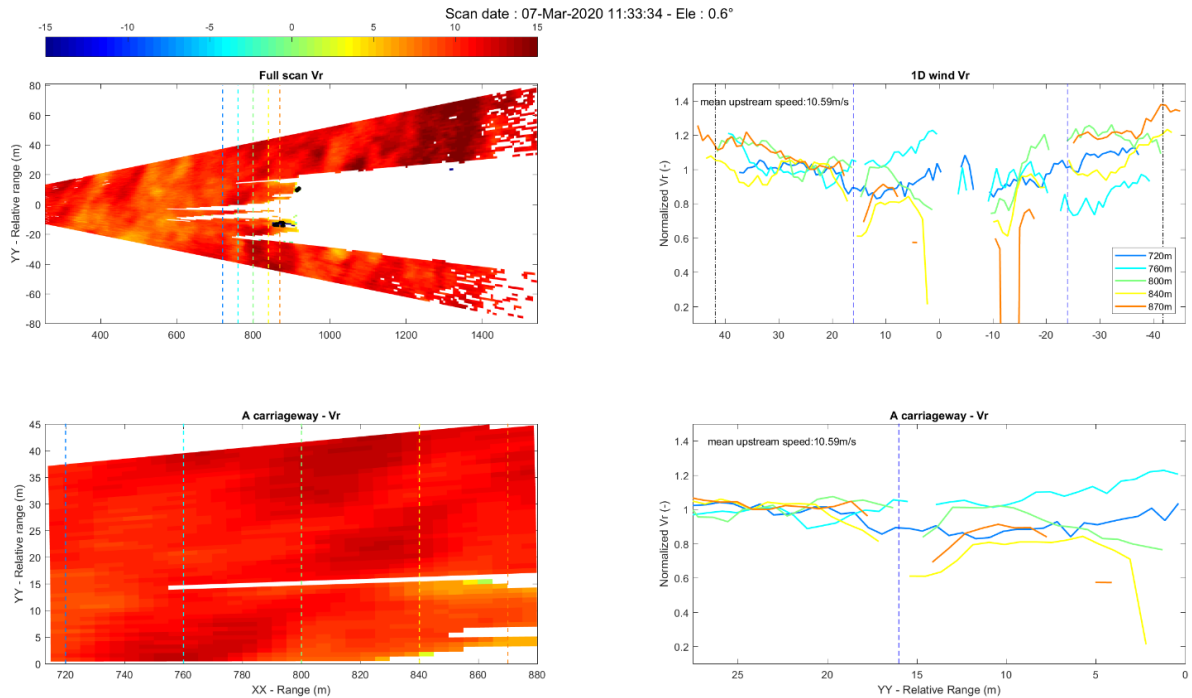


Figure 42 – 7th of March 2020 – 11:33:34 (0.6°)

## 9. Analysis – RHI

### 9.1.1. Tower and Gantry effect

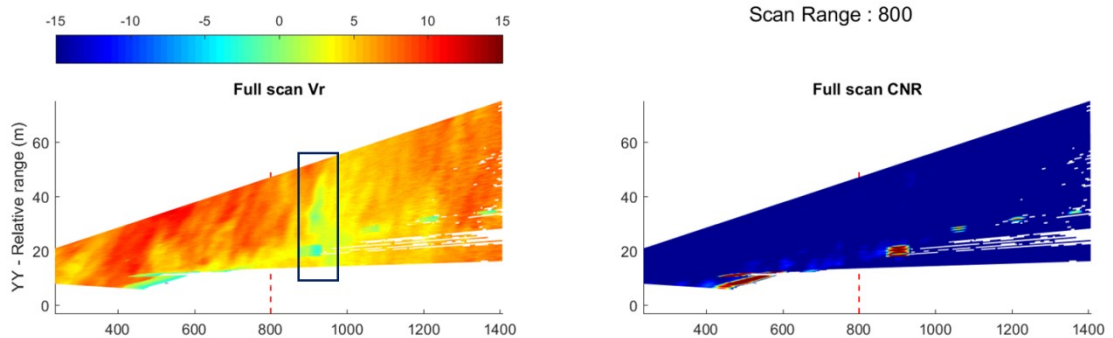


Figure 43 - 09/03/2020 – 14:54:27 (19.8°)

As the south Tower is positioned about 1km away, the effect seen on the scans were identified as being caused by the gantry located on the tower.

# Assessment of the impact of windshields on Queensferry bridge with Windcube 100S

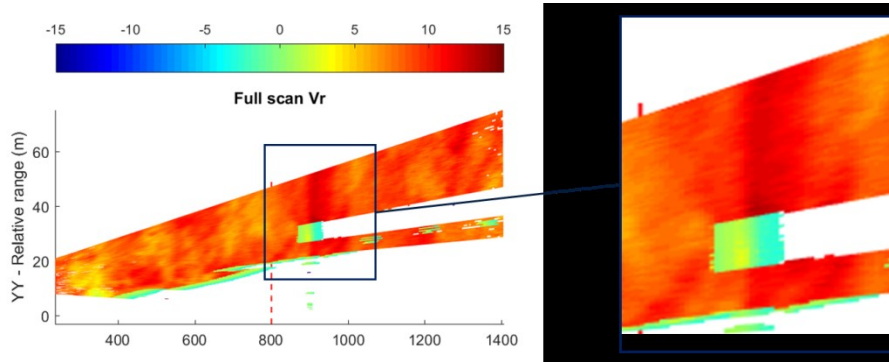


Figure 44 - 09/03/2020 – 22:55:46 (19.9°)

Appearing at regular space, with a seemingly constant elevation from ground, tower and gantry can be observed on the whole database.

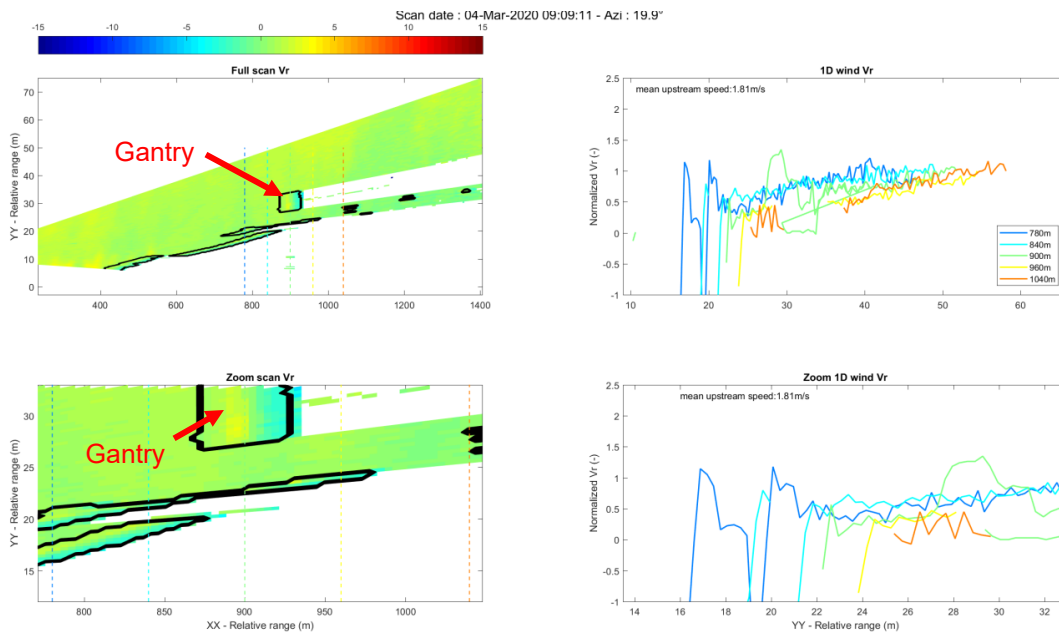


Figure 45 - 04/03/2020 – 09:04:12 (19.8°)

As this effect is seen on both type of RHI, the size of the object is far from negligible.

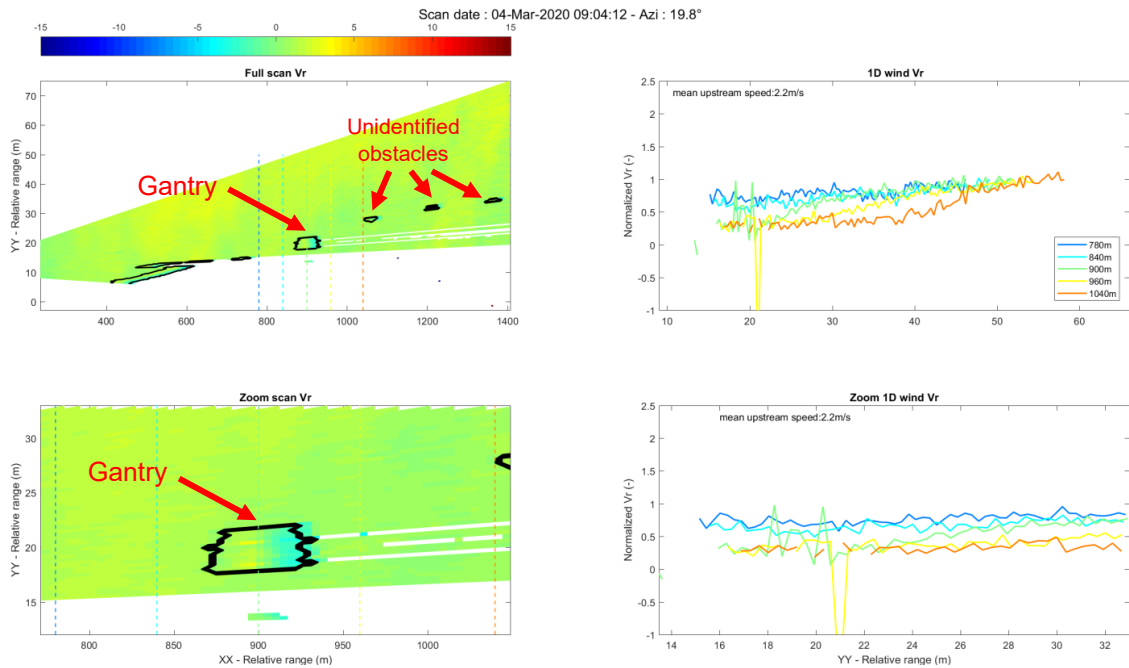


Figure 46 - 04/03/2020 – 09:09:11 (19.9°)

### 9.1.2. Complex wind

For most scans, very turbulent winds were observed.

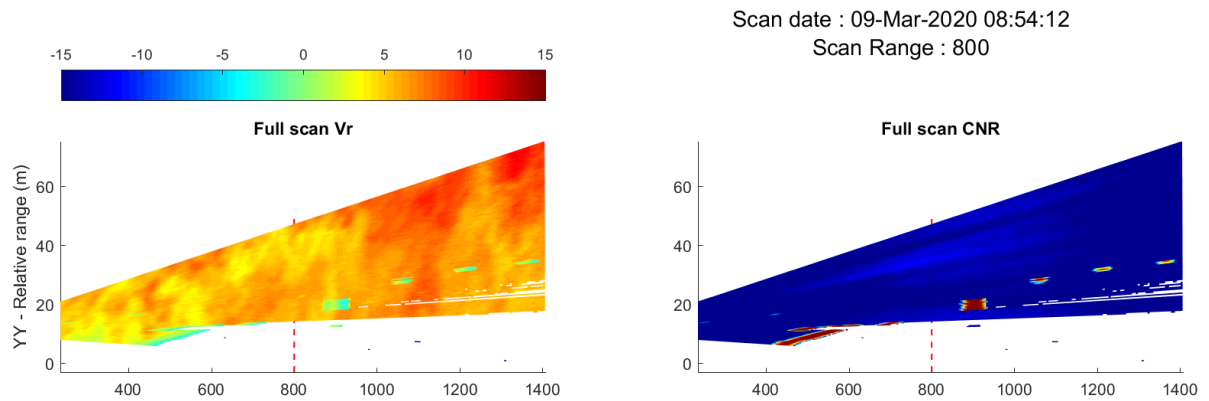


Figure 47 - 09/03/2020 – 08:54:12 (19.8°)

### 9.1.3. Rain

Light rain combined with high wind can be observed on RHI scan, characterized by their vertically layered structure and the high CNR associated.

The projection of water by passing vehicles reinforces this phenomenon near ground, leading to an effect of wind gust.

Assessment of the impact of windshields on Queensferry bridge with Windcube 100S

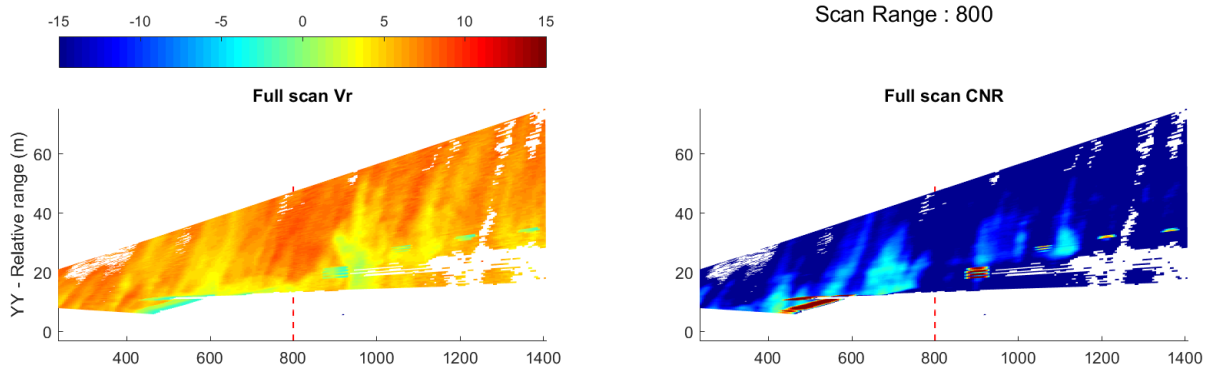


Figure 48 - 09/03/2020 – 15:53:57 (19.8°)

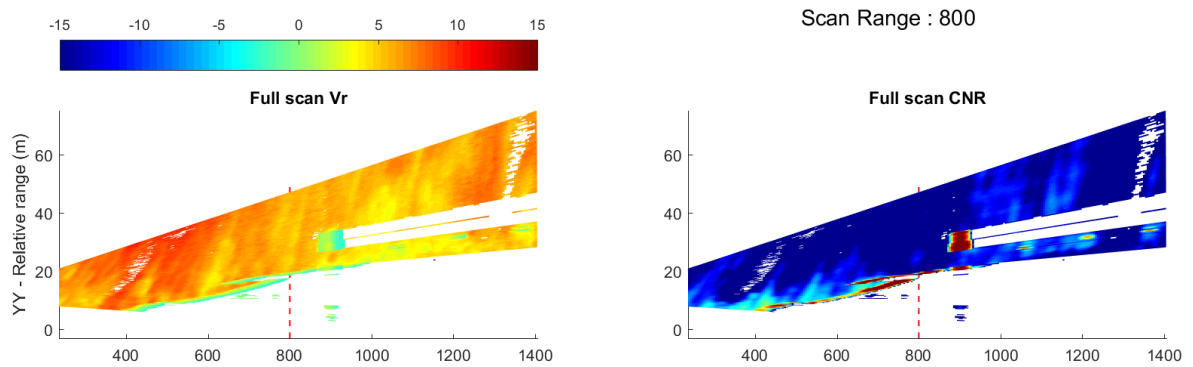


Figure 49 - 09/03/2020 – 15:54:43 (19.9°)

# 10. Some limitations of the dataset

## 10.1. Radial issue

On the second week of measurement, an issue with data generated was observed for all types of scan. Scans appeared as damaged, with erroneous wind speed displayed for a given distance.

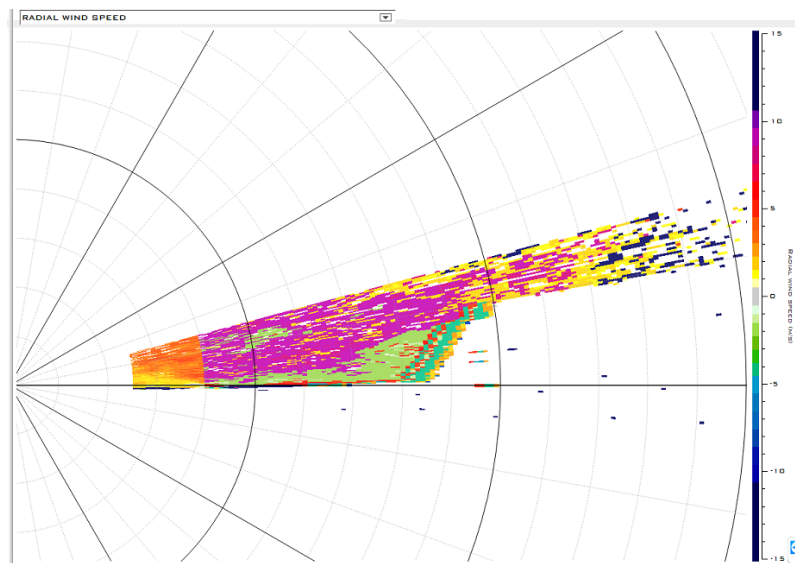


Figure 50 - RHI scan affected by radial error after 100m

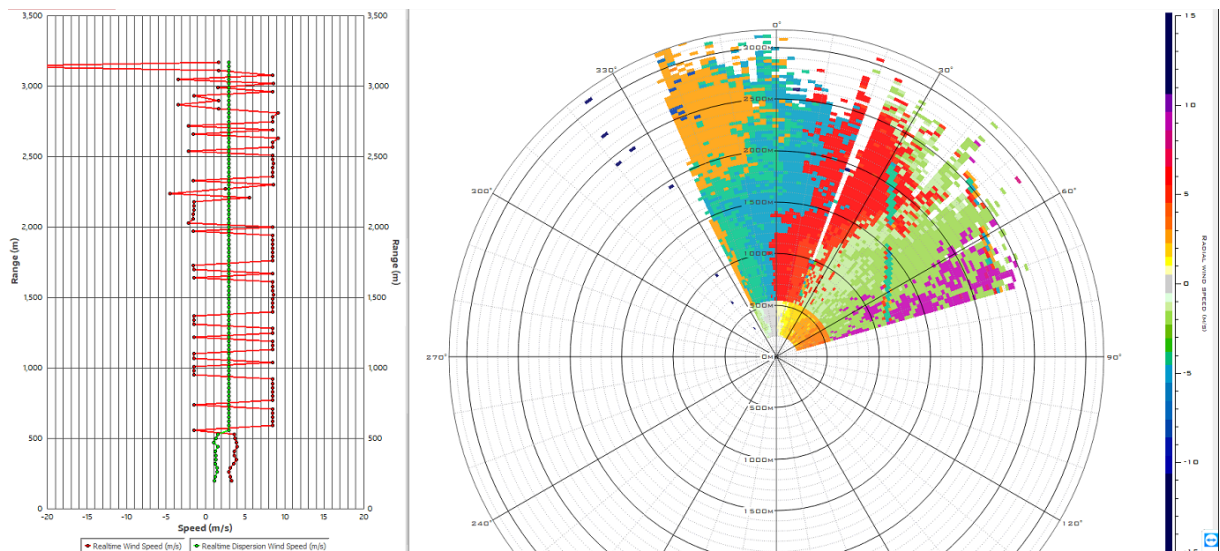


Figure 51 - PPI mesoscale affected by radial error

Once identified in software, the cause of the issue was successfully corrected.

It was found that 8 days (from 02/02/2020 to 10/02/2020) of data were corrupted. However, as the raw data were not affected by the issue, radial data could be reprocessed again.

After the development, test, and installation of a reprocess data tool on the remote computer, all data were successfully corrected and added to the database.

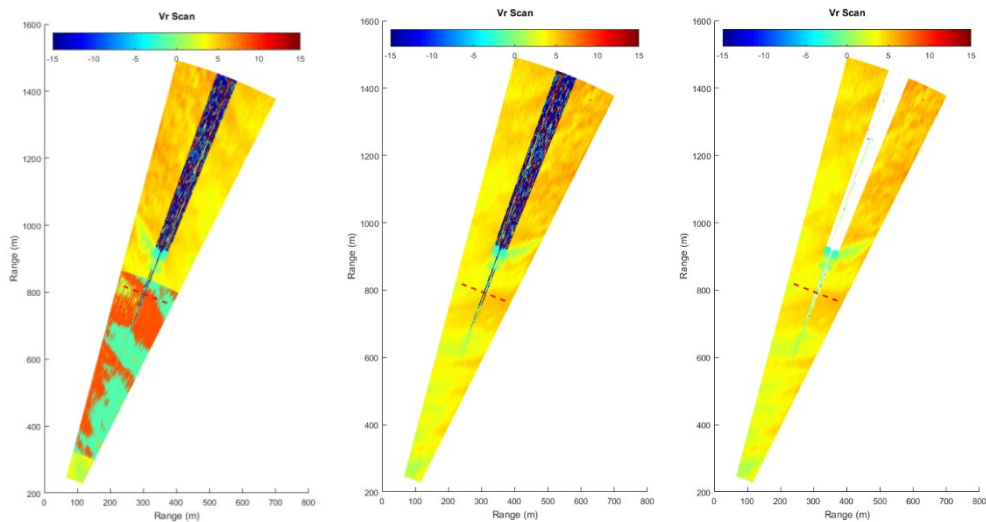


Figure 52 - On the left is the scan obtained with the radial issue. On center is the scan corrected. On the right is the corrected scan filtered

## 10.2. Backlash

After using the obstacles filter, some high CNR kept on appearing for the counter rotative scan.

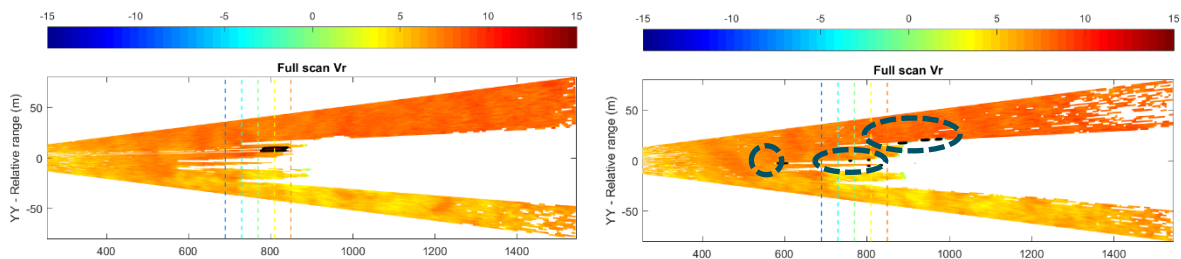
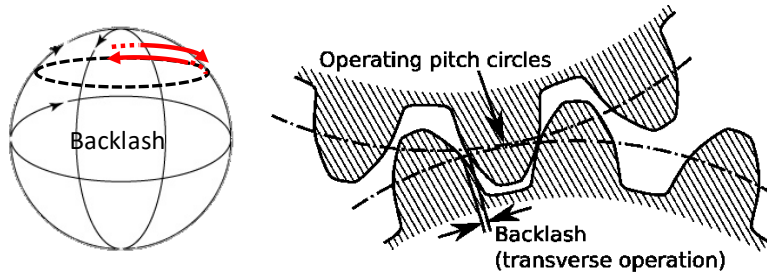


Figure 53 - Left scan was obtained in direct rotation while right scan is in indirect rotation. Circled in blue are the high CNR, representative of obstacles not filtered

In a scanning Lidar, backlash can appear if scans are performed successively in opposite directions, for instance with the following loop programming:

1. PPI in direct direction
2. Exactly same PPI in indirect direction



Here, we have a case where the variation of the backlash causes the filter to not fully capture the CNR.

To solve this issue, a new filter fully covering the CNR was created and is used to replace the older filter.

### 10.3. Difference in obstacle detection at same elevation

It was observed on several scans a lower than expected distance of both windshield to the Lidar.

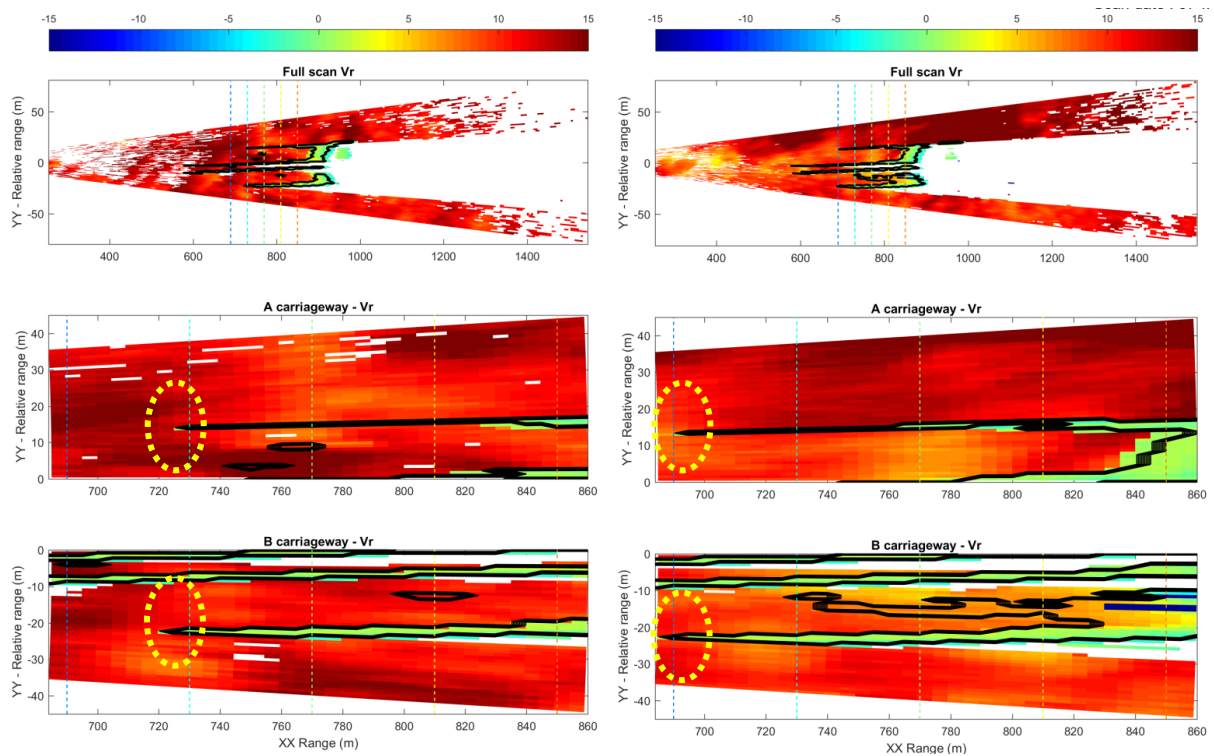


Figure 54 - Shift of windshield detection observed on second scan (circled in yellow)

With a same elevation, first detection of Windshield “jumps” here from ~720m to ~690m.

The issue was found to occur after a shift of scenario (for example, by changing the elevation from 0.5 to 0.6°) and concerns all 120 scans of the same sequence. The issue is solved after a new change of sequence, and don't seem to appear for the rest of the day.

The cause was limited to 3 possibilities:

- Shift of 1m attitude of the bridge
- Shift of few cm of the Lidar altitude
- Shift of tenths of degree of the scanning head angle

The altitude of both the Lidar and the bridge were found to be highly implausible reason as the change are too big to occur naturally and no correlation with live-event was found. The scanning head angle is the most probable cause.

The issue was identified to appear no more than twice per day, and thus concerns a low quantity of scans (estimated 1%). A deep statistical analysis is recommended to fully understand the impact on the database.

Data measured are still exploitable as only the angle displayed is off by some decimals; the main impact should be on display of data with the obstacle filter activated, where a part of the windshield might not be properly covered.

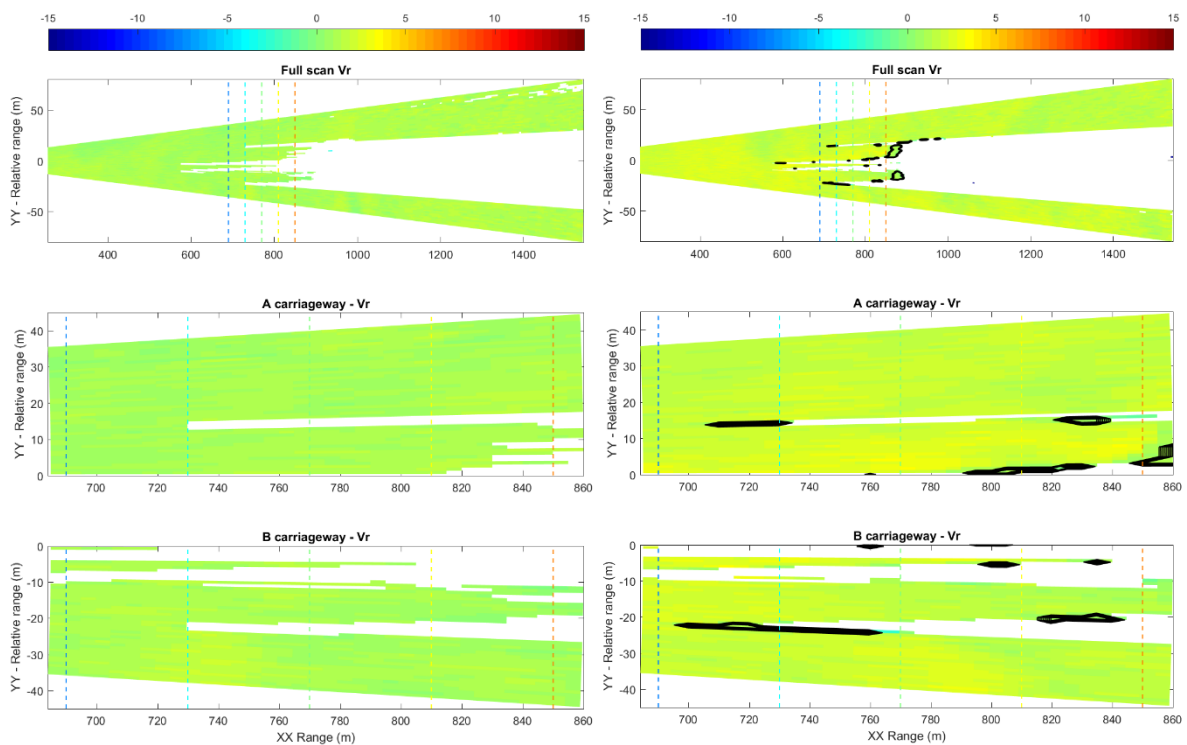


Figure 55 - No shift vs detection shift with obstacle filtering activated

# 11. Summary and Perspectives

## 11.1. Summary

### 11.1.1. Achievements

- Windcube100S was working continuously between February to May 2020. The data availability without rain allowed to reach at least 1.5km and thus to go beyond the South tower. In case of rains and of wet roads, lower data availabilities were observed as expected.
- The scenarios chosen were finally mostly based on microscale PPI to produce wind data every 1m across the bridge, every 5 m along the line of sight and every 10s.
- Some data are contaminated by road traffic (lower availability and measurement of wakes behind cars or trucks).
- Specific scripts have been adapted to
  - o Filter out as much as possible obstacles to only keep the measurement of winds
  - o Extract relevant data for the project profiles of wind across the bridge width at different distances to the Lidar to see the impact of the wind shields at different heights above the road
- Many different types of data are finally available to perform in-depth studies of the impact of wind shields: Doppler spectra, radial wind speeds, filtered radial wind speeds, extraction of profiles across the bridge at different distances from the Lidar and reconstructed wind upstream and downstream the bridge. The figures are also provided as well as the pictures for easing analysis by non-data scientists.

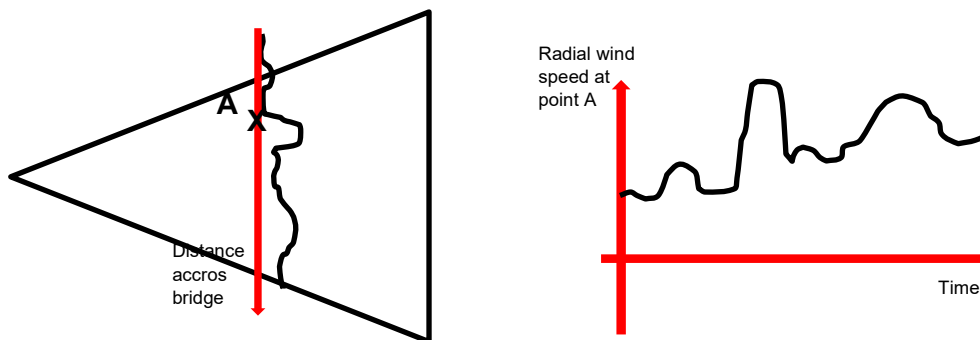
### 11.1.2. Main technical results

- Fluctuations of upstream winds of the bridge have been observed on all scans and no case with homogeneous and steady winds were observed. Their amplitude was usually between 10% to 30%. The Mesoscale PPI scans provide all the information needed to better characterize the properties of upstream wind.
- In many cases, decrease of wind speeds can be observed behind wind shields due to the blockage effect. This decrease is of about 10 to 30% depending on the upstream wind conditions and depending on the scan. Indeed, the strong fluctuations of upstream winds make difficult the assessment of the intrinsic impact of the wind shields on the wind.
- For moderate & strong winds, our observations show that
  - o Above the wind shields (profiles located before wind shield), the wind is not really impacted by the bridge itself.
  - o The wind slowdown just behind the wind shields is much lower than the upstream wind. The slowdown is greater closer to the ground.
  - o the wind accelerates again 5m after the wind shields inside the windshields. This increase of wind speed can't be fully explained. It may be partially explained by wind gusts as wind speed varies in time of about 20% in this case.
- When the wind is perpendicular to the bridge
  - o Completely perpendicular or weak, no impact of the wind shield can be seen since the radial wind speeds measured are too low. In addition they can measure the wakes of the vehicles.

- If the wind is sufficiently high, the same behaviors as mentioned previously can be observed.

## 11.2. Recommendations / Suggestions for future work

- To analyze in detail the mesoscale PPI scan to better characterize the upstream wind which was always observed as very unsteady. These results could help to perform new CFD simulations in using as inputs the characteristics of the upstream winds as measured by the Lidar: averaged wind speed, averaged wind direction, standard deviation of the wind speed (turbulent component), or imposed spatial heterogeneities
- To average PPI scans over a period like 10min with similar wind conditions to calculate statistical wind profiles across bridge. This will allow to remove the effect of the unsteadiness of the winds and thus highlight the impact of the wind shields
- To compare mesoscale and microscale PPI scans could allow to better remove the unsteadiness part of the upstream wind
- To analyze further the data, plot the radial wind speeds in time at several points behind wind shields instead of plotting profiles across the bridge.



## Annex

Angle	Micro-patterns above wind shields	Wind downstream wind shields	Bridge coverage	Wind downstream South tower
0°	[250 – 500m]	[500 – 600m]	[250 – 650m]	
0.5°	[250 – 700m]	[700 – 800m]	[250 – 850m]	
0.6°	[250 – 750m]	[750 – 900m]	[250 – 950m]	
0.7°	[250 – 800m]	[800 – 1000m]	[250 – 1050m]	
0.8°	[250 – 900m]	[900 – 1100m]	[250 – 1150m]	
0.9°	[250 – 1000m]	[1000 – 1150m]	[250 – 1200m]	
1.0°	[250 – 1000m]	[1000 - 1150m]	[250 – 1200m]	

Ranking table used to estimate best microscale PPI angle elevation

Color: Good / A priori Sufficient / Bad  
 [x - y]: data range availability



